

UCLA

UCLA Electronic Theses and Dissertations

Title

Novel Insights into Triglyceride and Cholesterol Metabolism

Permalink

<https://escholarship.org/uc/item/7z72w1zc>

Author

Hu, Xuchen

Publication Date

2019

Peer reviewed|Thesis/dissertation

UNIVERSITY OF CALIFORNIA

Los Angeles

Novel Insights into Triglyceride and Cholesterol Metabolism

A dissertation submitted in partial satisfaction of the requirements
for the degree Doctor of Philosophy in Molecular Biology

by

Xuchen Hu

2019

© Copyright by

Xuchen Hu

2019

ABSTRACT OF THE DISSERTATION

Novel Insight into Triglyceride and Cholesterol Metabolism

by

Xuchen Hu

Doctor of Philosophy in Molecular Biology

University of California, Los Angeles, 2019

Professor Stephen G. Young, Chair

Lipids are a class of biomolecules that play an essential role in numerous biochemical functions, including energy production and homeostasis, cellular communication, and plasma membrane structure. However, lipids are also linked to many diseases and pathological processes, the most common of which are heart disease, diabetes, and inflammation. In order to maintain homeostasis, the body has an intricate and complex transport system to deliver cholesterol and fatty acid from the diet to vital tissues and organs, as well as a method to transport excess cholesterol from tissues and cells back to the liver where it can be excreted or recycled. Disruption or dysregulation in any parts of this system results in life-threatening diseases such as coronary artery disease. Utilizing a variety of biochemical, cell biology, and imaging approaches, we describe several recent findings in two important aspects of lipid metabolism—intravascular triglyceride metabolism and macrophage reverse cholesterol transport.

In the first several sections, studies describe the protein GPIHBP1. GPIHBP1 is a protein of capillary endothelial cells that is responsible for capturing lipoprotein lipase (LPL) and

transporting it to the capillary lumen where LPL functions in hydrolysis of triglyceride-rich lipoproteins in the bloodstream, releasing fatty acids for use by surrounding tissues. Without GPIHBP1, LPL never reaches the capillary lumen and triglyceride hydrolysis is deficient, resulting in severe hypertriglyceridemia. In the following studies, we first developed and characterized several monoclonal antibodies (mAbs) against human GPIHBP1, then utilized these mAbs to better understand GPIHBP1's role in hypercholesterolemia and cancer lipid metabolism.

In the later sections, we investigated macrophages and their role in reverse cholesterol transport. Macrophages have been known to internalize cholesterol and offload excess cholesterol back to the bloodstream and the liver. Cholesterol efflux from macrophages has been studied extensively and has generally been thought to involve direct transport of cholesterol from ATP-binding cassette (ABC) transporters to acceptors in the plasma such as high density lipoproteins (HDL). In these studies, we demonstrate that macrophages release ~20 to 100-nm particles derived from the plasma membrane and that these particles are highly enriched in a pool of accessible cholesterol. This release of cholesterol-rich particles would greatly augment macrophages' ability to offload excess cholesterol in reverse cholesterol transport.

The dissertation for Xuchen Hu is approved.

Peter John Tontonoz

Dana Leanne Jones

Karen Reue

Stephen G. Young, Committee Chair

University of California, Los Angeles

2019

Table of Contents

Abstract of the Dissertation	ii
List of Figures and Tables.....	vii
Acknowledgements.....	xiv
Vita.....	xvii
Chapter 1 — GPIHBP1 in Plasma Triglyceride Metabolism; Macrophage Cholesterol Export.....	1
GPIHBP1 and Plasma Triglyceride Metabolism	2
Structure of GPIHBP1	2
GPIHBP1 Transports LPL to the Capillary Lumen.....	3
GPIHBP1 Expression in Tissues	3
GPIHBP1–LPL Complex Required for Triglyceride-rich Lipoprotein Margination	4
GPIHBP1 Mutations Cause Chylomicronemia	4
Conclusions.....	5
Macrophage and Atherosclerosis.....	7
Macrophage and Reverse Cholesterol Transport.....	7
Macrophages and Cholesterol Microdomains	8
Utilizing NanoSIMS Imaging to Visualize Lipids.....	8
Conclusions.....	10
Chapter 2 — Monoclonal Antibodies That Bind to the Ly6 Domain of GPIHBP1 Abolish the Binding of LPL.....	26
Chapter 3 — GPIHBP1 Autoantibodies in a Patient with Unexplained Chylomicronemia.....	35
Chapter 4 — GPIHBP1 Expression in Gliomas Promotes Utilization of Lipoprotein-derived Nutrients	44
Chapter 5 — Macrophages Release Plasma Membrane-derived Particles Rich in Accessible	

Cholesterol.....	92
Chapter 6 — Release of Cholesterol-Rich Particles from the Macrophage Plasma	
Membrane	103
Chapter 7 — Conclusions and Future Directions	139
Appendix I — A lipoprotein lipase (LPL)-specific monoclonal antibody, 88B8, that abolishes the binding of LPL to GPIHBP1	150
Appendix II — Lipoprotein Lipase Reaches the Capillary Lumen in Chickens Despite an Apparent Absence of GPIHBP1	161
Appendix III — High-resolution Imaging and Quantification of Plasma Membrane Cholesterol by NanoSIMS	179

List of Figures and Tables

Chapter 1

Figure 1 — Schematic of GPIHBP1's role in plasma triglyceride metabolism	12
Figure 2 — LPL is present in capillaries of skeletal muscle in wild-type mice but is mislocalized in skeletal muscle of <i>Gpihbp1</i> knockout mice	13
Figure 3 — GPIHBP1 is required for margination of triglyceride rich lipoproteins along the capillary lumen	14
Figure 4 — Schematic of the NanoSIMS instrument showing the focused primary ion beam and the collection and detection of secondary ion signals.....	15
Figure 5 — NanoSIMS imaging reveals total cholesterol and accessible cholesterol on the plasma membrane of CHO cell	16

Chapter 2

Figure 1 — Western blots with GPIHBP1-specific monoclonal antibodies.....	30
Figure 2 — Testing the ability of GPIHBP1-specific mAbs to bind to GPIHBP1 on the surface of GPIHBP1-transfected cells.....	30
Table 1 — Kinetic rate constants for GPIHBP1-specific mAbs by SPR.....	31
Figure 3 — Kinetics for the interaction between mAb RE3 and GPIHBP1 by surface plasmon resonance	31
Figure 4 — Monoclonal antibodies RG3 and RE3 block LPL binding to GPIHBP1 in a cell-free LPL–GPIHBP1 binding assay	32
Figure 5 — RG3 and RE3, but not RF4, block the binding of LPL to GPIHBP1 on the surface of cultured cells.....	32

Figure 6 — Dose-dependent inhibition of LPL binding to GPIHBP1 by mAbs RE3 and RG3	32
Figure 7 — Detection of GPIHBP1 in human tissues with GPIHBP1- specific monoclonal antibodies.....	33
Figure 8 — An ELISA to detect GPIHBP1 in human plasma.....	33

Chapter 3

Figure 1 — Detecting GPIHBP1 autoantibodies with a solid-phase ELISA.....	38
Figure 2 — Western blot demonstrating the binding of GPIHBP1 autoantibodies in the plasma from patient A1 to human GPIHBP1 in the medium of transfected Drosophila S2 cells.....	39
Figure 3 — GPIHBP1 autoantibodies in the plasma of patient A1 abolish the ability of GPIHBP1 to bind LPL	39
Figure 4 — Immunocytochemistry studies showing that the GPIHBP1 autoantibodies in the plasma of patient A1 bind to GPIHBP1 on the surface of GPIHBP1- transfected CHO pgsA-745 cells and abolish binding of LPL.....	40
Figure 5 — Levels of LPL catalytic activity in the postheparin plasma of patient A1 were low, whereas levels of hepatic lipase activity were high.....	41
Figure 6 — The plasma of patient A1 does not contain autoantibodies against LPL	41

Chapter 4

Table 1 — Human glioma tumor samples	50
Figure 1 — GPIHBP1 expression in endothelial cells of several human gliomas	51
Figure 2 — Detection of GPIHBP1 in capillaries of human glioma samples with three different monoclonal antibodies (mAbs) against GPIHBP1	52

Figure 3 — GPIHBP1 is expressed by capillary endothelial cells in mouse gliomas	53
Figure 4 — Expression of GPIHBP1 and GLUT1 in mouse glioma endothelial cells...	55
Figure 5 — Lipoprotein lipase colocalizes with GPIHBP1 in capillaries of gliomas	57
Figure 6 — NanoSIMS imaging reveals margination of [² H]TRLs in glioma capillaries and ² H enrichment in adjacent glioma cells	59
Figure 7 — NanoSIMS imaging showing increased ² H enrichment in glioma tissue 30 min after an intravenous injection of [² H]TRLs.....	60
Figure 8 — Tissue uptake of fatty acid and glucose-derived nutrients by mice harboring CT-2A gliomas	62
Figure 9 — Intravascular lipolysis as a source of lipid nutrients for gliomas	65

Chapter 5

Figure 1 — Release of particles from the plasma membrane of macrophages	94
Figure 2 — Macrophages release particles enriched in cholesterol	95
Figure 3 — NanoSIMS images of macrophages that were loaded with [¹³ C]cholesterol and then incubated with [¹⁵ N]ALO-D4 revealing that macrophage-derived particles are rich in cholesterol (high ¹⁵ N/ ¹⁴ N and ¹³ C/ ¹² C ratios)	96
Figure 4 — Macrophages release cholesterol-enriched particles when incubated in medium containing 1% LPDS.....	96
Figure 5 — CHO-K1 cells do not produce cholesterol-rich particles	97
Figure 6 — Particles released by macrophages contain cholesterol and sphingomyelin, as judged by ALO-D4 and lysenin binding.....	97
Figure 7 — Binding of [¹⁵ N]ALO-D4 to macrophage-derived particles depends on the cholesterol content in macrophages	98

Figure 8 — NanoSIMS analysis of [¹⁵ N]ALO-D4 binding to cholesterol-loaded wild-type macrophages or Lxr α /Lxr β double-knockout macrophages (LXR ^{-/-}) in the presence of LXR and RXR agonists or vehicle (DMSO) alone.....	99
Figure 9 — HDL removes cholesterol from macrophage-derived particles.....	100

Chapter 6

Figure 1 — Macrophages release particles from the plasma membrane by a process that resembles budding.....	126
Figure 2 — Macrophages release particles during movement (extension and retraction) of filopodia and lamellipodia	127
Figure 3 — Inhibiting macrophage movement with latrunculin A or blebbistatin abolishes release of particles onto the surrounding substrate.....	128
Figure 4 — Particles released from macrophages are released from the plasma membrane and are enriched in accessible cholesterol.....	129
Figure 5 — Visualization, by scanning EM, of particles released from the plasma membrane of macrophages.....	130
Figure 6 — Correlative SEM and NanoSIMS imaging of macrophages and the plasma membrane-derived particles on the surrounding substrate	131
Figure 7 — Isolation of particles released onto the substrate by RAW 264.7 macrophages.....	132
Figure 8 — An enrichment in proteins of focal adhesion complexes in particles released by macrophages.....	133

Figure 9 — Correlative live-cell, scanning EM, and NanoSIMS imaging, revealing that the particles released onto the substrate during the movement of filopodia are enriched in accessible cholesterol134

Figure 10 — Particles released by macrophages onto the surrounding substrate are enriched in accessible cholesterol but not sphingomyelin-bound cholesterol135

Figure 11 — Correlative live-cell, SEM, and NanoSIMS imaging, demonstrating that particles left on the substrate during movement of filopodia and lamellipodia are enriched in accessible cholesterol but not sphingolipid-bound cholesterol136

Figure 12 — Incubating macrophages with latrunculin A alters the distribution of ALO-D4 on mouse peritoneal macrophages.....137

Figure 13 — Macrophages release accessible cholesterol-rich particles onto a polymerized collagen IV matrix.....138

Appendix I

Figure 1 — List of the mLPL-hLPL chimeras, and of the human HL-hLPL chimeras generated for the studies.....152

Figure 2 — A cell-free LPL-GPIHBP1 binding assay to test the ability of LPL-specific mAbs 5D2, 57A5, and 88B8 to block the binding of V5-tagged hLPL to GPIHBP1.....153

Figure 3 — Immunofluorescence microscopy assay to evaluate the ability of mAbs 57A5, 88B8, and 5D2 to block the binding of LPL to GPIHBP1154

Figure 4 — Testing the ability of mAbs 88B8 and 5D2 to bind to mutant forms of LPL with impaired ability to bind to GPIHBP1154

Figure 5 — Western blot studies to assess epitopes for mAbs 88B8 and 57A5.....155

Figure 6 — Testing the ability of mAbs 5D2, 57A5, and 88B8 to inhibit the catalytic activity of purified hLPL.....155

Figure 7 — Immunofluorescence microscopy studies to assess the ability of LPL, HL, and LPL–HL chimeras to bind to GPIHBP1156

Figure 8 — Assessing the ability of mAbs 57A5, 88B8, and 5D2 bind to GPIHBP1-bound LPL.....157

Figure 9 — Testing the capacity of mAbs 57A5, 88B8, and 5D2 to bind to hLPL in capillaries of the skeletal muscle of *Lpl*^{-/-} mice carrying a hLPL transgene driven by the muscle creatine kinase promoter (*Lpl*^{-/-}MCK-hLPL).....158

Appendix II

Figure 1 — Testing the specificity of an immunopurified goat IgG against chicken lipoprotein lipase (cLPL) with Western blots164

Figure 2 — Testing the ability of an immunopurified goat IgG against chicken lipoprotein lipase (cLPL) to bind to cLPL in cultured cells.....165

Figure 3 — LPL in chicken tissues is associated with capillaries166

Figure 4 — Chicken lipoprotein lipase (cLPL) is located along the luminal surface of capillaries.....167

Figure 5 — Chicken lipoprotein lipase (cLPL) can be released from tissues with heparin.....168

Figure 6 — Chicken lipoprotein lipase (cLPL) is released from chicken hearts by phosphatidylinositol-specific phospholipase C (PIPLC)	169
Figure 7 — Chicken lipoprotein lipase (cLPL) binds to wild-type mouse GPIHBP1 (mGPIHBP1) or human GPIHBP1 (hGPIHBP1) but not to mutant GPIHBP1 proteins (mGPIHBP1-W108S, hGPIHBP1-W109S) that lack the ability to bind cLPL.....	170
Figure 8 — Wild-type chicken lipoprotein lipase (cLPL-wt), but not a mutant cLPL with a p.C420Y mutation, binds to GPIHBP1	171
Table 1 — The GPIHBP1 locus on human chromosome 8 and the syntenic region on chicken chromosome 2	173
Figure 9 — Testing the ability of chicken lipoprotein lipase (cLPL) to bind to chicken Ly6E-like proteins on the surface of transfected cells	174

Appendix III

Figure 1 — NanoSIMS imaging of cholesterol-binding proteins on the plasma membrane of CHO-K1 cells	182
Figure 2 — NanoSIMS analysis of [¹⁵ N]ALO-D4 binding to the plasma membrane of CHO-K1 cells grown under standard conditions.	182
Figure 3 — NanoSIMS imaging of [¹⁵ N]ALO-D4 binding to the plasma membrane of CHO-K1 cells that had been loaded with cholesterol	183
Figure 4 — NanoSIMS analysis of [¹⁵ N]ALO-D4 binding to CHO-K1 cells.....	183
Figure 5 — NanoSIMS imaging of [¹⁵ N]lysenin binding to CHO-K1 cells.....	184
Figure 6 — Immunofluorescence microscopy to assess the binding of ALO-D4 and mCherry-lysenin to CHO-K1 cells.....	184

Acknowledgements

I would like to first and foremost thank my exceptional advisor, Dr. Stephen Young, for his unwavering support, mentorship, and commitment to my learning and success. It has truly been a privilege to learn from not only one of the leaders in the field of lipid metabolism, but more importantly a terrific scientist, writer, and person. I am grateful for his constant guidance and mentorship throughout my years in graduate school, from learning how to design the perfect experiments to writing better grants and manuscript. Without him, none of this would be possible.

I also want to thank to my other two vital mentors in the lab, Drs. Loren Fong and Anne Beigneux, both of whom contributed immensely to my technical skills and scientific knowledge. It has been a pleasure to learn from two such amazing and successful scientists. Dr. Fong, thank you for all your time and patience in helping me design and troubleshoot experiments. Thank you for your always thoughtful suggestions, your microscopy expertise, and most importantly your constant encouragement, especially when experiments would inevitably fail. Dr. Beigneux, thank you for teaching me everything I needed to know to start working in the laboratory, from basic cell culture and western blotting, to cloning and immunoassays. It was a comfort to know that you were always there to answer any of my questions and to give advice. In addition, thank you for allowing me to work with you on several of your projects, two of which allowed me to publish my first two papers.

I would also like to thank my other committee members, Dr. Peter Tontonoz, Dr. Karen Reue, and Dr. Leanne Jones for their advice and support throughout my thesis work. I want to thank our collaborator Dr. Haibo Jiang for his expertise in NanoSIMS and electron microscopy and for his help in preparing several manuscripts. In addition, I want to thank all of our other

collaborators, Dr. Michael Ploug, Dr. David Nathanson, Dr. Holger Gerhardt, Dr. Ken Matsumoto for their help, advice, and work on different collaborative projects. I would like to also thank my funding sources, the UCLA-Caltech MSTP program, the MSTP training grant, and the Vascular Biology Training Grant.

Next, I would like to acknowledge members of the Young and Fong laboratory for making my four years enjoyable. Throughout these four years, I had the tremendous opportunity to work with talented post-doctoral fellows, graduate student, and research scientists. Thank you all for the constant encouragement, for listening to my struggles, for helping with experiments, and most importantly for the shared laughs and fun we had. I will always be grateful for their friendship and guidance. I would especially like to thank Dr. Christopher Allan for being the person I go to for almost every problem or question. I would also like to thank Dr. Cuiwen He for our collaborations on the macrophage project and for our endeavors with NanoSIMS. I would like to thank Thomas Weston for his help with electron microscopy and for teaching me scanning EM and EM sample preparation. Also, a big thank you to Rachel Jung and Norma Sandoval for their technical help with experiments and Patrick Heizer for his help related to all mouse work. Lastly, I would like to thank the other graduate student in our laboratory, Natalie Chen, for her always encouraging and enthusiastic attitude and for our talks about life as a Ph.D. student.

Finally, I would like to thank my friends and family for their unwavering support, love, and encouragement throughout my PhD. To all my medical school friends—Dr. Nick Uhm, Dr. Lydia Ann, Dr. Ryan Ou, Karen Hui, Dr. Annie Wang, Dr. Ngan Nguyen, Dr. Vien Nguyen, Dr. Nikki Nguyen, Dr. Shelley Shi, and Ryan Chan—thank you for being there through the good and the bad times during these amazing 5 years. To my mother, Chenqi Xi, and father, Jingyu Hu,

thank you for all the love and support you've given me, for all the lessons you've taught me, and for the never-ending love and guidance. I would not be who I am or where I am without you.

Vita

Education:

July 2014 – Present	David Geffen School of Medicine at UCLA, Los Angeles, California Medical Scientist Training Program M.D. – expected 2021 Ph.D. –expected 2019
Aug. 2010 – May 2014	University of California, Berkeley, California B.A. – Honors in Molecular and Cell Biology – Genetics, Genomics, and Development Highest Distinction in General Scholarship

Honors and Awards:

2018	Vascular Biology Training Grant
2017	1 st Place UCLA Medicine Research Day Poster Competition
2016	4 th Place UCLA Medicine Research Day Poster Competition
2016	Vascular Biology Training Grant

Publications:

1. **Hu, X.**, T. A. Weston, C. He, R. S. Jung, P. J. Heizer, B. D. Young, Y. Tu, J. A. Wohlschlegel, H. Jiang, L. G. Fong, and S. G. Young. 2019. Release of cholesterol-rich particles from the macrophage plasma membrane. **In preparation.**
2. **Hu, X.**, K. Matsumoto, R. S. Jung, T. A. Weston, P. J. Heizer, C., He, N. P. Sandoval, C. M. Allan, Y. Tu, H. V. Vinters, L. M. Liau, R. M. Ellison, J. E. Morales, L. J. Baufeld, N. A. Bayley, L. He, C. Betsholz, A. P. Beigneux, D. A. Nathanson, H. Gerhardt, S. G. Young, L. G. Fong, and H. Jiang. 2019. GPIHBP1 expression in gliomas promotes utilization of lipoprotein-derived nutrients. **Submitted for publication.**
3. Eguchi, J., K. Miyashita, I. Fukamachi, K. Nakajima, M. Murakami, Y. Kawahara, T. Yamashita, Y. Ohta, K. Abe, A. Nakatsuka, M. Mino, S. Takase, H. Okazaki, R. A. Hegele, M. Ploug, **X. Hu**, J. Wada, S. G. Young, and A. P. Beigneux. 2019. GPIHBP1 autoantibody syndrome during interferon beta1a treatment. *J Clin Lipidol* **13**: 62–69.
4. He, C., **X. Hu**, T. A. Weston, R. S. Jung, P. Heizer, Y. Tu, R. Ellison, K. Matsumoto, H. Gerhardt, P. Tontonoz, L. G. Fong, S. G. Young, and H. Jiang. 2018. NanoSIMS imaging reveals unexpected heterogeneity in nutrient uptake by brown adipocytes. *Biochem Biophys Res Commun* **504**: 899–902.
5. Kim, S. X., G. Camdere, **X. Hu**, D. Koshland, and H. Tapia. 2018. Synergy between the small intrinsically disordered protein Hsp12 and trehalose sustain viability after severe desiccation. *eLife* **7**.
6. He, C. *, **X. Hu*** (co-first authors), T. A. Weston, R. S. Jung, J. Sandhu, S. Huang, P. Heizer, J. Kim, R. Ellison, J. Xu, M. Kilburn, S. J. Bensinger, H. Riezman, P. Tontonoz, L. G. Fong, H. Jiang, and S. G. Young. 2018. Macrophages release plasma membrane-

derived particles rich in accessible cholesterol. *Proc Natl Acad Sci U S A* **115**: E8499–E8508.

7. He, C., T. A. Weston, R. S. Jung, P. Heizer, M. Larsson, **X. Hu**, C. M. Allan, P. Tontonoz, K. Reue, A. P. Beigneux, M. Ploug, A. Holme, M. Kilburn, P. Guagliardo, D. A. Ford, L. G. Fong, S. G. Young, and H. Jiang. 2018. NanoSIMS analysis of intravascular lipolysis and lipid movement across capillaries and into cardiomyocytes. *Cell Metab* **27**: 1055–1066e1053.
8. He, C., **X. Hu**, R. S. Jung, M. Larsson, Y. Tu, S. Duarte-Vogel, P. Kim, N. P. Sandoval, T. R. Price, C. M. Allan, B. Raney, H. Jiang, A. Bensadoun, R. L. Walzem, R. I. Kuo, A. P. Beigneux, L. G. Fong, and S. G. Young. 2017. Lipoprotein lipase reaches the capillary lumen in chickens despite an apparent absence of GPIHBP1. *JCI Insight* **2**.
9. He, C., **X. Hu**, R. S. Jung, T. A. Weston, N. P. Sandoval, P. Tontonoz, M. R. Kilburn, L. G. Fong, S. G. Young, and H. Jiang. 2017. High-resolution imaging and quantification of plasma membrane cholesterol by NanoSIMS. *Proc Natl Acad Sci U S A* **114**: 2000–2005.
10. **Hu, X.**, G. M. Dallinga-Thie, G. K. Hovingh, S. Y. Chang, N. P. Sandoval, T. L. P. Dang, I. Fukamachi, K. Miyashita, K. Nakajima, M. Murakami, L. G. Fong, M. Ploug, S. G. Young, and A. P. Beigneux. 2017. GPIHBP1 autoantibodies in a patient with unexplained chylomicronemia. *J Clin Lipidol* **11**: 964–971.
11. Beigneux, A. P., K. Miyashita, M. Ploug, D. J. Blom, M. Ai, M. F. Linton, W. Khovidhunkit, R. Dufour, A. Garg, M. A. McMahon, C. R. Pullinger, N. P. Sandoval, **X. Hu**, C. M. Allan, M. Larsson, T. Machida, M. Murakami, K. Reue, P. Tontonoz, I. J. Goldberg, P. Moulin, S. Charrière, L. G. Fong, K. Nakajima, and S. G. Young. 2017. Autoantibodies Against GPIHBP1 as a Cause of Hypertriglyceridemia. *N Engl J Med* **376**: 1647–1658.
12. **Hu, X.**, M. W. Sleeman, K. Miyashita, M. F. Linton, C. M. Allan, C. He, M. Larsson, Y. Tu, N. P. Sandoval, R. S. Jung, A. Mapar, T. Machida, M. Murakami, K. Nakajima, M. Ploug, L. G. Fong, S. G. Young, and A. P. Beigneux. 2017. Monoclonal antibodies that bind to the Ly6 domain of GPIHBP1 abolish the binding of LPL. *J Lipid Res* **58**: 208–215.
13. Allan, C. M., M. Larsson, **X. Hu**, C. He, R. S. Jung, A. Mapar, C. Voss, K. Miyashita, T. Machida, M. Murakami, K. Nakajima, A. Bensadoun, M. Ploug, L. G. Fong, S. G. Young, and A. P. Beigneux. 2016. A lipoprotein lipase (LPL)-specific monoclonal antibody, 88B8, that abolishes the binding of LPL to GPIHBP1. *J Lipid Res* **57**: 1889–1898.
14. Quintero-Rivera, F., Q. J. Xi, K. M. Keppler-Noreuil, J. H. Lee, A. W. Higgins, R. M. Anchan, A. E. Roberts, I. S. Seong, X. Fan, K. Lage, L. Y. Lu, J. Tao, **X. Hu**, R. Berezney, B. D. Gelb, A. Kamp, I. P. Moskowitz, R. V. Lacro, W. Lu, C. C. Morton, J. F. Gusella, and R. L. Maas. 2015. MATR3 disruption in human and mouse associated with bicuspid aortic valve, aortic coarctation and patent ductus arteriosus. *Hum Mol Genet* **24**: 2375–2389.

Chapter 1

GPIHBP1 in Plasma Triglyceride Metabolism;

Macrophage Cholesterol Export

GPIHBP1 and Plasma Triglyceride Metabolism

For more than 60 years, it has been known that triglycerides in the plasma are hydrolyzed by the enzyme lipoprotein lipase (LPL) along blood vessels (1, 2). Dietary fats are packaged into chylomicrons by the intestines and very low-density lipoproteins (VLDLs) are secreted by the liver into the circulation (3, 4). After reaching the bloodstream the triglycerides in these triglyceride-rich lipoproteins (TRLs) are hydrolyzed by LPL along the luminal surface of capillaries, mainly in heart, skeletal muscle and adipose tissue (3, 4). For a long time, it was assumed that LPL, secreted by myocytes and adipocytes, was attached to the surface of blood vessels by electrostatic interaction with heparan-sulfate proteoglycan that line the surface of endothelial cells (5, 6). However, how LPL reaches the luminal surface of capillaries remained a mystery until recently. Glycosylphosphatidylinositol-anchored high density lipoprotein-binding protein 1 (GPIHBP1) is a GPI-anchored protein of capillary endothelial cells that is responsible for capturing LPL in the interstitial spaces and shuttling the enzyme across endothelial cells into the capillary lumen (7). Mice lacking GPIHBP1 had severe hypertriglyceridemia, with plasma triglycerides ranging from 2000–5000 mg/dl on a chow diet (7, 8). The hypertriglyceridemia was due to defective processing of TRLs by LPL (7). It was quickly discovered that GPIHBP1 was expressed on capillary endothelial cells and had the ability to bind LPL avidly (7). Subsequent studies found that GPIHBP1 bound LPL and transported it to the capillary lumen and that GPIHBP1 was essential for TRL margination along capillaries (Figure 1) (9, 10).

Structure of GPIHBP1

GPIHBP1 is a member of the Ly6/uPAR (LU) protein family (7). The hallmark of this family is an ~80-amino acid “Ly6 domain” containing 8 or 10 cysteine, all in a characteristic spacing pattern and all disulfide bonded to create a three-fingered fold (11, 12). The LU domain

of GPIHBP1 contains an *N*-linked glycosylation site that is important for the trafficking of GPIHBP1 to the cell surface. Unlike other proteins in the Ly6 family, GPIHBP1 also contains an “acidic domain” at its amino terminus, with 17 of 25 residues in mouse and 21 of 26 residues in humans being aspartate or glutamate (7). It has been shown that GPIHBP1’s LU domain is largely responsible for the high-affinity interaction with LPL while the acidic domain facilitates the initial binding event and subsequent stability of LPL (13–15).

GPIHBP1 Transports LPL to the Capillary Lumen

GPIHBP1 is required for proper localization of LPL in tissues (9, 16, 17). GPIHBP1 binds LPL in the interstitial spaces and transports it into the capillary lumen. In wild-type mice given an intravenous injection of heparin, LPL was discovered to be rapidly released into the plasma (16). However, in *Gpihbp1*^{-/-} mice, this release was slowed, suggesting that LPL in wild-type mice was located inside the blood vessel, whereas the slow entry of LPL into the plasma in *Gpihbp1*^{-/-} suggested that LPL was mislocalized (16) This was indeed the case.

Immunohistochemical studies on wild-type mice showed that LPL perfectly colocalized with GPIHBP1 inside capillaries (Figure 2) (9, 17). However, in tissues of *Gpihbp1*^{-/-} mice, LPL was located within the interstitial spaces, bound to the outside surface of myocytes and adipocytes (Figure 2) (9).

GPIHBP1 Expression in Tissues

GPIHBP1 is detectable in nearly every peripheral tissue, but is found in especially high levels in brown adipose tissue and heart (7). This mirrors the high levels of LPL transcripts in those sites (7). However, there are two tissues where there is a discrepancy in the expression of GPIHBP1 and LPL. First, GPIHBP1 is completely absent from capillaries of the brain (7), whereas LPL is expressed in select areas of the brain (e.g., hippocampus) (18, 19). The absence

of GPIHBP1 from the brain capillaries make sense because the brain relies exclusively on glucose for fuel. However, the physiologic function of LPL in the brain remains unclear. Second, GPIHBP1 is expressed at high levels in the lung, while LPL expression is very low (7, 20). The GPIHBP1 in lung capillaries is functional in binding LPL as shown when bovine LPL intravenously injected into a wild-type mouse bound to GPIHBP1 on lung capillaries (10). It is likely that GPIHBP1 in lung capillaries appears to play a role in capturing LPL that escapes from peripheral tissues, however the physiologic importance of GPIHBP1 expression in the lung remains unclear (20, 21).

In mice, GPIHBP1 is present exclusively in capillaries and cannot be detected in larger blood vessels (9). GPIHBP1 expression completely disappears as the size of capillary vessels increase by even ~50% (9). How GPIHBP1 is regulated to be expressed solely in capillary endothelial cells is unclear and remains an important topic for future research (21).

GPIHBP1–LPL Complex Required for Triglyceride-rich Lipoprotein Margination

For TRL processing to occur, TRLs must stop along the luminal surface of capillaries. For years, the assumption was that TRLs stopped as a result of binding between TRLs and HSPGs along the lumen of capillaries (1, 2). However, Fong and coworkers proved that that it was GPIHBP1 that is crucial for the margination of TRLs to occur (10). Using confocal microscopy, transmission electron microscopy, and NanoSIMS imaging, it was shown that TRLs margined along capillaries in wild-type mice, but TRL margination was completely absent in *Gpihbp1*^{-/-} mice (Figure 3) (10). However, GPIHBP1 alone is insufficient for margination to occur, as shown by the lack of TRL margination in the capillaries of the lung, where LPL is absent (10). Therefore, the GPIHBP1–LPL complex is necessary for margination and binding of TRLs in the capillary lumen (10).

***GPIHBP1* Mutations Cause Chylomicronemia**

Mice lacking *Gpihbp1* have defective TRL processing, resulting in extremely elevated plasma triglycerides and chylomicronemia (7). In humans, several *GPIHBP1* mutations have been identified in patients with familial chylomicronemia (22–32). Most of these patients had missense mutations in *GPIHBP1* involving a cysteine in the LU domain, including mutations such as C65Y, C65S, C68Y, C68G, C68R, C83R, and C89F (22–27, 31). Introducing an unpaired cysteine into the LU domain (a S107C mutation) also causes chylomicronemia (28). In addition, residues adjacent to cysteines have also been implicated in chylomicronemia patients (29, 30). Q115P and T111P mutations, which introduce a proline adjacent to a conserved cysteine, have also been observed in chylomicronemia patients. Chylomicronemia has also been reported in association with mutations preventing *N*-linked glycosylation (T80K mutation) and mutations preventing the addition of a GPI anchor (G175R) (32).

Recent studies have shown that most of these mutations in *GPIHBP1* caused chylomicronemia due to the decreased ability of *GPIHBP1* to bind LPL, thus preventing LPL from reaching the capillary lumen (14). Beigneux and coworkers found that these mutations in *GPIHBP1* (cysteine and non-cysteine mutations) caused *GPIHBP1* to form dimers or multimers, which do not have the ability to bind LPL (28, 33). Interestingly, Beigneux and coworkers found an exception with the mutation in W109 (33). W109 mutations abolished binding of *GPIHBP1* to LPL, however it also had low propensities to dimerize or multimerize (33). This suggested that W109 was directly involved in the binding of LPL to *GPIHBP1* (33).

Conclusions

GPIHBP1 is crucial for LPL-mediated intravascular triglyceride metabolism. However, most of our understanding of *GPIHBP1* and LPL physiology had come from studies of mice. In

chapter 2, we created high-affinity monoclonal antibodies (mAbs) against human GPIHBP1 to study interactions between GPIHBP1 and LPL in humans. Our goal was to use these mAbs to elucidate the relevance of different GPIHBP1 domains in binding LPL. In addition, we wanted to determine if GPIHBP1 in humans was expressed solely in capillary endothelial cells, like in mice, or whether it might be expressed more broadly in all endothelial cells. Finally, we wished to determine if GPIHBP1 was detectable in human plasma, and if so, could it be used in the clinical setting to diagnose metabolic or vascular disease. In chapter 3, we expanded on our findings of GPIHBP1 in humans by utilizing a monoclonal antibody–based immunoassay to detect GPIHBP1 in human plasma. We discovered a patient with unexplained hypertriglyceridemia lacking mutations in *LPL*, *GPIHBP1*, *APOC2*, *LMF1*, or *APOA5* who's chylomicronemia was caused by GPIHBP1 autoantibodies. Finally, in chapter 4 we investigated whether GPIHBP1 was expressed in capillary endothelial cells of human and mouse gliomas. GPIHBP1 is expressed in almost all peripheral tissue, but is absent from capillaries of the brain, which uses glucose for fuel. We reasoned that if GPIHBP1 was expressed in glioma capillaries, it could be relevant to glioma metabolism. The GPIHBP1 might bind locally produced LPL, facilitating TRL margination and TRL processing, thereby providing lipid nutrients for glioma cells.

Macrophage and Atherosclerosis

Atherosclerosis is a progressive disease that is characterized by accumulation of fibrous elements and lipids in large arteries (34). It is a chronic inflammatory disease that arises from an imbalance in lipid metabolism and a maladaptive immune response driven by the accumulation of cholesterol-laden macrophages in the artery wall (35). Macrophages play an essential role in the initiation and progression of atherosclerosis (35). Lipoproteins such as LDL enter the intima where they can undergo modification such as oxidation (36). Modified LDL incites an inflammatory response characterized by chemokine secretion (35, 36). The modifications also contribute to lipoprotein aggregation and further promote lipoprotein retention (35, 36). The inflammatory signals lead to monocyte recruitment into the intima, where they differentiate into macrophages and internalize native and modified lipoproteins, resulting in foam cell formation (34–36). The inability of macrophages to efflux sufficient amounts of engorged cholesterol to the reverse cholesterol transport pathway contributes significantly to foam cell formation (34–36).

Macrophage and Reverse Cholesterol Transport

Reverse cholesterol transport is the process by which cholesterol deposited in tissue is returned to the liver for excretion or reutilization (37–39). Defects in the regulation of cholesterol in a cell underlies many disorders, including atherosclerotic heart disease, which happens to be the leading cause of mortality worldwide (35). An early step in reverse cholesterol transport is cholesterol efflux from macrophages (35). Cholesterol in macrophages is initially stored in cytosolic cholesterol ester droplets, but ultimately the cholesterol must be returned to the bloodstream for uptake and excretion by the liver. Cholesterol export is essential for maintaining cholesterol homeostasis in macrophages and for minimizing the inflammatory response caused by cholesterol accumulation (37, 39–42). Extensive research has been done in this area, and it is

widely accepted that macrophages have four pathways for exporting cholesterol (39, 43, 44). Two passive processes involve aqueous diffusion and facilitated transport by macrophage scavenger receptor class B type I (SR-B1) (44). Two active transport pathways involve members of the ATP-binding cassette (ABC) transporter family, ABCA1 and ABCG1 (39, 43, 44). In cholesterol-loaded macrophages, two-thirds of the cholesterol efflux is mediated by active transport by ABCA1 from the cell plasma membrane to high density lipoproteins (HDL) (44). ABCA1 and ABCG1 are both increased by the liver X receptor (LXR) transcription factor, which is vital in modulating cholesterol efflux in macrophages (45). LXRs are activated by oxysterols in cholesterol-loaded macrophages to increase transcription of several genes involved in cholesterol efflux, including *Abca1*, *Abcg1*, and *ApoE* (39, 45).

Macrophages and Cholesterol Microdomains

Another potential mechanism for macrophage cholesterol efflux is the release of particles containing cholesterol (43, 46–52). This was described previously as “microparticles,” or “cholesterol microdomains” (43, 47–49). Phillips and coworkers proposed in 2007 that a significant fraction of the cholesterol released by cultured macrophages is due to the release of microparticles (43). They proposed that the particles originated from the plasma membrane (43). Kruth and coworkers proposed that cultured macrophages released cholesterol microdomains (47, 48, 52). These microdomains were detected by immunocytochemistry using a cholesterol-specific monoclonal antibody (47, 48, 52). In contrast to Philip’s work, they proposed that the cholesterol microdomains are not vesicles but irregularly shaped cholesterol deposits that originate from the plasma membrane. They suggested that the release of cholesterol microdomains could be important for reverse cholesterol transport (52). However, how these microdomains or microparticles were formed remained a mystery,

Utilizing NanoSIMS Imaging to Visualize Lipids

To visualize lipids in cells and tissues, Young and coworkers developed a technique utilizing nanoscale secondary ion mass spectrometry (NanoSIMS) (Figure 4) (53–55).

NanoSIMS uses a Cs^+ beam to bombard the surface of a cell or tissue, releasing secondary ions (e.g., $^{12}\text{C}^{14}\text{N}^-$, $^{12}\text{C}^{15}\text{N}^-$, $^1\text{H}^-$, $^2\text{H}^-$, $^{12}\text{C}^-$, $^{13}\text{C}^-$) that are collected and used to create high-resolution images of cells based solely on isotopic content. NanoSIMS images have ~40-nm lateral resolution, greater than that of super-resolution microscopes, but lower than with transmission electron microscopy. The NanoSIMS instrument records millions of secondary ions (10–2000 ions/pixel and >260,000 pixels/image); thus, secondary ion distributions can be quantified in different cells and subcellular compartments. By obtaining NanoSIMS images and backscattered electron images on the same surface, we are able to correlate the chemical information of a NanoSIMS image (*i.e.*, isotope distribution) with ultrastructural features of cells and tissues.

Young and coworkers further developed a method for cholesterol analysis by incorporating a new probe for visualizing and quantifying “accessible cholesterol” (54). Recently, studies of cholesterol distribution and metabolism have defined several pools of cholesterol on the plasma membrane (56, 57). One pool of cholesterol in the plasma membrane is “accessible” to cholesterol-binding proteins, whereas a second pool is “inaccessible” due to sequestration by sphingomyelin. A third pool (“essential cholesterol”) is not detectable by cholesterol-binding proteins (56, 57). “Accessible cholesterol” appears to be highly relevant to cholesterol movement into and out of cells (58). Based on these biochemical studies, He and coworkers used an ^{15}N -labeled cholesterol-binding protein ($[^{15}\text{N}]\text{ALO-D4}$; a modified anthrolysin O) along with NanoSIMS imaging to visualize and quantify “accessible cholesterol” in the plasma membrane of CHO cells (54). This method allows investigators to both see and

quantify the metabolically active cholesterol pool at a spatial resolution of ~70 nm. They found that this “accessible cholesterol” pool is enriched in the microvilli of cells (Figure 5) (54). They also quantified that, by loading CHO cells with acetylated LDL, CHO cells preferentially put the excess cholesterol on the microvilli rather than “non-villi” areas (Figure 5) (54). This was judged by the fact that [¹⁵N]ALO-D4 binding on the microvilli increased significantly but not on the “non-villi” areas of the plasma membrane after cholesterol loading (54). In addition to utilizing ALO-D4 to measure “accessible cholesterol”, He and coworkers developed a method to measure total cholesterol (all three pools) by loading the cells with uniformly labeled [¹³C]cholesterol and detecting ¹³C signal by NanoSIMS (Figure 5) (54). They showed that the distributions of the total cholesterol and the “accessible cholesterol” on the plasma membrane of CHO cells are similar (54).

Conclusions

One of the reasons for the slow progress in the field of cholesterol export is due to the absence of experimental approaches for visualizing the movement of cholesterol away from macrophages. For several decades, the methods for studying cholesterol efflux have relied largely on indirect studies of measuring extracted lipids or by tracing the movement of radiolabeled or fluorescently labeled cholesterol away from cells. Although these techniques have proven to be useful, they fell short of providing visual insights into cholesterol movement by macrophages. In chapter 5, we utilized NanoSIMS imaging to determine a potential new mechanism for macrophage cholesterol efflux by release of particles containing cholesterol. We show that these macrophage-derived particles are enriched in an “accessible” pool of cholesterol that can be increased by LXR agonists and depleted by HDL. These particles released from macrophages in atherosclerotic plaques could be a mechanism for unloading cholesterol and

promoting reverse cholesterol transport. In chapter 6, we further characterized these macrophage particles by determining that macrophages release particles during filopodia/lamellipodia projection and retraction. Additionally, we confirm that macrophage particles indeed derive from the plasma membrane and contain plasma membrane-associated proteins. Finally, we documented that macrophage particles were enriched in “accessible cholesterol” but not sphingomyelin-sequestered cholesterol.

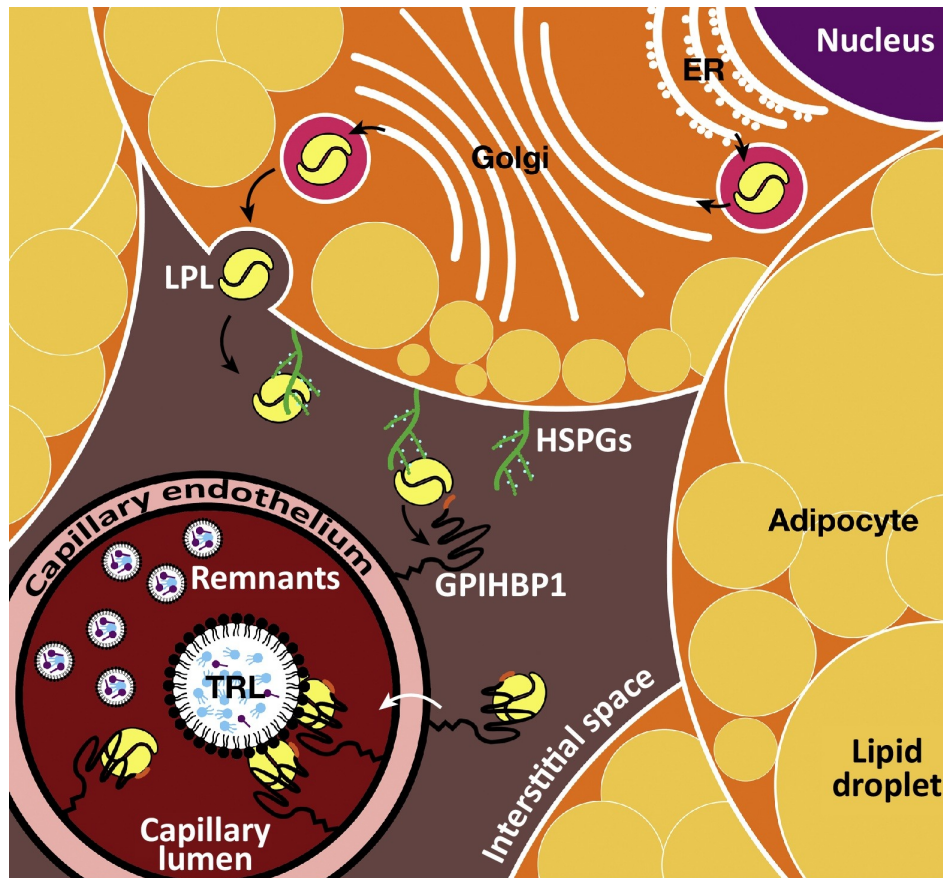


Figure 1. Schematic of GPIHBP1’s role in plasma triglyceride metabolism. Lipoprotein lipase (LPL) is produced by parenchymal cells (adipocytes) and secreted into the interstitial spaces. LPL is first captured by heparan sulfate proteoglycans (HSPGs) but then is quickly transferred to GPIHBP1 on the capillary endothelial cell. GPIHBP1 then transports LPL within vesicles across the endothelial cell into the capillary lumen. In the capillary lumen, the GPIHBP1–LPL complex is responsible for the margination of triglyceride-rich lipoproteins (TRLs) in the bloodstream which allows hydrolysis of triglycerides to proceed. Following LPL-mediated triglyceride hydrolysis, the remnant lipoprotein particles (remnants) are released back into the bloodstream. Reproduced with permission from Fong *et al.* 2016 (21).

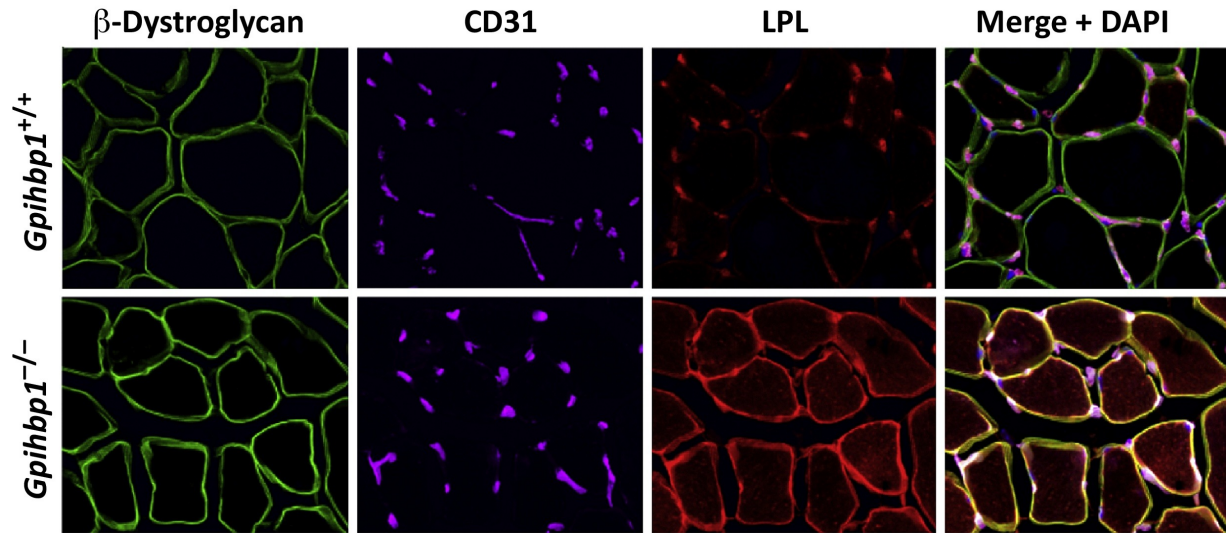


Figure 2. LPL is present in capillaries of skeletal muscle in wild-type mice but is mislocalized in skeletal muscle of *Gpihbp1* knockout mice. Immunofluorescent confocal micrograph of skeletal muscle from wild-type (*Gpihbp1*^{+/+}) and *Gpihbp1* knockout (*Gpihbp1*^{-/-}) mice. LPL (*red*) is largely bound to capillaries, colocalizing with CD31 (marker for endothelial cells, *purple*) in wild-type mice, but is mislocalized to the interstitial spaces around myocytes in *Gpihbp1*^{-/-} mice, colocalizing with β -dystroglycan (marker for skeletal myocytes, *green*). Reproduced with permission from Davies *et al.* 2010 (9).

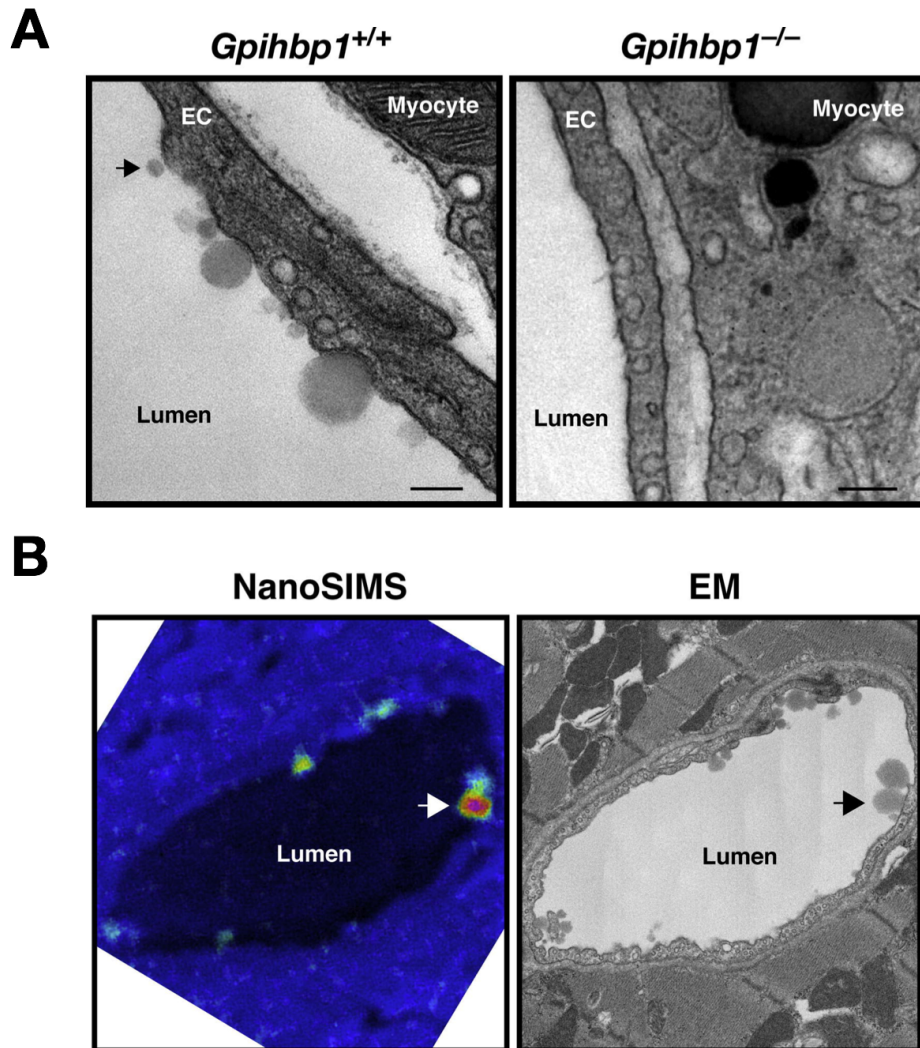


Figure 3. GPIHBP1 is required for margination of triglyceride rich lipoproteins along the capillary lumen. (A) Transmission EM showing triglyceride-rich lipoproteins (TRLs) along the luminal surface of capillaries in the wild-type heart. No TRLs are present along the capillary of *Gpibp1*^{-/-} heart. Scale bar, 200 nm. (B) NanoSIMS imaging showing TRL binding to capillary endothelial cells in the heart. A wild-type mouse was intravenously injected with ¹³C-labeled TRLs. After 8 min, the mouse was perfused with PBS to remove any unbound lipoproteins. Heart tissue was sectioned and analyzed by correlative NanoSIMS imaging and backscattered electron (BSE) imaging. On the left is a ¹³C/¹²C ratio image showing enrichment of [¹³C]TRLs at the capillary lumen. ¹³C/¹²C natural abundance range appears blue, whereas an increased ¹³C/¹²C signal appears yellow-red. Arrow points to the [¹³C]TRLs visualized by backscatter electron imaging. Modified with permission, from Goulbourne *et al.* 2014 (10).

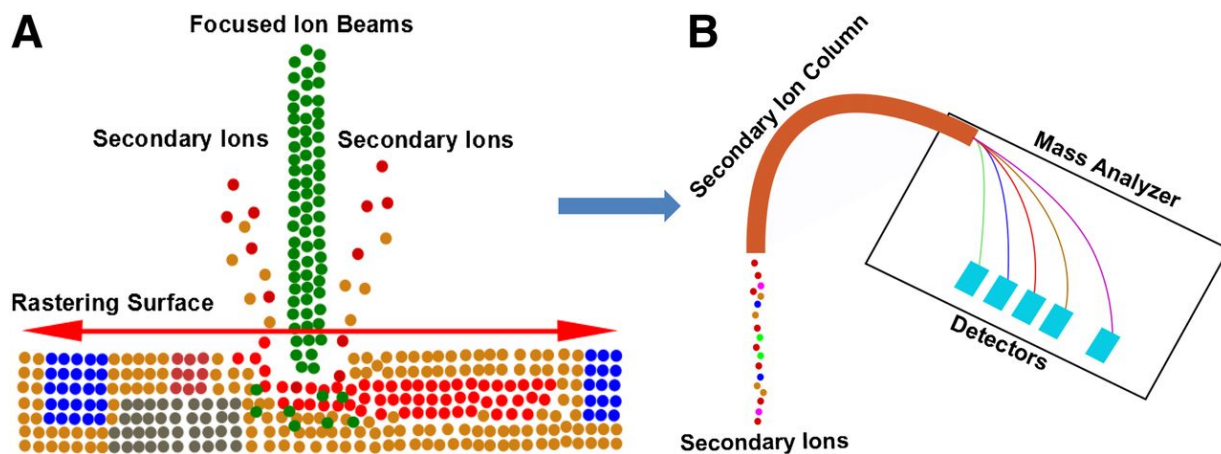


Figure 4. Schematic of the NanoSIMS instrument showing the focused primary ion beam and the collection and detection of secondary ion signals. (A) Cs^+ or O^- beam is used to bombard the surface of a sample (e.g., a tissue section or a cell), and secondary ions are released from the surface. Charged secondary ions can be detected by a mass spectrometer **(B)** The secondary ions from the surface of the sample pass through a secondary ion column and are analyzed by a Mauttach-Herzog configuration mass analyzer. The mass analyzer detects secondary ions with high resolution and high sensitivity, generating an image based on individual secondary ions.

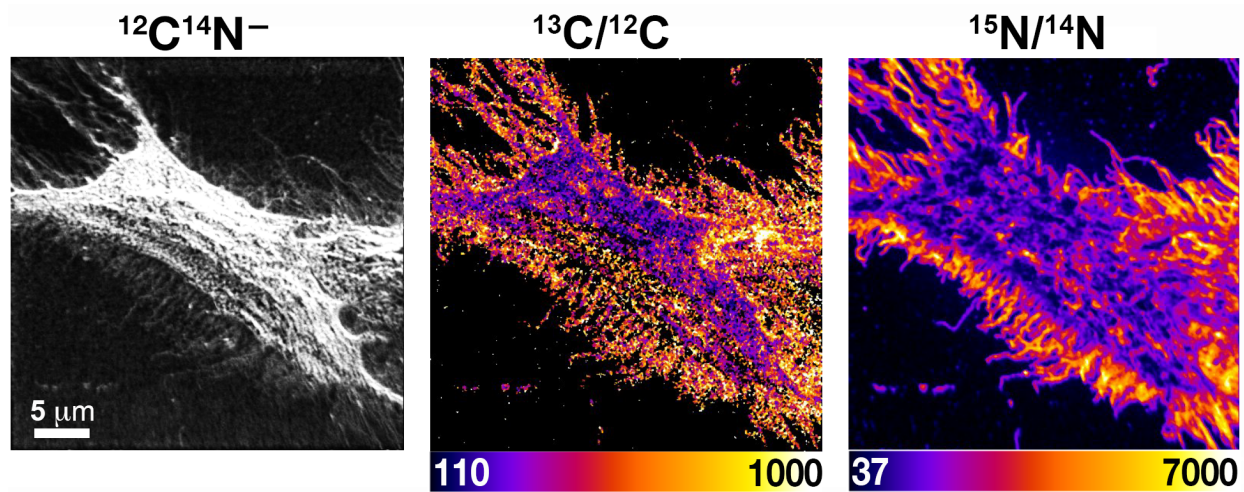


Figure 5. NanoSIMS imaging reveals total cholesterol and accessible cholesterol on the plasma membrane of CHO cell. NanoSIMS images revealing increased cholesterol in microvilli of a CHO cell that was loaded with [^{13}C]cholesterol for 24 h and then incubated for 2 h with [^{15}N]ALO-D4. The $^{12}\text{C}^{14}\text{N}^-$ image reveals cell morphology; the $^{13}\text{C}/^{12}\text{C}$ and $^{15}\text{N}/^{14}\text{N}$ ratio images show distribution of total cholesterol and accessible cholesterol, respectively. Both were enriched in microvilli. Reproduced with permission from He *et al.* 2017 (54).

References

1. Korn, E. D. 1955. Clearing factor, a heparin-activated lipoprotein lipase. II. Substrate specificity and activation of coconut oil. *J Biol Chem* **215**: 15–26.
2. Korn, E. D. 1955. Clearing factor, a heparin-activated lipoprotein lipase. I. Isolation and characterization of the enzyme from normal rat heart. *J Biol Chem* **215**: 1–14.
3. Havel, R. J., and J. P. Kane. 2001. Introduction: Structure and metabolism of plasma lipoproteins. *In* The Metabolic and Molecular Bases of Inherited Disease. C. R. Scriver, A. L. Beaudet, W. S. Sly, D. Valle, B. Childs, K. W. Kinzler, and B. Vogelstein, editors. McGraw-Hill, New York. 2705–2716.
4. Havel, R. J. 2010. Triglyceride-rich lipoproteins and plasma lipid transport. *Arterioscler Thromb Vasc Biol* **30**: 9–19.
5. Wang, H., and R. H. Eckel. 2009. Lipoprotein lipase: from gene to obesity. *Am J Physiol Endocrinol Metab* **297**: E271–E288.
6. Lookene, A., R. Savonen, and G. Olivecrona. 1997. Interaction of lipoproteins with heparan sulfate proteoglycans and with lipoprotein lipase. Studies by surface plasmon resonance technique. *Biochemistry* **36**: 5267–5275.
7. Beigneux, A. P., B. Davies, P. Gin, M. M. Weinstein, E. Farber, X. Qiao, P. Peale, S. Bunting, R. L. Walzem, J. S. Wong, W. S. Blaner, Z. M. Ding, K. Melford, N. Wongsiriroj, X. Shu, F. de Sauvage, R. O. Ryan, L. G. Fong, A. Bensadoun, and S. G. Young. 2007. Glycosylphosphatidylinositol-anchored high density lipoprotein-binding protein 1 plays a critical role in the lipolytic processing of chylomicrons. *Cell Metab* **5**: 279–291.
8. Weinstein, M. M., L. Yin, Y. Tu, X. Wang, X. Wu, L. W. Castellani, R. L. Walzem, A. J. Lusis, L. G. Fong, A. P. Beigneux, and S. G. Young. 2010. Chylomicronemia elicits atherosclerosis in mice—brief report. *Arterioscler Thromb Vasc Biol* **30**: 20–23.

9. Davies, B. S., A. P. Beigneux, R. H. Barnes, 2nd, Y. Tu, P. Gin, M. M. Weinstein, C. Nobumori, R. Nyren, I. Goldberg, G. Olivecrona, A. Bensadoun, S. G. Young, and L. G. Fong. 2010. GPIHBP1 is responsible for the entry of lipoprotein lipase into capillaries. *Cell Metab* **12**: 42–52.
10. Goulbourne, C., P. Gin, A. Tatar, C. Nobumori, A. Hoenger, H. Jiang, C. Grovenor, O. Adeyo, J. Esko, I. Goldberg, K. Reue, P. Tontonoz, A. Bensadoun, A. Beigneux, S. Young, and L. Fong. 2014. The GPIHBP1–LPL complex is responsible for the margination of triglyceride-rich lipoproteins in capillaries. *Cell Metab* **19**: 849–860.
11. Galat, A. 2008. The three-fingered protein domain of the human genome. *Cellular and molecular life sciences : CMLS* **65**: 3481–3493.
12. Kjaergaard, M., L. V. Hansen, B. Jacobsen, H. Gårdsvoll, and M. Ploug. 2008. Structure and ligand interactions of the urokinase receptor (uPAR). *Front Biosci* **13**: 5441–5461.
13. Gin, P., L. Yin, B. S. J. Davies, M. M. Weinstein, R. O. Ryan, A. Bensadoun, L. G. Fong, S. G. Young, and A. P. Beigneux. 2008. The acidic domain of GPIHBP1 is important for the binding of lipoprotein lipase and chylomicrons. *J Biol Chem* **283**: 29554–29562.
14. Beigneux, A. P., P. Gin, B. S. J. Davies, M. M. Weinstein, A. Bensadoun, L. G. Fong, and S. G. Young. 2009. Highly conserved cysteines within the Ly6 domain of GPIHBP1 are crucial for the binding of lipoprotein lipase. *J Biol Chem* **284**: 30240–30247.
15. Beigneux, A. P., B. S. J. Davies, S. Tat, J. Chen, P. Gin, C. V. Voss, M. M. Weinstein, A. Bensadoun, C. R. Pullinger, L. G. Fong, and S. G. Young. 2011. Assessing the role of the glycosylphosphatidylinositol-anchored high density lipoprotein-binding protein 1 (GPIHBP1) three-finger domain in binding lipoprotein lipase. *J Biol Chem* **286**: 19735–19743.

16. Weinstein, M. M., L. Yin, A. P. Beigneux, B. S. J. Davies, P. Gin, K. Estrada, K. Melford, J. R. Bishop, J. D. Esko, G. M. Dallinga-Thie, L. G. Fong, A. Bensadoun, and S. G. Young. 2008. Abnormal patterns of lipoprotein lipase release into the plasma in GPIHBP1-deficient mice. *J Biol Chem* **283**: 34511–34518.
17. Davies, B. S., C. N. Goulbourne, R. H. Barnes, 2nd, K. A. Turlo, P. Gin, S. Vaughan, D. J. Vaux, A. Bensadoun, A. P. Beigneux, L. G. Fong, and S. G. Young. 2012. Assessing mechanisms of GPIHBP1 and lipoprotein lipase movement across endothelial cells. *J Lipid Res* **53**: 2690–2697.
18. Vilaro, S., L. Camps, M. Reina, J. Perez-Clausell, M. Llobera, and T. Olivecrona. 1990. Localization of lipoprotein lipase to discrete areas of the guinea pig brain. *Brain Res* **506**: 249–253.
19. Ben-Zeev, O., M. H. Doolittle, N. Singh, C. H. Chang, and M. C. Schotz. 1990. Synthesis and regulation of lipoprotein lipase in the hippocampus. *J Lipid Res* **31**: 1307–1313.
20. Olafsen, T., S. G. Young, B. S. J. Davies, A. P. Beigneux, V. E. Kenanova, C. Voss, G. Young, K.-P. Wong, R. H. Barnes, Y. Tu, M. M. Weinstein, C. Nobumori, S.-C. Huang, I. J. Goldberg, A. Bensadoun, A. M. Wu, and L. G. Fong. 2010. Unexpected expression pattern for glycosylphosphatidylinositol-anchored HDL-binding protein 1 (GPIHBP1) in mouse tissues revealed by positron emission tomography scanning. *J Biol Chem* **285**: 39239–39248.
21. Fong, L. G., S. G. Young, A. P. Beigneux, A. Bensadoun, M. Oberer, H. Jiang, and M. Ploug. 2016. GPIHBP1 and plasma triglyceride metabolism. *Trends Endocrinol Metab* **27**: 455–469.
22. Franssen, R., S. G. Young, F. Peelman, J. Hertecant, J. A. Sierts, A. W. M. Schimmel, A. Bensadoun, J. J. P. Kastelein, L. G. Fong, G. M. Dallinga-Thie, and A. P. Beigneux. 2010.

- Chylomicronemia with low postheparin lipoprotein lipase levels in the setting of GPIHBP1 defects. *Circ Cardiovasc Genet* **3**: 169–178.
23. Olivecrona, G., E. Ehrenborg, H. Semb, E. Makoveichuk, A. Lindberg, M. R. Hayden, P. Gin, B. S. J. Davies, M. M. Weinstein, L. G. Fong, A. P. Beigneux, S. G. Young, T. Olivecrona, and O. Hernell. 2010. Mutation of conserved cysteines in the Ly6 domain of GPIHBP1 in familial chylomicronemia. *J Lipid Res* **51**: 1535–1545.
 24. Charrière, S., N. Peretti, S. Bernard, M. Di Filippo, A. Sassolas, M. Merlin, M. Delay, C. Debard, E. Lefai, A. Lachaux, P. Moulin, and C. Marçais. 2011. GPIHBP1 C89F neomutation and hydrophobic C-terminal domain G175R mutation in two pedigrees with severe hyperchylomicronemia. *J Clin Endocrinol Metab* **96**: E1675–E1679.
 25. Yamamoto, H., M. Onishi, N. Miyamoto, R. Oki, H. Ueda, M. Ishigami, H. Hiraoka, Y. Matsuzawa, and S. Kihara. 2013. Novel combined GPIHBP1 mutations in a patient with hypertriglyceridemia associated with CAD. *Journal of atherosclerosis and thrombosis* **20**: 777–784.
 26. Rios, J. J., S. Shastry, J. Jasso, N. Hauser, A. Garg, A. Bensadoun, J. C. Cohen, and H. H. Hobbs. 2012. Deletion of GPIHBP1 causing severe chylomicronemia. *Journal of inherited metabolic disease* **35**: 531–540.
 27. Coca-Prieto, I., O. Kroupa, P. Gonzalez-Santos, J. Magne, G. Olivecrona, E. Ehrenborg, and P. Valdivielso. 2011. Childhood-onset chylomicronaemia with reduced plasma lipoprotein lipase activity and mass: identification of a novel GPIHBP1 mutation. *Journal of internal medicine* **270**: 224–228.
 28. Plengpanich, W., S. G. Young, W. Khovidhunkit, A. Bensadoun, H. Karnman, M. Ploug, H. Gardsvoll, C. S. Leung, O. Adeyo, M. Larsson, S. Muanpetch, S. Charoen, L. G. Fong, S. Niramitmahapanya, and A. P. Beigneux. 2014. Multimerization of GPIHBP1 and familial

- chylomicronemia from a serine-to-cysteine substitution in GPIHBP1's Ly6 domain. *J Biol Chem* **289**: 19491–19499.
29. Beigneux, A. P., R. Franssen, A. Bensadoun, P. Gin, K. Melford, J. Peter, R. L. Walzem, M. M. Weinstein, B. S. Davies, J. A. Kuivenhoven, J. J. Kastelein, L. G. Fong, G. M. Dalling-Thie, and S. G. Young. 2009. Chylomicronemia with a mutant GPIHBP1 (Q115P) that cannot bind lipoprotein lipase. *Arterioscler Thromb Vasc Biol* **29**: 956–962.
 30. Gonzaga-Jauregui, C., S. Mir, S. Penney, S. Jhangiani, C. Midgen, M. Finegold, D. M. Muzny, M. Wang, C. A. Bacino, R. A. Gibbs, J. R. Lupski, R. Kellermayer, and N. A. Hanchard. 2014. Whole-exome sequencing reveals GPIHBP1 mutations in infantile colitis with severe hypertriglyceridemia. *J. Pediatr. Gastroenterol. Nutr.* **59**: 17–21.
 31. Rabacchi, C., S. D'Addato, S. Palmisano, T. Lucchi, S. Bertolini, S. Calandra, and P. Tarugi. 2016. Clinical and genetic features of 3 patients with familial chylomicronemia due to mutations in GPIHBP1 gene. *J Clin Lipidol* **10**: 915–921 e914.
 32. Ariza, M. J., P. L. Martinez-Hernandez, D. Ibarretxe, C. Rabacchi, J. Rioja, C. Grande-Aragon, N. Plana, P. Tarugi, G. Olivecrona, S. Calandra, and P. Valdivielso. 2016. Novel mutations in the GPIHBP1 gene identified in 2 patients with recurrent acute pancreatitis. *J Clin Lipidol* **10**: 92–100 e101.
 33. Beigneux, A. P., L. G. Fong, A. Bensadoun, B. S. Davies, M. Oberer, H. Gardsvoll, M. Ploug, and S. G. Young. 2014. GPIHBP1 missense mutations often cause multimerization of GPIHBP1 and thereby prevent lipoprotein lipase binding. *Circ. Res.* **116**: 624–632.
 34. Lusis, A. J. 2000. Atherosclerosis. *Nature* **407**: 233–241.
 35. Moore, K. J., F. J. Sheedy, and E. A. Fisher. 2013. Macrophages in atherosclerosis: a dynamic balance. *Nat Rev Immunol* **13**: 709–721.

36. Linton, M. R. F., P. G. Yancey, S. S. Davies, W. G. Jerome, E. F. Linton, W. L. Song, A. C. Doran, and K. C. Vickers. 2000. The role of lipids and lipoproteins in atherosclerosis. *In* Endotext. K. R. Feingold, B. Anawalt, A. Boyce, G. Chrousos, K. Dungan, A. Grossman, J. M. Hershman, G. Kaltsas, C. Koch, P. Kopp, M. Korbonits, R. McLachlan, J. E. Morley, M. New, L. Perreault, J. Purnell, R. Rebar, F. Singer, D. L. Trencce, A. Vinik, and D. P. Wilson, editors, South Dartmouth (MA).
37. Rosenson, R. S., H. B. Brewer, Jr., W. S. Davidson, Z. A. Fayad, V. Fuster, J. Goldstein, M. Hellerstein, X. C. Jiang, M. C. Phillips, D. J. Rader, A. T. Remaley, G. H. Rothblat, A. R. Tall, and L. Yvan-Charvet. 2012. Cholesterol efflux and atheroprotection: advancing the concept of reverse cholesterol transport. *Circulation* **125**: 1905–1919.
38. Fisher, E. A., J. E. Feig, B. Hewing, S. L. Hazen, and J. D. Smith. 2012. High-density lipoprotein function, dysfunction, and reverse cholesterol transport. *Arterioscler Thromb Vasc Biol* **32**: 2813–2820.
39. Tall, A. R., P. Costet, and N. Wang. 2002. Regulation and mechanisms of macrophage cholesterol efflux. *J Clin Invest* **110**: 899–904.
40. Rothblat, G. H., and M. C. Phillips. 2010. High-density lipoprotein heterogeneity and function in reverse cholesterol transport. *Curr Opin Lipidol* **21**: 229–238.
41. Yvan-Charvet, L., N. Wang, and A. R. Tall. 2010. Role of HDL, ABCA1, and ABCG1 transporters in cholesterol efflux and immune responses. *Arterioscler Thromb Vasc Biol* **30**: 139–143.
42. Westerterp, M., A. E. Bochem, L. Yvan-Charvet, A. J. Murphy, N. Wang, and A. R. Tall. 2014. ATP-binding cassette transporters, atherosclerosis, and inflammation. *Circ Res* **114**: 157–170.

43. Duong, P. T., H. L. Collins, M. Nickel, S. Lund-Katz, G. H. Rothblat, and M. C. Phillips. 2006. Characterization of nascent HDL particles and microparticles formed by ABCA1-mediated efflux of cellular lipids to apoA-I. *J Lipid Res* **47**: 832–843.
44. Adorni, M. P., F. Zimetti, J. T. Billheimer, N. Wang, D. J. Rader, M. C. Phillips, and G. H. Rothblat. 2007. The roles of different pathways in the release of cholesterol from macrophages. *J Lipid Res* **48**: 2453–2462.
45. Lee, S. D., and P. Tontonoz. 2015. Liver X receptors at the intersection of lipid metabolism and atherogenesis. *Atherosclerosis* **242**: 29–36.
46. He, C., X. Hu, T. A. Weston, R. S. Jung, J. Sandhu, S. Huang, P. Heizer, J. Kim, R. Ellison, J. Xu, M. Kilburn, S. J. Bensinger, H. Riezman, P. Tontonoz, L. G. Fong, H. Jiang, and S. G. Young. 2018. Macrophages release plasma membrane-derived particles rich in accessible cholesterol. *Proc Natl Acad Sci U S A* **115**: E8499–E8508.
47. Jin, X., D. Sviridov, Y. Liu, B. Vaisman, L. Addadi, A. T. Remaley, and H. S. Kruth. 2016. ABCA1 (ATP-binding cassette transporter A1) mediates apoA-I (apolipoprotein A-I) and apoA-I mimetic peptide mobilization of extracellular cholesterol microdomains deposited by macrophages. *Arterioscler Thromb Vasc Biol* **36**: 2283–2291.
48. Jin, X., S. R. Freeman, B. Vaisman, Y. Liu, J. Chang, N. Varsano, L. Addadi, A. Remaley, and H. S. Kruth. 2015. ABCA1 contributes to macrophage deposition of extracellular cholesterol. *J Lipid Res* **56**: 1720–1726.
49. Freeman, S. R., X. Jin, J. J. Anzinger, Q. Xu, S. Purushothaman, M. B. Fessler, L. Addadi, and H. S. Kruth. 2014. ABCG1-mediated generation of extracellular cholesterol microdomains. *J Lipid Res* **55**: 115–127.

50. Ong, D. S., J. J. Anzinger, F. J. Leyva, N. Rubin, L. Addadi, and H. S. Kruth. 2010. Extracellular cholesterol-rich microdomains generated by human macrophages and their potential function in reverse cholesterol transport. *J Lipid Res* **51**: 2303–2313.
51. Hafiane, A., and J. Genest. 2017. ATP binding cassette A1 (ABCA1) mediates microparticle formation during high-density lipoprotein (HDL) biogenesis. *Atherosclerosis* **257**: 90–99.
52. Jin, X., E. K. Dimitriadis, Y. Liu, C. A. Combs, J. Chang, N. Varsano, E. Stempinski, R. Flores, S. N. Jackson, L. Muller, A. S. Woods, L. Addadi, and H. S. Kruth. 2018. Macrophages Shed Excess Cholesterol in Unique Extracellular Structures Containing Cholesterol Microdomains. *Arterioscler Thromb Vasc Biol.*
53. Jiang, H., C. N. Goulbourne, A. Tatar, K. Turlo, D. Wu, A. P. Beigneux, C. R. Grovenor, L. G. Fong, and S. G. Young. 2014. High-resolution imaging of dietary lipids in cells and tissues by NanoSIMS analysis. *J Lipid Res* **55**: 2156–2166.
54. He, C., X. Hu, R. S. Jung, T. A. Weston, N. P. Sandoval, P. Tontonoz, M. R. Kilburn, L. G. Fong, S. G. Young, and H. Jiang. 2017. High-resolution imaging and quantification of plasma membrane cholesterol by NanoSIMS. *Proc Natl Acad Sci U S A* **114**: 2000–2005.
55. He, C., L. G. Fong, S. G. Young, and H. Jiang. 2017. NanoSIMS imaging: an approach for visualizing and quantifying lipids in cells and tissues. *J Investig Med* **65**: 669–672.
56. Das, A., M. S. Brown, D. D. Anderson, J. L. Goldstein, and A. Radhakrishnan. 2014. Three pools of plasma membrane cholesterol and their relation to cholesterol homeostasis. *eLife* **3**: e02882.
57. Das, A., J. L. Goldstein, D. D. Anderson, M. S. Brown, and A. Radhakrishnan. 2013. Use of mutant 125I-perfringolysin O to probe transport and organization of cholesterol in membranes of animal cells. *Proc Natl Acad Sci U S A* **110**: 10580–10585.

58. Infante, R. E., and A. Radhakrishnan. 2017. Continuous transport of a small fraction of plasma membrane cholesterol to endoplasmic reticulum regulates total cellular cholesterol. *eLife* **6**.

Chapter 2

Monoclonal Antibodies That Bind to the Ly6 Domain of GPIHBP1 Abolish the Binding of LPL



Monoclonal antibodies that bind to the Ly6 domain of GPIHBP1 abolish the binding of LPL[§]

Xuchen Hu,* Mark W. Sleeman,[†] Kazuya Miyashita,[§] MacRae F. Linton,** Christopher M. Allan,* Cuiwen He,* Mikael Larsson,* Yiping Tu,* Norma P. Sandoval,* Rachel S. Jung,* Alaleh Mapar,* Tetsuo Machida,[§] Masami Murakami,[§] Katsuyuki Nakajima,[§] Michael Ploug,^{††,§§} Loren G. Fong,^{**1} Stephen G. Young,^{***1} and Anne P. Beigneux^{*1}

Departments of Medicine* and Human Genetics,** David Geffen School of Medicine, University of California Los Angeles, Los Angeles, CA; Monash Biomedicine Discovery Institute and Antibody Technologies Facility,[†] Monash University, Victoria, Australia; Department of Clinical Laboratory Medicine,[§] Graduate School of Medicine, Gunma University, Maebashi, Japan; Departments of Medicine and Pharmacology,** Vanderbilt University Medical Center, Nashville, TN; Finsen Laboratory,^{††} Rigshospitalet, Copenhagen, Denmark; and Biotech Research and Innovation Centre,^{§§} University of Copenhagen, Copenhagen, Denmark

Abstract GPIHBP1, an endothelial cell protein, binds LPL in the interstitial spaces and shuttles it to its site of action inside blood vessels. For years, studies of human GPIHBP1 have been hampered by an absence of useful antibodies. We reasoned that monoclonal antibodies (mAbs) against human GPIHBP1 would be useful for 1) defining the functional relevance of GPIHBP1's Ly6 and acidic domains to the binding of LPL; 2) ascertaining whether human GPIHBP1 is expressed exclusively in capillary endothelial cells; and 3) testing whether GPIHBP1 is detectable in human plasma.^{¶¶} Here, we report the development of a panel of human GPIHBP1-specific mAbs. Two mAbs against GPIHBP1's Ly6 domain, RE3 and RG3, abolished LPL binding, whereas an antibody against the acidic domain, RF4, did not. Also, mAbs RE3 and RG3 bound with reduced affinity to a mutant GPIHBP1 containing an Ly6 domain mutation (W109S) that abolishes LPL binding. Immunohistochemistry studies with the GPIHBP1 mAbs revealed that human GPIHBP1 is expressed only in capillary endothelial cells. Finally, we created an ELISA that detects GPIHBP1 in human plasma. That ELISA should make it possible for clinical lipidologists to determine whether plasma GPIHBP1 levels are a useful biomarker of metabolic or vascular disease.—Hu, X., M. W. Sleeman, K. Miyashita, M. F. Linton, C. M. Allan, C. He, M. Larsson, Y. Tu, N. P. Sandoval, R. S. Jung, A. Mapar, T. Machida, M. Murakami, K. Nakajima, M. Ploug, L. G. Fong, S. G. Young, and A. P. Beigneux. Monoclonal antibodies that bind to the Ly6 domain of GPIHBP1 abolish the binding of LPL. *J. Lipid Res.* 2017. 58: 208–215.

This work was supported by grants from the National Heart, Lung, and Blood Institute (HL090553, HL087228, and HL125335) and a Transatlantic Network Grant from the Leucoc Foundation (12CVD04). Xuchen Hu was supported by a Ruth L. Kirschstein National Research Service Award (T32HL69766); the National Institutes of Health National Institute of General Medical Science Training Grant (T32GM08042); and the University of California, Los Angeles, Medical Scientist Training Program. The authors have no financial conflicts of interest to declare.

Manuscript received 5 October 2016 and in revised form 31 October 2016. Published, JLR Papers in Press, November 15, 2016. DOI 10.1194/jlr.M072462

Supplementary key words chylomicrons • dyslipidemias • endothelial cells • lipoprotein lipase • triglycerides

LPL, a triglyceride hydrolase secreted by myocytes and adipocytes, is crucial for the lipolytic processing of triglyceride-rich lipoproteins inside blood vessels (1–3). For decades, the mechanism by which LPL reaches its site of action inside blood vessels was mysterious. However, we now know that GPIHBP1, a GPI-anchored protein of endothelial cells, binds LPL in the subendothelial spaces and transports it across endothelial cells to the capillary lumen (4, 5). GPIHBP1 is a member of the Ly6/uPAR protein family. The hallmark of this family is an ~80-amino acid “Ly6 domain” containing 8 or 10 cysteines—all in a characteristic spacing pattern and all disulfide bonded so as to create a three-fingered fold (6). Unlike other Ly6 family members, GPIHBP1 contains an acidic domain at its amino terminus, with 21 of 26 consecutive residues in human GPIHBP1 being aspartate or glutamate (7). Surface plasmon resonance (SPR) studies with purified proteins have strongly suggested that GPIHBP1's Ly6 domain is largely responsible for high-affinity interactions with LPL, whereas the acidic domain simply facilitates the initial binding event and stabilizes LPL activity (8). It would be desirable to confirm that finding by testing the capacity of monoclonal antibodies (mAbs) against GPIHBP1's Ly6 and acidic

Abbreviations: DAPI, 4',6-diamidino-2-phenylindole; mAb, monoclonal antibody; SPR, surface plasmon resonance; uPAR, urokinase-type plasminogen activator receptor; vWF, von Willebrand factor.

¹To whom correspondence should be addressed.
e-mail: lfong@mednet.ucla.edu (L.G.F.); sgyoung@mednet.ucla.edu (S.G.Y.); abeigneux@mednet.ucla.edu (A.P.B.)

[§]The online version of this article (available at <http://www.jlr.org>) contains a supplement.

Copyright © 2017 by the American Society for Biochemistry and Molecular Biology, Inc.

This article is available online at <http://www.jlr.org>

domains to block the binding of LPL to GPIHBP1. Unfortunately, mAb tools for studying GPIHBP1 have been lacking.

Thus far, most of our understanding of GPIHBP1/LPL physiology has come from studies of mice, and the majority of those studies have relied on a rat mAb against mouse GPIHBP1, 11A12, that binds downstream from GPIHBP1's Ly6 domain (9). Experiments with mAb 11A12 were essential for proving that GPIHBP1 transports LPL to the capillary lumen (4, 5, 10). Also, immunohistochemistry studies with mAb 11A12 showed that GPIHBP1 was expressed in endothelial cells of capillaries but not in endothelial cells of larger blood vessels (e.g., venules) (5). The majority of the LPL in mouse tissues was located on capillaries, mirroring the expression of GPIHBP1. Currently, it is unclear whether this peculiar pattern of GPIHBP1 expression (i.e., specificity for capillary endothelial cells) is unique to the mouse or is also found in humans. Unfortunately, monoclonal antibody 11A12 was not helpful for resolving this issue because it binds exclusively to mouse GPIHBP1.

In this study, our goal was to create high-affinity mAbs against human GPIHBP1—for three reasons. First, we wanted to generate mAbs against both the acidic and Ly6 domains of GPIHBP1 and then use the mAbs to elucidate the relevance of those domains for LPL binding. Second, we wanted to determine whether GPIHBP1 is expressed only in capillary endothelial cells in humans or whether it might be expressed more broadly in all endothelial cells. Studies of the domestic pig (11) and guinea pig (12) found LPL along endothelial cells of large blood vessels, raising the possibility that GPIHBP1 might be expressed in all endothelial cells in some mammalian species. Third, we wanted to determine whether GPIHBP1 is present in human plasma. We were not successful in detecting GPIHBP1 in mouse plasma by Western blotting, but we were intrigued that another GPI-anchored Ly6 protein, urokinase-type plasminogen activator receptor (uPAR), is easily detectable in human plasma with solid-phase immunoassays (ELISAs) (13). For that reason, we wanted to test whether an ELISA would be capable of detecting GPIHBP1 in human plasma. We reasoned that the development of a GPIHBP1 ELISA might allow clinical investigators to test whether GPIHBP1 levels are perturbed in the setting of metabolic or vascular diseases.

MATERIAL AND METHODS

GPIHBP1 expression vectors

The production of human GPIHBP1 in insect cells was described previously (14). Briefly, a secreted version of human GPIHBP1 with an N-terminal uPAR epitope tag (detectable by mAb R24) (15) and a carboxyl-terminal 11A12 epitope tag from the mouse GPIHBP1 sequence (9) was expressed in *Drosophila* S2 cells. The medium was concentrated 20-fold with Amicon Ultra 10k MWCO centrifugal filters (Millipore), and the concentration of human GPIHBP1 in the medium was determined by Western blotting using a highly purified GPIHBP1 standard (8). Point mutations in GPIHBP1 were introduced in expression vectors by PCR with the QuickChange Lightning kit (Agilent Technologies).

Deletions were introduced by linearizing the wild-type expression vector by PCR (using 5'-phosphorylated primers), followed by ligation. Expression vectors for S-protein-tagged CD59 and a GPIHBP1-CD59 chimeric protein were described previously (16). The integrity of all vectors was confirmed by DNA sequencing.

Monoclonal antibodies

Mice were immunized intraperitoneally with purified full-length human GPIHBP1 (8). Antibody titers in the plasma of immunized mice were monitored by ELISA, and splenocytes were fused with Sp2/0-Ag14 myeloma cells. Hybridomas were grown under azaserine hypoxanthine selection, and ~20,000 hybridoma supernatants were screened for high-affinity antibodies with a high-throughput antigen microarray and an ELISA. The top 24 clones were expanded and subcloned by serial dilution. Monoclonal antibodies were isotyped by commercially available assay kits (IsoStrip, Roche) and adapted to serum-free medium. Antibodies were purified from cell culture medium with a protein G-agarose column. All monoclonal antibodies are available upon request.

Western blots

Purified GPIHBP1 proteins or conditioned medium from GPIHBP1-expressing *Drosophila* S2 cells were size-fractionated on 12% Bis-Tris SDS-PAGE gels in MES buffer (Thermo Fisher Scientific). After transferring the proteins to a nitrocellulose membrane, the membrane was incubated with GPIHBP1-specific mAbs (4 µg/ml) in blocking buffer (LI-COR). After washing, binding of primary antibodies was detected with an IRDye800-labeled donkey anti-mouse IgG (1:2,000; LI-COR). In other Western blots, we used an IRDye680-labeled antibody 11A12 (1:500); an IRDye680-labeled antibody R24 (1:500); or an IRDye800-labeled V5 antibody (1:500). Western blots were scanned—and band intensities quantified—with an Odyssey infrared scanner (LI-COR).

Immunocytochemistry studies

CHO pgsA-745 cells (1×10^6 cells) were electroporated with 2 µg of plasmid DNA and then plated on coverslips in 24-well plates. The next day, the cells were fixed in 100% methanol, permeabilized with 0.2% Triton X-100, and blocked in 10% donkey serum. The cells were then incubated overnight at 4°C with GPIHBP1-specific mAbs (diluted to 10 µg/ml in blocking buffer), followed by an Alexa488-conjugated donkey anti-mouse IgG (Thermo Fisher Scientific; 1:800), a goat polyclonal antibody against the S-protein tag (Abcam; 1:800), and an Alexa555-conjugated donkey anti-goat IgG (Thermo Fisher Scientific; 1:800). DNA was stained with 4',6-diamidino-2-phenylindole (DAPI). Images were recorded with an Axiovert 200M confocal fluorescence microscope and processed with the Zen 2010 software (all from Zeiss).

Kinetics for the interaction between mAbs and GPIHBP1 by SPR

Purified mAbs RG3 and RE3 in 10 mM of sodium acetate (pH 5.0) were covalently immobilized on a CM5 sensor chip that had been preactivated with NHS/EDC (N-ethyl-N'-[3-dimethylaminopropyl] carbodiimide), with the goal of achieving a surface density of 1,500 resonance units. mAb RF4 could be immobilized by this procedure, but the immobilized RF4 did not bind GPIHBP1. In hindsight, this was probably due to the fact that this mAb binds the disordered acidic domain of GPIHBP1 containing a high density of carboxylates. We suspect that mAb RF4 bound noncovalently to the carboxymethylated dextran matrix on the sensor chip and that this binding event inactivated the mAb. To circumvent this problem, we captured mAb RF4 on the sensor chip via a high-affinity interaction with covalently

immobilized rabbit anti-mouse IgG (GE Healthcare Life Science, Uppsala, Sweden). Binding was recorded at 20°C, and the buffer flow rate was 50 $\mu\text{l}/\text{min}$ (10 mM HEPES, 150 mM NaCl, 3 mM EDTA, pH 7.4, containing 0.05% [v/v] surfactant P20). For multicycle kinetics, three-fold dilution series of GPIHBP1 (spanning a concentration from 1 to 90 nM) were injected for 200 s, followed by a 1,200-s dissociation step. For single-cycle kinetic titration of the RF4 \times GPIHBP1 interaction, five consecutive injections of 20 μl of purified GPIHBP1 (two-fold dilutions ranging from 12 to 200 nM) were recorded. In the between cycles, the sensor chip was regenerated with two consecutive 10- μl injections of 0.1 M acetic acid/HCl (pH 2.5) in 0.5 M NaCl and 20 mM H_3PO_4 . For multicycle analyses, the kinetic rate constants (k_{on} and k_{off}) for the mAb \times GPIHBP1 interactions were derived by local nonlinear regression fitting of the data after double-buffer referencing to a simple bimolecular interaction model assuming pseudo first-order reaction conditions with BIA evaluation 4.1 software (Biacore, Uppsala, Sweden). For single-cycle kinetic analyses of the interaction between captured mAb RF4 and GPIHBP1, the rate constants were fitted to a simple bimolecular interaction model with global fitting (T200 Evaluation Software 2.0, GE Healthcare Life Science).

Epitope binning of GPIHBP1 mAbs was performed with a Biacore3000 (GE Healthcare Life Science), as described (17).

Testing the ability of GPIHBP1-specific mAbs to block LPL binding in a cell-free LPL-GPIHBP1 binding assay

Human GPIHBP1 containing carboxyl-terminal sequences encoding the mAb 11A12 epitope (from *Drosophila* S2 cells) was first incubated for 1 h at 4°C with mAb 11A12-coated agarose beads and then incubated for 30 min at 4°C with or without GPIHBP1-specific mAbs (final concentration, 5 $\mu\text{g}/\text{ml}$) and V5-tagged human LPL (18). After washing the beads, the GPIHBP1 (and any GPIHBP1-bound LPL) were eluted from the agarose beads by heating in SDS sample buffer for 5 min at 90°C. The amounts of GPIHBP1 and LPL in the flow-through, washes, and elution fractions were assessed by Western blotting with an IRDye680-labeled mAb 11A12 and an IRDye800-labeled V5 antibody, respectively.

Testing the ability of GPIHBP1-specific antibodies to block LPL binding to GPIHBP1-expressing cells

CHO pgsA-745 cells (2×10^6 cells and 2 μg plasmid DNA) were electroporated with expression vectors for S-protein-tagged human wild-type GPIHBP1 (wt) or a mutant GPIHBP1 that cannot bind LPL (GPIHBP1-W109S) (14). After 1 day, cells were washed and subsequently incubated for 1 h at 4°C with mAbs RG3, RF4, or RE3 (20 $\mu\text{g}/\text{ml}$). After washing, the cells were incubated for 1 h at 4°C with V5-tagged human LPL (200 ng/well). The cells were then washed six times in PBS and fixed in 100% methanol, and we performed immunocytochemistry studies on nonpermeabilized cells. After blocking with 10% donkey serum in PBS/Ca/Mg, the cells were incubated with an Alexa488-conjugated donkey anti-mouse IgG (Thermo Fisher Scientific; 50 ng/ml), a rabbit anti-S-protein tag (Abcam; 1:1,000), an Alexa647-conjugated donkey anti-rabbit IgG (Thermo Fisher Scientific; 2.5 $\mu\text{g}/\text{ml}$), and an Alexa555-conjugated mouse anti-V5 antibody (1:50). DNA was stained with DAPI. Images were recorded with an Axiovert 200M confocal fluorescence microscope.

Immunohistochemistry studies on human adipose tissue

Frozen sections (20 μm) of human cardiac adipose tissue (from the Duke Human Heart Repository) were placed on glass slides, fixed with 3% paraformaldehyde, permeabilized in 0.2% Triton X-100, blocked in 10% donkey serum, and then incubated overnight at 4°C with a mixture of mAbs RE3 and RF4 (10 $\mu\text{g}/\text{ml}$

each), a rabbit polyclonal antibody against human von Willebrand factor (vWF) (Dako; 1:200), and a goat polyclonal antibody against human collagen IV (Novus Biologicals; 1:200), followed by 1-h incubations with an Alexa647-conjugated donkey anti-mouse IgG (Thermo Fisher Scientific; 1:500), an Alexa488-conjugated donkey anti-rabbit IgG (Thermo Fisher Scientific; 1:500), and an Alexa555-conjugated donkey anti-goat IgG (Thermo Fisher Scientific; 1:500). DNA was stained with DAPI. Images were recorded with an Axiovert 200M microscope with a $\times 20$ objective and processed with the Zen 2010 software (Zeiss).

Immunoperoxidase studies were performed with the ImmPRESS Excel Staining Kit (Vector Laboratories). The sections were quenched of endogenous peroxidase activity with the BLOXALL buffer (Vector Laboratories) and blocked in 10% normal horse serum. Next, the sections were incubated for 1 h with mAb RF4 (1 $\mu\text{g}/\text{ml}$) or a rabbit polyclonal antibody against vWF (Dako; 1:200), followed by a 15-min incubation with a goat anti-mouse IgG (Vector Laboratories) or a goat anti-rabbit IgG (Vector Laboratories), and a 30-min incubation with a horse anti-goat IgG (ImmPRESS Excel Reagent, Vector Laboratories). Sections were then stained with ImmPACT DAB EqV (Vector Laboratories) until color change was apparent (~ 10 s). Finally, sections were counterstained with hematoxylin and mounted with 90% glycerol in PBS. Images were taken with a Nikon Eclipse E600 microscope (Plan Fluor $\times 20/0.50$ NA or $\times 60/0.75$ NA objectives) equipped with a DS-Fi2 camera (Nikon).

An ELISA to detect the binding of LPL to human GPIHBP1

We coated 96-well plates overnight at 4°C with mAb R24 (0.5 $\mu\text{g}/\text{well}$). On the next day, the plates were blocked for 4 h at room temperature in Starting Block buffer (Pierce) and then incubated overnight at 4°C with 0.5 $\mu\text{g}/\text{well}$ of human GPIHBP1-uPAR fusion protein from *Drosophila* S2 cells in the presence or absence of mAbs RG3, RF4, and RE3. Serial dilutions of the mAbs were tested in triplicate (from 20 to 0.1 $\mu\text{g}/\text{ml}$ of mAb). After washing, the wells were incubated with 200 ng/well of V5-tagged human LPL for 1 h at 4°C, then washed and subsequently incubated for 1 h at 4°C with an HRP-labeled V5 antibody (Thermo Fisher Scientific; 1:5,000) to detect bound LPL. The presence of GPIHBP1 on the plates was verified in duplicate wells incubated with HRP-labeled 11A12 (1:50,000). To document mAb binding to GPIHBP1, we incubated replicate wells with HRP-labeled versions of RG3, RF4, and RE3. After washing the plates, 50 μl of one-step ultra 3,3',5,5'-tetramethylbenzidine (TMB) ELISA substrate (Pierce) was added to each well. The plate was incubated at room temperature for 5 min before stopping the reaction with 50 μl of 2 M sulfuric acid. The optical density was read immediately at 450 nm on a Spectra Max 190 plate reader (Molecular Devices).

An ELISA to detect GPIHBP1 in human plasma

We coated 96-well plates with 1 $\mu\text{g}/\text{well}$ of mAb RF4 overnight at 4°C. After blocking overnight at 4°C with PBS containing 1% BSA and 0.05% NaN_3 , the wells were incubated overnight at 4°C with the plasma samples. Serial dilution of the plasma samples (1:2 to 1:256) was performed in 1% BSA, 0.05% Tween 20, 0.05% ProClin 300, 50 $\mu\text{g}/\text{ml}$ normal mouse IgG, and 5g/L polyoxyethylene alkyl ether in PBS. On the next day, plates were washed, and the captured GPIHBP1 was detected with 0.5 $\mu\text{g}/\text{well}$ of HRP-labeled mAb RE3 Fab' (diluted in PBS containing 1% BSA, 0.05% Tween 20, and 0.05% ProClin 300). After incubating for 30 min at 4°C, plates were washed, and 50 μl of TMB substrate (Kem-entec) was added per well. After 30 min, the reaction was stopped by adding 50 μl of 2 M sulfuric acid. The optical density was read at 450 nm.

RESULTS

Defining the binding properties of the monoclonal antibodies

By screening hybridoma culture supernatants with Western blots, we identified 23 clones that secreted mAbs that bound to GPIHBP1 (supplemental Fig. S1). Some of the mAbs bound exclusively to nonreduced GPIHBP1; some bound exclusively to GPIHBP1 monomers; others bound both monomers and multimers. Several mAbs did not bind to a mutant GPIHBP1 lacking the acidic domain (GPIHBP1- Δ acidic) (supplemental Fig. S2). We chose five mAbs for further study: RG3 (IgG2b κ), RE3 (IgG2a κ), RH1 (IgG1 κ), RE6 (IgG1 κ), and RF4 (IgG2b κ). RG3, RE3, and RH1 bound to wild-type GPIHBP1 and GPIHBP1- Δ acidic. RE6 bound to wild-type GPIHBP1 and weakly to GPIHBP1- Δ acidic. RG3 and RE3 bound preferentially to GPIHBP1 monomers, whereas RE6, RH1, and RF4 bound to both monomers and dimers. RF4 did not bind to GPIHBP1- Δ acidic (Fig. 1) and bound avidly to a GPIHBP1-CD59 chimera containing GPIHBP1's acidic domain but CD59's Ly6 domain (supplemental Fig. S3). All mAbs except RH1 detected GPIHBP1 on the surface of GPIHBP1-transfected CHO cells (Fig. 2).

The binding of three mAbs (RE3, RG3, RF4) was evaluated by real-time surface plasmon resonance studies. All three mAbs bound GPIHBP1 with high affinity ($K_D \leq 5$ nM) (Table 1, Fig. 3). The kinetics of RE3 and RG3 binding to full-length GPIHBP1 and GPIHBP1- Δ acidic were virtually identical, indicating that their epitopes are not dependent

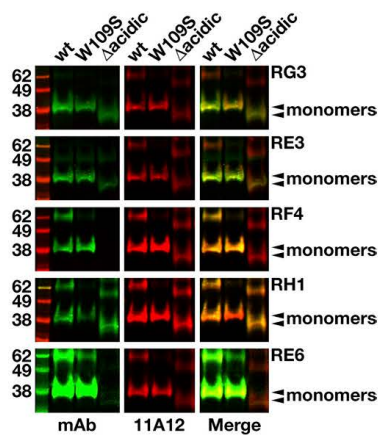


Fig. 1. Western blots with GPIHBP1-specific monoclonal antibodies. Soluble versions of wild-type (wt) human GPIHBP1, GPIHBP1-W109S, and GPIHBP1- Δ acidic (in which GPIHBP1's acidic domain had been deleted) were expressed in *Drosophila* S2 cells; all constructs had a carboxyl-terminal mAb 11A12 epitope tag (9). Western blot analysis was performed on the conditioned medium of the *Drosophila* S2 cell cultures under nonreducing conditions using IRDye800-labeled GPIHBP1-specific mAbs RG3, RE3, RF4, RH1, and RE6 (green) and an IRDye680-labeled mAb 11A12 (red). Monomers are indicated by arrowheads.

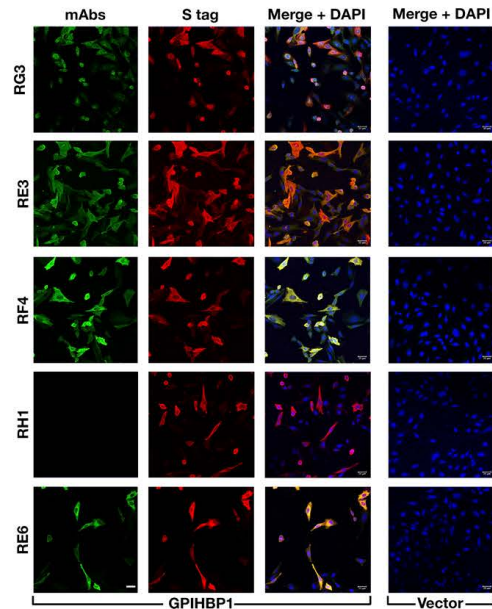


Fig. 2. Testing the ability of GPIHBP1-specific mAbs to bind to GPIHBP1 on the surface of GPIHBP1-transfected cells. CHO pgsA-745 cells were transiently transfected with empty vector or with an expression vector for S-protein-tagged human GPIHBP1. After 1 day, the cells were fixed with methanol, and immunocytochemistry studies were performed on permeabilized cells with mAbs RG3, RE3, RF4, RH1, and RE6 (10 μ g/ml; green) and a rabbit antibody against the S-protein tag (red). DNA was stained with DAPI (blue). Scale bar (lower left panel), 20 μ m.

on GPIHBP1's acidic domain. Both RG3 and RE3 bound to GPIHBP1-W109S with reduced affinity—a consequence of an increase in k_{off} (Table 1, Fig. 3). The W109S mutation eliminates LPL binding and does so without disrupting the formation of disulfide bonds in the Ly6 domain (19).

Epitope binning by pair-wise comparison of antibody binding to GPIHBP1 by SPR (Table 1, Fig. 3, supplemental Fig. S4) revealed that the epitopes for RE3 and RG3 are overlapping and distinct from that of RF4. This finding suggested a strategy for developing a sandwich ELISA for detecting GPIHBP1 (using mAb RF4 to capture GPIHBP1 and either RE3 or RG3 to detect GPIHBP1).

Testing the ability of GPIHBP1-specific mAbs to block LPL binding to GPIHBP1

To determine whether any of the mAbs blocked the binding of LPL to GPIHBP1, we initially utilized a cell-free LPL-GPIHBP1 binding assay (9). Equimolar amounts of LPL, recombinant human GPIHBP1 harboring the mAb 11A12 epitope, and GPIHBP1-specific mAbs were incubated with agarose beads coated with mAb 11A12. After 1 h, the beads were washed, and the amount of GPIHBP1 (and GPIHBP1-bound LPL) captured by the beads was assessed by Western blotting. RG3 and RE3 abolished the

TABLE 1. Kinetic rate constants for GPIHBP1-specific mAbs by SPR

mAb	Analyte	k_{on} (10^5 M ⁻¹ s ⁻¹)	k_{off} (10^{-3} s ⁻¹)	K_D (nM)	n	Nonoverlapping Epitopes
RE3	GPIHBP1	4.2 ± 1.8	1.64 ± 0.27	4.4 ± 1.8	4	RF4
RE3	GPIHBP1-W109S	8.2 ± 1.9	7.82 ± 1.80	10.0 ± 3.3	3	
RE3	GPIHBP1-Δacidic	7.6 ± 2.7	1.34 ± 0.11	2.0 ± 0.6	3	
RG3	GPIHBP1	0.64 ± 0.22	0.17 ± 0.04	3.1 ± 1.8	4	RF4
RG3	GPIHBP1-W109S	0.93 ± 0.15	1.23 ± 0.06	13.7 ± 2.4	3	
RG3	GPIHBP1-Δacidic	1.26 ± 0.21	0.27 ± 0.11	2.3 ± 1.3	2	
RF4	GPIHBP1	5.4 ± 1.9	0.74 ± 0.06	1.4 ± 0.2	3	RE3, RG3

Kinetics rate constants were derived from data recorded with a BiacoreT200 for three-fold dilutions of various purified GPIHBP1 proteins (8) and were fitted to a 1:1 binding model. GPIHBP1 is full-length GPIHBP1; GPIHBP1-W109S contains a serine for tryptophan mutation in a highly conserved region of the Ly6 domain; GPIHBP1-Δacidic contains a deletion of the acidic domain (the first 31 amino acids of the mature protein). Data for mAbs RE3 and RG3 were processed by a multicycle protocol with mAbs that had been directly immobilized on the chip (1,000 RU), whereas the data for mAb RF4 were processed by a single-cycle protocol in which mAb RF4 was captured by an immobilized rabbit anti-mouse IgG. Epitope mapping was performed with sequential injections, as is illustrated by Fig. 3.

binding of LPL to GPIHBP1, whereas RH1, RE6, and RF4 did not (Fig. 4). The ability of GPIHBP1-specific mAbs to block LPL binding was further tested with a cell-based LPL-GPIHBP1 binding assay and an ELISA. Again, these studies revealed that the binding of mAbs RG3 and RE3 to GPIHBP1 abolished LPL binding (Figs. 5, 6). Of note, mAb RF4 bound avidly to GPIHBP1 but did not block LPL binding (Figs. 5, 6).

Detecting GPIHBP1 in capillaries of human adipose tissue

We tested the ability of RE3 and RF4 to detect human GPIHBP1 in human adipose tissue by confocal immunofluorescence microscopy and by immunoperoxidase staining.

RE3 and RF4 detected GPIHBP1 in capillaries of epicardial adipose tissue, colocalizing with vWF (Fig. 7, supplemental Fig. S5). GPIHBP1 was found only in capillaries and not in endothelial cells of venules, whereas vWF was found in endothelial cells of both capillaries and venules (Fig. 7, supplemental Fig. S5). Despite considerable effort, we were unsuccessful in detecting GPIHBP1 in capillaries of post-mortem human heart tissue by confocal immunofluorescence microscopy or immunoperoxidase staining. This was not entirely surprising because the expression of GPIHBP1 in human heart is much lower than in human adipose tissue, as judged by RNA seq data (Human Protein Atlas database; www.proteinatlas.org) (20). A caveat to our

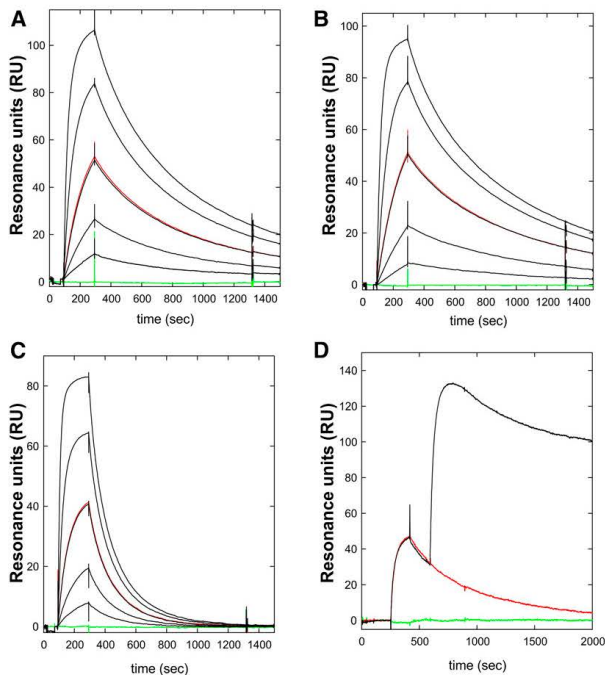


Fig. 3. Kinetics for the interaction between mAb RE3 and GPIHBP1 by surface plasmon resonance. The real-time kinetic interactions between immobilized mAb RE3 and different GPIHBP1 proteins were measured with a BiacoreT200 system. A three-fold dilution series of wild-type GPIHBP1 (A); GPIHBP1-Δacidic (B); and GPIHBP1-W109S (C) were injected between 100 and 300 s, followed by a dissociation phase from 300 to 1,500 s. The concentrations analyzed were 90, 30, 10, 3, and 1 nM GPIHBP1 (black curves). One repeat measurement of 10 nM GPIHBP1 was performed at the end of each analysis (red); a buffer control curve is also shown (green). (D) Example of epitope binning. RE3 was immobilized on the sensor chip and 100 nM GPIHBP1 was captured by injection at 300 s, followed by a second injection of either buffer (red curve) or 100 nM mAb RF4 (black curve). The sensorgrams show that RE3 and RF4 belong to separate epitope bins and that their binding to GPIHBP1 was not mutually exclusive.

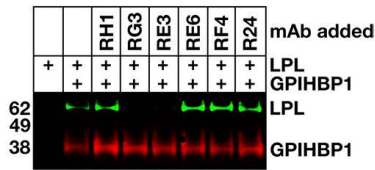


Fig. 4. Monoclonal antibodies RG3 and RE3 block LPL binding to GPIHBP1 in a cell-free LPL-GPIHBP1 binding assay. Soluble wild-type human GPIHBP1 with a carboxyl-terminal 11A12 epitope tag was incubated with 11A12-coated agarose beads and V5-tagged human LPL, in the presence or absence of mAbs RH1, RG3, RE3, RE6, RF4, or R24. After washing the beads, GPIHBP1 and any GPIHBP1-bound LPL was eluted from the beads by heating in SDS loading buffer. Shown is a Western blot on the eluted proteins with IRDye680-labeled mAb 11A12 (red) and an IRDye800-labeled V5 antibody (green).

immunohistochemistry studies on human heart is that we examined heart tissue that was harvested from patients with devastating and irreversible disease after the heart had stopped beating (“donation after cardiac death”), and we

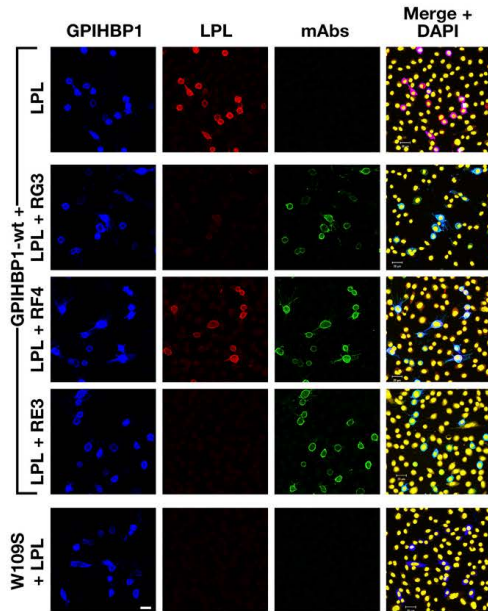


Fig. 5. RG3 and RE3, but not RF4, block the binding of LPL to GPIHBP1 on the surface of cultured cells. CHO pgsA-745 cells were transfected with vectors for S-protein-tagged versions of wild-type human GPIHBP1 (wt) or GPIHBP1-W109S. After 1 day, the cells were washed and preincubated with mAbs RG3, RF4, or RE3 (20 μ g/ml) or PBS alone. After washing, the cells were incubated with V5-tagged human LPL (200 ng/well). The cells were washed and fixed with methanol, and immunocytochemistry was performed on non-permeabilized cells with an Alexa488-conjugated donkey anti-mouse IgG (green), a rabbit anti-S-protein tag (blue), and an Alexa555-conjugated mouse anti-V5 antibody (red). DNA was stained with DAPI (yellow). Scale bar (lower left panel), 20 μ m.

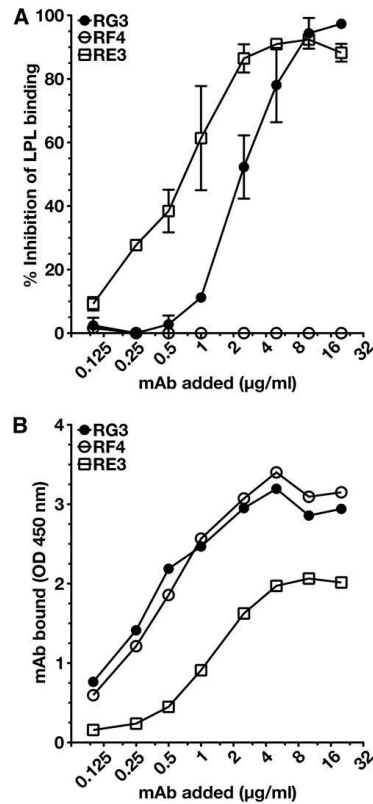


Fig. 6. Dose-dependent inhibition of LPL binding to GPIHBP1 by mAbs RE3 and RG3. We coated 96-well ELISA plates with the uPAR-specific mAb R24, blocked, and then incubated them with uPAR-tagged human GPIHBP1 (0.5 μ g/well) in the presence or absence of serial dilutions of mAbs RG3, RE3, or RF4. After washing, the plates were incubated with V5-tagged LPL (200 ng/well). GPIHBP1-bound LPL was detected with an HRP-labeled V5 antibody. The binding of the GPIHBP1-specific mAbs to GPIHBP1 was documented in an independent assay with HRP-labeled mAbs RG3, RE3, or RF4. (A) Inhibition of LPL binding to GPIHBP1 by mAbs RE3 and RG3. Antibody RF4 had no effect on LPL binding. (B) Amount of mAb bound to GPIHBP1 for each amount of the GPIHBP1-specific mAb added.

simply do not know how these circumstances affected GPIHBP1 expression in capillaries.

Detecting GPIHBP1 in human plasma

Because another GPI-anchored Ly6 protein, uPAR, can be detected in human plasma by ELISA (13), we suspected that it might be possible to detect GPIHBP1 in plasma. To explore that possibility, we created a sandwich ELISA in which mAb RF4 was used to capture the GPIHBP1 in plasma, and HRP-labeled mAb RE3 was used to detect the captured GPIHBP1. This ELISA readily detected a recombinant GPIHBP1 standard and was able to detect GPIHBP1 in normal human plasma. In two normal subjects, the plasma

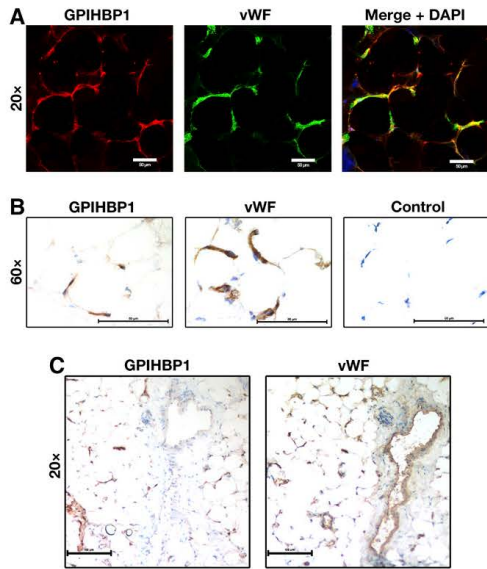


Fig. 7. Detection of GPIIb/IIIa in human tissues with GPIIb/IIIa-specific monoclonal antibodies. Sections of human cardiac adipose tissue (20 μ m) were fixed with 3% paraformaldehyde and processed for confocal immunofluorescence microscopy (A) or light microscopy (B, C). (A) Confocal microscopy images showing GPIIb/IIIa (in this case, detected by a combination of mAbs RE3 and RF4, 10 μ g/ml each; red) and von Willebrand Factor (vWF, a marker for endothelial cells; green) in the capillaries of human cardiac adipose tissue. (B) Consecutive HRP-stained sections showing GPIIb/IIIa (left panel, mAb RF4, 1 μ g/ml) and vWF (middle panel) in capillaries of human cardiac adipose tissue. No primary antibody was added in the control panel (right). (C) Consecutive HRP-stained sections showing expression of vWF in both capillaries and a large venule, whereas GPIIb/IIIa was expressed in endothelial cells of capillaries but not in endothelial cells of the venule. In B and C, sections were counterstained with hematoxylin. Scale bar for A, 20 μ m; B, 50 μ m; C, 100 μ m.

GPIIb/IIIa levels were \sim 1 ng/ml (Fig. 8). As negative controls, we included three subjects who were homozygous for *GPIIb/IIIa* mutations [a deletion of the entire *GPIIb/IIIa* gene in subject 3 (21), and a C89X nonsense mutation in subjects 11 and 15 (supplemental Fig. S6)]. As was expected, the plasma levels of GPIIb/IIIa in those subjects were essentially undetectable (Fig. 8).

DISCUSSION

We identified 23 mAbs against human GPIIb/IIIa in our initial screening efforts and selected five for further study—four against GPIIb/IIIa's cysteine-rich Ly6 domain (RG3, RE3, RH1, RE6) and one against the acidic domain (RF4). These mAbs proved to be useful for three lines of investigation. First, we found that two mAbs against the Ly6 domain, RG3 and RE3, blocked the binding of LPL to GPIIb/IIIa, whereas a mAb against the acidic domain (RF4) did not. Of

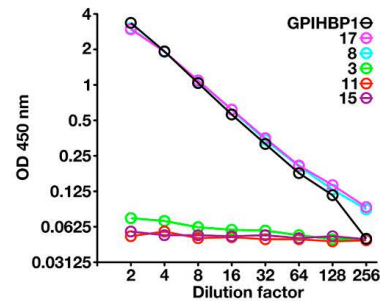



Fig. 8. An ELISA to detect GPIIb/IIIa in human plasma. We coated 96-well plates with mAb RF4 (1 μ g/well), blocked them with BSA, and incubated them overnight at 4°C with dilutions of human plasma (ranging from 1:2 to 1:256) or dilutions of purified human GPIIb/IIIa. In the case of the purified GPIIb/IIIa, the “1:2 dilution” corresponds to 500 pg/ml of recombinant GPIIb/IIIa, and the “1:256 dilution” corresponds to buffer alone (no recombinant GPIIb/IIIa). After washing the plates, GPIIb/IIIa captured by mAb RF4 was detected with HRP-labeled RE3 Fab’. Samples 8 and 17 were normal control plasma samples; sample 3 was from a subject homozygous for a deletion of *GPIIb/IIIa* (21); samples 11 and 15 were from subjects homozygous for a *GPIIb/IIIa* nonsense mutation (C89X). The plasma GPIIb/IIIa levels in samples 8 and 17 were 1,043 and 1,051 pg/ml, respectively. As expected, the GPIIb/IIIa levels in the GPIIb/IIIa-deficient subjects were essentially absent. (Note that GPIIb/IIIa-C89X is not bound by mAb RE3 [see supplemental Fig. S6] and therefore cannot be detected by this ELISA.) The plot represents a log-transformation of the data.

note, both RG3 and RE3 bound preferentially to nonreduced GPIIb/IIIa, implying that the epitopes for those mAbs depend on intact disulfide bonds in the Ly6 domain. Also, by SPR, mAbs RG3 and RE3 bound with reduced affinity to GPIIb/IIIa-W109S, an “Ly6 domain mutant” that lacks the capacity to bind LPL (19). Those findings provide strong support for recent SPR studies (8) that concluded that GPIIb/IIIa's Ly6 domain is largely responsible for high-affinity interactions with LPL. Second, immunohistochemistry studies of human adipose tissue with mAbs RE3 and RF4 revealed that GPIIb/IIIa is expressed only in capillary endothelial cells and not in venules—the same pattern observed previously in mice (5). From the standpoint of lipoprotein physiology, this pattern of expression makes sense. LPL is secreted by adipocytes and is subject to local regulation by ANGPTL4 (22). The fact that GPIIb/IIIa is expressed specifically in capillaries—the blood vessels that are immediately adjacent to adipocytes—facilitates the capture of locally produced LPL and serves to focus lipolytic activity, according to the requirements of nearby parenchymal cells. Third, we found, using a mAb-based ELISA, that GPIIb/IIIa can be detected in the plasma of normal subjects but not subjects with *GPIIb/IIIa* deficiency.

In our immunohistochemistry studies, we were able to detect GPIIb/IIIa on capillary endothelial cells of human adipose tissue by confocal immunofluorescence microscopy and by immunoperoxidase staining, but we could not detect GPIIb/IIIa in capillaries of the heart. Our inability to detect GPIIb/IIIa in heart capillaries was initially perplexing

because we invariably observed robust GPIHBP1 expression in mouse heart capillaries (4, 5). Follow-up studies revealed that our inability to detect GPIHBP1 in heart capillaries was probably related to lower amounts of GPIHBP1 expression in human heart.

One of our principal goals in creating GPIHBP1-specific monoclonal antibodies was to develop an ELISA for the detection of GPIHBP1 in human plasma, just as others had done for uPAR, another GPI-anchored Ly6 protein (13). The combination of mAb RF4 (to capture GPIHBP1 in the plasma) and HRP-labeled mAb RE3 (to detect captured GPIHBP1) proved successful. Our ELISA detected GPIHBP1 in serial dilutions of plasma from normal subjects but not from subjects with *GPIHBP1* deficiency. At this point, we do not understand why GPIHBP1 circulates in the plasma, but there are several possibilities. One is that exosomes containing GPIHBP1 are shed from capillary endothelial cells. Another is that GPIHBP1 is released into the plasma by an enzyme that cleaves the GPI anchor or cleaves GPIHBP1 downstream from the Ly6 domain. Another possibility is that soluble GPIHBP1 (GPIHBP1 lacking a GPI anchor) is secreted from capillary endothelial cells as a consequence of inefficiencies in the transamidase reaction that ordinarily replaces GPIHBP1's carboxyl-terminal hydrophobic signal peptide with a GPI anchor (23). We favor the latter possibility because cultured cells that overexpress the GPI-anchored form of GPIHBP1 invariably secrete large amounts of soluble GPIHBP1 (9). Regardless of the mechanism, our discovery that GPIHBP1 can be detected in human plasma is exciting. With the experimental approaches described here and our new GPIHBP1-specific mAbs, clinical lipidologists will now be able to test the utility of plasma GPIHBP1 levels as a biomarker for metabolic disease, vascular disease, or both. 

We thank personnel at Finsen Laboratory for the purified GPIHBP1 immunogen; the Monash Antibody Technologies Facility for creating the monoclonal antibodies; and Helen H. Hobbs for plasma samples from subjects with *GPIHBP1* deficiency.

REFERENCES

- Korn, E. D. 1955. Clearing factor, a heparin-activated lipoprotein lipase. I. Isolation and characterization of the enzyme from normal rat heart. *J. Biol. Chem.* **215**: 1–14.
- Korn, E. D. 1955. Clearing factor, a heparin-activated lipoprotein lipase. II. Substrate specificity and activation of coconut oil. *J. Biol. Chem.* **215**: 15–26.
- Havel, R. J., and R. S. Gordon, Jr. 1960. Idiopathic hyperlipemia: metabolic studies in an affected family. *J. Clin. Invest.* **39**: 1777–1790.
- Beigneux, A. P., B. Davies, P. Gin, M. M. Weinstein, E. Farber, X. Qiao, P. Peale, S. Bunting, R. L. Walzem, J. S. Wong, et al. 2007. Glycosylphosphatidylinositol-anchored high density lipoprotein-binding protein 1 plays a critical role in the lipolytic processing of chylomicrons. *Cell Metab.* **5**: 279–291.
- Davies, B. S., A. P. Beigneux, R. H. Barnes 2nd, Y. Tu, P. Gin, M. M. Weinstein, C. Nobumori, R. Nyren, I. Goldberg, G. Olivecrona, et al. 2010. GPIHBP1 is responsible for the entry of lipoprotein lipase into capillaries. *Cell Metab.* **12**: 42–52.
- Fry, B. C., W. Wuster, R. M. Kini, V. Brusic, A. Khan, D. Venkataraman, and A. P. Rooney. 2003. Molecular evolution and phylogeny of elapid snake venom three-finger toxins. *J. Mol. Evol.* **57**: 110–129.
- Ioka, R. X., M. J. Kang, S. Kamiyama, D. H. Kim, K. Magoori, A. Kamataki, Y. Ito, Y. A. Takei, M. Sasaki, T. Suzuki, et al. 2003. Expression cloning and characterization of a novel glycosylphosphatidylinositol-anchored high density lipoprotein-binding protein, GPIHBP1. *J. Biol. Chem.* **278**: 7344–7349.
- Myssling, S., K. K. Kristensen, M. Larsson, A. P. Beigneux, H. Gardsvoll, L. G. Fong, A. Bensadoun, T. J. Jorgensen, S. G. Young, and M. Ploug. 2016. The acidic domain of the endothelial membrane protein GPIHBP1 stabilizes lipoprotein lipase activity by preventing unfolding of its catalytic domain. *eLife*. **5**: e12095.
- Beigneux, A. P., P. Gin, B. S. J. Davies, M. M. Weinstein, A. Bensadoun, L. G. Fong, and S. G. Young. 2009. Highly conserved cysteines within the Ly6 domain of GPIHBP1 are crucial for the binding of lipoprotein lipase. *J. Biol. Chem.* **284**: 30240–30247.
- Davies, B. S., C. N. Goulbourne, R. H. Barnes 2nd, K. A. Turlo, P. Gin, S. Vaughan, D. J. Vaux, A. Bensadoun, A. P. Beigneux, L. G. Fong, et al. 2012. Assessing mechanisms of GPIHBP1 and lipoprotein lipase movement across endothelial cells. *J. Lipid Res.* **53**: 2690–2697.
- Vodenicharov, A., P. Atanassova, P. Yonkova, G. Kostadinov, and H. Hristov. 2007. Expression of lipoprotein lipase in the renal artery and vein of the domestic pig—an enzyme-histochemical study. *Bulg. J. Vet. Med.* **10**: 155–160.
- Camps, L., M. Reina, M. Llobera, S. Vilaro, and T. Olivecrona. 1990. Lipoprotein lipase: cellular origin and functional distribution. *Am. J. Physiol.* **258**: C673–C681.
- Piironen, T., B. Laursen, J. Pass, K. List, H. Gardsvoll, M. Ploug, K. Dano, and G. Hoyer-Hansen. 2004. Specific immunoassays for detection of intact and cleaved forms of the urokinase receptor. *Clin. Chem.* **50**: 2059–2068.
- Beigneux, A. P., B. S. J. Davies, S. Tat, J. Chen, P. Gin, C. V. Voss, M. M. Weinstein, A. Bensadoun, C. R. Pullinger, L. G. Fong, et al. 2011. Assessing the role of the glycosylphosphatidylinositol-anchored high density lipoprotein-binding protein 1 (GPIHBP1) three-finger domain in binding lipoprotein lipase. *J. Biol. Chem.* **286**: 19735–19743.
- Cårdsvoll, H., L. V. Hansen, T. J. Jorgensen, and M. Ploug. 2007. A new tagging system for production of recombinant proteins in *Drosophila* S2 cells using the third domain of the urokinase receptor. *Protein Expr. Purif.* **52**: 384–394.
- Gin, P., L. Yin, B. S. J. Davies, M. M. Weinstein, R. O. Ryan, A. Bensadoun, L. G. Fong, S. G. Young, and A. P. Beigneux. 2008. The acidic domain of GPIHBP1 is important for the binding of lipoprotein lipase and chylomicrons. *J. Biol. Chem.* **283**: 29554–29562.
- Zhao, B., S. Gandhi, C. Yuan, Z. Luo, R. Li, H. Gardsvoll, V. de Lorenzi, N. Sidenius, M. Huang, and M. Ploug. 2015. Stabilizing a flexible interdomain hinge region harboring the SMB binding site drives uPAR into its closed conformation. *J. Mol. Biol.* **427**: 1389–1403.
- Ben-Zeev, O., H. Z. Mao, and M. H. Doolittle. 2002. Maturation of lipoprotein lipase in the endoplasmic reticulum. Concurrent formation of functional dimers and inactive aggregates. *J. Biol. Chem.* **277**: 10727–10738.
- Beigneux, A. P., L. G. Fong, A. Bensadoun, B. S. Davies, M. Oberer, H. Gardsvoll, M. Ploug, and S. G. Young. 2015. GPIHBP1 missense mutations often cause multimerization of GPIHBP1 and thereby prevent lipoprotein lipase binding. *Circ. Res.* **116**: 624–632.
- Uhlen, M., L. Fagerberg, B. M. Hallstrom, C. Lindskog, P. Oksvold, A. Mardinoglu, A. Sivertsson, C. Kampf, E. Sjostedt, A. Asplund, et al. 2015. Proteomics. Tissue-based map of the human proteome. *Science*. **347**: 1260419.
- Rios, J. J., S. Shastry, J. Jasso, N. Hauser, A. Garg, A. Bensadoun, J. C. Cohen, and H. H. Hobbs. 2012. Deletion of GPIHBP1 causing severe chylomicronemia. *J. Inher. Metab. Dis.* **35**: 531–540.
- Yoshida, K., T. Shimizugawa, M. Ono, and H. Furukawa. 2002. Angiotensin-like protein 4 is a potent hyperlipidemia-inducing factor in mice and inhibitor of lipoprotein lipase. *J. Lipid Res.* **43**: 1770–1772.
- Kinoshita, T., and M. Fujita. 2016. Biosynthesis of GPI-anchored proteins: special emphasis on GPI lipid remodeling. *J. Lipid Res.* **57**: 6–24.

Chapter 3

GPIHBP1 Autoantibodies in a Patient with Unexplained Chylomicronemia

GPIHBP1 autoantibodies in a patient with unexplained chylomicronemia



Xuchen Hu, Geesje M. Dallinga-Thie, G. Kees Hovingh, Sandy Y. Chang, Norma P. Sandoval, Tiffany Ly P. Dang, Isamu Fukamachi, Kazuya Miyashita, Katsuyuki Nakajima, Masami Murakami, Loren G. Fong, Michael Ploug, Stephen G. Young*, Anne P. Beigneux*

Department of Medicine, David Geffen School of Medicine, University of California, Los Angeles, Los Angeles, CA, USA (Drs Hu, Chang, Sandoval, Dang, Fong, Young, and Beigneux); Department of Vascular Medicine, Academic Medical Center, Amsterdam, The Netherlands (Drs Dallinga-Thie and Hovingh); Department of Experimental Vascular Medicine, Academic Medical Center, Amsterdam, The Netherlands (Drs Dallinga-Thie and Hovingh); Immuno-Biological Laboratories (IBL) Co, Ltd, Fujioka, Gunma, Japan (Drs Fukamachi and Miyashita); Department of Clinical Laboratory Medicine, Gunma University, Graduate School of Medicine, Maebashi, Japan (Drs Miyashita, Nakajima, and Murakami); Finsen Laboratory, Rigshospitalet, Copenhagen, Denmark (Dr Ploug); Biotech Research and Innovation Centre (BRIC), University of Copenhagen, Copenhagen, Denmark (Dr Ploug); and Department of Human Genetics, David Geffen School of Medicine, University of California, Los Angeles, Los Angeles, CA, USA (Dr Young)

KEYWORDS:

Chylomicrons;
Endothelial cells;
Lipids;
Intravascular lipolysis;
Triglycerides

BACKGROUND: GPIHBP1, a glycolipid-anchored protein of capillary endothelial cells, binds lipoprotein lipase (LPL) in the interstitial spaces and transports it to the capillary lumen. GPIHBP1 deficiency prevents LPL from reaching the capillary lumen, resulting in low intravascular LPL levels, impaired intravascular triglyceride processing, and severe hypertriglyceridemia (chylomicronemia). A recent study showed that some cases of hypertriglyceridemia are caused by autoantibodies against GPIHBP1 (“GPIHBP1 autoantibody syndrome”).

OBJECTIVE: Our objective was to gain additional insights into the frequency of the GPIHBP1 autoantibody syndrome in patients with unexplained chylomicronemia.

METHODS: We used enzyme-linked immunosorbent assays to screen for GPIHBP1 autoantibodies in 33 patients with unexplained chylomicronemia and then used Western blots and immunocytochemistry studies to characterize the GPIHBP1 autoantibodies.

RESULTS: The plasma of 1 patient, a 36-year-old man with severe hypertriglyceridemia, contained GPIHBP1 autoantibodies. The autoantibodies, which were easily detectable by Western blot, blocked the ability of GPIHBP1 to bind LPL. The plasma levels of LPL mass and activity were low. The patient had no history of autoimmune disease, but his plasma was positive for antinuclear antibodies.

CONCLUSIONS: One of 33 patients with unexplained chylomicronemia had the GPIHBP1 autoantibody syndrome. Additional studies in large lipid clinics will be helpful for better defining the frequency of this syndrome and for exploring the best strategies for treatment.

© 2017 National Lipid Association. All rights reserved.

* Corresponding author. University of California, Los Angeles, 4506 Gonda Bldg., 695 Charles E. Young Dr. South, Los Angeles, CA 90095, USA.

E-mail addresses: sgyoung@mednet.ucla.edu (S.G. Young); abeigneux@mednet.ucla.edu (A.P. Beigneux)

Submitted May 10, 2017. Accepted for publication May 23, 2017.

Introduction

GPIHBP1 is a glycolipid-anchored protein of capillary endothelial cells that binds lipoprotein lipase (LPL) in the subendothelial spaces and shuttles it across endothelial cells to its site of action in the capillary lumen.¹ In the absence of GPIHBP1, LPL remains stranded in the interstitial spaces where it is unable to process triglyceride-rich lipoproteins in the plasma.^{1–3} Homozygosity for mutations in *GPIHBP1*, like homozygosity for mutations in *LPL*, causes a chylomicronemia syndrome⁴ associated with a substantial risk of acute pancreatitis. A variety of different *GPIHBP1* mutations have been described,^{5–14} and most have been missense mutations that result in a mutant GPIHBP1 protein that lacks the ability to bind LPL. A hallmark of genetic forms of GPIHBP1 deficiency is low levels of LPL in the preheparin and postheparin plasma (consistent with reduced delivery of LPL to the capillary lumen).^{5–7,15} Recent studies showed that it is possible to measure GPIHBP1 in human plasma with a monoclonal antibody (mAb)-based immunoassay.¹⁶ In the setting of *GPIHBP1* mutations, the plasma levels of GPIHBP1 are very low.^{16,17}

Beigneux et al¹⁷ recently identified 6 patients with chylomicronemia caused by autoantibodies against GPIHBP1 (“GPIHBP1 autoantibody syndrome”). They demonstrated that GPIHBP1 autoantibodies interfere with the ability of GPIHBP1 to bind LPL. Several patients with the GPIHBP1 autoantibody syndrome had clinical and/or serological evidence of an autoimmune disease (eg, systemic lupus erythematosus), but others did not. The plasma levels of LPL in patients with the GPIHBP1 autoantibody syndrome were low¹⁷ (again reduced delivery of LPL to the capillary lumen). The levels of GPIHBP1 in the plasma were also low, likely because the GPIHBP1 autoantibodies interfere with the detection of GPIHBP1 in an enzyme-linked immunosorbent assay (ELISA).¹⁷

The frequency of the GPIHBP1 autoantibody syndrome has not been clearly defined. Beigneux et al¹⁷ identified 6 cases of the GPIHBP1 autoantibody syndrome by screening ~200 miscellaneous plasma samples, including 130 patients with hypertriglyceridemia. In the current studies, we screened for GPIHBP1 autoantibodies in 33 patients with unexplained hypertriglyceridemia from the Academic Medical Center in Amsterdam. Each of these patients had undergone testing for *LPL*, *GPIHBP1*, *APOC2*, *LMF1*, or *APOA5* mutations, and none were identified.

Materials and methods

Plasma samples

Plasma samples from 33 patients from the Academic Medical Center (Amsterdam) were sent to the University of California, Los Angeles (UCLA) for GPIHBP1 autoantibody screening. All patients had been referred because of a

suspicion of LPL deficiency; the mean plasma triglyceride level in this group of patients was 1673 ± 2310 mg/dL (range: 171–11,327 mg/dL). All tested negative for mutations in *LPL*, *GPIHBP1*, *APOC2*, *LMF1*, and *APOA5*. Samples were taken under a protocol approved by the Academic Medical Center in Amsterdam. Because the plasma samples sent to UCLA were deidentified, the studies were exempt from Institutional Review Board approval by the UCLA Office of Human Use Protection.

Two GPIHBP1 autoantibody ELISAs

Recombinant human GPIHBP1 (rhGPIHBP1) with an amino-terminal urokinase plasminogen activator receptor (uPAR) tag¹⁸ were expressed in *Drosophila* S2 cells.^{18,19} The recombinant GPIHBP1 also contained a carboxyl-terminal tag for the mouse GPIHBP1-specific mAb 11A12.²⁰ To detect GPIHBP1 autoantibodies in plasma samples,¹⁷ 96-well plates were coated with uPAR-specific mAb (R24)²¹ and then incubated with GPIHBP1 for 2 hours. After washing the plates, human plasma samples (1:500 dilution) were added to the wells and incubated overnight at 4°C. After washing, binding of autoantibodies to GPIHBP1 was detected with a horseradish peroxidase (HRP)-labeled goat anti-human Ig(G + M). A second ELISA for GPIHBP1 autoantibodies was identical except that the 96-well plates were coated directly with purified, untagged GPIHBP1. To gauge levels of GPIHBP1 autoantibodies, we also added the HRP-labeled goat anti-human immunoglobulin (Ig[G + M]) to wells that had been coated with dilutions of purified human IgG. We also used an ELISA to screen for autoantibodies against other members in the Ly6 protein family (C4.4 A, CD59, and CD177).^{17,18,22,23}

Detecting GPIHBP1 autoantibodies with Western blots

The medium from *Drosophila* S2 cells expressing rhGPIHBP1 was size fractionated on 12% Bis-Tris sodium dodecyl sulfate polyacrylamide gel electrophoresis (SDS-PAGE) gels, then transferred to a nitrocellulose membrane. The membrane was blocked in Odyssey Blocking Buffer (LI-COR). Membranes were then incubated with the plasma from patient A1 (20 AU of GPIHBP1 autoantibodies/mL). The binding of autoantibodies to GPIHBP1 was detected with an IRDye680–donkey anti-human IgG (1:200). rhGPIHBP1 was also detected with an IRDye800-conjugated mAb against human GPIHBP1 (RF4)¹⁷ (1:500).

Western blots to detect LPL autoantibodies

The medium from V5-tagged human LPL-transfected CHO cells was size fractionated by SDS-PAGE under reducing and nonreducing conditions. Gels were then transferred to a nitrocellulose membrane and blocked in

Odyssey blocking buffer (Li-COR). Western blots were performed with the plasma from patient A1 (20 AU GPIHBP1 autoantibodies/mL) followed by an IRDye680-labeled goat anti-human IgG (LI-COR; 1:200) and IR-Dye800-labeled antibody against the V5 tag (1:500).

Measurements of LPL, hepatic lipase (HL), endothelial lipase (EL), and GPIHBP1

Plasma levels of LPL, HL, and EL were measured with mAb-based sandwich immunoassays.^{17,24–28} An ELISA was also used to measure plasma levels of GPIHBP1.¹⁶ In the latter assay, 96-well plates were coated with the GPIHBP1-specific mAb RF4. Dilutions of human plasma were then added and incubated at 4°C. After washing the wells, GPIHBP1 was detected with HRP-labeled mAb RE3. The amount of GPIHBP1 in the plasma was measured against a recombinant GPIHBP1 standard curve. Levels of LPL and HL activity in the plasma at baseline and 2, 3, 6, 9, 12, and 15 minutes after an intravenous injection of heparin (50 IU/kg) were measured as described.^{24,25}

ELISA to test the ability of GPIHBP1 autoantibodies to prevent LPL binding to GPIHBP1

To test the ability of GPIHBP1 autoantibodies to block the binding of LPL to GPIHBP1, 96-well plates were coated with mAb R24 and then incubated overnight at 4°C with an uPAR-tagged GPIHBP1, either alone or with various dilutions of human plasma samples. On the next day, the plates were washed, and human LPL (200 ng/well) was added to the wells and incubated for 2 hours at 4°C. The plates were washed, and an HRP-labeled LPL-specific mAb (5D2) was used to measure LPL binding. In other wells, an HRP-labeled goat anti-human Ig(G + M) was added to detect binding of GPIHBP1 autoantibodies to the immobilized GPIHBP1. HRP-labeled mAb 11A12 was used to confirm the presence of GPIHBP1 on the plates. A GPIHBP1-specific mAb (RE3) that blocks LPL binding to GPIHBP1 was used as an experimental control.¹⁶

Immunocytochemistry

CHO pgsA-745 (2×10^6) cells were electroporated with 2 µg of plasmid DNA encoding S-protein-tagged versions of human GPIHBP1, GPIHBP1-W109S, or CD59. After 24 hours, cells were washed in phosphate-buffered saline and incubated with plasma samples for 1 h at 4°C. Cells were washed and incubated for 1 h at 4°C with V5-tagged human LPL (200 ng/well). After washing, cells were fixed with methanol. Immunocytochemistry studies were performed on nonpermeabilized cells with a rabbit antibody against the S-protein tag (0.2 µg/mL) followed by an Alexa Fluor 647-conjugated donkey anti-rabbit IgG (ThermoFisher, 2.5 µg/mL); Alexa Fluor 568-conjugated mouse anti-V5 antibody (1:50); and Alexa Fluor 488-conjugated

goat anti-human Ig(G + M) (50 ng/mL). Images were taken with an Axiovert 200M microscope and processed with Zen 2010 software (Zeiss).

Results

We used an ELISA test with uPAR-tagged human GPIHBP1 to screen plasma samples from 33 patients with unexplained hypertriglyceridemia for autoantibodies against GPIHBP1 (Fig. 1A). The plasma samples from 32 patients were negative for autoantibodies, but one (from patient A1) was positive. The presence of GPIHBP1 autoantibodies in the plasma of patient A1 was confirmed in a separate ELISA with untagged, purified GPIHBP1 (Fig. 1B). In the latter assay, the level of GPIHBP1 autoantibodies was measured against a standard curve of human IgG, and the concentration was judged to be ~1 mg of

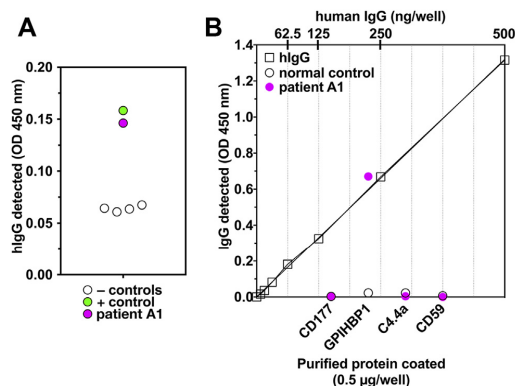


Figure 1 Detecting GPIHBP1 autoantibodies with a solid-phase ELISA. (A) Screening plasma samples for GPIHBP1 autoantibodies. Plasma samples were added to 96-well plates that had been coated with an anti-uPAR mAb and subsequently incubated with conditioned medium from *Drosophila* S2 cells expressing uPAR-tagged human GPIHBP1. After washing the plates, the binding of GPIHBP1 autoantibodies to immobilized GPIHBP1 was detected with an HRP-labeled anti-hIgG. One patient (patient A1; pink circle) had GPIHBP1 autoantibodies (dilution, 1:500), as did the positive control patient (patient 102,¹⁷ dilution, 1:12,500) (green circle). Levels of IgG binding were lower in four normal controls (black circles). (B) Testing the binding of plasma samples (1:500) to wells coated with purified, untagged human GPIHBP1 and 3 other Ly6 proteins (CD177, C4.4 A, and CD59). The plasma from patient A1 (1:500; pink circle) bound to GPIHBP1 but not to the other Ly6 proteins; the control plasma (1:500; open circles) did not bind to any of the proteins. The level of antibody binding to the GPIHBP1-coated wells was judged according to a human IgG standard curve (top x-axis); wells of a 96-well plate were coated with dilutions of normal human IgG, and the amount of IgG bound to those wells was assessed by quantifying binding of the HRP-labeled anti-human IgG (open squares). ELISA, enzyme-linked immunosorbent assay; hIgG, human immunoglobulin G; IgG, immunoglobulin G.

GPIHBP1 autoantibodies/mL. The Ig's in the plasma from patient A1 did not bind to other proteins of the Ly6 protein family (CD177, C4.4 A, and CD59).

Patient A1 is a 36-year-old male who was born in Eritrea. Screening revealed that he was free of *LPL*, *GPIHBP1*, *LMF1*, *APOC2*, or *APOA5* mutations. He was obese (body mass index: 35.5 kg/m²) and was taking anti-psychotic medications that had been prescribed by a psychiatrist. He smoked marijuana daily. In 2011, he had acute pancreatitis; at that time, the plasma triglyceride and cholesterol levels were 2188 and 318 mg/dL, respectively. Over the next year, the patient had 4 additional bouts of pancreatitis. Plasma samples were taken and archived during 2 hospitalizations for pancreatitis (in 2011 and 2012); the plasma triglyceride levels in those samples were 580 and 1929 mg/dL, respectively. Those samples, both positive for GPIHBP1 autoantibodies, were analyzed at UCLA.

Western blots confirmed the presence of GPIHBP1 autoantibodies in the plasma samples from patient A1. The autoantibodies in the plasma sample detected GPIHBP1 produced in *Drosophila* S2 cells (Fig. 2).

We suspected that the GPIHBP1 autoantibodies would block the ability of GPIHBP1 to bind LPL. Indeed, the plasma from patient A1 blocked the binding of human LPL to GPIHBP1 in an ELISA, whereas control plasma samples lacking autoantibodies did not block (Fig. 3). Plasma A1 blocked LPL binding to GPIHBP1 on the surface of GPIHBP1-transfected cells by immunocytochemistry,

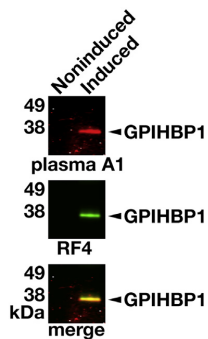


Figure 2 Western blot demonstrating the binding of GPIHBP1 autoantibodies in the plasma from patient A1 to human GPIHBP1 in the medium of transfected *Drosophila* S2 cells. The expression human GPIHBP1¹⁹ in *Drosophila* S2 cells was induced with 0.5 mM CuSO₄. Proteins in the medium from copper-induced and noninduced cells were size fractionated by SDS-PAGE and then transferred to a sheet of nitrocellulose for western blots. The membrane was incubated with the plasma from patient A1, followed by an IRDye680-labeled donkey anti-human IgG (red), and then with IRDye800-labeled human GPIHBP1-specific monoclonal antibody RF4 (green).¹⁶ Both RF4 and the IgGs in the plasma of patient A1 bound avidly to GPIHBP1 in the medium of cells that had been induced with CuSO₄ (induced); GPIHBP1 was absent from the medium of noninduced cells (noninduced). IgG, immunoglobulin G.

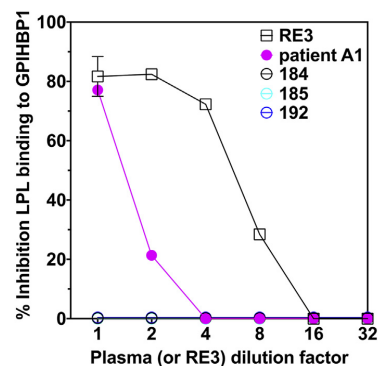


Figure 3 GPIHBP1 autoantibodies in the plasma of patient A1 abolish the ability of GPIHBP1 to bind LPL. The 96-well plates were coated with an anti-uPAR mAb and then incubated overnight at 4°C with uPAR-tagged GPIHBP1, either alone or in the presence of dilutions of human plasma. After washing the plates, human LPL (200 ng) was added to each well and incubated for 2 hours at 4°C. The plates were then washed, and the binding of LPL was detected with an HRP-labeled LPL-specific monoclonal antibody (5D2). The plasma of patient A1 blocked the binding of LPL to GPIHBP1 (pink solid circles), whereas plasma samples from 3 controls (184, 185, and 192) did not block. The GPIHBP1-specific mAb RE3 (black open squares) also blocked binding of LPL to GPIHBP1 (the “1:1 dilution” of mAb RE3 represents 20 µg/mL of purified IgG). LPL, lipoprotein lipase.

whereas control plasma samples lacking GPIHBP1 autoantibodies did not block (Fig. 4).

We predicted that the GPIHBP1 autoantibodies in patient A1 would be accompanied by low plasma levels of LPL. Indeed, the LPL mass level in the plasma of A1 was very low, 23.1 ng/mL (normal range: 40–156 ng/mL; mean, 84 ng/mL), consistent with reduced LPL binding to GPIHBP1 and reduced delivery of LPL to the intravascular compartment. We suspected that the levels of hepatic triglyceride lipase (HL) and EL, which do not bind GPIHBP1,³⁰ would not be low. Indeed, the HL level in the plasma of A1, 59.8 ng/mL, was not low (normal range: 18–136 ng/mL; mean, 60 ng/mL). The EL level, 133.8 ng/mL, was also not low (normal range: 41–141 ng/mL; mean, 77 ng/mL). After an intravenous injection of 5000 IU of heparin, the LPL activity level in patient A1 was less than one-half of those in a pool of 6 normal control subjects, whereas the HL activity was significantly higher than the activity in the pooled plasma of normal subjects (Fig. 5).

In the recent study by Beigneux et al.¹⁷ several patients with the GPIHBP1 autoantibody syndrome had systemic lupus erythematosus, and their plasma tested positive for antinuclear antibodies. Patient A1 had no clinical evidence of autoimmune disease, but testing revealed that his plasma was positive for antinuclear antibodies. The plasma of patient A1 did not have autoantibodies against LPL, as judged by an ELISA¹⁷ or a Western blot assay (Fig. 6).

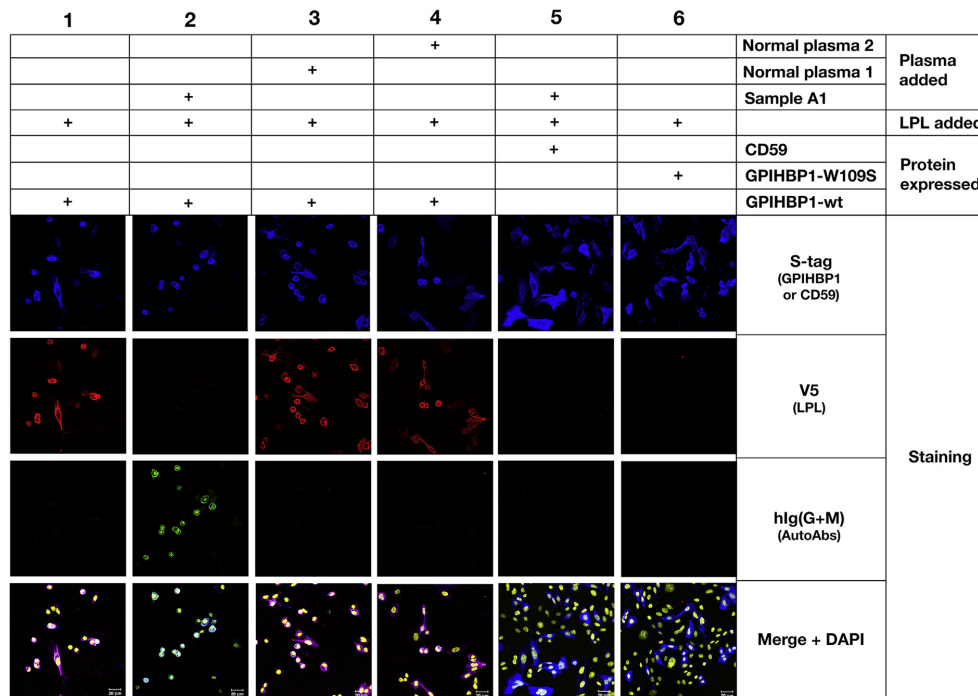


Figure 4 Immunocytochemistry studies showing that the GPIHBP1 autoantibodies in the plasma of patient A1 bind to GPIHBP1 on the surface of GPIHBP1-transfected CHO pgsA-745 cells and abolish binding of LPL. GPIHBP1 autoantibodies (green) in the plasma from patient A1 (1:20 dilution) bound to cells expressing S-protein-tagged human GPIHBP1 (column 2), but not to cells expressing S-protein-tagged CD59 (column 5). CD59 and GPIHBP1 expression on cells was detected with an antibody against the S-protein tag (blue). V5-tagged wild-type human LPL (detected with a V5 tag-specific antibody; red) binds avidly and specifically to GPIHBP1-transfected cells (column 1). The binding of GPIHBP1 autoantibodies (in the plasma of patient A1) to GPIHBP1 abolished LPL binding (column 2). In contrast, control plasma samples 1 and 2 (which did not contain GPIHBP1 autoantibodies) did not block the binding of LPL to GPIHBP1 (columns 3 and 4, respectively). Cells expressing a mutant GPIHBP1 (GPIHBP1-W109S)^{12,29} did not bind LPL (column 6). DNA was stained with DAPI (yellow). LPL, lipoprotein lipase.

The plasma triglycerides in patient A1 were 130 mg/dL in 2014, but no plasma samples were archived and available for analysis. The patient was subsequently lost to follow-up.

Discussion

We recently described autoantibodies against GPIHBP1, the endothelial cell LPL transporter, as a cause of acquired forms of chylomicronemia (“GPIHBP1 autoantibody syndrome”).¹⁷ In the present study, to increase our understanding of the frequency of this syndrome, we screened 33 patients with unexplained chylomicronemia from the Amsterdam Medical Center. Using a pair of ELISAs, we identified a single patient (patient A1) with the GPIHBP1 autoantibody syndrome. The GPIHBP1 autoantibodies were identified in 2 plasma samples obtained during 2011 and 2012 hospitalizations for chylomicronemia and acute pancreatitis. The GPIHBP1 autoantibodies in patient A1 interfered with the main function of GPIHBP1, which is

to bind LPL and transport it to the capillary lumen. When GPIHBP1 is absent or functionally defective, LPL remains stranded within the interstitial spaces and never reaches the capillary lumen.¹

In the initial description of the GPIHBP1 autoantibody syndrome, Beigneux et al¹⁷ identified 6 patients with GPIHBP1 autoantibodies by screening ~200 miscellaneous plasma samples, including many with hypertriglyceridemia and a handful from patients with both hypertriglyceridemia and autoimmune diseases. In that study, the information about the patient population, including genetic testing, was minimal. In the present study, we screened 33 hypertriglyceridemic patients in whom extensive genetic screening had failed to identify *LPL*, *GPIHBP1*, *APOC2*, *LMF1*, or *APOA5* mutations. The sole patient identified as having GPIHBP1 autoantibodies (patient A1) did not have any clinical signs of autoimmune disease, but his plasma tested positive for antinuclear antibodies. In the earlier study, 4 of the 6 patients with the GPIHBP1 autoantibody syndrome had

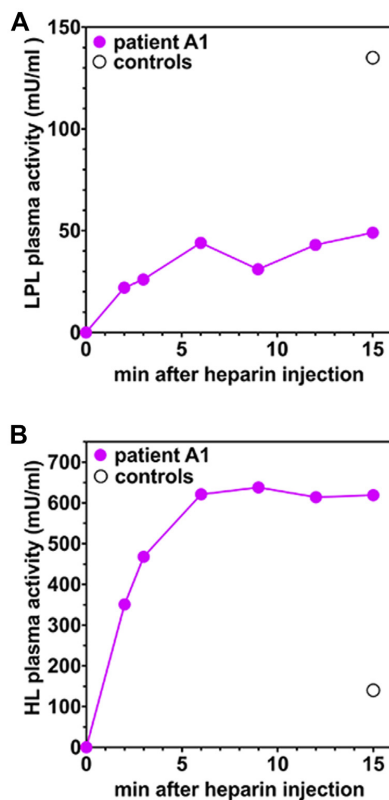


Figure 5 Levels of LPL catalytic activity in the postheparin plasma of patient A1 were low, whereas levels of hepatic lipase activity were high. Plasma samples were obtained from patient A1 at baseline, and at 6 time points after an intravenous injection of heparin, and LPL (A) and HL (B) activity levels were measured (pink solid circles). As a control, LPL and HL activity levels were also measured in a pool of plasma samples from 6 normal control subjects at the 15-minute time point (black open circle). LPL, lipoprotein lipase.

autoimmune diseases. At this point, the frequency of the GPIHBP1 autoantibody syndrome in patients with acquired forms of chylomicronemia remains incompletely defined, but it would appear that it is not rare—particularly in patients with clinical or serological evidence of autoimmune diseases. Additional studies are needed to gauge the overall frequency of GPIHBP1 autoantibodies in patients with acquired forms of hypertriglyceridemia.

In the study by Beigneux et al,¹⁷ the hypertriglyceridemia in 2 GPIHBP1 autoantibody syndrome patients (patients 157 and 164) responded to treatment with immunosuppressive therapy (rituximab and mycophenolate mofetil).^{17,31,32} In one of the patients, normalization of plasma triglyceride levels during therapy was accompanied by a complete disappearance of GPIHBP1 autoantibodies.¹⁷ The identification of additional patients with the GPIHBP1

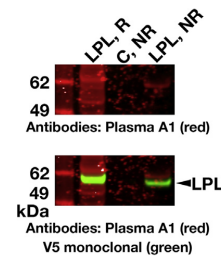


Figure 6 The plasma of patient A1 does not contain autoantibodies against LPL. Medium from V5-tagged human LPL-transfected CHO cells was size fractionated by SDS-PAGE under reducing (R) and nonreducing (NR) conditions. Western blots were performed with plasma from patient A1 (20 AU GPIHBP1 autoantibodies/mL) followed by IRDye680-labeled goat anti-human IgG (red). V5-tagged LPL on the same membrane was detected with an IRDye800-labeled V5 antibody (green). In the Western blot with the plasma from patient A1, several bands with a size roughly similar to that of LPL were detected. However, the V5 antibody Western blot revealed that the bands in the “plasma A1 Western blot” were distinct from authentic V5-tagged LPL. As a negative control (C), we tested medium from nontransfected CHO cells. LPL, lipoprotein lipase.

autoantibody syndrome will help to define optimal strategies for treatment. More patients would also help to define the relationship, if any, between GPIHBP1 autoantibody titers and plasma triglyceride levels.

The plasma triglyceride levels in patient A1 normalized several years after the hospitalizations for pancreatitis, raising the possibility that the GPIHBP1 autoantibody syndrome can, at least in some cases, resolve spontaneously. The plasma triglyceride levels in another patient with the GPIHBP1 autoantibody syndrome (patient 38 in the study by Beigneux et al¹⁷) also normalized in the absence of immunosuppressive drugs. In that case, however, the normalization of plasma triglyceride levels occurred in the setting of suboptimal nutritional status accompanying exocrine pancreatic insufficiency (from recurrent bouts of acute pancreatitis).

A hallmark of both genetic GPIHBP1 deficiency and the GPIHBP1 autoantibody syndrome is low plasma levels of LPL.^{5–7,15} In patient A1, both the preheparin LPL mass level and the postheparin LPL catalytic activity levels were low. These findings make sense, given that GPIHBP1 is solely responsible for shuttling LPL to the capillary lumen.¹ In the present study, we also examined plasma levels of 2 related lipases in the same protein family—HL and EL. We suspected that the levels of HL and EL would not be perturbed by GPIHBP1 autoantibodies, given that neither lipase binds to GPIHBP1.³⁰ Indeed, HL and EL mass levels were not reduced in the plasma of patient A1. In addition, after an injection of heparin, HL activity levels in plasma A1 were higher than in the normal controls. High levels of HL activity in postheparin plasma were noted previously in *Gpihbp1* knockout mice² and in a chylomicronemia patient who was homozygous for a p.Q115P missense mutation in

GPIHBP1.⁵ These observations suggest that defective GPIHBP1 function, whether genetic or acquired, does not reduce postheparin HL activity levels and in some cases may lead to higher-than-normal plasma levels of HL.

Acknowledgments

This work was supported by grants from the NHLBI (HL090553, HL087228, and HL125335) and a Transatlantic Network Grant from the Leducq Foundation (12CVD04). Mr Hu is supported by a Ruth L. Kirschstein National Research Service Award (T32HL69766), the NIH NIGMS Training Grant (T32GM08042), and the UCLA Medical Scientist Training Program. GKH is supported by a VIDI grant (016.156.445).

Author Contributions: Mr Hu performed experiments, analyzed the data, wrote the first draft of the manuscript, and edited the manuscript. Dr Dallinga-Thie generated the patient cohort and contributed to scientific discussions. Dr Hovingh provided background and insights into the patient with GPIHBP1 autoantibodies. Dr Chang performed ELISAs. Ms Sandoval performed ELISAs. Ms Dang generated monoclonal antibodies for ELISAs, Western blots, and immunocytochemistry studies. Dr Fukamachi performed ELISAs. Dr Miyashita performed ELISAs. Dr Nakajima performed ELISA analyses and contributed to scientific discussions. Dr Murakami performed ELISA analyses and contributed to scientific discussions. Dr Fong provided important scientific insights and edited the paper. Dr Ploug provided important scientific insights, edited the manuscript, and generated purified proteins (including GPIHBP1) for ELISAs. Dr Young analyzed the data and wrote the manuscript. Dr Beigneux performed experiments, analyzed the data, and wrote the manuscript. All authors approved the final version of the manuscript.

Financial disclosures

The authors have no financial interests to declare.

References

- Davies BS, Beigneux AP, Barnes RH 2nd, et al. GPIHBP1 is responsible for the entry of lipoprotein lipase into capillaries. *Cell Metab*. 2010;12:42–52.
- Beigneux AP, Davies B, Gin P, et al. Glycosylphosphatidylinositol-anchored high density lipoprotein-binding protein 1 plays a critical role in the lipolytic processing of chylomicrons. *Cell Metab*. 2007;5:279–291.
- Goulbourne C, Gin P, Tatar A, et al. The GPIHBP1–LPL complex is responsible for the margination of triglyceride-rich lipoproteins in capillaries. *Cell Metab*. 2014;19:849–860.
- Chait A, Brunzell JD. Chylomicronemia syndrome. *Adv Intern Med*. 1992;37:249–273.
- Franssen R, Young SG, Peelman F, et al. Chylomicronemia with low postheparin lipoprotein lipase levels in the setting of GPIHBP1 defects. *Circ Cardiovasc Genet*. 2010;3:169–178.
- Olivecrona G, Ehrenborg E, Semb H, et al. Mutation of conserved cysteines in the Ly6 domain of GPIHBP1 in familial chylomicronemia. *J Lipid Res*. 2010;51:1535–1545.
- Plempianich W, Young SG, Khovidhunkit W, et al. Multimerization of GPIHBP1 and familial chylomicronemia from a serine-to-cysteine substitution in GPIHBP1's Ly6 domain. *J Biol Chem*. 2014;289:19491–19499.
- Ariza MJ, Martinez-Hernandez PL, Ibarretxe D, et al. Novel mutations in the GPIHBP1 gene identified in 2 patients with recurrent acute pancreatitis. *J Clin Lipidol*. 2016;10:92–100.e1.
- Rabacchi C, D'Addato S, Palmisano S, et al. Clinical and genetic features of 3 patients with familial chylomicronemia due to mutations in GPIHBP1 gene. *J Clin Lipidol*. 2016;10:915–921.e4.
- Ahmad Z, Wilson DP. Familial chylomicronemia syndrome and response to medium-chain triglyceride therapy in an infant with novel mutations in GPIHBP1. *J Clin Lipidol*. 2014;8:635–639.
- Buonuomo PS, Bartuli A, Rabacchi C, Bertolini S, Calandra S. A 3-day-old neonate with severe hypertriglyceridemia from novel mutations of the GPIHBP1 gene. *J Clin Lipidol*. 2015;9:265–270.
- De Castro-Oros I, Civeira F, Pueyo MJ, et al. Rare genetic variants with large effect on triglycerides in subjects with a clinical diagnosis of familial vs nonfamilial hypertriglyceridemia. *J Clin Lipidol*. 2016;10:790–797.
- Chokshi N, Blumenschein SD, Ahmad Z, Garg A. Genotype-phenotype relationships in patients with type I hyperlipoproteinemia. *J Clin Lipidol*. 2014;8:287–295.
- Patri N, Brothers J, Xing C, Garg A. Type I hyperlipoproteinemia in a child with large homozygous deletion encompassing GPIHBP1. *J Clin Lipidol*. 2016;10:1035–1039.e2.
- Rios JJ, Shastry S, Jasso J, et al. Deletion of GPIHBP1 causing severe chylomicronemia. *J Inherit Metab Dis*. 2012;35:531–540.
- Hu X, Sleeman MW, Miyashita K, et al. Monoclonal antibodies that bind to the Ly6 domain of GPIHBP1 abolish the binding of LPL. *J Lipid Res*. 2017;58:208–215.
- Beigneux AP, Miyashita K, Ploug M, et al. Autoantibodies Against GPIHBP1 as a Cause of Hypertriglyceridemia. *N Engl J Med*. 2017;376:1647–1658.
- Gårdsvoll H, Hansen LV, Jorgensen TJ, Ploug M. A new tagging system for production of recombinant proteins in *Drosophila* S2 cells using the third domain of the urokinase receptor. *Protein Expr Purif*. 2007;52:384–394.
- Beigneux AP, Fong LG, Bensadoun A, et al. GPIHBP1 Missense Mutations Often Cause Multimerization of GPIHBP1 and Thereby Prevent Lipoprotein Lipase Binding. *Circ Res*. 2014;116:624–632.
- Beigneux AP, Gin P, Davies BSI, et al. Highly conserved cysteines within the Ly6 domain of GPIHBP1 are crucial for the binding of lipoprotein lipase. *J Biol Chem*. 2009;284:30240–30247.
- Gårdsvoll H, Jacobsen B, Kriegbaum MC, et al. Conformational regulation of urokinase receptor function: impact of receptor occupancy and epitope-mapped monoclonal antibodies on lamellipodia induction. *J Biol Chem*. 2011;286:33544–33556.
- Hansen LV, Gårdsvoll H, Nielsen BS, et al. Structural analysis and tissue localization of human C4.4A: a protein homologue of the urokinase receptor. *Biochem J*. 2004;380:845–857.
- Mysling S, Kristensen KK, Larsson M, et al. The acidic domain of the endothelial membrane protein GPIHBP1 stabilizes lipoprotein lipase activity by preventing unfolding of its catalytic domain. *Elife*. 2016;5:e12095.
- Surendran RP, Visser ME, Heemelaar S, et al. Mutations in LPL, APOC2, APOA5, GPIHBP1 and LMF1 in patients with severe hypertriglyceridaemia. *J Intern Med*. 2012;272:185–196.
- Kastelein JJ, Jukema JW, Zwinderman AH, et al. Lipoprotein lipase activity is associated with severity of angina pectoris. REGRESS Study Group. *Circulation*. 2000;102:1629–1633.

26. Ishida T, Miyashita K, Shimizu M, et al. ELISA system for human endothelial lipase. *Clin Chem*. 2012;58:1656–1664.
27. Machida T, Miyashita K, Sone T, et al. Determination of serum lipoprotein lipase using a latex particle-enhanced turbidimetric immunoassay with an automated analyzer. *Clin Chim Acta*. 2015;442:130–135.
28. Miyashita K, Kobayashi J, Imamura S, et al. A new enzyme-linked immunosorbent assay system for human hepatic triglyceride lipase. *Clin Chim Acta*. 2013;424:201–206.
29. Beigneux AP, Davies BSI, Tat S, et al. Assessing the role of the glycosylphosphatidylinositol-anchored high density lipoprotein-binding protein 1 (GPIHBP1) three-finger domain in binding lipoprotein lipase. *J Biol Chem*. 2011;286:19735–19743.
30. Gin P, Beigneux AP, Voss C, et al. Binding preferences for GPIHBP1, a glycosylphosphatidylinositol-anchored protein of capillary endothelial cells. *Arterioscler Thromb Vasc Biol*. 2011;31:176–182.
31. Blom DJ, Marais AD. Severe hypertriglyceridemia in a patient with lupus. *Am J Med*. 2005;118:443–444.
32. Ashraf AP, Beukelman T, Pruneta-Deloché V, Kelly DR, Garg A. Type I hyperlipoproteinemia and recurrent acute pancreatitis due to lipoprotein lipase antibody in a young girl with Sjogren's syndrome. *J Clin Endocrinol Metab*. 2011;96:3302–3307.

Chapter 4

GPIHBP1 Expression in Gliomas Promotes Utilization of Lipoprotein-derived Nutrients

GPIHBP1 expression in gliomas promotes utilization of lipoprotein-derived nutrients

Xuchen Hu¹, Ken Matsumoto², Rachel S. Jung¹, Thomas A. Weston¹, Patrick J. Heizer¹, Cuiwen He¹, Norma P. Sandoval¹, Christopher M. Allan¹, Yiping Tu¹, Harry V. Vinters³, Linda M. Liaw^{4,5}, Rochelle M. Ellison¹, Jazmin E. Morales¹, Lynn J. Baufeld^{6,7}, Nicholas A. Bayley^{6,7}, Liqun He⁸, Christer Betsholtz^{8,9}, Anne P. Beigneux¹, David A. Nathanson^{6,7}, Holger Gerhardt^{2,10}, Stephen G. Young^{1,11,‡}, Loren G. Fong^{1,‡}, and Haibo Jiang^{1,12,‡}

¹Department of Medicine, David Geffen School of Medicine, University of California, Los Angeles, CA 90095; ²VIB-KU Leuven Center for Cancer Biology (CCB), Leuven, Belgium
Departments of ³Pathology and Laboratory Medicine, ⁴Neurosurgery, ⁵Jonsson Comprehensive Cancer Center (JCCC), ⁶Molecular and Medical Pharmacology, and ⁷Ahmanson Translational Imaging Division, David Geffen School of Medicine, University of California, Los Angeles, CA 90095; ⁸Department of Immunology, Genetics and Pathology, Rudbeck Laboratory, Uppsala University, Uppsala, Sweden; ⁹Integrated Cardio Metabolic Centre (ICMC), Karolinska Institutet, Huddinge, Sweden; ¹⁰Max Delbrück Center for Molecular Medicine, Berlin, Germany; ¹¹Department of Human Genetics, David Geffen School of Medicine, University of California, Los Angeles, CA 90095; ¹²School of Molecular Sciences, University of Western Australia, 6009 Perth, WA, Australia;

‡Address correspondence to Stephen G. Young or Loren G. Fong, University of California, Los Angeles, 4506 Gonda Bldg., 695 Charles E. Young Dr. South, Los Angeles, CA 90095. Tel: (310) 825-4422; Fax: (310) 206-0865; E-mail: lfong@mednet.ucla.edu, sgyoung@mednet.ucla.edu; or Haibo Jiang, School of Molecular Sciences; Perth WA 6009 Australia; E-mail: haibo.jiang@uwa.edu.au

Conflict of Interest: The authors have declared that no conflict of interest exists.

Running title: *GPIHBP1 expression in capillaries of gliomas*

Abstract

GPIHBP1, a GPI-anchored protein of capillary endothelial cells, binds lipoprotein lipase (LPL) within the subendothelial spaces and shuttles it to the capillary lumen. The GPIHBP1-bound LPL is essential for the margination of triglyceride-rich lipoproteins (TRLs) along capillaries, allowing the lipolytic processing of TRLs to proceed. In peripheral tissues, the intravascular processing of TRLs by the GPIHBP1–LPL complex is crucial for generating lipid nutrients for adjacent parenchymal cells. GPIHBP1 is absent in capillaries of the brain, which uses glucose for fuel; however, GPIHBP1 is expressed in capillaries of mouse and human gliomas. Importantly, the GPIHBP1 in glioma capillaries captures locally produced LPL. We document, by NanoSIMS imaging, that TRLs marginate along glioma capillaries and that there is uptake of TRL-derived lipid nutrients by surrounding glioma cells. Thus, GPIHBP1 expression in gliomas facilitates TRL processing and provides a source of lipid nutrients for glioma cells.

Keywords: endothelial cells, glioma, lipids, triglycerides, cancer metabolism

Introduction

GPIHBP1, a GPI-anchored protein of capillary endothelial cells, is required for lipoprotein lipase (LPL)-mediated processing of triglyceride-rich lipoproteins (TRLs) (3). GPIHBP1's principal function is to capture LPL within the interstitial spaces, where it is secreted by parenchymal cells, and then shuttle the enzyme to the luminal surface of capillary endothelial cells (4). GPIHBP1 is a long-lived protein (1, 5) that moves bidirectionally across endothelial cells, with each trip to the abluminal plasma membrane representing an opportunity to capture LPL and bring it to the capillary lumen (6). When GPIHBP1 is absent or defective, LPL is stranded within the interstitial spaces, where it remains bound to sulfated proteoglycans near the surface of cells (1, 4, 7, 8). The inability of LPL to reach the capillary lumen in the absence of GPIHBP1 expression profoundly impairs TRL processing, resulting in severe hypertriglyceridemia (chylomicronemia) (3, 4, 9).

GPIHBP1 is expressed in capillary endothelial cells of peripheral tissues, with particularly high levels of expression in heart and brown adipose tissue (3, 4, 8). Most of the LPL within those tissues is bound to GPIHBP1 on capillaries (3, 4, 6–8, 10, 11), and the processing of TRLs is robust, generating fatty acid nutrients for nearby parenchymal cells (8, 12, 13). In contrast, GPIHBP1 is absent in capillaries of the brain (1, 4, 5), a tissue that depends on glucose for fuel (14). When wild-type mice are injected intravenously with a GPIHBP1-specific antibody, the antibody rapidly binds to GPIHBP1-expressing capillaries in peripheral tissues and disappears from the plasma (4, 5). In contrast, there is no antibody binding to capillaries of the brain (4, 5).

For the lipolytic processing of TRLs to proceed, lipoproteins in the bloodstream must marginate along the luminal surface of capillaries (9). TRL margination along capillaries depends on GPIHBP1—and more specifically on GPIHBP1-bound LPL (9). In GPIHBP1-deficient mice, TRLs never stop along heart capillaries and instead simply “flow on by” in the bloodstream (9). In wild-type mice, TRLs marginate along heart capillaries, but TRL margination is absent along capillaries of the brain (9).

Even though GPIHBP1 is not found in brain capillaries, there is ample evidence for LPL expression within the brain (15–20). Several groups found LPL in the rat brain, specifically in neurons of the dentate gyrus and hippocampus, pyramidal cells of the cortex, and Purkinje cells of the cerebellum (15–18, 20). By single-cell RNA sequencing, Zhang and colleagues (21) found *Lpl* transcripts in the resident macrophages of the brain (microglia), with lower levels in astrocytes, neurons, and oligodendrocytes. Using the same approach, Vanlandewijck and coworkers (22) found LPL expression in brain smooth muscle cells and in perivascular fibroblasts (at even higher levels than in microglial cells). Given the absence of GPIHBP1 expression in brain capillaries and the absence of TRL margination along brain capillaries, we have proposed that the LPL in the brain likely has an extravascular function, presumably to hydrolyze glycerolipids within the extracellular spaces (1, 2).

Despite the absence of GPIHBP1 expression in brain capillaries, we were curious about whether GPIHBP1 might be expressed in capillaries of gliomas. Glioma capillaries are morphologically distinct from normal brain capillaries (23–26), and the blood–brain barrier is often defective (27). By electron microscopy, glioblastoma capillaries have been reported to resemble capillaries in peripheral tissues (28).

If GPIHBP1 were to be expressed in glioma capillaries, it could be relevant to glioma metabolism. The GPIHBP1 might capture locally produced LPL, allowing for TRL margination and TRL processing, thereby providing a source of lipid nutrients for glioma cells. Interestingly, Dong *et al.* (29) documented LPL expression in gliomas. Also, several studies have raised the possibility that glioma cells use fatty acids for fuel (30–34) and that levels of free fatty acids are higher in gliomas than in normal brain tissue (34, 35).

In the current study, we sought to determine if glioma capillaries express GPIHBP1 and if so, whether it would bind LPL and facilitate TRL margination and lipolytic processing of TRLs. In our study, we took advantage of NanoSIMS imaging, a high-resolution mass spectrometry–based imaging modality that makes it possible to visualize TRL margination and TRL processing in

tissue sections (13, 36–41). This imaging modality allowed us to visualize TRL margination in glioma capillaries as well as the entry of TRL-derived nutrients into tumor cells.

Results

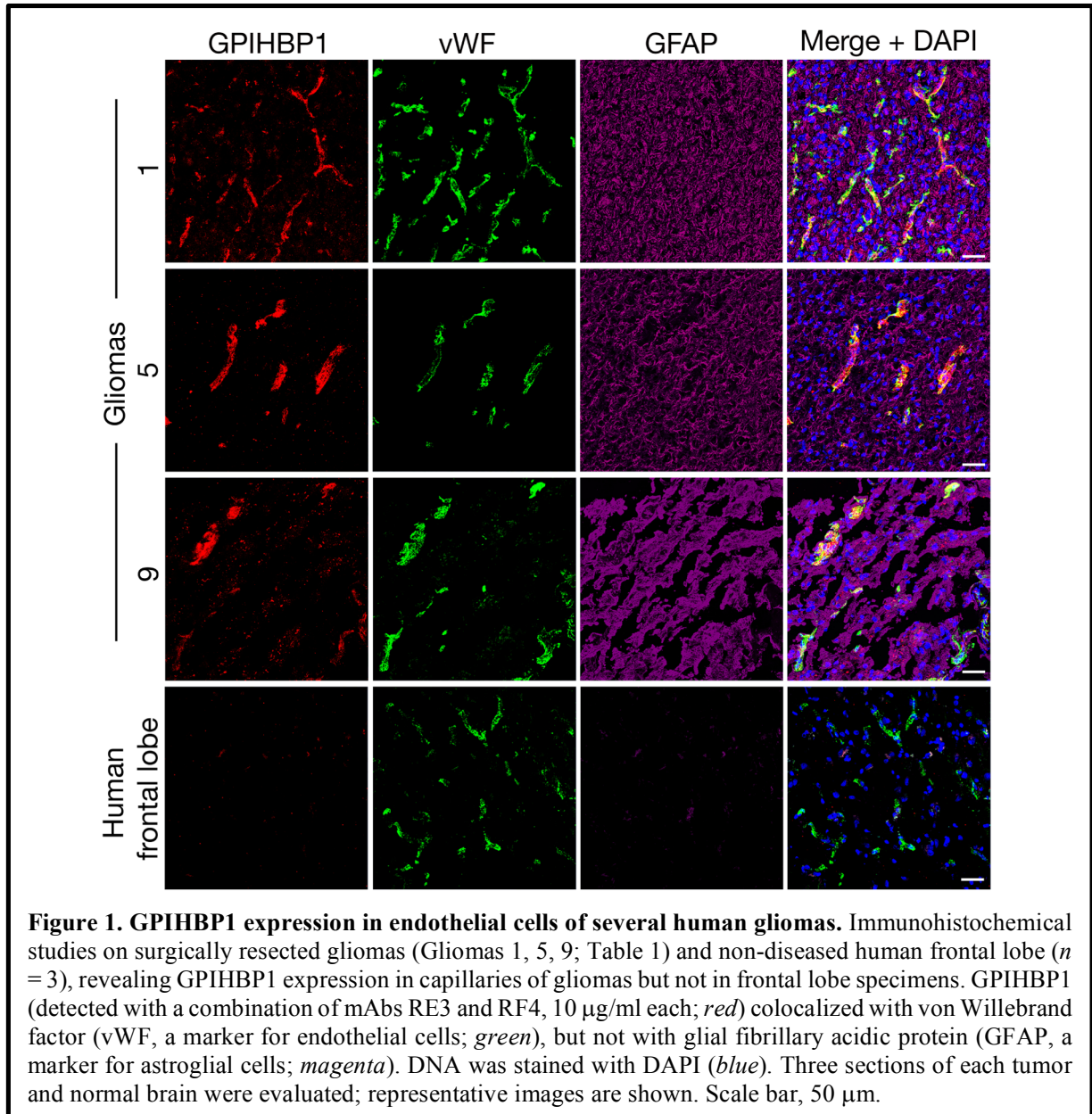
GPIHBP1 is expressed in endothelial cells of human gliomas

We sectioned 20 human gliomas (Table 1) and screened them for GPIHBP1 expression by confocal microscopy with three GPIHBP1-specific monoclonal antibodies (mAbs) [RF4, which

Sample ID	Tissue Diagnosis	Location	1p/19q co-deletion	IDH1 Mutation	GPIHBP1
1	GBM	Right Frontal, Parietal	No	Negative	Yes
2	GBM	Left Temporal	No	Negative	Yes
3	GBM	Right Occipital	No	Negative	Yes
4	GBM	Left Frontal	No	Negative	Yes
5	Oligodendroglioma Grade II	Left Anterior Temporal, Left Posterior Temporal	Yes	Negative	Yes
6	Oligoastrocytoma Grade III	Right Temporal	No	Negative	Yes
7	GBM + oligodendroglial component	Left Frontal	Yes	Negative	Yes
8	GBM + extensive oligodendroglial component	Right Frontal	No	Negative	Yes
9	Oligodendroglioma Grade III	Left Frontal	Yes	+ R132H	Yes
10	Oligodendroglioma Grade III	Left Frontal	Yes	+ R132H	Yes
11	Oligoastrocytoma	Right Parietal	No	Negative	Yes
12	Oligodendroglioma Grade III	Right Parietal	Yes	+ R132H	Yes
13	Oligodendroglioma Grade III	Right Parietal	Yes	Negative	Yes
14	Oligoastrocytoma Grade III	Left Temporal	No	+ R132H	Yes
15	Oligoastrocytoma Grade III	Right Temporal	No	+ R132G	No
16	Oligoastrocytoma Grade III	Right Frontal	No	+ R132H	No
17	Oligodendroglioma Grade III	Left Frontal	Yes	Negative	No
18	Oligodendroglioma Grade III	Left Frontal	Yes	+ R132H	No
19	Oligodendroglioma Grade III	Left Temporal	Yes	Negative	No
20	Oligodendroglioma Grade III	Right Temporal	Yes	+ R132H	No

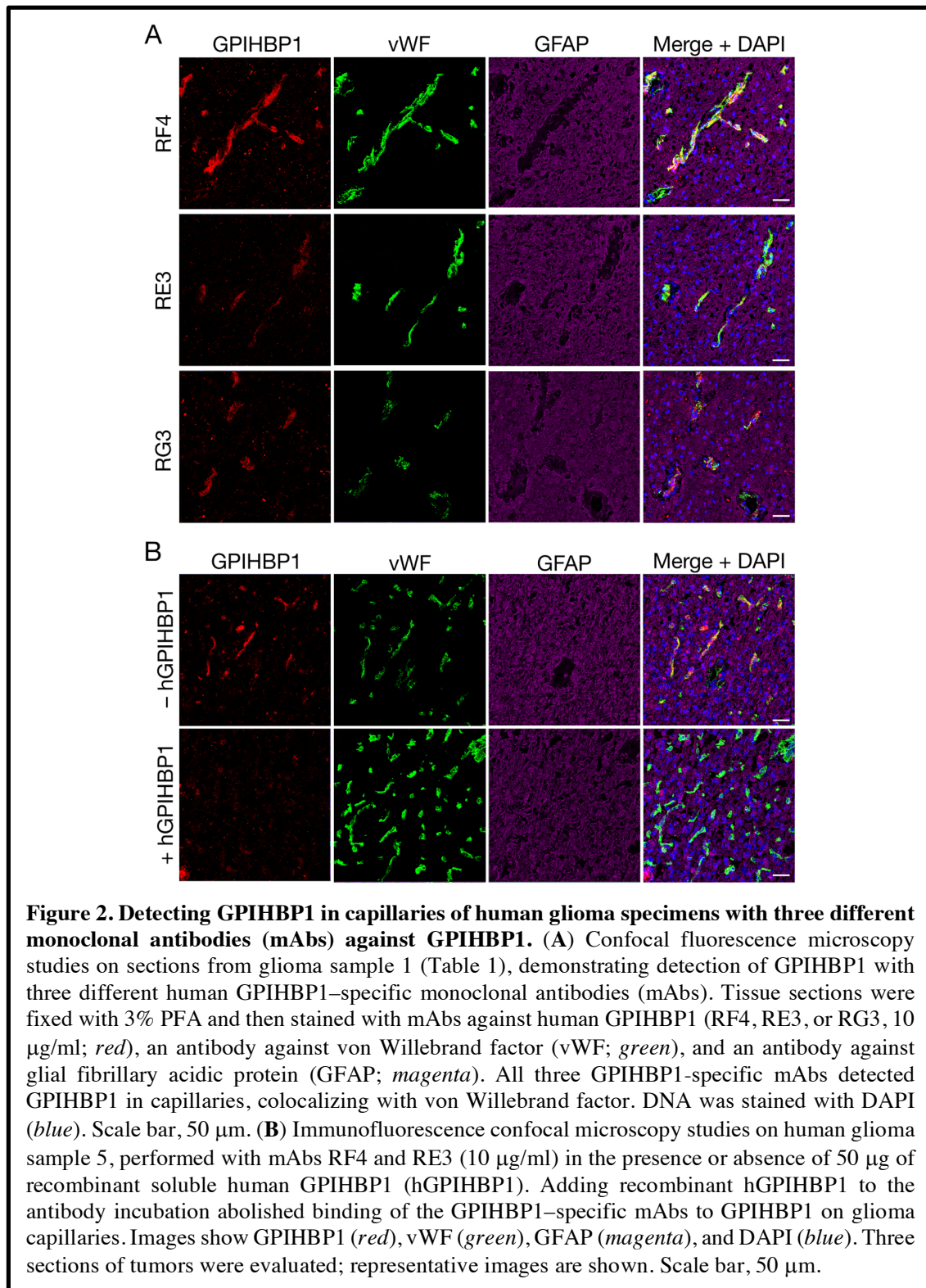
Table 1. Human glioma tumor specimens. Expression of GPIHBP1 was assessed by immunohistochemistry with mAbs against human GPIHBP1 (RF4, RE3, RG3). Those conducting the studies were blinded to diagnoses. The table details the tumor diagnosis, location, 1p/19q co-deletion, and IDH1 mutation status, as well as the presence of GPIHBP1.

binds to residues 27–44 downstream from GPIHBP1’s acidic domain (42); RE3 and RG3, which bind to GPIHBP1’s LU (Ly6/uPAR) domain) (43)]. GPIHBP1 in capillary endothelial cells was detected in 14 of 20 gliomas (Table 1) and colocalized with von Willebrand factor, an endothelial cell marker (Figure 1). GPIHBP1 expression in glioma capillaries did not appear to correlate with

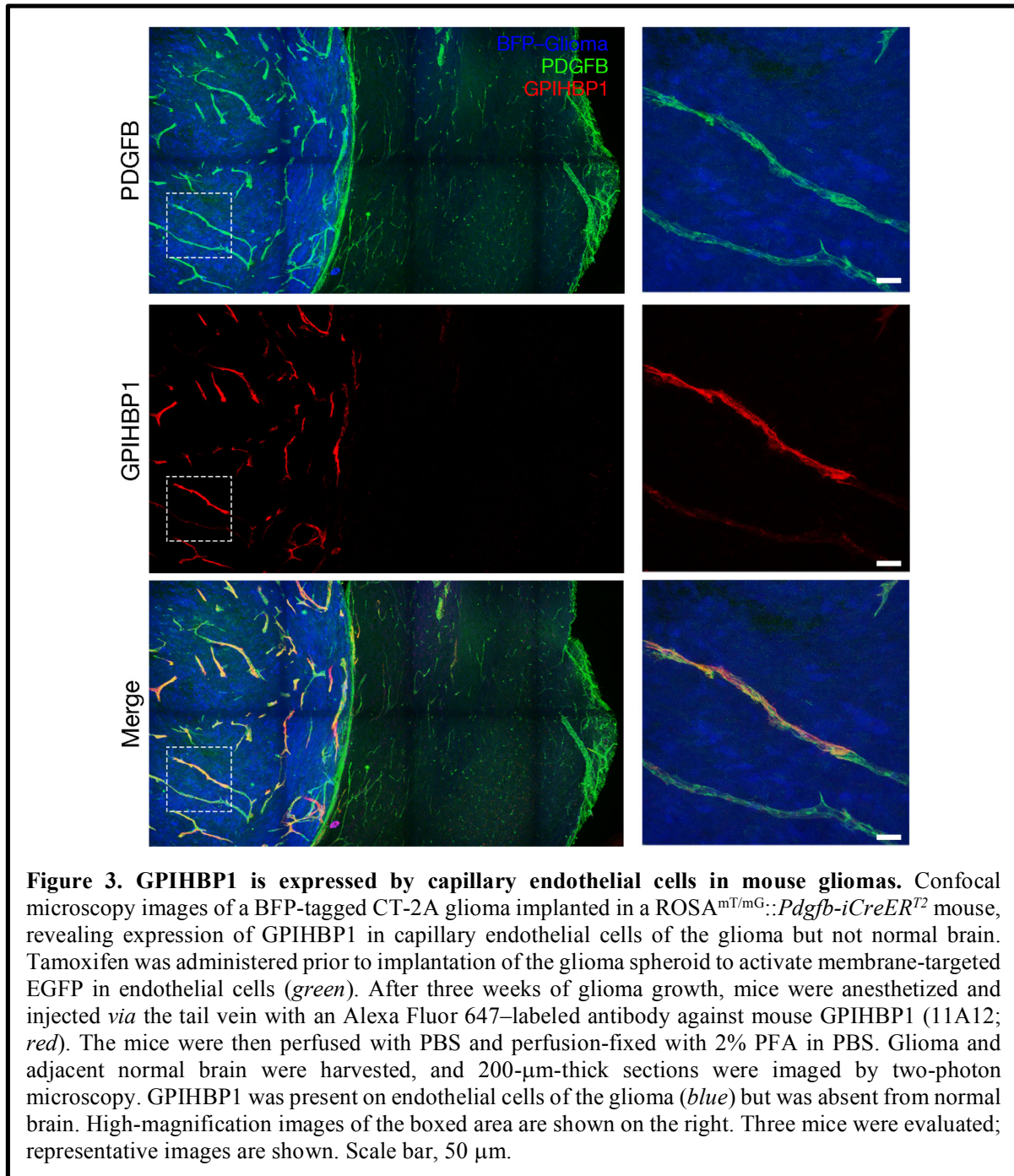


glioma grade, 1p/19q co-deletions, or IDH1 mutations (Table 1). GPIHBP1 was not detectable in capillaries of human brain specimens (Figure 1). The GPIHBP1 in glioma capillaries could be

detected with all three GPIHBP1–specific mAbs (Figure 2A). To be confident in the specificity of the antibodies, we performed studies in which recombinant human GPIHBP1 was added to the



GPIHBP1-specific mAbs before incubating the solution with the glioma sections. As expected, the presence of recombinant GPIHBP1 eliminated binding of the GPIHBP1-specific mAbs to glioma capillaries (Figure 2B). GPIHBP1 expression in glioma capillaries could also be detected by immunoperoxidase staining (Figure 1—figure supplement 1).



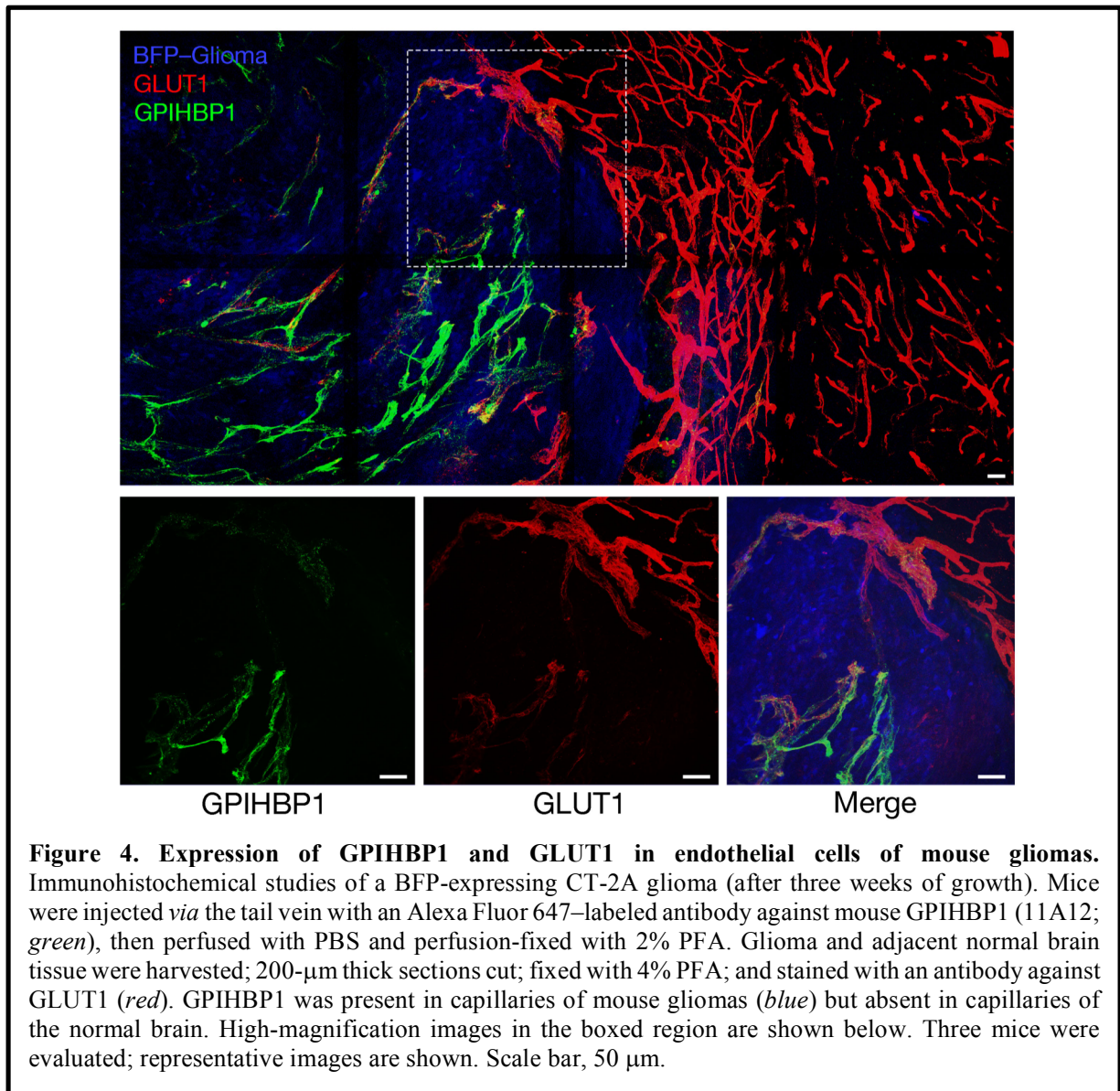
GPIHBP1 is present in the capillary endothelial cells of mouse gliomas

To determine if GPIHBP1 is expressed in a mouse model of glioblastoma, spheroids of syngeneic C57BL/6 mouse CT-2A glioma cells (44, 45), modified to express a blue fluorescent protein (BFP) (46), were engrafted into brains of mice harboring an endothelial cell-specific *Pdgfb-iCreER^{T2}* transgene (47) and a *ROSA^{mT/mG}* reporter allele (48). *ROSA^{mT/mG}* is a two-color fluorescent, membrane-targeted Cre-dependent reporter allele. In the absence of Cre, all cells express a membrane-localized tdTomato and fluoresce red. In the setting of Cre expression, cells express membrane-localized EGFP (rather than tdTomato) and fluoresce green. Before tumor implantation, mice were injected with tamoxifen to induce *Pdgfb*-driven Cre expression in endothelial cells; thus, the endothelial cells of the mice expressed EGFP and fluoresced green. Mice harboring gliomas (after three weeks of growth) were injected intravenously with an Alexa Fluor 647–conjugated antibody against mouse GPIHBP1 (11A12) (49). Mice were perfused with PBS and then perfusion-fixed with 2% PFA, and tumor sections were processed for two-photon immunofluorescence microscopy. GPIHBP1 was detected in endothelial cells of the gliomas, colocalizing with EGFP (brain endothelial cells), but GPIHBP1 was absent in capillaries in the adjacent normal brain (Figure 3, Figure 3—figure supplement 1). By transmission electron microscopy, we observed large and irregularly shaped capillaries in gliomas, with numerous villus-like structures on the luminal surface of endothelial cells (Figure 3—figure supplement 2), similar to findings reported for capillaries in human gliomas (28, 50, 51).

The factors that regulate *Gpihbp1* expression in capillary endothelial cells of peripheral tissues and gliomas are incompletely understood. However, a recent study found that *Gpihbp1* transcript levels in rat aortic endothelial cells are upregulated by vascular endothelial growth factor (VEGF) (52), an angiogenic factor known to be expressed at high levels by glioma cells (53–55). We found that *Gpihbp1* expression in the mouse brain endothelial cell line bEnd.3 is upregulated by recombinant VEGF (Figure 3—figure supplement 3).

GLUT1 is expressed in capillaries of gliomas and normal brain

We used immunofluorescence microscopy to examine the expression of GPIHBP1 and GLUT1 [the main glucose transporter in brain capillaries (56, 57)] in mouse gliomas and adjacent normal brain. GPIHBP1 expression was detected in gliomas but was absent in the normal brain; the signal for GLUT1 was strong in endothelial cells of the normal brain and was easily detectable in



capillaries of gliomas (Figure 4, Figure 4—figure supplements 1–2). Consistent findings were observed in single-cell RNA-seq studies on vascular cells of gliomas [Ken Matsumoto, manuscript in preparation (58)] and normal brain vascular cells (22, 59). Endothelial cells of gliomas (high *vWF* expression) exhibit high expression of *Gpihbp1* and somewhat lower levels of *Glut1*

expression (*e.g.*, Endothelial cell cluster 5; Figure 4—figure supplement 3). In normal brain, *Glut1* was expressed highly in endothelial cells, whereas *Gpihbp1* expression was absent (Figure 4—figure supplement 3). In *Gpihbp1*-deficient mice, GLUT1 expression was detectable in capillaries of gliomas and normal brain (Figure 4—figure supplement 4).

LPL is present on GPIHBP1-expressing capillaries of mouse gliomas

Most of the LPL in peripheral tissues (*e.g.*, heart, brown adipose tissue) is bound to GPIHBP1 on capillaries; consequently, LPL and GPIHBP1 colocalize in tissue sections (1, 4, 6–8, 10, 11). We hypothesized that GPIHBP1-expressing endothelial cells of gliomas could capture LPL. Several observations prompted us to consider this hypothesis. First, as noted earlier, there is ample evidence for LPL expression in the brain (15–19, 21), and it seemed reasonable that some of that LPL would reach high-affinity GPIHBP1 binding sites on endothelial cells. Second, gliomas contain large numbers of macrophages (F4/80-expressing cells; Figure 5—figure supplement 1), and macrophages are known to express LPL (60). We found that LPL could be detected in peritoneal macrophages from wild-type mice but not in macrophages harvested from *Lpl*^{-/-} mice carrying a skeletal muscle-specific human LPL transgene (*Lpl*^{-/-}MCK-hLPL) (61) (Figure 5—figure supplement 2). Also, we found that LPL could be detected in some of the macrophages in mouse gliomas and normal brain of wild-type mice, but not in the brain of *Lpl*^{-/-}MCK-hLPL mice (Figure 5—figure supplement 3). These findings were consistent with single-cell RNA-seq data from glioma and normal brain, where *Lpl* transcripts were found in macrophages of gliomas and microglia of normal brain (Figure 4—figure supplement 3). *Lpl* transcripts are not present in capillary endothelial cells. Third, the most highly upregulated fatty acid metabolism gene in human gliomas, compared to normal brain tissue, is *LPL* (Figure 5—figure supplement 4). The second most perturbed gene in gliomas is CD36, which encodes a putative fatty acid transporter (Figure 5—figure supplement 4).

To determine if LPL is bound to GPIHBP1-expressing capillaries of gliomas, we performed immunohistochemical studies, taking advantage of an affinity-purified goat antibody against

mouse LPL (62). These studies revealed colocalization of GPIHBP1 and LPL in glioma capillaries (Figure 5, Figure 5—figure supplement 5). LPL was not present in capillaries of the normal brain

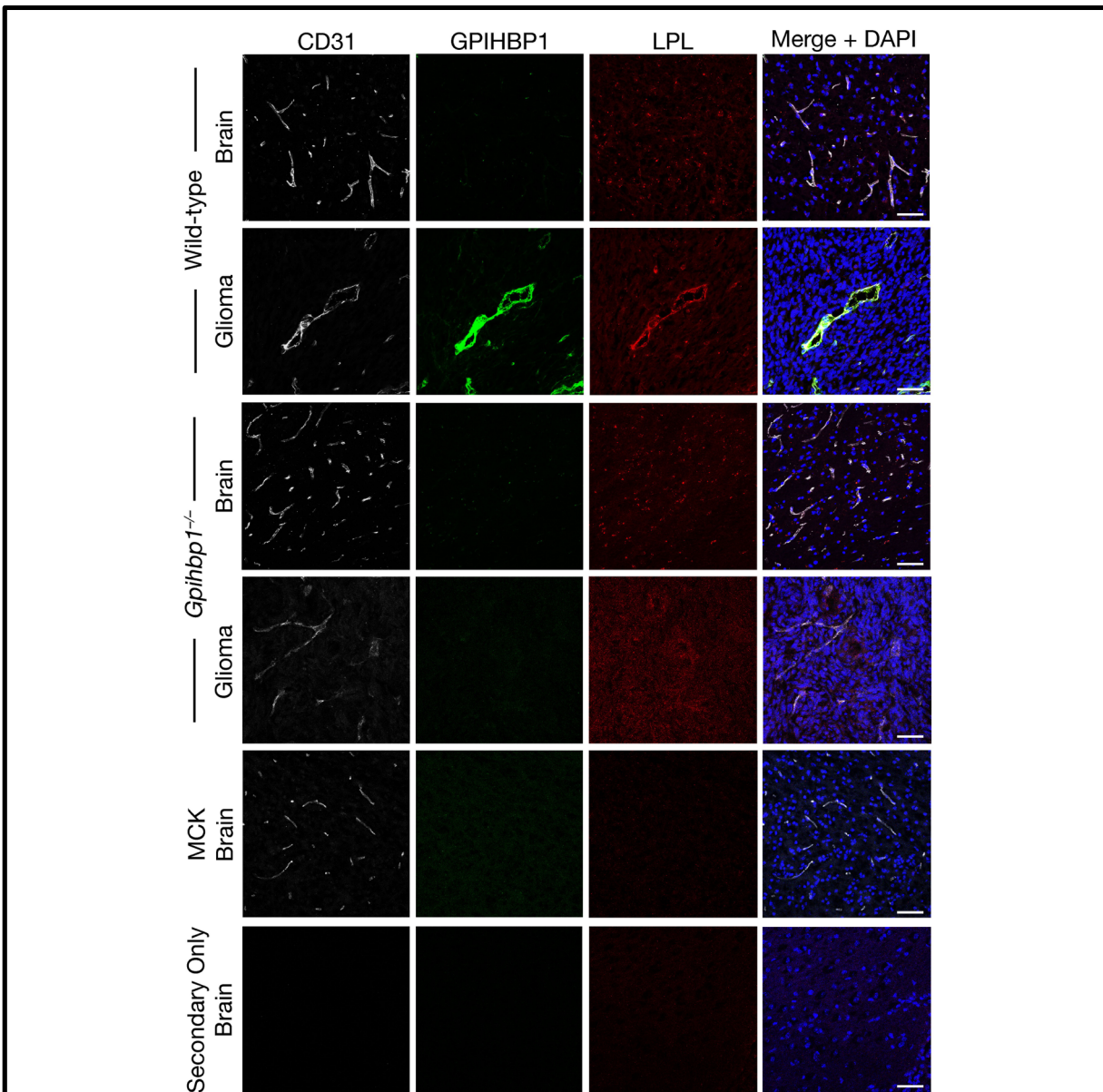


Figure 5. Lipoprotein lipase colocalizes with GPIHBP1 in glioma capillaries. Confocal immunofluorescence microscopy studies on glioma and normal brain from wild-type and *Gpnhbp1*^{-/-} mice, along with the brain from an *Lpl*^{-/-} mouse carrying a skeletal muscle-specific human LPL transgene (MCK). Glioma and brain sections (10- μ m-thick) were fixed with 3% PFA and then stained with a mAb against mouse GPIHBP1 (11A12; *green*), a goat antibody against mouse LPL (*red*), and a rabbit antibody against CD31 (*white*). LPL colocalizes with GPIHBP1 and CD31 in capillaries of gliomas; GPIHBP1 and LPL were absent in normal brain capillaries and absent in glioma capillaries in *Gpnhbp1*^{-/-} mice. DNA was stained with DAPI (*blue*). No LPL was detected in the capillaries the *Lpl*-deficient mice (MCK) or when the incubation with primary antibodies was omitted (“Secondary Only”). Staining of all tissue sections was performed simultaneously, and all images were recorded with identical microscopy settings. Three mice per genotype were evaluated; representative images are shown. Scale bar, 50 μ m.

or in capillaries of gliomas from *Gpihbp1*^{-/-} mice (Figure 5, Figure 5—figure supplement 5). As expected, the binding of the goat LPL antibody to tissues of *Lpl*^{-/-}MCK-hLPL mice was low (Figure 5, Figure 5—figure supplement 5), whereas mouse LPL was easily detectable in heart capillaries of wild-type mice (colocalizing with GPIHBP1) (Figure 5—figure supplement 6). Consistent with earlier publications (15, 18), we observed a strong mouse LPL signal in hippocampal neurons of wild-type mice but not *Lpl*^{-/-}MCK-hLPL mice (Figure 5—figure supplement 7). Of note, LPL was undetectable in “secondary antibody-only” experiments (*i.e.*, when the incubation of the primary antibody with tissue sections was omitted) (Figure 5, Figure 5—figure supplement 5–7).

There is little reason to suspect that expression of LPL influences the expression of GPIHBP1 in capillaries. The overexpression of human LPL in the skeletal muscle of *Lpl*^{-/-}MCK-hLPL mice did not alter levels of *Gpihbp1* expression (Figure 5—figure supplement 8).

Margination of TRLs along glioma capillaries and uptake of TRL-derived nutrients in glioma cells

Given the presence of GPIHBP1-bound LPL on glioma capillaries, we suspected that we might find evidence for TRL margination and processing in gliomas. To test this idea, TRLs that were heavily labeled with deuterated lipids ([²H]TRLs) (13) were injected intravenously into mice harboring CT-2A gliomas (after three weeks of glioma growth). After allowing the [²H]TRLs to circulate for either 1 min or 30 min, the mice were euthanized, extensively perfused with PBS, and perfusion-fixed with carbodiimide/glutaraldehyde. Heart, brain, and glioma specimens were harvested and processed for NanoSIMS imaging. ¹²C¹⁴N⁻ or ¹H⁻ images were used to visualize tissue morphology, and ²H/¹H images were used to identify regions of ²H enrichment. The scale in ²H/¹H images for brain and glioma specimens ranges from 0.00018 to 0.0003 (*i.e.*, from levels slightly above ²H natural abundance to levels twice as high as ²H natural abundance). The scale in the heart ²H/¹H images ranges from 0.00018 to 0.0006. In mice euthanized 1 min after the [²H]TRLs injection, [²H]TRL margination was visualized along the luminal surface of glioma and heart capillaries, but not along capillaries of normal brain (Figure 6A–B). After 1 min, deuterated

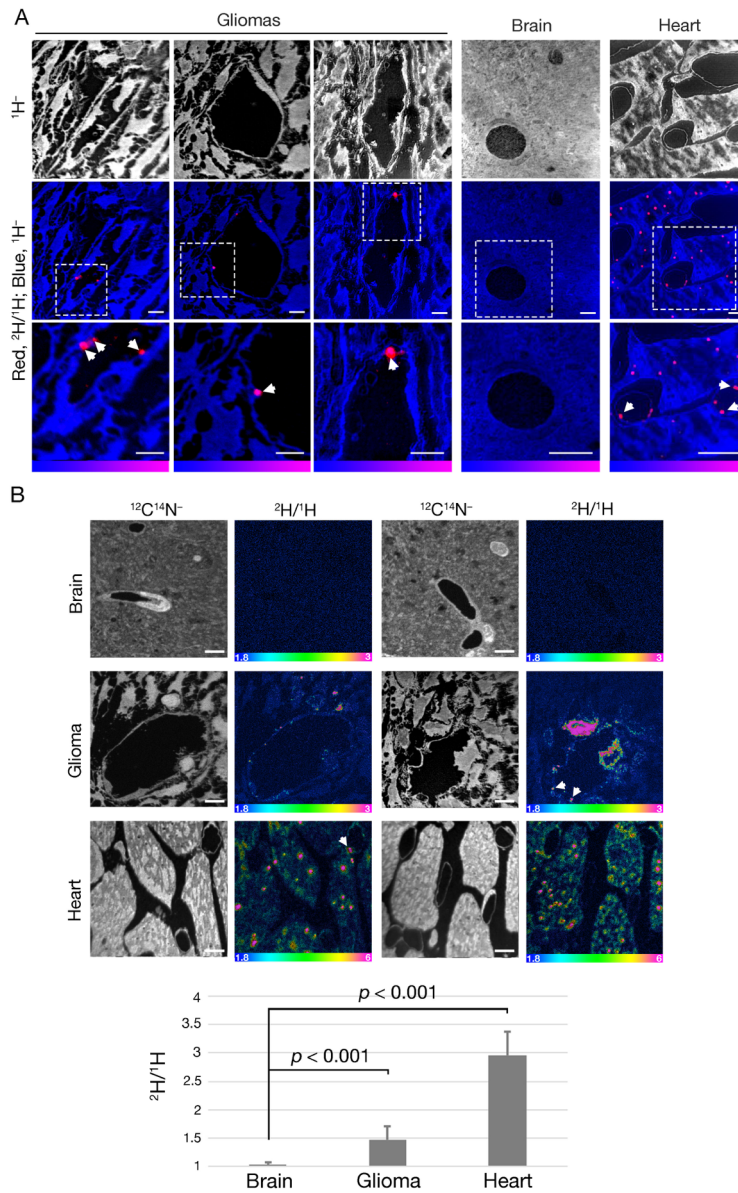
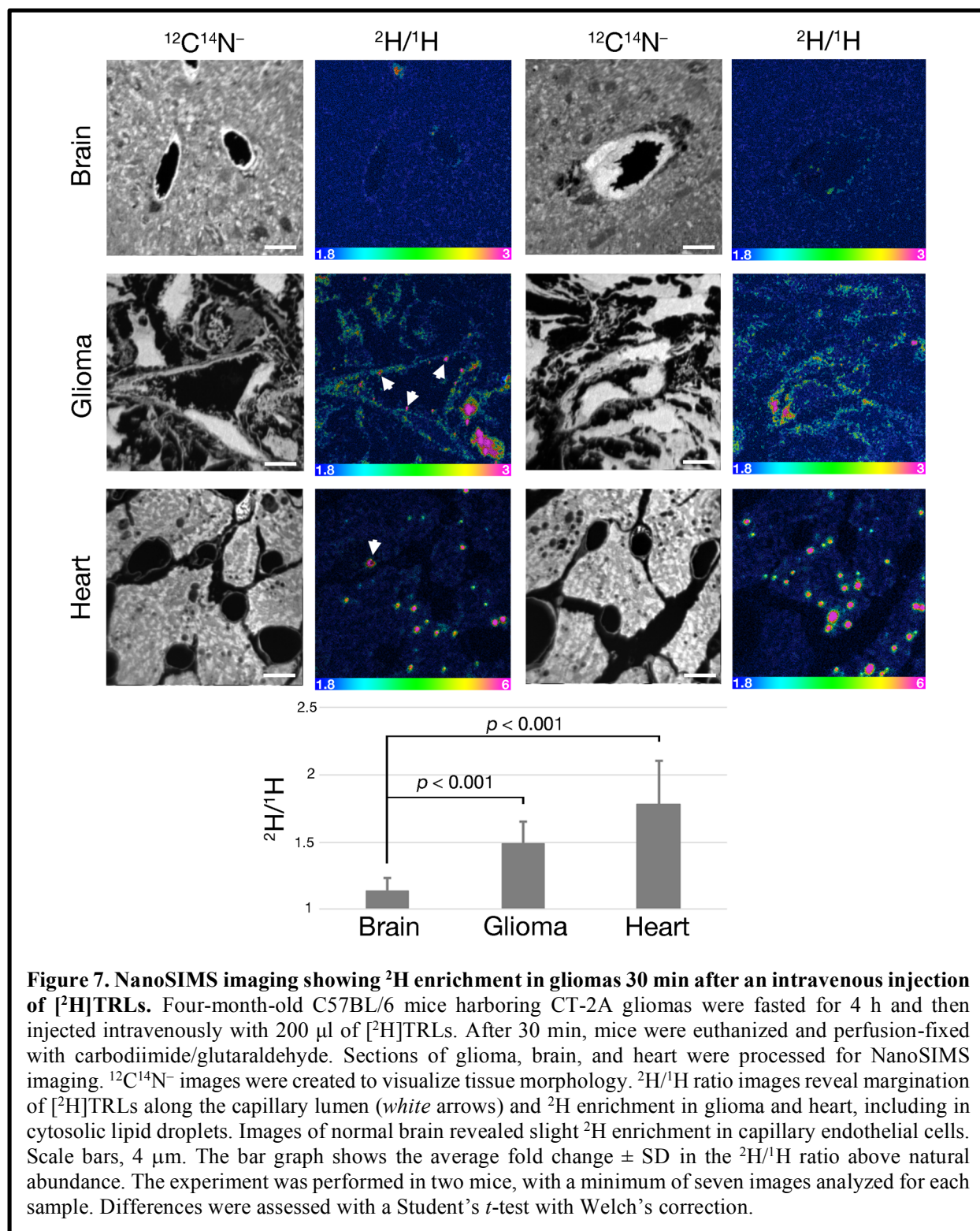


Figure 6. NanoSIMS imaging reveals margination of $[^2\text{H}]\text{TRLs}$ along glioma capillaries and ^2H enrichment in adjacent glioma cells. Four-month-old C57BL/6 mice harboring CT-2A gliomas were fasted for 4 h and then injected intravenously with 200 μl of $[^2\text{H}]\text{TRLs}$. After 1 min, mice were euthanized; perfusion-fixed with carbodiimide/glutaraldehyde; and tissue sections were processed for NanoSIMS imaging. **(A)** NanoSIMS images showing margination of $[^2\text{H}]\text{TRLs}$ in glioma capillaries. $^1\text{H}^-$ images were created to visualize tissue morphology (upper panels). Composite $^2\text{H}/^1\text{H}$ (red) and $^1\text{H}^-$ (blue) images reveal $[^2\text{H}]\text{TRLs}$ (white arrows) in glioma and heart capillaries (middle and lower panels). The lower panels are close-up images of regions outlined in the middle panels. $^2\text{H}/^1\text{H}$ ratio scales were set to show margined TRLs. Scale bars, 4 μm . **(B)** NanoSIMS images showing ^2H -enrichment in glioma tissue. $^{12}\text{C}^{14}\text{N}^-$ images were generated to visualize tissue morphology. $^2\text{H}/^1\text{H}$ ratio images reveal margination of $[^2\text{H}]\text{TRLs}$ within the capillary lumen and ^2H -enriched lipid droplets in gliomas and heart. There was no ^2H enrichment in normal brain. Scale bars, 4 μm . The bar graph shows the average fold change \pm SD in the $^2\text{H}/^1\text{H}$ ratio above natural abundance. The experiment was performed in two mice with a minimum of seven images analyzed for each sample. Differences were assessed using a Student's *t*-test with Welch's correction.

lipids from the $[^2\text{H}]$ TRLs had already entered glioma cells and were even found in cytosolic neutral lipid droplets of those cells (Figure 6B). In contrast, ^2H enrichment was virtually absent in normal



brain. As expected (13), we observed substantial amounts of [^2H]TRL-derived lipids in cardiomyocytes, including in cytosolic lipid droplets. In gliomas harvested 30 min after the injection of [^2H]TRLs, we observed similar findings: TRL margination along capillaries of gliomas and heart and the uptake of TRL-derived nutrients by glioma cells and cardiomyocytes (Figure 7). Again, [^2H]TRL margination was absent in capillaries of the normal brain at the 30-min time point, and we did not find ^2H enrichment in the parenchymal cells of the normal brain. However, we did observe very low levels of ^2H enrichment in capillary endothelial cells of normal brain. Given the absence of TRL margination in normal brain capillaries, we speculate that the very low amounts of ^2H enrichment in brain capillary endothelial cells may relate to [^2H]TRL processing in the periphery, followed by uptake of unesterified [^2H]fatty acids by endothelial cells of the brain.

At both the 1- and 30-min time points, we observed heterogeneity in ^2H enrichment in glioma cells, with occasional perivascular cells exhibiting striking ^2H enrichment. We do not know the identity of the highly enriched perivascular cells (*i.e.*, whether they are tumor cells, pericytes, or macrophages), nor do we understand why some cells within the glioma took up more [^2H]TRL-derived lipids than other cells.

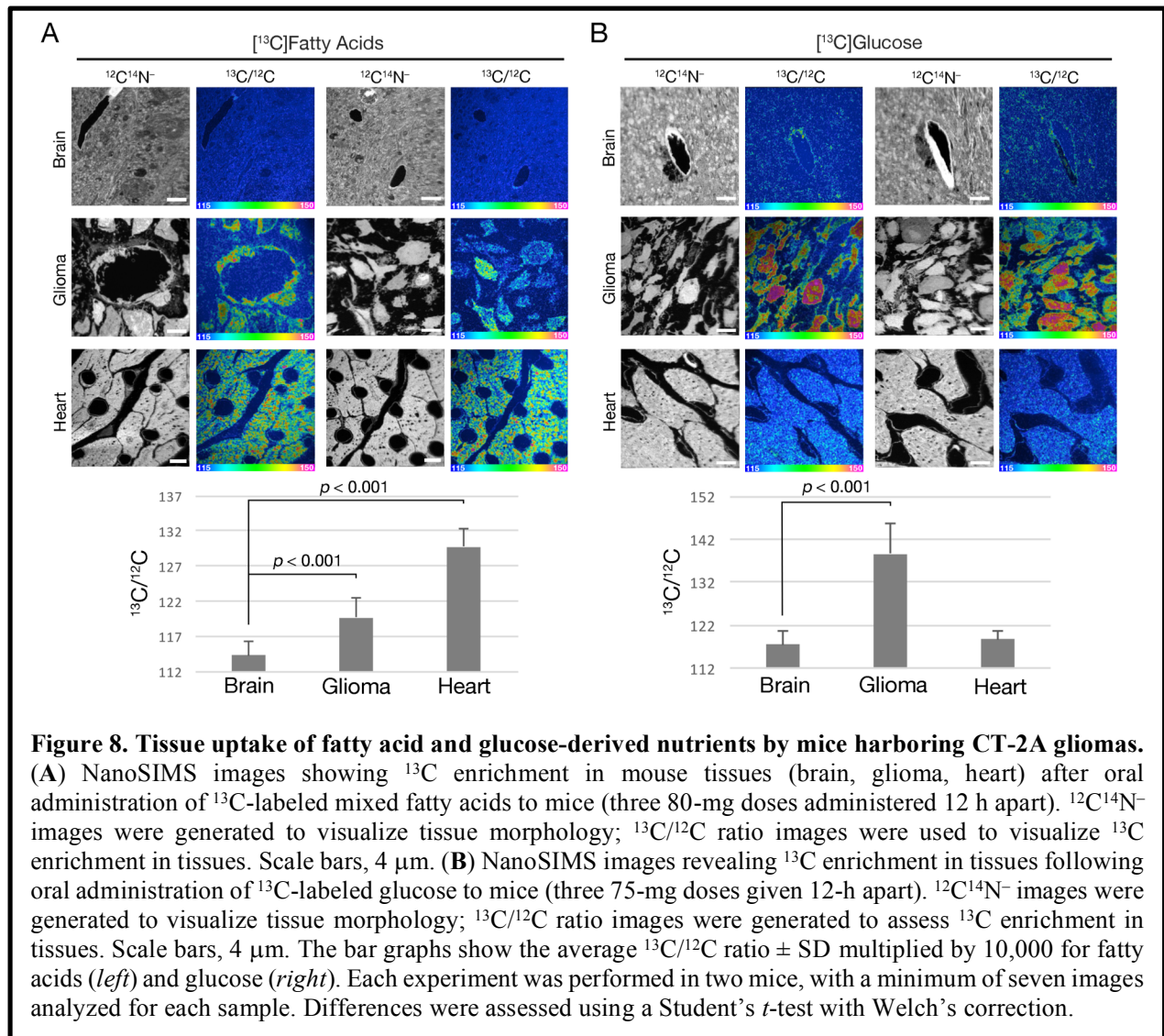
As an experimental control, we injected a mouse with PBS alone rather than [^2H]TRLs. As expected, there was no ^2H enrichment in the tissues of that mouse (Figure 7—figure supplement 1).

We performed an additional study in which [^2H]TRLs were injected intravenously into a wild-type mouse and a *Gpihbp1*^{-/-} mouse. After 15 min, the heart and brain from these mice were harvested and processed for NanoSIMS imaging. The $^2\text{H}/^1\text{H}$ ratio images revealed ^2H enrichment in the heart of the wild-type mouse but negligible ^2H enrichment in the heart of the *Gpihbp1*^{-/-} mouse (^2H enrichment in cardiomyocyte lipid droplets was only ~10% greater than natural abundance) (Figure 7—figure supplement 2). In hindsight, the negligible amounts of ^2H enrichment in the heart of the *Gpihbp1*^{-/-} mouse was probably not surprising, given the very large pool of unlabeled triglycerides in the bloodstream of *Gpihbp1*^{-/-} mice (~50–100-fold higher than

in wild-type mice). At the 15-min time point, we were unable to detect ^2H enrichment in the brain of either the wild-type mouse or the *Gpihbp1*^{-/-} mouse (Figure 7—figure supplement 2).

¹³C enrichment in gliomas following administration of ¹³C-labeled fatty acids or ¹³C-labeled glucose by gastric gavage

In addition to studies of gliomas after an intravenous injection of [^2H]TRLs, we performed NanoSIMS imaging after administering ^{13}C -labeled fatty acids or ^{13}C -labeled glucose by gastric gavage (three doses over 36 h) (Figure 8). In the case of the ^{13}C -labeled fatty acid experiments, it is likely that most of the ^{13}C -labeled lipids entered the bloodstream in chylomicrons. Once again,



$^{12}\text{C}^{14}\text{N}^-$ images were useful for tissue morphology, and the $^{13}\text{C}/^{12}\text{C}$ ratio images were useful to identify regions of ^{13}C enrichment. The scale for the $^{13}\text{C}/^{12}\text{C}$ images ranges from 0.0115 to 0.0150 (from slightly above ^{13}C natural abundance to ~36% greater than natural abundance). After administering ^{13}C -labeled fatty acids, ^{13}C enrichment was observed in both glioma cells and capillary endothelial cells of gliomas (Figure 8A). In some images, ^{13}C -enriched cytosolic lipid droplets were visible in glioma cells (Figure 8—figure supplement 1). ^{13}C enrichment was virtually absent in normal brain (Figure 8A). However, after adjusting the scale of the NanoSIMS images, a small amount of ^{13}C enrichment was observed in capillary endothelial cells within the brain parenchyma (Figure 8—figure supplement 2). As expected (13), we observed substantial amounts of ^{13}C enrichment in cardiomyocytes (Figure 8A).

After administering [^{13}C]glucose to mice, ^{13}C enrichment was easily detectable in normal brain but was even ~20% higher in gliomas (Figure 8B). We also observed ^{13}C enrichment in cardiomyocytes (Figure 8B). As expected, there was no ^{13}C enrichment in tissues of a mouse that was administered PBS alone (Figure 8—figure supplement 3).

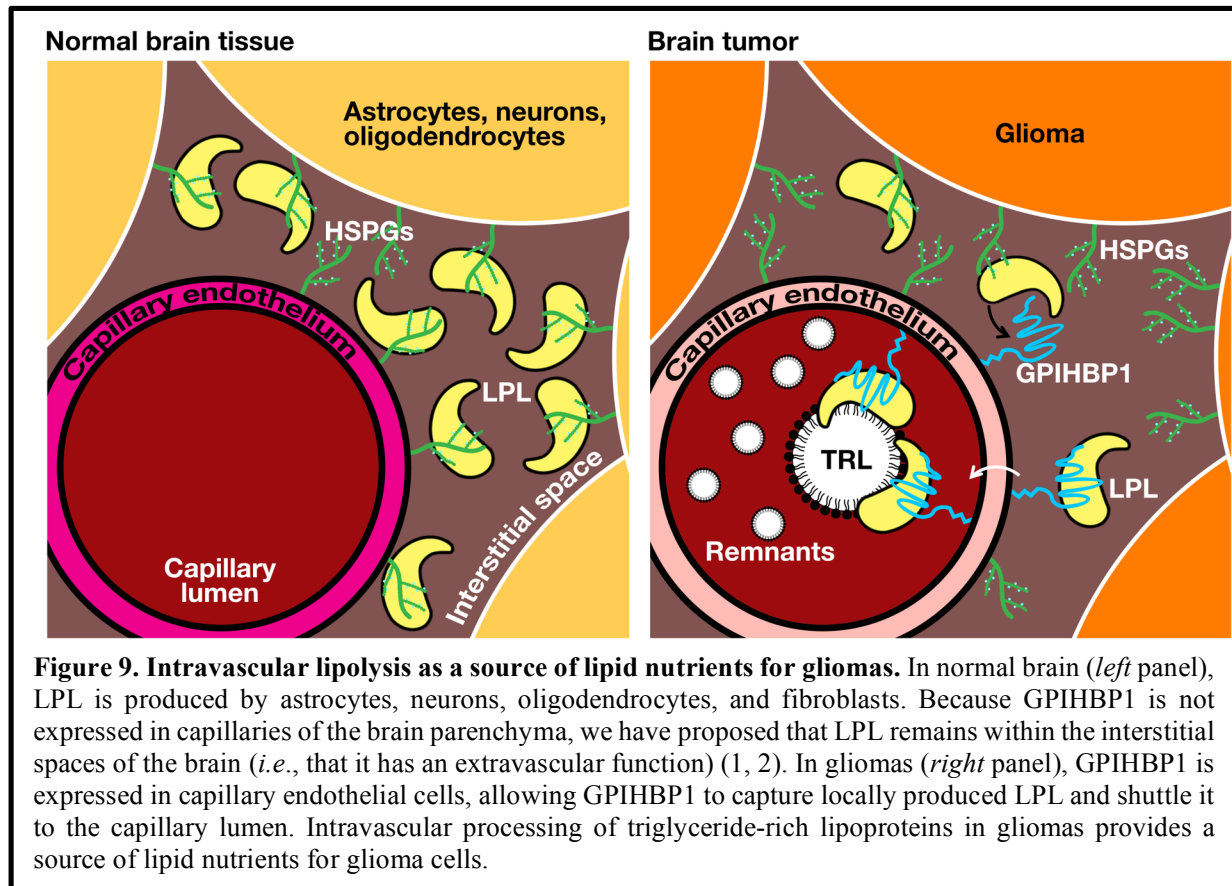
To determine whether an absence of GPIHBP1 expression would influence the growth of glioma tumors, CT-2A glioma cells that had been stably transfected with a Gaussia luciferase reporter were injected into the brain of wild-type and *Gpihbp1*^{-/-} mice ($n = 11/\text{group}$). Tumor burden was assessed in live animals by measuring luciferase activity in blood (63, 64). We observed no statistically significant differences in tumor growth, tumor size, or survival between wild-type and *Gpihbp1*^{-/-} mice (Figure 8—figure supplement 4). This result was not particularly surprising, given that gliomas have a robust capacity to utilize glucose-derived nutrients (Figure 8B).

Discussion

We sought to determine whether GPIHBP1, despite its complete absence from capillaries of the brain, might nevertheless be expressed in capillaries of gliomas. Using standard immunohistochemistry procedures, we documented GPIHBP1 expression in capillary endothelial cells of human gliomas and CT-2A-derived mouse gliomas. The expression of GPIHBP1 in glioma capillaries was intriguing, but the crucial issue is whether LPL would be bound to the GPIHBP1. Additional immunohistochemistry studies on mouse gliomas revealed that LPL colocalizes with GPIHBP1 on glioma capillaries, just as LPL colocalizes with GPIHBP1 in capillaries of heart and brown adipose tissue (1, 4, 6–8, 10, 11). The binding of LPL to GPIHBP1 was specific; the LPL-specific goat antibody did not detect LPL in the capillaries of gliomas in *Gpihbp1*^{-/-} mice, nor did it detect any LPL in macrophages or hippocampal neurons of *Lpl*^{-/-}MCK-hLPL mice. Finding colocalization of GPIHBP1 and LPL in capillaries of gliomas implied that we might find evidence for TRL margination and processing in the tumors. Indeed, we observed [²H]TRL margination along glioma capillaries and the entry of TRL-derived nutrients into glioma cells. Consistent with results of earlier studies (9, 13), TRL margination was absent in capillaries of normal brain, and we did not find any ²H enrichment in the brain parenchyma. We did, however, find very low levels of ²H enrichment in capillary endothelial cells of normal brain, perhaps due to the uptake of fatty acids derived from TRL processing in peripheral tissues. We observed consistent findings after administering [¹³C]fatty acids to mice by gastric gavage. In those experiments, we observed strong ¹³C enrichment in gliomas but no ¹³C enrichment in the normal brain (except for low levels of enrichment in capillary endothelial cells). After administering [¹³C]glucose by gavage, ¹³C enrichment was observed in both gliomas and normal brain. It is important to note that the [¹³C]fatty acids and the [¹³C]glucose were administered in three doses over 36 h before harvesting tissues for NanoSIMS analyses, allowing ample time for labeled nutrients to be utilized as fuel or to be converted into other nutrients (*e.g.*, nonessential amino acids) (13, 65, 66). Thus, after

administering ^{13}C -labeled fatty acids or glucose to mice, the ^{13}C in glioma cells was likely present in a variety of macromolecules (*e.g.*, glucose, lipids, proteins, nucleic acids).

Documenting GPIHBP1 and LPL in glioma capillaries, combined with the discovery that TRL-derived nutrients are taken up and utilized by glioma cells, opens a new chapter in glioma metabolism research (Figure 9). Laboratories interested in glioma metabolism have typically



focused on the intrinsic metabolic properties of glioma cells and how metabolic pathways in gliomas differ from those in normal brain (30, 32–35, 67, 68). There have been suggestions, based on indirect observations of substrate utilization, that glioma tumors are capable of utilizing fatty acids for fuel and for anabolic processes (30, 34, 69–71). However, in those studies, the assumption has been that the fatty acids probably originated from the tumor cells by *de novo* lipogenesis (31–33). No one, as far as we are aware, had ever considered the possibility that gliomas might be capable of taking up and utilizing nutrients from LPL-mediated intravascular processing of TRLs.

In an ultrastructural study of human gliomas, Vaz *et al.* (28) commented that the morphology of endothelial cells in gliomas resembles that of capillary endothelial cells in peripheral tissues, with euchromatin-rich nuclei, occasional fenestrations, and numerous pinocytotic vesicles within the cytoplasm. The expression of GPIHBP1 (a hallmark of capillary endothelial cells in peripheral tissues) in gliomas provides biochemical support for the notion that glioma capillaries resemble capillaries in peripheral tissues (28). Our electron microscopy studies confirmed that the morphological features of glioma capillaries and normal brain capillaries differ substantially.

We have relatively few insights into the molecular basis for GPIHBP1 expression in glioma capillaries. One possibility is that the absence of a blood–brain barrier in glioma capillaries (72–75) permits exposure of endothelial cells to a paracrine factor that activates GPIHBP1 expression. Another possibility is that GPIHBP1 expression is stimulated by the expression of VEGF produced by glioma cells (53–55). In our studies, VEGF increased GPIHBP1 expression in the mouse brain endothelial cell line bEnd.3.

In the past, other laboratories have reported that glioma tumor cells can transdifferentiate into endothelial cells, thereby augmenting the vascular supply to tumors (76–78). For example, endothelial cells in human glioblastomas were reported to harbor the same genetic alterations as the tumor cells, implying that at least some of the glioblastoma endothelial cells originate from stem cells within the tumor (76, 77). In another model (78), a *Cre* recombinase (*Cre*)-loxP–controlled lentiviral vector encoding activated forms of H-Ras and Akt was injected into the hippocampus of GFAP-*Cre* p53 mice, eliciting glioblastomas. In that model, the oncogenes were expressed in the GFAP+ cells, and the resulting tumors expressed GFP, H-Ras, and Akt and the loss of p53. Some GFP+ endothelial cells were observed in tumors, implying that those endothelial cells had originated from tumor cells. Furthermore, implanting a tumor cell line (generated from tumors induced with the same lentiviral vector) into the brain of immunocompromised mice was reported to yield tumors containing GFP+ endothelial cells. In our current studies, we did not observe evidence for differentiation of glioma cells into capillary endothelial cells. The glioma

cell line that we used expressed blue fluorescent protein (BFP), but we did not find BFP expression in capillary endothelial cells of gliomas.

Mass spectrometry–based analyses of homogenized tissue extracts from mouse gliomas and normal brain tissue, along with similar observations in tumors from human patients, suggested differences in acetate oxidation in gliomas vs. normal brain (69). While these studies of tissue extracts have been useful, they obviously cannot provide anatomical insights into metabolism. We have argued that NanoSIMS imaging studies are particularly useful when the goal is to understand metabolism at an anatomic level (cellular or subcellular) (13). In the current studies, NanoSIMS imaging provided anatomic insights into glioma metabolism. For example, we observed TRL margination along capillaries of gliomas but not in capillaries of adjacent normal brain tissue. We also showed that the transport of TRL-derived nutrients across glioma capillaries and into glioma cells is rapid, occurring within 1 min, and that there is heterogeneity in nutrient uptake by different cells within the tumor. We found no uptake of TRL-derived nutrients by normal brain 1 or 15 min after the injection of [²H]TRLs and only very small amounts after 30 min (confined to capillary endothelial cells). Also, following the administration of [¹³C]glucose, we found more ¹³C enrichment in gliomas than in normal brain. As far as we are aware, our study is the first to use NanoSIMS analyses to investigate cancer metabolism *in vivo*. As we look to the future, we have little doubt that NanoSIMS imaging will be an important tool for understanding tumor metabolism, making it possible to investigate metabolic heterogeneity in tumor cells along with the metabolic properties of vascular cells, fibroblasts, and macrophages within the tumor. However, it is important to point out that NanoSIMS imaging is not high-throughput, at least with the current instruments, and for that reason NanoSIMS imaging is best used (as in this study) for addressing discrete anatomic issues in metabolism. Examining large numbers of tumors or large numbers of mice would be difficult. Also, NanoSIMS imaging is very expensive.

Our studies provided fresh insights into the uptake of lipid nutrients by gliomas, but many issues remain to be investigated. For example, in the current studies, we found numerous

macrophages within gliomas, but we did not address differences in nutrient uptake by macrophages and glioma cells. In future studies, it should be possible to examine the uptake of TRL-derived nutrients into tumor cells, macrophages, and other immune cells within gliomas [identifying specific cell types with ¹⁵N-labeled monoclonal antibodies or antibodies tagged with different lanthanide metals (79–82)]. It would also be desirable to determine if the uptake of TRL-derived nutrients in gliomas correlates with levels of GPIHBP1 and LPL in glioma capillaries (quantified with LPL- and GPIHBP1-specific antibodies tagged with different lanthanide metals). Finally, it would be desirable to investigate whether the presence of GPIHBP1 and LPL in glioma capillaries could be exploited for patient care. For example, it is conceivable that fluorescently labeled GPIHBP1 antibodies or DiI-labeled TRLs could guide surgical resection of tumors. Also, a localized injection of GPIHBP1-specific monoclonal antibodies conjugated to chemotherapeutic agents into gliomas might be useful in targeting tumor vasculature (83). A localized injection of gold-conjugated GPIHBP1-specific monoclonal antibodies could augment the efficacy of external beam radiotherapy (84–86).

Methods

Key resources table

Reagent type (species) or resource	Designation	Source or reference	Identifiers	Additional information
Genetic reagent (<i>M. musculus</i>)	<i>Gpihbp1</i> ^{-/-}	PMID: 17403372	RRID: MGI:3771172	Dr. Stephen G. Young (UCLA)
Genetic reagent (<i>M. musculus</i>)	<i>Lpl</i> ^{-/-} MCK-hLPL	PMID: 7635990	RRID: MGI:3624988	Dr. Rudolph Zechner (Graz University)
Genetic reagent (<i>M. musculus</i>)	ROSA ^{mT/mG} Pdgfb-iCre ^{T2}	PMID: 29038312		Dr. Holger Gerhardt (VIB KU-Leuven)
Cell line (<i>M. musculus</i>)	CT-2A	PMID: 1418222		Dr. Thomas Seyfried (Boston College)
Cell line (<i>M. musculus</i>)	CT-2A-BFP	PMID: 24658686		Dr. Holger Gerhardt (VIB KU-Leuven)
Cell line (<i>M. musculus</i>)	bEnd.3	ATCC	Catalog No. CRL-2299 RRID: CVCL_0170	
Transfected construct (lentiviral plasmid)	plenti-GLuc-IRES-EGFP	Targeting Systems	Catalog No. GL-GFP	
Antibody	Rat monoclonal anti-mouse GPIHBP1 (11A12)	PMID: 19726683		Dr. Stephen G. Young (UCLA); IHC (10 µg/ml)
Antibody	Mouse monoclonal anti-human GPIHBP1 (RE3)	PMID: 27875259		Dr. Stephen G. Young (UCLA); IHC (10 µg/ml)
Antibody	Mouse monoclonal anti-human GPIHBP1 (RF4)	PMID: 27875259		Dr. Stephen G. Young (UCLA); IHC (10 µg/ml)

Antibody	Mouse monoclonal anti-human GPIHBP1 (RG3)	PMID: 27875259		Dr. Stephen G. Young (UCLA); IHC (10 µg/ml)
Antibody	Rabbit polyclonal anti-vWF	Dako	Catalog No. A0082 RRID: AB_2315602	IHC (1:200)
Antibody	Goat polyclonal anti-GFAP	Abcam	Catalog No. ab53554 RRID: AB_880202	IHC (1:200)
Antibody	Rabbit polyclonal anti-GLUT1	Millipore-Sigma	Catalog No. 07-1401 RRID: AB_1587074	IHC (1:200)
Antibody	Rabbit polyclonal anti-CD31	Abcam	Catalog No. ab28364 RRID: AB_726362	IHC (1:50)
Antibody	Rat monoclonal anti-F4/80	Abcam	Catalog No. ab6640 RRID: AB_1140040	IHC (10 µg/ml)
Antibody	Goat polyclonal anti-mouse LPL	PMID: 16517593		Dr. André Bensadoun (Cornell); IHC (12 µg/ml)
Antibody	Alexa Fluor 488, 568, 647 secondaries	ThermoFisher Scientific		IHC (1:500)
Commercial assay or kit	ImmPRESS Excel Staining Kit	Vector Laboratory	Catalog No. MP-7602	
Sequence-based reagent	Mouse <i>Gpihbp1</i> primers			5'-AGCAGGGACAGAGCACCTCT-3' and 5'-AGACGAGCGTGATGCAGAG-3'
Sequence-based reagent	Mouse <i>Cd31</i> primers			5'-AACCGTATCTCCAAAGCCAGT-3' and 5'-CCAGACGACTGGAGGAGAACT-3'

Sequence-based reagent	Mouse primers <i>Angpt2</i>			5'- AACTCGCTCCTTCAGAAGC AGC-3' and 5'- TTCCGCACAGTCTCTGAAG GTG-3'
Sequence-based reagent	Mouse primers <i>Dusp5</i>			5'- TCGCCTACAGACCAGCCTA TGA-3' and 5'- TGATGTGCAGGTTGGCGAG GAA-3'
Sequence-based reagent	Mouse primers <i>Cxcr4</i>			5'- GACTGGCATAGTCGGCAAT GGA-3' and 5'- CAAAGAGGAGGTCAGCCA CTGA-3'
Sequence-based reagent	Mouse primers <i>Lpl</i>			5'- AGGTGGACATCGGAGAAC TG-3' and 5'- TCCCTAGCACAGAAGATG ACC-3'
Sequence-based reagent	Human primers <i>LPL</i>			5'- TAGCTGGTCAGACTGGTGG A-3' and 5'- TTCACAAATACCGCAGGTG -3'
Recombinant DNA reagent	ALO-D4 plasmid	PMID: 25809258		Dr. Arun Radhakrishnan (UT Southwestern)
Chemical compound, drug	N-(3-Dimethylamino propyl)-N'-ethylcarbodiimide hydrochloride (carbodiimide)	Millipore-Sigma	Catalog No. 03449	
Chemical compound, drug	Glutaraldehyde 25% solution	Electron Microscopy Sciences	Catalog No. 16220	
Chemical compound, drug	Osmium tetroxide 4% solution	Electron Microscopy Sciences	Catalog No. 18459	
Chemical compound, drug	Paraformaldehyde 16% solution	Electron Microscopy Sciences	Catalog No. 15170	
Chemical compound, drug	EMbed 812	Electron Microscopy Sciences	Catalog No. 14120	

Chemical compound, drug	Sodium cacodylate trihydrate	Electron Microscopy Sciences	Catalog No. 12300	
Chemical compound, drug	Uranyl acetate	SPI-Chem	Catalog No. 02624AB	
Chemical compound, drug	DAPI	ThermoFisher Scientific	Catalog No. 1306	IHC (3 µg/ml)
Chemical compound, drug	Mouse VEGF	Millipore-Sigma	Catalog No. V4512	
Software, algorithm	LIMMA	PMID: 25605792	RRID: SCR_010943	
Other	D-GLUCOSE (U-13C6, 99%)	Cambridge Isotope Laboratories	Catalog No. CLM-1396-PK	
Other	Mixed fatty acids (U-D, 96–98%)	Cambridge Isotope Laboratories	Catalog No. DLM-8572-PK	
Other	Mixed fatty acids (13C, 98%+)	Cambridge Isotope Laboratories	Catalog No. CLM-8455-PK	

Immunohistochemical studies on human glioma specimens

Frozen surgical glioma specimens were obtained from the UCLA Department of Neurosurgery. Frozen autopsy control brain samples (frontal lobe, occipital lobe, and cerebellum) were obtained from the UCLA Section of Neuropathology. Samples were sectioned to 8 µm and placed on glass slides. All samples were fixed with 3% paraformaldehyde (PFA) in PBS/Ca/Mg and permeabilized in 0.2% Triton X-100 in PBS/Ca/Mg. Tissues were blocked with PBS/Ca/Mg containing 5% donkey serum and 0.2% bovine serum albumin (BSA) and incubated overnight at 4°C with one or more mouse monoclonal antibodies (mAbs) against human GPIHBP1 (RF4, RE3, RG3; 10 µg/ml) (43), a rabbit polyclonal antibody against von Willebrand factor (vWF) (Dako; 1:200), and a goat polyclonal antibody against human glial fibrillary acidic protein (GFAP) (Abcam; 1:500). In some experiments, recombinant soluble human GPIHBP1 (50 µg) was added to the primary antibody incubation. After washing the slides, 1-h incubations were performed with an Alexa Fluor 647–conjugated donkey anti–mouse IgG (ThermoFisher Scientific; 1:500), an Alexa Fluor 488–

conjugated donkey anti-rabbit IgG (ThermoFisher Scientific; 1:500), and an Alexa Fluor 568-conjugated donkey anti-goat IgG (ThermoFisher Scientific; 1:500). DNA was stained with 4',6-diamidino-2-phenylindole (DAPI). Images were taken with an LSM700 confocal microscope with an Axiovert 200M stand and processed with Zen 2010 software (Zeiss).

Immunoperoxidase staining was performed with the ImmPRESS Excel Staining Kit (Vector Laboratories). Endogenous peroxidase activity was quenched with BLOXALL Blocking Solution (Vector Laboratories). After incubating sections in 10% normal horse serum, they were incubated for 1 h with mAb RF4 (5 μ g/ml), followed by a 15-min incubation with a goat anti-mouse IgG (10 μ g/ml, Vector Laboratories). Slides were then incubated for 30 min with a horseradish peroxidase-conjugated horse anti-goat IgG (ImmPRESS Excel Reagent, Vector Laboratories). After washing, the slides were incubated with ImmPACT DAB EqV (Vector Laboratories) until a color change was evident (~30 sec). Finally, sections were counterstained with hematoxylin and mounted with Vectashield Mounting Media (Vector Laboratories). Images were recorded with a Nikon Eclipse E600 microscope (Plan Fluor 40 \times /0.50 NA or 100 \times /0.75 NA objectives) equipped with a DS-Fi2 camera (Nikon).

Genome dataset and gene-expression analyses

Cohorts for RNA-seq analysis were obtained from two databases—The Cancer Genome Atlas (TCGA) for tumor samples and Genotype-Tissue Expression (GTEx) for normal brain samples. Samples from TCGA ($n = 157$) and GTEx ($n = 283$) were processed with the TOIL pipeline as described (87). Differential expression analysis of fatty acid metabolism genes was carried out with a linear model RNA-seq analysis software (LIMMA) (88). Genes were considered differentially expressed if the p -values were < 0.05 and the \log_2 changes were $>$ twofold. A heatmap was generated with the software R (89).

Animal procedures and glioma implantation

Mice on a C57BL/6 background expressing both the ROSA^{mT/mG} *Cre*-reporter (48) and tamoxifen-inducible *Pdgfb-iCreER^{T2}* alleles (47) were generated by breeding. In those mice, the administration of tamoxifen induces *Cre* recombinase expression in *Pdgfb*-positive cells. The recombination event results in the expression of EGFP in endothelial cells; all other cells express TdTomato. For the glioma implantation studies, mice (8–12-weeks-old) were injected intraperitoneally with tamoxifen (65 µg/g body weight, 4 injections in 2 weeks) before surgery. Mice were anesthetized with ketamine/xylazine, and a craniotomy was performed by drilling a 5-mm hole between the lambdoid, sagittal, and coronal sutures. A blue fluorescent protein (BFP)-tagged CT-2A glioblastoma spheroid (250-µm in diameter) (44, 45) was injected into the cortex and sealed by cementing a glass coverslip on the skull. The CT-2A cell line was generated by Seyfried and coworkers through chemical induction with 20-methylcholanthrene in the brain of C57BL/6 mice and was extensively characterized (44). In other experiments, CT-2A glioblastoma spheroids were implanted into the cortex in C57BL/6 wild-type mice and *Gpihbp1*^{-/-} mice (3). Those procedures were performed as described previously (90).

Immunohistochemical studies on mouse gliomas

Mice harboring BFP-expressing CT-2A gliomas (44, 45) were anesthetized with ketamine/xylazine and then injected intravenously (*via* the tail vein) with 100 µg of an Alexa Fluor 647–conjugated antibody against mouse GPIHBP1 (11A12) (49). After 1 min, the mice were perfused through the heart with 15 ml of PBS, followed by 10 ml of 2% PFA in PBS. Brain and glioma tissues were harvested and fixed overnight in 4% PFA. Tissue sections (200-µm-thick) were prepared with a vibratome. For immunofluorescence microscopy studies, the sections were fixed with 4% PFA in PBS and blocked and permeabilized in TNBT (0.1 M Tris, pH 7.4, 150 mM NaCl, 0.5% blocking reagent from Perkin Elmer, 0.5% Triton X-100) for 4 h at room temperature. Tissues were incubated with an antibody against GLUT1 (Millipore; 1:200) diluted in TNBT buffer overnight at 4°C, washed in TNT buffer (0.1 M Tris pH 7.4; 150 mM NaCl, 0.5% Triton X-100) and incubated with an Alexa Fluor 488–conjugated donkey anti–rabbit IgG (ThermoFisher

Scientific; 1:200). Tissues were washed and mounted in fluorescent mounting medium (Dako). Images were obtained with a Leica TCS SP8 confocal microscope.

For the analysis of tissues from mice not injected with anti-GPIHBP1 antibodies, tissues were embedded in OCT medium, and 10- μ m sections were cut with a cryostat. Sections were fixed with 3% PFA in PBS/Ca/Mg, permeabilized with 0.2% Triton X-100 in PBS/Ca/Mg, and blocked with PBS/Ca/Mg containing 5% donkey serum and 0.2% BSA. Tissue sections were incubated overnight at 4°C with a rabbit antibody against CD31 (Abcam; 1:50), a goat antibody against mouse LPL (12 μ g/ml) (62), an Alexa Fluor 488–conjugated antibody against F4/80, or an Alexa Fluor 647–conjugated antibody against mouse GPIHBP1 (11A12, 10 μ g/ml) (49). After removing non-bound antibodies and washing the sections, unlabeled primary antibodies were detected with an Alexa Fluor 488–conjugated donkey anti–rabbit IgG (ThermoFisher Scientific; 1:500) or an Alexa Fluor 568–conjugated donkey anti–goat IgG (ThermoFisher Scientific; 1:500). DNA was stained with DAPI, and tissues were mounted with ProLong Gold mounting media (ThermoFisher Scientific). Images were recorded on an LSM 800 confocal microscope (Zeiss).

Immunocytochemistry studies on mouse peritoneal macrophages

Macrophages were collected by peritoneal lavage of C57BL/6 wild-type and *Lpl*^{-/-}MCK-hLPL mice. Cells were centrifuged at 400 \times g for 5 min at 4°C, washed with 5 ml of red blood cell lysing buffer (Sigma) for 5 min, washed two times with cold PBS, and then plated onto FBS-coated Petri dishes. Cells were cultured overnight in macrophage medium (Dulbecco Modified Eagle Medium with 10% FBS, 1% glutamine, and 1% sodium pyruvate). On the next day, macrophages were lifted with cold PBS containing 5 mM EDTA for 30 min at 4°C. Cells were then plated onto poly-D-lysine–coated glass coverslips (75,000 cells/coverslip) and incubated overnight in macrophage media. On the following day, the cells were washed three times for 10 min in PBS/Ca/Mg containing 0.2% BSA and then incubated with Alexa Fluor 568–labeled ALO-D4 (a modified cytolysin that binds to “accessible cholesterol” in the plasma membrane) (91–93) for 2 h at 4°C. Samples were washed three times for 1 min with PBS/Ca/Mg, fixed with 3% PFA in PBS/Ca/Mg,

permeabilized with 0.2% Triton X-100 in PBS/Ca/Mg, and blocked with PBS/Ca/Mg containing 5% donkey serum and 0.2% BSA. Cells were then incubated with a goat antibody against mouse LPL (12 $\mu\text{g/ml}$) (62) for 1 h at room temperature followed by a 30-min incubation with an Alexa Fluor 647–labeled donkey anti–goat IgG (ThermoFisher Scientific; 1:500). DNA was stained with DAPI, and coverslips were mounted onto glass slides in ProLong Gold mounting media (ThermoFisher Scientific). Images were recorded with a Zeiss LSM700 confocal microscope.

Administration of [^{13}C]fatty acids, [^{13}C]glucose, and [^2H]TRLs to mice

C57BL/6 mice with CT-2A gliomas (three-week duration) were given 80 μl of [^{13}C]fatty acids (~ 1 mg/ μl ; Cambridge Isotope Laboratories) or 80 μl of [^{13}C]glucose (3 mg/kg body weight; Cambridge Isotope Laboratories) by oral gavage every 12 h for 36 h (three doses). To study TRL metabolism, mice were injected intravenously with a single bolus of [^2H]TRLs (40 μg triglycerides in 100 μl) *via* the tail vein. The [^2H]TRLs were isolated from the plasma of *Gpihbp1*^{-/-} mice after administering deuterated fatty acids by gastric gavage (13). After allowing the [^2H]TRLs to circulate for 1 min or 30 min, the mice were perfused through the heart with 15 ml of ice-cold PBS/Ca/Mg at 3 ml/min (10 ml through the left ventricle and 5 ml through the right ventricle). Next, the mice were perfusion-fixed through the left ventricle with 10 ml of ice-cold 4% N-(3-dimethylaminopropyl)-N'-ethylcarbodiimide hydrochloride (“carbodiimide;” Sigma-Aldrich) (mass/vol) and 0.4% glutaraldehyde (Electron Microscopy Sciences) (vol/vol) in 0.1 M phosphate buffer. The heart, brain, and glioma tumors were collected and placed in 0.1 M phosphate buffer containing 4% carbodiimide and 2.5% glutaraldehyde for 2 h at 4°C. Tissues were cut into 1-mm³ pieces and fixed overnight in 2.5% glutaraldehyde, 3.7% PFA, and 2.1% sucrose in 0.1 M sodium cacodylate (pH 7.4).

Preparation of tissue sections for NanoSIMS imaging and electron microscopy

After fixation, 1-mm³ pieces of tissue were rinsed three times (10 min each) in 0.1 M sodium cacodylate buffer (pH 7.4) and fixed with 2% OsO₄ (Electron Microscopy Sciences) in 0.1 M

sodium cacodylate on ice for 90 min. The samples were rinsed three times (10 min each) with distilled water and stained overnight with 2% uranyl acetate at 4°C. On the following day, the samples were rinsed three times for 10 min each with distilled water and then dehydrated with increasing amounts of ethanol (30, 50, 70, 85, 95, and 100%; 3 × 10 min) before infiltration with Embed812 resin (Electron Microscopy Sciences) diluted in acetone (33% for 2 h; 66% overnight; 100% for 3 h). The samples were embedded in polyethylene molds (Electron Microscopy Sciences) with fresh resin and polymerized in a vacuum oven at 65°C for 48 h. The polymerized blocks were then removed from the molds, trimmed, and sectioned.

For transmission electron microscopy, 65-nm sections were cut and collected on freshly glow-discharged copper grids (Ted Pella) that were coated with formvar and carbon. Sections were then stained with Reynold's lead citrate solution for 10 min. Images were acquired with an FEI T12 transmission electron microscope set to 120 kV accelerating voltage and a Gatan 2K × 2K digital camera (Electron Imaging Center).

For NanoSIMS analyses, 500-nm sections were cut with a Leica UC6 ultramicrotome and collected on silicon wafers. Sections of tissue were coated with ~5-nm of platinum and analyzed with NanoSIMS 50L or NanoSIMS 50 instruments (CAMECA). Samples were scanned with a 16-KeV $^{133}\text{Cs}^+$ beam, and secondary electrons (SEs) and secondary ions ($^1\text{H}^-$, $^2\text{H}^-$, $^{12}\text{C}^-$, $^{13}\text{C}^-$, $^{12}\text{C}^{14}\text{N}^-$) were collected. A $50 \times 50\text{-}\mu\text{m}$ region of the section was pre-sputtered with a ~1.2-nA beam current (primary aperture D1=1) to reach a dose of $\sim 1 \times 10^{17}$ ions/cm² to remove the platinum coating and implant $^{133}\text{Cs}^+$ to ensure a steady state of secondary ion release. A $\sim 40 \times 40\text{-}\mu\text{m}$ region was imaged with an ~3-pA beam current (primary aperture D1=2) and a dwell time of ~10 ms/pixel per frame for multiple frames. Both 256×256 - and 512×512 -pixel images were obtained. Images were prepared using the OpenMIMS plugin in ImageJ. For image quantification, $^2\text{H}/^1\text{H}$ and $^{13}\text{C}/^{12}\text{C}$ ratios of regions-of-interests were calculated with the OpenMIMS plugin and processed by GraphPad Prism 7.0.

Tumor studies in wild-type and Gpibp1-deficient mice

3-month-old C57BL/6 wild-type (5 females, 6 males) and *Gpihbp1*^{-/-} mice (6 females, 5 males) were injected intracranially with CT-2A glioma cells stably expressing a Gaussia luciferase reporter gene (4×10^5 cells/mouse). Cells were injected 1 mm posterior and 2 mm lateral to the bregma at a depth of 2 mm. Tumor burden was monitored every three days by measuring Gaussia luciferase in the blood (63, 64). Mice were weighed at weekly intervals and were euthanized when they lost >20% of their body weight. After the mice were euthanized, tumors and brains were weighed. All studies were approved by UCLA's Animal Research Committee.

Gaussia luciferase measurements

To measure the levels of secreted Gaussia luciferase (sGluc), blood was obtained from the tail vein of mice and mixed with 50 mM EDTA to prevent coagulation. 5 μ l of blood was transferred to a 96-well plate, and sGluc activity was measured by chemiluminescence after injecting 100 μ l of 100 μ M coelenterazine (Nanolight) (63, 64). Data were plotted as relative light units (RLU).

Quantifying mouse and human transcripts by qRT-PCR

C57BL/6 wild-type mice and *Lpl*^{-/-}MCK-hLPL mice were anesthetized with isoflurane and perfused with PBS. Heart, brown adipose tissue (BAT), and quadriceps were harvested and flash-frozen in liquid nitrogen. RNA was isolated with TRI reagent (Molecular Research), and quantitative (q)RT-PCR measurements were performed in triplicate with a 7900HT Fast real-time PCR system (Applied Biosystems). Gene expression was calculated with a comparative CT method and normalized to levels of cyclophilin A expression. Primers for mouse *Gpihbp1*, mouse *Lpl*, and human *LPL* are described in the Key Resources Table.

VEGF treatment of brain endothelial cells

Mouse brain microvascular endothelial cells (bEnd.3; ATCC #CRL-2299) were plated into 6-well plates and grown in DMEM media containing 10% FBS, 1% glutamine, and 1% sodium pyruvate overnight. On the next day, cells were rinsed with PBS and incubated in medium containing recombinant mouse VEGF (100 ng/ml; Sigma) for another 24 h. RNA was isolated with TRI

reagent (Molecular Research), and qRT-PCR measurements were performed in triplicate with a 7900HT Fast real-time PCR system (Applied Biosystems). Gene expression was calculated with a comparative CT method and normalized to cyclophilin A expression. Primers for mouse *Gpihbp1*, *Cd31*, *Angpt2*, *Cxcr4*, and *Dusp5* are described in the Key Resources Table.

Cell lines

CT-2A cells were obtained originally from the Seyfried laboratory and has been extensively tested and characterized (44). These cells also robustly expressed GFAP. bEnd.3 cells were obtained from ATCC with proper "certificate of analysis". All cell lines were negative for mycoplasma contamination.

Statistics

Statistical analyses of data were performed with GraphPad Prism 7.0 software. All data are shown as the means \pm standard deviations. Differences were assessed using a Student's *t*-test with Welch's correction.

Study approval

All tissue samples from patients were obtained after informed consent and with approval from the UCLA Institutional Review Board (IRB; protocol 10-000655). Animal housing and experimental protocols were approved by UCLA's Animal Research Committee (ARC; 2004-125-51, 2016-005) and the Institutional Animal Care and Research Advisory Committee of the KU Leuven (085/2016). The animals were housed in an AAALAC (Association for Assessment and Accreditation of Laboratory Animal Care International)-approved facility and cared for according to guidelines established by UCLA's Animal Research Committee. The mice were fed a chow diet and housed in a barrier facility with a 12-h light-dark cycle.

Acknowledgments

This work was supported by grants from the NHLBI (HL090553, HL087228, HL125335), a Transatlantic Network Grant from the Leducq Foundation (12CVD04), and the Belgian Cancer Foundation (Stichting Tegen Kanker, grant 2012-181, 2018-074). Xuchen Hu was supported by a Ruth L. Kirschstein National Research Service Award (T32HL69766) and the UCLA Medical Scientist Training Program. Ken Matsumoto was supported by a Japan Society for the Promotion of Science Postdoctoral Fellowship. Linda Liao was supported by a NCI Brain Tumor SPORE grant (P50-CA211015). Haibo Jiang was supported by an Australian Research Council Discovery Early Career Researcher Award and a Cancer Council Western Australia Early Career Investigator Grant. We thank Andre Bensadoun (Cornell University) for goat anti-mouse LPL antibodies; we also thank Anna Nowak (University of Western Australia) and the late Ben Barres (Stanford University) for helpful discussions.

References

1. Young SG, Davies BSJ, Voss CV, Gin P, Weinstein MM, Tontonoz P, et al. GPIHBP1, an endothelial cell transporter for lipoprotein lipase. *J Lipid Res.* 2011;52(11):1869–84.
2. Adeyo O, Goulbourne CN, Bensadoun A, Beigneux AP, Fong LG, and Young SG. Glycosylphosphatidylinositol-anchored high-density lipoprotein-binding protein 1 and the intravascular processing of triglyceride-rich lipoproteins. *J Intern Med.* 2012;272(6):528–40.
3. Beigneux AP, Davies B, Gin P, Weinstein MM, Farber E, Qiao X, et al. Glycosylphosphatidylinositol-anchored high density lipoprotein-binding protein 1 plays a critical role in the lipolytic processing of chylomicrons. *Cell Metab.* 2007;5:279–91.
4. Davies BS, Beigneux AP, Barnes RH, 2nd, Tu Y, Gin P, Weinstein MM, et al. GPIHBP1 is responsible for the entry of lipoprotein lipase into capillaries. *Cell Metab.* 2010;12(1):42–52.
5. Olafsen T, Young SG, Davies BSJ, Beigneux AP, Kenanova VE, Voss C, et al. Unexpected expression pattern for glycosylphosphatidylinositol-anchored HDL-binding protein 1 (GPIHBP1) in mouse tissues revealed by positron emission tomography scanning. *J Biol Chem.* 2010;285(50):39239–48.
6. Davies BS, Goulbourne CN, Barnes RH, 2nd, Turlo KA, Gin P, Vaughan S, et al. Assessing mechanisms of GPIHBP1 and lipoprotein lipase movement across endothelial cells. *J Lipid Res.* 2012;53(12):2690–7.
7. Allan CM, Larsson M, Jung RS, Ploug M, Bensadoun A, Beigneux AP, et al. Mobility of "HSPG-bound" LPL explains how LPL is able to reach GPIHBP1 on capillaries. *J Lipid Res.* 2017;58(1):216–25.

8. Fong LG, Young SG, Beigneux AP, Bensadoun A, Oberer M, Jiang H, et al. GPIHBP1 and plasma triglyceride metabolism. *Trends Endocrinol Metab.* 2016;27(7):455–69.
9. Goulbourne C, Gin P, Tatar A, Nobumori C, Hoenger A, Jiang H, et al. The GPIHBP1–LPL complex is responsible for the margination of triglyceride-rich lipoproteins in capillaries. *Cell Metab.* 2014;19(5):849–60.
10. Allan CM, Jung CJ, Larsson M, Heizer PJ, Tu Y, Sandoval NP, et al. Mutating a conserved cysteine in GPIHBP1 reduces amounts of GPIHBP1 in capillaries and abolishes LPL binding. *J Lipid Res.* 2017;58(7):1453–61.
11. Allan CM, Larsson M, Hu X, He C, Jung RS, Mapar A, et al. A lipoprotein lipase (LPL)-specific monoclonal antibody, 88B8, that abolishes the binding of LPL to GPIHBP1. *J Lipid Res.* 2016;57(10):1889–98.
12. Jiang H, Goulbourne CN, Tatar A, Turlo K, Wu D, Beigneux AP, et al. High-resolution imaging of dietary lipids in cells and tissues by NanoSIMS analysis. *J Lipid Res.* 2014;55(10):2156–66.
13. He C, Weston TA, Jung RS, Heizer P, Larsson M, Hu X, et al. NanoSIMS analysis of intravascular lipolysis and lipid movement across capillaries and into cardiomyocytes. *Cell Metab.* 2018;27(5):1055–66e3.
14. Mergenthaler P, Lindauer U, Dienel GA, and Meisel A. Sugar for the brain: the role of glucose in physiological and pathological brain function. *Trends Neurosci.* 2013;36(10):587–97.
15. Ben-Zeev O, Doolittle MH, Singh N, Chang CH, and Schotz MC. Synthesis and regulation of lipoprotein lipase in the hippocampus. *J Lipid Res.* 1990;31(7):1307–13.

16. Bessesen DH, Richards CL, Etienne J, Goers JW, and Eckel RH. Spinal cord of the rat contains more lipoprotein lipase than other brain regions. *J Lipid Res.* 1993;34(2):229–38.
17. Goldberg IJ, Soprano DR, Wyatt ML, Vanni TM, Kirchgessner TG, and Schotz MC. Localization of lipoprotein lipase mRNA in selected rat tissues. *J Lipid Res.* 1989;30(10):1569–77.
18. Vilaro S, Camps L, Reina M, Perez-Clausell J, Llobera M, and Olivecrona T. Localization of lipoprotein lipase to discrete areas of the guinea pig brain. *Brain Res.* 1990;506(2):249–53.
19. Yacoub LK, Vanni TM, and Goldberg IJ. Lipoprotein lipase mRNA in neonatal and adult mouse tissues: Comparison of normal and combined lipase deficiency (cld) mice assessed by in situ hybridization. *J Lipid Res.* 1990;31:1845–52.
20. Eckel RH, and Robbins RJ. Lipoprotein lipase is produced, regulated, and functional in rat brain. *Proc Natl Acad Sci U S A.* 1984;81(23):7604–7.
21. Zhang Y, Chen K, Sloan SA, Bennett ML, Scholze AR, O'Keeffe S, et al. An RNA-sequencing transcriptome and splicing database of glia, neurons, and vascular cells of the cerebral cortex. *J Neurosci.* 2014;34(36):11929–47.
22. Vanlandewijck M, He L, Mae MA, Andrae J, Ando K, Del Gaudio F, et al. A molecular atlas of cell types and zonation in the brain vasculature. *Nature.* 2018;554(7693):475–80.
23. Yuan F, Salehi HA, Boucher Y, Vasthare US, Tuma RF, and Jain RK. Vascular permeability and microcirculation of gliomas and mammary carcinomas transplanted in rat and mouse cranial windows. *Cancer Res.* 1994;54(17):4564–8.

24. Hobbs SK, Monsky WL, Yuan F, Roberts WG, Griffith L, Torchilin VP, et al. Regulation of transport pathways in tumor vessels: role of tumor type and microenvironment. *Proc Natl Acad Sci U S A*. 1998;95(8):4607–12.
25. Monsky WL, Fukumura D, Gohongi T, Ancukiewicz M, Weich HA, Torchilin VP, et al. Augmentation of transvascular transport of macromolecules and nanoparticles in tumors using vascular endothelial growth factor. *Cancer Res*. 1999;59(16):4129–35.
26. Bullitt E, Zeng D, Gerig G, Aylward S, Joshi S, Smith JK, et al. Vessel tortuosity and brain tumor malignancy: a blinded study. *Acad Radiol*. 2005;12(10):1232–40.
27. Zhang RD, Price JE, Fujimaki T, Bucana CD, and Fidler IJ. Differential permeability of the blood-brain barrier in experimental brain metastases produced by human neoplasms implanted into nude mice. *Am J Pathol*. 1992;141(5):1115–24.
28. Vaz R, Borges N, Sarmiento A, and Azevedo I. Reversion of phenotype of endothelial cells in brain tissue around glioblastomas. *J Neurooncol*. 1996;27(2):127–32.
29. Dong W, Gong H, Zhang G, Vuletic S, Albers J, Zhang J, et al. Lipoprotein lipase and phospholipid transfer protein overexpression in human glioma cells and their effect on cell growth, apoptosis, and migration. *Acta Biochim Biophys Sin (Shanghai)*. 2017;49(1):62–73.
30. Lin H, Patel S, Affleck VS, Wilson I, Turnbull DM, Joshi AR, et al. Fatty acid oxidation is required for the respiration and proliferation of malignant glioma cells. *Neuro Oncol*. 2017;19(1):43–54.
31. Guo D, Reinitz F, Youssef M, Hong C, Nathanson D, Akhavan D, et al. An LXR agonist promotes glioblastoma cell death through inhibition of an EGFR/AKT/SREBP-1/LDLR-dependent pathway. *Cancer Discov*. 2011;1(5):442–56.

32. Guo D, Hildebrandt IJ, Prins RM, Soto H, Mazzotta MM, Dang J, et al. The AMPK agonist AICAR inhibits the growth of EGFRvIII-expressing glioblastomas by inhibiting lipogenesis. *Proc Natl Acad Sci U S A*. 2009;106(31):12932–7.
33. Guo D, Prins RM, Dang J, Kuga D, Iwanami A, Soto H, et al. EGFR signaling through an Akt-SREBP-1-dependent, rapamycin-resistant pathway sensitizes glioblastomas to antilipogenic therapy. *Sci Signal*. 2009;2(101):ra82.
34. Guo D, Bell EH, and Chakravarti A. Lipid metabolism emerges as a promising target for malignant glioma therapy. *CNS Oncol*. 2013;2(3):289–99.
35. Gopal K, Grossi E, Paoletti P, and Usardi M. Lipid composition of human intracranial tumors: a biochemical study. *Acta Neurochir (Wien)*. 1963;11:333–47.
36. Jiang H, Goulbourne CN, Tatar A, Turlo K, Wu D, Beigneux AP, et al. High-resolution imaging of dietary lipids in cells and tissues by NanoSIMS analysis. *J Lipid Res*. 2014;55(10):2156–66.
37. Jiang H, Favaro E, Goulbourne CN, Rakowska PD, Hughes GM, Ryadnov MG, et al. Stable isotope imaging of biological samples with high resolution secondary ion mass spectrometry and complementary techniques. *Methods*. 2014;68(2):317–24.
38. He C, Hu X, Jung RS, Weston TA, Sandoval NP, Tontonoz P, et al. High-resolution imaging and quantification of plasma membrane cholesterol by NanoSIMS. *Proc Natl Acad Sci U S A*. 2017;114(8):2000–5.
39. He C, Fong LG, Young SG, and Jiang H. NanoSIMS imaging: an approach for visualizing and quantifying lipids in cells and tissues. *J Investig Med*. 2017;65(3):669–72.
40. He C, Hu X, Weston TA, Jung RS, Heizer P, Tu Y, et al. NanoSIMS imaging reveals unexpected heterogeneity in nutrient uptake by brown adipocytes. *Biochem Biophys Res Commun*. 2018;504(4):899–902.

41. He C, Hu X, Weston TA, Jung RS, Sandhu J, Huang S, et al. Macrophages release plasma membrane-derived particles rich in accessible cholesterol. *Proc Natl Acad Sci U S A*. 2018;115(36):E8499–E508.
42. Kristensen KK, Midtgaard SR, Mysling S, Kovrov O, Hansen LB, Skar-Gislinge N, et al. A disordered acidic domain in GPIHBP1 harboring a sulfated tyrosine regulates lipoprotein lipase. *Proc Natl Acad Sci U S A*. 2018;115(26):E6020–E9.
43. Hu X, Sleeman MW, Miyashita K, Linton MF, Allan CM, He C, et al. Monoclonal antibodies that bind to the Ly6 domain of GPIHBP1 abolish the binding of LPL. *J Lipid Res*. 2017;58(1):208–15.
44. Seyfried TN, el-Abbadi M, and Roy ML. Ganglioside distribution in murine neural tumors. *Mol Chem Neuropathol*. 1992;17(2):147–67.
45. Oh T, Fakurnejad S, Sayegh ET, Clark AJ, Ivan ME, Sun MZ, et al. Immunocompetent murine models for the study of glioblastoma immunotherapy. *J Transl Med*. 2014;12:107.
46. Mathivet T, Bouleti C, Van Woensel M, Stanchi F, Verschuere T, Phng LK, et al. Dynamic stroma reorganization drives blood vessel dysmorphia during glioma growth. *EMBO Mol Med*. 2017;9(12):1629–45.
47. Claxton S, Kostourou V, Jadeja S, Chambon P, Hodivala-Dilke K, and Fruttiger M. Efficient, inducible Cre-recombinase activation in vascular endothelium. *Genesis*. 2008;46(2):74–80.
48. Muzumdar MD, Tasic B, Miyamichi K, Li L, and Luo L. A global double-fluorescent Cre reporter mouse. *Genesis*. 2007;45(9):593–605.
49. Beigneux AP, Gin P, Davies BSJ, Weinstein MM, Bensadoun A, Fong LG, et al. Highly conserved cysteines within the Ly6 domain of GPIHBP1 are crucial for the binding of lipoprotein lipase. *J Biol Chem*. 2009;284(44):30240–7.

50. Coomber BL, Stewart PA, Hayakawa K, Farrell CL, and Del Maestro RF. Quantitative morphology of human glioblastoma multiforme microvessels: structural basis of blood-brain barrier defect. *J Neurooncol.* 1987;5(4):299–307.
51. Weller ROF, M.; Cox, S. The development and ultrastructure of the microvasculature in malignant gliomas. *Neuropathol Appl Neurobiol.* 1977;3:307–22.
52. Chiu AP, Wan A, Lal N, Zhang D, Wang F, Vlodaysky I, et al. Cardiomyocyte VEGF regulates endothelial cell GPIHBP1 to relocate lipoprotein lipase to the coronary lumen During Diabetes Mellitus. *Arterioscler Thromb Vasc Biol.* 2016;36(1):145–55.
53. Plate KH, Breier G, Weich HA, Mennel HD, and Risau W. Vascular endothelial growth factor and glioma angiogenesis: coordinate induction of VEGF receptors, distribution of VEGF protein and possible in vivo regulatory mechanisms. *Int J Cancer.* 1994;59(4):520–9.
54. Pietsch T, Valter MM, Wolf HK, von Deimling A, Huang HJ, Cavenee WK, et al. Expression and distribution of vascular endothelial growth factor protein in human brain tumors. *Acta Neuropathol.* 1997;93(2):109–17.
55. Christov C, Adle-Biassette H, Le Guerinel C, Natchev S, and Gherardi RK. Immunohistochemical detection of vascular endothelial growth factor (VEGF) in the vasculature of oligodendrogliomas. *Neuropathol Appl Neurobiol.* 1998;24(1):29–35.
56. Maher F, Vannucci SJ, and Simpson IA. Glucose transporter proteins in brain. *FASEB J.* 1994;8(13):1003–11.
57. Pardridge WM, Boado RJ, and Farrell CR. Brain-type glucose transporter (GLUT-1) is selectively localized to the blood-brain barrier. Studies with quantitative western blotting and in situ hybridization. *J Biol Chem.* 1990;265(29):18035–40.

58. Matsumoto K, Rambow F, Stanchi F, Mathivet T, Qian J, Lambrechts D, et al. Progressive endothelial cell heterogeneity in gliomas. 2019. *Manuscript in preparation*.
59. He L, Vanlandewijck M, Mae MA, Andrae J, Ando K, Del Gaudio F, et al. Single-cell RNA sequencing of mouse brain and lung vascular and vessel-associated cell types. *Sci Data*. 2018;5:180160.
60. Mahoney EM, Khoo JC, and Steinberg D. Lipoprotein lipase secretion by human monocytes and rabbit alveolar macrophages in culture. *Proc Natl Acad Sci U S A*. 1982;79(5):1639–42.
61. Levak-Frank S, Radner H, Walsh A, Stollberger R, Knipping G, Hoefler G, et al. Muscle-specific overexpression of lipoprotein lipase causes a severe myopathy characterized by proliferation of mitochondria and peroxisomes in transgenic mice. *J Clin Invest*. 1995;96:976–86.
62. Page S, Judson A, Melford K, and Bensadoun A. Interaction of lipoprotein lipase and receptor-associated protein. *J Biol Chem*. 2006;281(20):13931–8.
63. Mai WX, Gosa L, Daniels VW, Ta L, Tsang JE, Higgins B, et al. Cytoplasmic p53 couples oncogene-driven glucose metabolism to apoptosis and is a therapeutic target in glioblastoma. *Nat Med*. 2017;23(11):1342–51.
64. Tannous BA. Gaussia luciferase reporter assay for monitoring biological processes in culture and in vivo. *Nat Protoc*. 2009;4(4):582–91.
65. Sidossis LS, Coggan AR, Gastaldelli A, and Wolfe RR. Pathway of free fatty acid oxidation in human subjects. Implications for tracer studies. *J Clin Invest*. 1995;95(1):278–84.
66. Schneider JP, VR. Alternate pathways of glucose metabolism. *Cancer Res*. 1957;17(7):701–6.

67. Strickland M, and Stoll EA. Metabolic reprogramming in glioma. *Front Cell Dev Biol.* 2017;5:43.
68. Agnihotri S, and Zadeh G. Metabolic reprogramming in glioblastoma: the influence of cancer metabolism on epigenetics and unanswered questions. *Neuro Oncol.* 2016;18(2):160–72.
69. Mashimo T, Pichumani K, Vemireddy V, Hatanpaa KJ, Singh DK, Sirasanagandla S, et al. Acetate is a bioenergetic substrate for human glioblastoma and brain metastases. *Cell.* 2014;159(7):1603–14.
70. Ru P, Williams TM, Chakravarti A, and Guo D. Tumor metabolism of malignant gliomas. *Cancers (Basel).* 2013;5(4):1469–84.
71. Zaidi N, Lupien L, Kuemmerle NB, Kinlaw WB, Swinnen JV, and Smans K. Lipogenesis and lipolysis: the pathways exploited by the cancer cells to acquire fatty acids. *Prog Lipid Res.* 2013;52(4):585–9.
72. Dubois LG, Campanati L, Righy C, D'Andrea-Meira I, Spohr TC, Porto-Carreiro I, et al. Gliomas and the vascular fragility of the blood brain barrier. *Front Cell Neurosci.* 2014;8:418.
73. Wolburg H, Noell S, Fallier-Becker P, Mack AF, and Wolburg-Buchholz K. The disturbed blood-brain barrier in human glioblastoma. *Mol Aspects Med.* 2012;33(5–6):579–89.
74. Liebner S, Fischmann A, Rascher G, Duffner F, Grote EH, Kalbacher H, et al. Claudin-1 and claudin-5 expression and tight junction morphology are altered in blood vessels of human glioblastoma multiforme. *Acta Neuropathol.* 2000;100(3):323–31.
75. Sage MR, and Wilson AJ. The blood-brain barrier: an important concept in neuroimaging. *AJNR Am J Neuroradiol.* 1994;15(4):601–22.

76. Wang R, Chadalavada K, Wilshire J, Kowalik U, Hovinga KE, Geber A, et al. Glioblastoma stem-like cells give rise to tumour endothelium. *Nature*. 2010;468(7325):829–33.
77. Ricci-Vitiani L, Pallini R, Biffoni M, Todaro M, Invernici G, Cenci T, et al. Tumour vascularization via endothelial differentiation of glioblastoma stem-like cells. *Nature*. 2010;468(7325):824–8.
78. Soda Y, Marumoto T, Friedmann-Morvinski D, Soda M, Liu F, Michiue H, et al. Transdifferentiation of glioblastoma cells into vascular endothelial cells. *Proc Natl Acad Sci U S A*. 2011;108(11):4274–80.
79. Waentig L, Jakubowski N, Hardt S, Scheler C, Roos PH, and Linscheid MW. Comparison of different chelates for lanthanide labeling of antibodies and application in a Western blot immunoassay combined with detection by laser ablation (LA-)ICP-MS. *J Anal At Spectrom*. 2012;27(8):1311–20.
80. Kanje S, Herrmann AJ, Hober S, and Mueller L. Next generation of labeling reagents for quantitative and multiplexing immunoassays by the use of LA-ICP-MS. *Analyst*. 2016;141(23):6374–80.
81. Angelo M, Bendall SC, Finck R, Hale MB, Hitzman C, Borowsky AD, et al. Multiplexed ion beam imaging of human breast tumors. *Nat Med*. 2014;20(4):436–42.
82. Keren L, Bosse M, Marquez D, Angoshtari R, Jain S, Varma S, et al. A structured tumor-immune microenvironment in triple negative breast cancer revealed by multiplexed ion beam imaging. *Cell*. 2018;174(6):1373–87.e19.
83. Schrama D, Reisfeld RA, and Becker JC. Antibody targeted drugs as cancer therapeutics. *Nat Rev Drug Discov*. 2006;5(2):147–59.

84. Haume K, Rosa S, Grellet S, Smialek MA, Butterworth KT, Solov'yov AV, et al. Gold nanoparticles for cancer radiotherapy: a review. *Cancer Nanotechnol.* 2016;7(1):8.
85. Hainfeld JF, Slatkin DN, and Smilowitz HM. The use of gold nanoparticles to enhance radiotherapy in mice. *Phys Med Biol.* 2004;49(18):N309–15.
86. Hainfeld JF, Dilmanian FA, Slatkin DN, and Smilowitz HM. Radiotherapy enhancement with gold nanoparticles. *J Pharm Pharmacol.* 2008;60(8):977–85.
87. Vivian J, Rao AA, Nothaft FA, Ketchum C, Armstrong J, Novak A, et al. Toil enables reproducible, open source, big biomedical data analyses. *Nat Biotechnol.* 2017;35(4):314–6.
88. Ritchie ME, Phipson B, Wu D, Hu Y, Law CW, Shi W, et al. limma powers differential expression analyses for RNA-sequencing and microarray studies. *Nucleic Acids Res.* 2015;43(7):e47.
89. Kolde R. Pheatmap: pretty heatmaps. *R package version 1.08.* 2015.
90. Stanchi F, Matsumoto K, and Gerhardt H. Imaging glioma progression by intravital microscopy. *Methods Mol Biol.* 2019;1862:227–43.
91. Das A, Brown MS, Anderson DD, Goldstein JL, and Radhakrishnan A. Three pools of plasma membrane cholesterol and their relation to cholesterol homeostasis. *eLife.* 2014;3:e02882.
92. Das A, Goldstein JL, Anderson DD, Brown MS, and Radhakrishnan A. Use of mutant 125I-perfringolysin O to probe transport and organization of cholesterol in membranes of animal cells. *Proc Natl Acad Sci U S A.* 2013;110(26):10580–5.
93. Gay A, Rye D, and Radhakrishnan A. Switch-like responses of two cholesterol sensors do not require protein oligomerization in membranes. *Biophys J.* 2015;108(6):1459–69.

Chapter 5

Macrophages Release Plasma Membrane-derived Particles

Rich in Accessible Cholesterol



Macrophages release plasma membrane-derived particles rich in accessible cholesterol

Cuiwen He^{a,1}, Xuchen Hu^{a,1}, Thomas A. Weston^a, Rachel S. Jung^a, Jaspreet Sandhu^b, Song Huang^c, Patrick Heizer^a, Jason Kim^b, Rochelle Ellison^a, Jiake Xu^d, Matthew Kilburn^c, Steven J. Bensinger^{e,f}, Howard Riezman^g, Peter Tontonoz^b, Loren G. Fong^a, Haibo Jiang^{a,c,h,2,3}, and Stephen G. Young^{a,i,2,3}

^aDepartment of Medicine, University of California, Los Angeles, CA 90095; ^bDepartment of Pathology and Laboratory Medicine, University of California, Los Angeles, CA 90095; ^cCentre for Microscopy, Characterisation and Analysis, University of Western Australia, 6009 Perth, WA, Australia; ^dSchool of Biomedical Sciences, University of Western Australia, 6009 Perth, WA, Australia; ^eDepartment of Microbiology, Immunology and Molecular Genetics, University of California, Los Angeles, CA 90095; ^fDepartment of Molecular and Medical Pharmacology, University of California, Los Angeles, CA 90095; ^gDepartment of Biochemistry, National Centre of Competence in Research in Chemical Biology, University of Geneva, 1205 Geneva, Switzerland; ^hSchool of Molecular Sciences, University of Western Australia, 6009 Perth, WA, Australia; and ⁱDepartment of Human Genetics, University of California, Los Angeles, CA 90095

Contributed by Stephen G. Young, July 17, 2018 (sent for review June 21, 2018; reviewed by Arun Radhakrishnan and David L. Silver)

Macrophages are generally assumed to unload surplus cholesterol through direct interactions between ABC transporters on the plasma membrane and HDLs, but they have also been reported to release cholesterol-containing particles. How macrophage-derived particles are formed and released has not been clear. To understand the genesis of macrophage-derived particles, we imaged mouse macrophages by EM and nanoscale secondary ion mass spectrometry (nanoSIMS). By scanning EM, we found that large numbers of 20- to 120-nm particles are released from the fingerlike projections (filopodia) of macrophages. These particles attach to the substrate, forming a “lawn” of particles surrounding macrophages. By nanoSIMS imaging we showed that these particles are enriched in the mobile and metabolically active accessible pool of cholesterol (detectable by ALO-D4, a modified version of a cholesterol-binding cytolysin). The cholesterol content of macrophage-derived particles was increased by loading the cells with cholesterol or by adding LXR and RXR agonists to the cell-culture medium. Incubating macrophages with HDL reduced the cholesterol content of macrophage-derived particles. We propose that release of accessible cholesterol-rich particles from the macrophage plasma membrane could assist in disposing of surplus cholesterol and increase the efficiency of cholesterol movement to HDL.

cholesterol efflux | accessible cholesterol | nanoSIMS

Macrophages ingest senescent erythrocytes, remove cellular debris after an injury or infection, and ingest lipoproteins that enter the arterial intima. In carrying out these functions, macrophages internalize cholesterol. Some of the cholesterol is initially stored in cytosolic cholesterol ester droplets, but ultimately the cholesterol must be returned to the bloodstream for uptake and excretion by the liver. Cholesterol efflux from cells has been studied intensively and involves multiple mechanisms; the one that is generally highlighted involves movement of cellular cholesterol to HDL through direct interactions between HDL and ATP-binding cassette (ABC) transporters on the surface of the plasma membrane (1, 2). ABC transporters move phospholipids and cholesterol to the exofacial leaflet of the plasma membrane, facilitating uptake of the cholesterol by HDL. The expression of ABC transporters is regulated by liver X receptor (LXR) transcription factors, which are activated by sterols.

Another potential mechanism for macrophage cholesterol efflux is the release of particles containing cholesterol, variously described as “microparticles,” “cholesterol microdomains,” or “exosomes” (2–7). Phillips and coworkers (2) proposed in 2007 that a significant fraction of the cholesterol released by cultured macrophages is due to the release of microparticles. They proposed that the particles originated from the plasma membrane, but how the microparticles were released was not clear. A 2014 review of cholesterol efflux by Phillips did not mention a role for microparticle release (8). Kruth and co-

workers (3–6, 9) have published a series of articles on the release of cholesterol microdomains by cultured macrophages. The microdomains were detected by immunocytochemistry using a cholesterol-specific monoclonal antibody. In contrast to Phillip’s work, they proposed that the cholesterol microdomains are not vesicles but are branching, irregularly shaped deposits that originate from the plasma membrane. How they were released was not defined. They suggested that the release of cholesterol microdomains could be important for reverse cholesterol transport.

Efforts to visualize cholesterol efflux by EM have been limited. The microparticles described by Phillips and coworkers (2) had a mean diameter of 24 nm, as judged by negative-staining EM. Transmission electron micrographs showing binding of apo-AI to poorly defined protrusions on the surface of ABCA1-expressing macrophages (10) and a budding vesicle on the plasma membrane of ABCA1-expressing baby hamster kidney (BHK) cells have been published (7), but the images were not optimal, and whether plasma membrane protrusions were enriched in cholesterol was unclear.

Significance

Earlier studies suggested that particles are released from the macrophage plasma membrane, but the mechanism has been unclear. We found that filopodia of macrophages release large numbers of vesicular particles. Nanoscale secondary ion mass spectrometry revealed that these particles are enriched in cholesterol, including the “accessible” pool of cholesterol detectable by the cholesterol-binding protein. The cholesterol content of macrophage particles increased when the cells were loaded with cholesterol and could be depleted by incubating the cells with high-density lipoproteins. Our studies suggest that the release of particles by macrophages could be one mechanism for cholesterol efflux and that particles could be an intermediate in the movement of cholesterol to high-density lipoproteins.

Author contributions: C.H., L.G.F., H.J., and S.G.Y. designed research; C.H., X.H., T.A.W., R.S.J., J.S., S.H., P.H., J.K., R.E., H.R., and H.J. performed research; J.X., M.K., S.J.B., H.R., and P.T. contributed new reagents/analytic tools; C.H., X.H., J.S., L.G.F., H.J., and S.G.Y. analyzed data; and C.H., H.J., and S.G.Y. wrote the paper.

Reviewers: A.R., University of Texas Southwestern Medical Center at Dallas; and D.L.S., Duke-National University of Singapore Medical School.

The authors declare no conflict of interest.

Published under the PNAS license.

¹C.H. and X.H. contributed equally to this work.

²H.J. and S.G.Y. contributed equally to this work.

³To whom correspondence may be addressed. Email: haibo.jiang@uwa.edu.au or sgyoung@mednet.ucla.edu.

This article contains supporting information online at www.pnas.org/lookup/suppl/doi:10.1073/pnas.1810724115/-DC5 Supplemental.

Published online August 20, 2018.

We suspected that a combination of EM and nanoscale secondary ion mass spectrometry (nanoSIMS) would make it possible to define the origin of macrophage particles and gain fresh insights into the cholesterol content of those particles. NanoSIMS uses a Cs^+ beam to bombard a cell, releasing secondary ions (e.g., $^{12}\text{C}^-$, $^{13}\text{C}^-$, $^{12}\text{C}^{14}\text{N}^-$, and $^{12}\text{C}^{15}\text{N}^-$) that are collected and used to create high-resolution images of cells based solely on their isotopic content. When cultured cells are loaded with cholesterol containing a stable isotope (e.g., ^{13}C), nanoSIMS images can define the distribution of cholesterol on the plasma membrane (11). NanoSIMS can also be used to assess the distribution of the “accessible” pool of cholesterol (12) on the plasma membrane. The accessible pool—a pool not sequestered by sphingomyelin or phospholipids—is present when the cholesterol content of the plasma membrane is high and can be detected because it binds specifically to modified versions of cholesterol-binding cytolysins (e.g., domain 4 of anthrolysin O; ALO-D4) (12, 13). The accessible pool of cholesterol on the plasma membrane is metabolically important because it is mobile, capable of moving to the endoplasmic reticulum and participating in the regulation of cholesterol biosynthetic enzymes (14). Recently, He et al. (15) used nanoSIMS, along with an ^{15}N -labeled ALO-D4, to show that the accessible pool of cholesterol on the plasma membrane of CHO-K1 cells is concentrated on microvilli.

In the current study, we used SEM to visualize the formation and release of particles from the plasma membrane of macrophages. Using nanoSIMS imaging, we investigated the cholesterol content of particles, including the content of accessible cholesterol, under different cell-culture conditions. We also tested whether HDL is capable of removing cholesterol from particles after they have been released by macrophages.

Results

In our first experiments, we use SEM to visualize the release of particles from the plasma membrane of macrophages. Mouse peritoneal macrophages were plated on poly-D-lysine-coated silicon wafers, loaded with cholesterol by incubating the cells with acetylated LDLs (acetyl-LDLs) (16), and then visualized by SEM. SEM images revealed numerous particles on the substrate surrounding macrophages (Fig. 1*A*). The particles, ~20–120 nm in diameter, were released from the filopodia of both primary macrophages (Fig. 1*B*) and RAW 264.7 cells (a mouse macrophage cell line) (Fig. 1*C*). The lawn of particles around macrophages was most often located preferentially on one or two sides of the cell rather than surrounding the entire circumference of the cell (Figs. 1*A* and 2*A*); the preferential localization of the lawn of particles on one side of the macrophage did not change when the cells were grown on an orbital shaker. The macrophage-derived particles were unilamellar and were surrounded by a lipid bilayer, as judged by transmission electron microscopy (TEM) (Fig. 1*D*). By TEM, we occasionally observed osmophilic material within particles.

To determine if macrophage-derived particles contained accessible cholesterol, we loaded macrophages with acetyl-LDL (50 $\mu\text{g}/\text{mL}$) or cholesterol in complex with methyl- β -cyclodextrin (M β CD) and then incubated the macrophages with [^{15}N]ALO-D4 for 2 h at 4 °C. After fixation, the cells were imaged by SEM and nanoSIMS. NanoSIMS revealed avid binding of [^{15}N]ALO-D4 to the particles (Fig. 2), implying that the particles contained accessible cholesterol. Higher-magnification nanoSIMS images of macrophages showed that the particles are visible with secondary electrons, $^{12}\text{C}^{14}\text{N}^-$ (Fig. 2*B*) ions, and other secondary ion signals and confirmed the binding of [^{15}N]ALO-D4 to the macrophage-derived particles (Fig. 2*B*).

To further assess the cholesterol content of macrophage-derived particles, M β CD was used to load mouse peritoneal macrophages with [^{13}C]cholesterol. We then lifted the cells with EDTA and replated them onto fresh poly-D-lysine-coated silicon

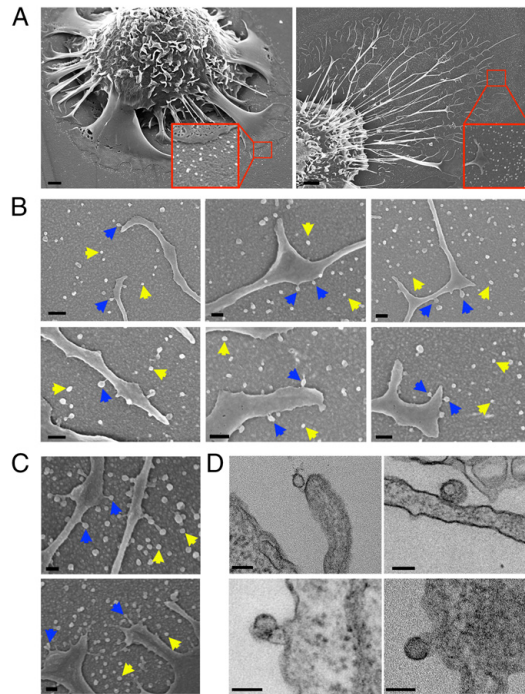


Fig. 1. Release of particles from the plasma membrane of macrophages. (*A*) Scanning electron micrographs of mouse peritoneal macrophages surrounded by a lawn of small particles (attached to a poly-D-lysine-coated silicon wafer). The macrophages had been loaded with acetyl-LDL (50 $\mu\text{g}/\text{mL}$). (Scale bars, 2 μm .) (*B* and *C*) Scanning electron micrographs show particles surrounding filopodia of mouse peritoneal macrophages (*B*) and RAW 264.7 cells (*C*). Yellow arrows show particles attached to the poly-D-lysine-coated substrate. Blue arrows show the release of particles from the filopodia. (Scale bars, 100 nm.) (*D*) Transmission electron micrographs of particle release from filopodia of mouse peritoneal macrophages. (Scale bars, 100 nm.)

wafers. After the cells were allowed to recover for 24 h, they were incubated with [^{15}N]ALO-D4 for 2 h and processed for nanoSIMS imaging. $^{13}\text{C}/^{12}\text{C}$ nanoSIMS images revealed that the particles on the substrate surrounding macrophages were enriched in [^{13}C]cholesterol (Fig. 3). The $^{15}\text{N}/^{14}\text{N}$ image of the same macrophage revealed that the particles contained accessible cholesterol, as judged by [^{15}N]ALO-D4 binding (Fig. 3). The $^{13}\text{C}/^{12}\text{C}$ and $^{15}\text{N}/^{14}\text{N}$ ratios in 150 particles were positively correlated ($P < 0.0001$), and the r^2 value was somewhat lower than we had expected (0.3663) (Fig. 3*B*). In hindsight, however, the low r^2 value is probably not surprising. The primary Cs^+ beam vaporizes cells and tissues to a depth of several nanometers, releasing secondary ions that are collected for analysis. We suspect that the depth of [^{15}N]ALO-D4 overlying the [^{13}C]cholesterol was variable in different particles, depending on particle size and geometry, and that this variability may have contributed, at least in part, to the moderate correlation between the $^{13}\text{C}/^{12}\text{C}$ and $^{15}\text{N}/^{14}\text{N}$ ratios. The negligible binding of ALO-D4 to particles with low levels of cholesterol probably contributed to the lower-than-expected correlation between ^{15}N and ^{13}C enrichments.

The release of particles and their attachment to the substrate was also observed in macrophages that had been incubated in

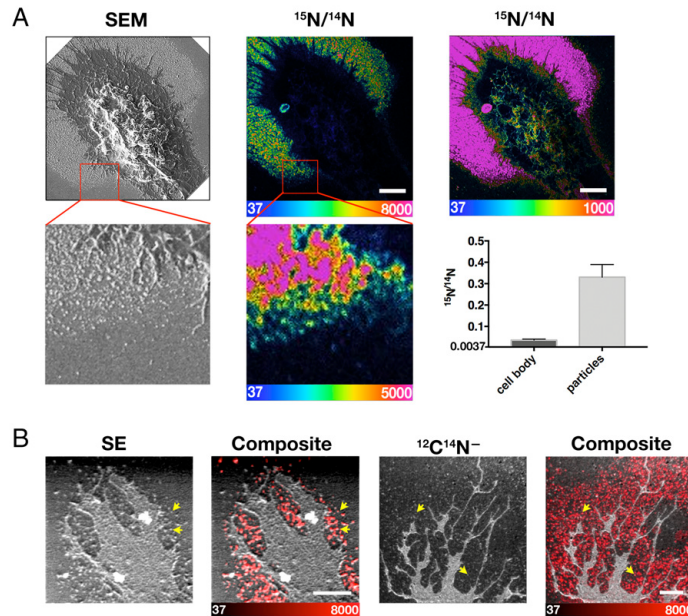


Fig. 2. Macrophages release particles enriched in cholesterol. (A) Macrophages were loaded with cholesterol/MβCD. SEM and nanoSIMS images of the macrophage after a short incubation with [¹⁵N]ALO-D4. The SEM image shows a lawn of particles outside the macrophage; the nanoSIMS image (scaled at two different settings) reveals binding of [¹⁵N]ALO-D4 to the particles, indicating that they contain accessible cholesterol. The boxed regions are shown below at higher magnification, again showing binding of [¹⁵N]ALO-D4 to macrophage-derived particles. (Scale bars, 5 μm.) The bar graph shows ¹⁵N/¹⁴N levels for the cell body and particles of two cells (60 particles were quantified). The y axis starts at 0.0037, the natural abundance of ¹⁵N. Data are shown as mean ± SD. (B) Macrophages were loaded with acetyl-LDL. Particles released by macrophages that had been loaded with acetyl-LDL (50 μg/mL) (yellow arrows) are visible in secondary electron (SE) and ¹²C¹⁴N⁻ nanoSIMS images. Composite ¹²C¹⁴N⁻ or secondary electron (SE) (gray) and ¹⁵N/¹⁴N ratio (red) images show binding of [¹⁵N]ALO-D4 to particles. (Scale bars, 2 μm.)

medium containing 1% lipoprotein-deficient serum (LPDS) and not loaded with cholesterol (Fig. 4A). By nanoSIMS, the particles released from these macrophages contained accessible cholesterol, as judged by the binding of [¹⁵N]ALO-D4 (Fig. 4B and C), even though accessible cholesterol was nearly absent from the plasma membrane of adjacent filopodia. In these studies, the ¹⁵N enrichment of particles was lower than in the studies shown in Fig. 2, in which cells had been loaded with cholesterol (note the different ¹⁵N/¹⁴N scales).

Our SEM and nanoSIMS findings in cultured CHO-K1 cells were different from the findings in macrophages (Fig. 5). The microvilli of CHO cells, both those over the cell body and those projecting from the perimeter of the cell, were enriched in accessible cholesterol, as judged by nanoSIMS images of [¹⁵N]ALO-D4 binding. Unlike the observations in macrophages, we did not observe particle release from the plasma membrane of CHO cells by SEM, and there were very few structures on the substrate resembling macrophage particles. By nanoSIMS, there was very little [¹⁵N]ALO-D4 binding to the substrate between the microvilli that projected from the perimeter of the cell (Fig. 5).

When a ¹³C atom in one molecule and a ¹⁵N atom in a second molecule are located within 3 nm (as is the case when [¹⁵N]ALO-D4 is bound to [¹³C]cholesterol), ¹³C and ¹⁵N atoms released from the two molecules can combine to create a cluster secondary ion, ¹³C¹⁵N⁻ (17). Thus, in experiments involving binding of [¹⁵N]ALO-D4 to [¹³C]cholesterol-loaded macrophages, we expected to observe a robust ¹³C¹⁵N⁻ signal. Indeed, that was the case; we could image both macrophages and the surrounding particles based solely on ¹³C¹⁵N⁻ secondary ions (*SI Appendix*,

Fig. S1). In our experiments, the number of ¹³C¹⁵N⁻ ions in particles surrounding macrophages was more than 2,000 times greater than expected from the natural abundance of the two stable isotopes.

Because the particles originate from the plasma membrane, we suspected that they would contain sphingomyelin. To test this idea, we incubated cholesterol-loaded RAW 264.7 macrophages and primary macrophages with [¹⁵N]ALO-D4 and [¹³C]lysenin [a sphingomyelin-binding cytolytic (15)]. ¹⁵N/¹⁴N and ¹³C/¹²C nanoSIMS images revealed that macrophage-derived particles were enriched in both ¹⁵N and ¹³C (Fig. 6). Interestingly, [¹³C]lysenin bound more to filopodia than to particles (i.e., the ¹³C/¹²C ratio was higher in filopodia than in particles). In contrast, the ¹⁵N/¹⁴N ratio, reflecting [¹⁵N]ALO-D4 binding to accessible cholesterol, was greater in particles than in the filopodia (Fig. 6). We found a significant inverse correlation between ¹³C/¹²C and ¹⁵N/¹⁴N ratios in the primary macrophages (Fig. 6B).

Next, we compared the binding of [¹⁵N]ALO-D4 to particles from macrophages that had been incubated in medium containing 10% FBS and to particles from macrophages that had been incubated in medium containing 1% LPDS. Mouse peritoneal macrophages were incubated overnight in medium containing 10% FBS and then were incubated for two more days in medium containing either 10% FBS or 1% LPDS. The cells were then lifted, replated, and incubated in either 10% FBS or 1% LPDS for 12 h (allowing cells to release particles). Finally, the cells were incubated with [¹⁵N]ALO-D4 and processed for nanoSIMS. The ¹⁵N/¹⁴N ratio in particles was approximately sixfold higher in the cells incubated in 10% FBS than in the cells

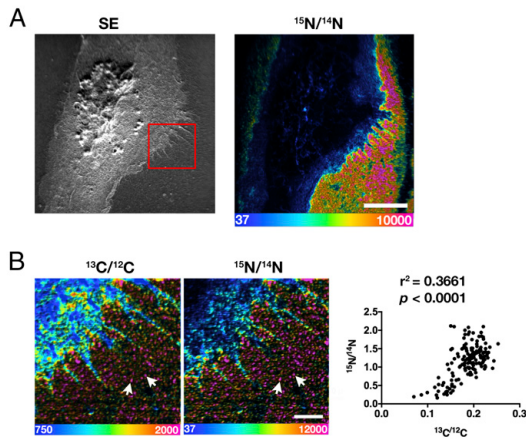


Fig. 3. NanoSIMS images of macrophages that were loaded with [^{13}C]cholesterol and then incubated with [^{15}N]ALO-D4 revealing that macrophage-derived particles are rich in cholesterol (high $^{15}\text{N}/^{14}\text{N}$ and $^{13}\text{C}/^{12}\text{C}$ ratios). (A) Low-magnification secondary electron (SE) and $^{15}\text{N}/^{14}\text{N}$ nanoSIMS images. The lawn of particles surrounding the macrophages is enriched in ^{15}N , reflecting the binding of [^{15}N]ALO-D4 to accessible cholesterol. (Scale bar, 10 μm .) (B) The boxed region in A is shown at higher magnification. $^{13}\text{C}/^{12}\text{C}$ ratio and $^{15}\text{N}/^{14}\text{N}$ ratio images reveal that the particles surrounding the macrophages are enriched in both ^{13}C and ^{15}N . (Scale bar, 2 μm .) The scatter plot shows the $^{15}\text{N}/^{14}\text{N}$ and $^{13}\text{C}/^{12}\text{C}$ ratios for 150 particles. A linear regression analysis revealed a positive correlation between ^{15}N and ^{13}C enrichments ($P < 0.0001$). $^{15}\text{N}/^{14}\text{N}$ and $^{13}\text{C}/^{12}\text{C}$ scales are multiplied by 10,000.

incubated in 1% LPDS (*SI Appendix, Fig. S2*). The $^{15}\text{N}/^{14}\text{N}$ ratio in projections (or filopodia) incubated in 10% FBS was only approximately twofold higher.

To determine whether cholesterol loading increases the binding of [^{15}N]ALO-D4 to the particles, peritoneal macrophages were collected, and one-half of the cells were loaded with [^{13}C]cholesterol. After incubation in medium containing 1% LPDS for 24 h, the cells were lifted with EDTA, replated, and incubated in 1% LPDS medium for 12 h. Finally, the cells were incubated with [^{15}N]ALO-D4 for 2 h and processed for nanoSIMS (*Fig. 7A*). The $^{13}\text{C}/^{12}\text{C}$ ratios in the particles and projections of the [^{13}C]cholesterol-loaded macrophages were similar (*Fig. 7B*). In contrast, the $^{15}\text{N}/^{14}\text{N}$ ratio was higher in the particles than in the filopodia, implying that accessible cholesterol is more abundant in particles than in filopodia (*Fig. 7B*).

To determine whether the cholesterol content of particles is influenced by the LXR signaling pathway, we tested the effects of LXR/retinoid X receptor (RXR) agonists on the cholesterol content of particles from peritoneal macrophages of wild-type and *Lxra/Lxr β* double-knockout (*LXR $^{-/-}$*) mice. Macrophages were loaded with acetyl-LDL, lifted with EDTA, and replated. The cells were then treated with the LXR/RXR agonists or vehicle (DMSO) alone for 12 h. As expected, cholesterol levels in wild-type macrophages fell during treatment with LXR/RXR agonists; cholesterol levels in *LXR $^{-/-}$* macrophages were somewhat higher and did not fall when the cells were treated with LXR/RXR agonists (*Fig. 8A*). The LXR/RXR agonists increased ABCA1 and ABCG1 expression levels in wild-type but not in *LXR $^{-/-}$* macrophages (*Fig. 8A*).

Particle release from the plasma membrane was observed in both wild-type and *LXR $^{-/-}$* macrophages (*SI Appendix, Fig. S3*). LXR/RXR agonist treatment of wild-type macrophages increased accessible cholesterol in both particles and the filopodia, as judged by [^{15}N]ALO-D4 binding (*Fig. 8B*). In-

terestingly, the LXR/RXR agonist-induced increase in [^{15}N]ALO-D4 binding was greater in particles than in filopodia (*Fig. 8B and C*). In *LXR $^{-/-}$* macrophages, LXR/RXR agonists resulted in little or no change in [^{15}N]ALO-D4 binding to either particles or filopodia (*Fig. 8B and C*). In an independent experiment, LXR/RXR agonists had little or no effect on [^{15}N]ALO-D4 binding to *LXR $^{-/-}$* macrophages, but they increased [^{15}N]ALO-D4 binding to particles and projections of wild-type macrophages in both the presence and absence of cholesterol loading (*SI Appendix, Fig. S4*). Again, the LXR/RXR agonist-induced increase

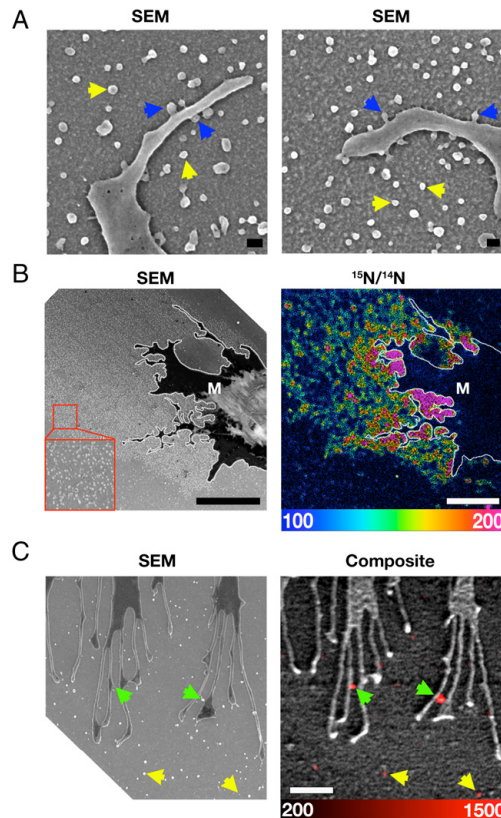


Fig. 4. Macrophages release cholesterol-enriched particles when incubated in medium containing 1% LPDS. (A) Scanning electron micrographs show the release of particles from the filopodia of macrophages. Blue arrows indicate particle formation on filopodia; yellow arrows show particles on the substrate. (Scale bars, 100 nm.) (B) SEM and nanoSIMS images after a short incubation with [^{15}N]ALO-D4. The scanning electron micrograph shows a lawn of particles on the substrate; the $^{15}\text{N}/^{14}\text{N}$ image shows [^{15}N]ALO-D4 binding (enrichment of the particles with accessible cholesterol). The filopodia of the macrophage (M) are outlined by a dotted white line. The $^{15}\text{N}/^{14}\text{N}$ ratio scale is multiplied by 10,000 and is between two and five times the natural abundance of ^{15}N . (Scale bars, 5 μm .) (C) Higher-magnification SEM and nanoSIMS images of the filopodia of macrophages in the absence of cholesterol loading. Note the binding of [^{15}N]ALO-D4 to particles on the surface of filopodia (green arrows) and to particles on the surrounding substrate (yellow arrows). The $^{15}\text{N}/^{14}\text{N}$ ratio scale is multiplied by 10,000 and is between 5 and 40 times the natural abundance of ^{15}N . (Scale bar, 1 μm .) Note that the scale in this figure differs from that in *Fig. 2B*, making it possible to visualize ^{15}N enrichment that is lower than in cholesterol-loaded cells.

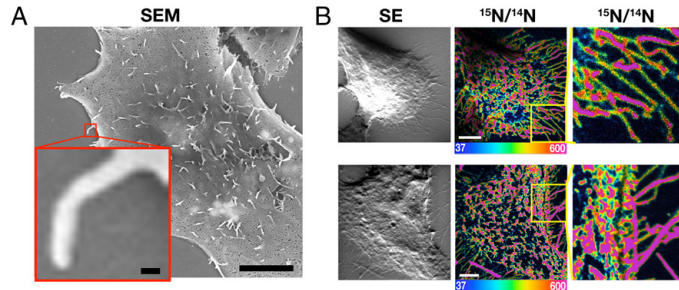


Fig. 5. CHO-K1 cells do not produce cholesterol-rich particles. (A) SEM image of CHO-K1 cells grown in medium containing 10% FBS reveals very few particles on the substrate surrounding the cell. (Scale bar in the low-magnification image, 5 μm ; scale bar in the boxed image, 100 nm.) (B) nanoSIMS secondary electron (SE) images show a lack of particles on the substrate surrounding the cell. NanoSIMS $^{15}\text{N}/^{14}\text{N}$ images reveal binding of [^{15}N]ALO-D4 to the microvilli on the cell body and the microvilli that extend from the perimeter of the cell. (Scale bars, 5 μm .) The boxed regions are shown at higher magnification on the right.

in [^{15}N]ALO-D4 binding was greater in particles than in filopodia (SI Appendix, Fig. S4).

To determine if HDL is capable of unloading cholesterol from macrophage-derived particles, we loaded macrophages with [^{13}C]cholesterol/M β CD for 24 h, lifted the cells with EDTA, and

replated the cells in medium in the presence or absence of HDL for 24 h. Next, the cells were incubated with [^{15}N]ALO-D4 for 2 h and processed for nanoSIMS. The HDL incubation did not have an obvious effect on particle production, as judged by SEM (SI Appendix, Fig. S3). However, the incubation with HDL

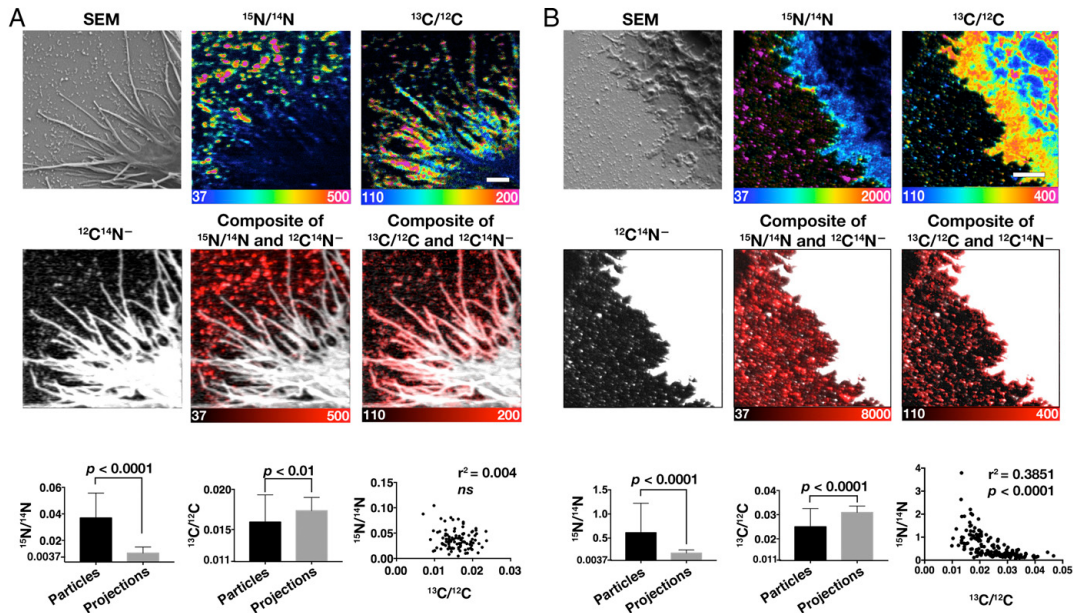


Fig. 6. Particles released by macrophages contain cholesterol and sphingomyelin, as judged by ALO-D4 and lysine binding. (A) RAW 267.4 murine macrophages were loaded with cholesterol/M β CD for 2 h. The cells were incubated for 2 h with [^{15}N]ALO-D4 and for 1 h with [^{13}C]lysine and then were prepared for SEM and nanoSIMS imaging. A scanning electron micrograph showed particle formation on the filopodia of macrophages and particles attached to the poly-D-lysine-coated substrate. $^{15}\text{N}/^{14}\text{N}$ and $^{13}\text{C}/^{12}\text{C}$ images reveal [^{15}N]ALO-D4 and [^{13}C]lysine, respectively, on macrophage-derived particles. $^{15}\text{N}/^{14}\text{N}$ ratio and $^{13}\text{C}/^{12}\text{C}$ ratio scales are multiplied by 10,000. Composite $^{12}\text{C}^{14}\text{N}^-$ (gray) and $^{15}\text{N}/^{14}\text{N}$ ratio (red) or $^{13}\text{C}/^{12}\text{C}$ and $^{12}\text{C}^{14}\text{N}^-$ (red) images show binding of [^{15}N]ALO-D4 and [^{13}C]lysine to particles and projections. (Scale bar, 1 μm .) ns, not significant. (B) Primary macrophages were loaded with acetyl-LDL (50 $\mu\text{g}/\text{mL}$), incubated with [^{15}N]ALO-D4 and [^{13}C]lysine, and were prepared for SEM and nanoSIMS imaging. $^{15}\text{N}/^{14}\text{N}$ ratio and $^{13}\text{C}/^{12}\text{C}$ ratio scales are multiplied by 10,000. Composite $^{12}\text{C}^{14}\text{N}^-$ (gray) and $^{15}\text{N}/^{14}\text{N}$ ratio (red) or $^{13}\text{C}/^{12}\text{C}$ ratio (red) images show binding of [^{15}N]ALO-D4 and [^{13}C]lysine to particles and the filopodial projections. (Scale bar, 2 μm .) For quantification of $^{15}\text{N}/^{14}\text{N}$ ratios in particles released by macrophages and in the filopodia (projections) of macrophages, ratios in 150 particles and 20 projections were measured. The y axis in the $^{15}\text{N}/^{14}\text{N}$ bar graphs starts at 0.0037 (the natural abundance of ^{15}N). The y axis in the $^{13}\text{C}/^{12}\text{C}$ bar graph starts at 0.011 (the natural abundance of ^{13}C). Data are presented as mean \pm SD. Differences were assessed with a Student's *t* test with Welch's correction. The scatter plot shows the correlation between $^{15}\text{N}/^{14}\text{N}$ and $^{13}\text{C}/^{12}\text{C}$ ratios for 150 particles. A linear regression analysis revealed a significant inverse correlation between ^{15}N and ^{13}C enrichments in primary macrophages ($P < 0.0001$).

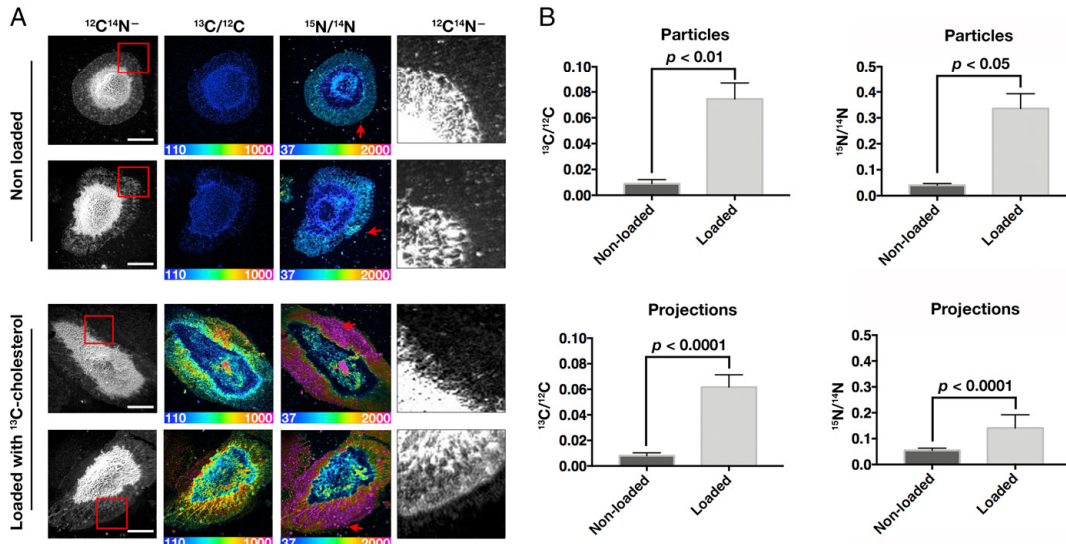


Fig. 7. Binding of [^{15}N]ALO-D4 to macrophage-derived particles depends on the cholesterol content in macrophages. (A) NanoSIMS images assessing the binding of [^{15}N]ALO-D4 to macrophages that were not loaded with cholesterol (Upper) and macrophages that had been loaded with [^{13}C]cholesterol (Lower). Cell morphology was visualized with [$^{12}\text{C}^{14}\text{N}$] $^{-}$ images. The $^{13}\text{C}/^{12}\text{C}$ and $^{15}\text{N}/^{14}\text{N}$ images depict [^{13}C]cholesterol and [^{15}N]ALO-D4, respectively. Boxed areas in the [$^{12}\text{C}^{14}\text{N}$] $^{-}$ images are shown at higher magnification in the images on the right, revealing particles on the substrate (red arrows). $^{15}\text{N}/^{14}\text{N}$ and $^{13}\text{C}/^{12}\text{C}$ ratio scales are multiplied by 10,000. (Scale bar, 10 μm .) (B) Bar graphs show the $^{13}\text{C}/^{12}\text{C}$ (Left) and $^{15}\text{N}/^{14}\text{N}$ (Right) ratios in particles (Upper) and macrophage projections (Lower). Three $40 \times 40\text{-}\mu\text{m}$ images, each containing one or two macrophages, were quantified. For particle quantification, a minimum of 50 particles per image was selected on the basis of the [$^{12}\text{C}^{14}\text{N}$] $^{-}$ image, and the mean $^{15}\text{N}/^{14}\text{N}$ ratio in 15–30 projections per cell was calculated. Data are presented as mean \pm SD. Differences were assessed with a Student's *t* test with Welch's correction.

reduced both the [^{13}C]cholesterol content of particles and the binding of [^{15}N]ALO-D4 to the particles (Fig. 9). Even after the HDL incubation, it was possible to visualize particles by adjusting the scale of the nanoSIMS images (SI Appendix, Fig. S5). Interestingly, the $^{15}\text{N}/^{14}\text{N}$ ratio in particles fell by $\sim 75\%$ with the HDL incubation, while the $^{13}\text{C}/^{12}\text{C}$ ratio fell by only $\sim 40\%$ (Fig. 9B). HDL reduced [^{13}C]cholesterol content and [^{15}N]ALO-D4 binding to filopodia of macrophages but to a lesser extent than with particles. A 15-min incubation of macrophages with M β CD also reduced the binding of [^{15}N]ALO-D4 to the particles and projections of macrophages (SI Appendix, Fig. S6). Interestingly, the decrease in [^{15}N]ALO-D4 binding to particles with M β CD treatment was proportionately greater than the decrease in [^{15}N]ALO-D4 binding to the filopodia (SI Appendix, Fig. S6).

Discussion

We found that filopodia of mouse peritoneal macrophages and RAW 264.7 cell macrophages release ~ 20 - to 120 -nm unilamellar vesicular particles. In the past, macrophages have been reported to release ~ 24 -nm particles into the cell-culture medium (2) or to deposit irregularly shaped cholesterol microdomains on the substrate (3), but mechanisms for the genesis and release of the particles and microdomains have never been clear. In the current study, we demonstrated by SEM and TEM that particles appear to be released from the plasma membrane of filopodia, attaching to the surrounding substrate. By nanoSIMS analyses, these particles are enriched in cholesterol. When macrophages were loaded with [^{13}C]cholesterol, the particles on the surrounding substrate were enriched in ^{13}C . The particles also bound [^{15}N]ALO-D4 avidly. Because macrophage-derived particles originate from the plasma membrane, we expected that they

would contain sphingomyelin. Indeed, nanoSIMS studies showed that lysoenin, a sphingomyelin-specific cytolysin, bound to macrophage-derived particles.

The appearance and release of particles from the macrophage plasma membrane was evident under multiple conditions—whether the cells were incubated in LPDS- or FBS-containing medium, whether or not the macrophages were loaded with cholesterol, whether or not they were deficient in LXRs, whether or not they were treated with LXR/RXR agonists, and whether or not the medium contained HDL. While we could not discern clear differences in particle size or numbers under these different conditions, we certainly cannot exclude the possibility that such differences exist, given that we do not have protocols for accurately quantifying particle numbers or measuring the dynamics of particle formation and release. On the other hand, we are confident that the cholesterol content of particles changes with different conditions. Loading macrophages with cholesterol, incubating the cells in FBS rather than LPDS, or adding LXR/RXR agonists to the cell-culture medium increases the content of cholesterol in particles, as judged by nanoSIMS analyses.

Using biochemical approaches, Radhakrishnan and coworkers (12) demonstrated that ALO-D4 binds to an accessible pool of cholesterol on the plasma membrane. The accessible pool is not sequestered by sphingomyelin or phospholipids and appears when the cholesterol content of the plasma membrane exceeds ~ 30 mol% (12, 14). More recently, the same group showed that the accessible pool in the plasma membrane is mobile, readily moving to the endoplasmic reticulum and participating in the regulation of genes involved in cholesterol synthesis (14). Our studies revealed that the particles released from macrophage filopodia are enriched in accessible cholesterol. (i) [^{15}N]ALO-D4 binds avidly to macrophage particles even when the macrophages

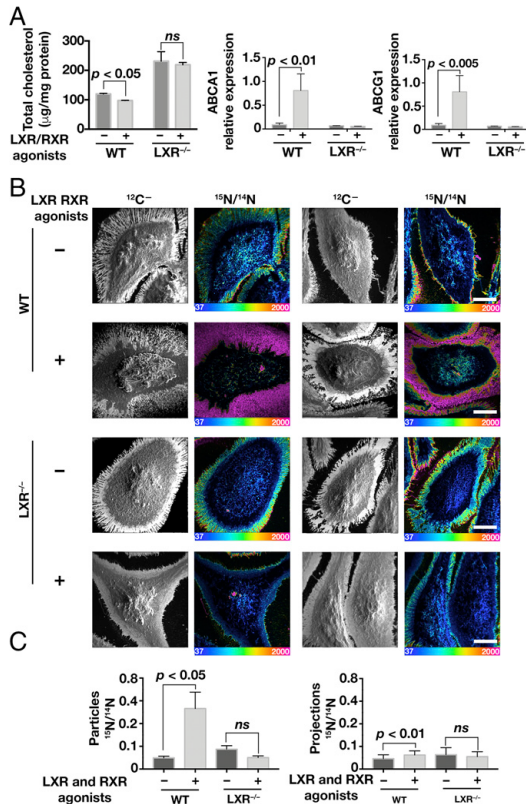


Fig. 8. NanoSIMS analysis of [¹⁵N]ALO-D4 binding to cholesterol-loaded wild-type macrophages or *Lxra/Lxrβ* double-knockout macrophages (LXR^{-/-}) in the presence of LXR and RXR agonists or vehicle (DMSO) alone. Macrophages were loaded with acetyl-LDL before being lifted with EDTA, replated, and incubated with LXR/RXR agonists or DMSO alone for 12 h. (A) Bar graphs depicting cellular cholesterol levels and ABC transporter expression levels in wild-type and LXR^{-/-} macrophages treated with LXR/RXR agonists or DMSO alone. Cholesterol was measured in two wells of macrophages in a six-well plate; each data point in the bar graph represents cholesterol content in one well of macrophages. RNA was isolated from macrophages in a six-well plate, and levels of gene expression were measured (*n* = 5 for WT and *n* = 3 for LXR^{-/-}). Data are presented as mean ± SD. Differences were assessed with a Student's *t* test with Welch's correction. (B) NanoSIMS images of WT and LXR^{-/-} macrophages after incubation with [¹⁵N]ALO-D4. Cell morphology was visualized with ¹²C⁻ images; ¹⁵N/¹⁴N images show binding of [¹⁵N]ALO-D4 to macrophages and macrophage-derived particles. ¹⁵N/¹⁴N ratio scales are multiplied by 10,000. (Scale bars, 10 μm.) (C) Quantification of ¹⁵N/¹⁴N ratios in particles and filopodia (projections) of wild-type and LXR^{-/-} macrophages. Two or three 40 × 40-μm images, each containing one or two macrophages, were quantified. A minimum of 50 particles per image were selected from the ¹²C⁻ image (particles were visible after adjusting the contrast of the images), and the mean ¹⁵N/¹⁴N ratio was calculated. For the filopodial projections, the ¹⁵N/¹⁴N ratio in 15–30 projections per cell was calculated. The ¹³C/¹²C ratios in cells that did not receive [¹³C]cholesterol reflected the natural abundance of ¹³C. Data are presented as mean ± SD. Differences were assessed with a Student's *t* test with Welch's correction; ns, not significant.

were incubated in medium containing 1% LPDS and the binding of the [¹⁵N]ALO-D4 to the surrounding filopodia was extremely low (Fig. 4). (ii) When macrophages were incubated in

medium containing 10% FBS (rather than 1% LPDS), the amount of accessible cholesterol in particles increased substantially while the increase in filopodia was modest (*SI Appendix, Fig. S2*). (iii) When macrophages were loaded with [¹³C]cholesterol, [¹⁵N]ALO-D4 binding to particles increased substantially more than the increase in binding to the macrophage plasma membrane (Fig. 7). (iv) When cells were loaded with cholesterol, adding LXR/RXR agonists to the cell-culture medium increased [¹⁵N]ALO-D4 binding to both particles and filopodia, but the increase in the binding of [¹⁵N]ALO-D4 to particles was greater (Fig. 8). (v) [¹³C]lysenin bound preferentially to the filopodial projections of macrophages, whereas [¹⁵N]ALO-D4 bound preferentially to particles (Fig. 6). Each of these observations suggests that the particles that are formed and then released from the plasma membrane are enriched in accessible cholesterol.

The combination of LXR and RXR agonists increased the cholesterol content of macrophage particles, as judged by nanoSIMS analyses. These drugs induce the production of many proteins involved in cholesterol metabolism and cholesterol efflux. We suspect that increased expression of ABC transporters is important for enriching the macrophage plasma membrane and plasma membrane-derived particles with cholesterol. By nanoSIMS analyses, we also found that HDL unloads cholesterol from macrophage-derived particles. It is noteworthy that the decrease in [¹⁵N]ALO-D4 binding to particles with the HDL incubation was greater than the decrease in the [¹³C]cholesterol content of the particles. We suspect that this difference relates to the greater mobility of accessible cholesterol.

We do not yet have a firm understanding of the mechanisms for the formation and release of particles from the plasma membrane of macrophages. By SEM, the particles appear to bud from the plasma membrane. One possibility is that the particles form by ballooning or outpouching of a segment of the plasma membrane that is not firmly attached to the cytoskeleton. However, a second possibility is that discrete segments of the macrophage plasma membrane are strongly affixed to the substrate by substrate adhesion proteins and that those segments are left behind in the form of vesicular particles as the cell “pulls away” during locomotion. This second possibility is attractive because it would help explain why the lawn of particles is generally located on one or two sides of the macrophage rather than around the entire circumference of the cell. (Note that the two possibilities are not mutually exclusive.) However, if we assume that cell mobility is largely responsible for the genesis of particles, the remaining mystery is why the particles are more enriched in accessible cholesterol than the adjacent filopodia and lamellipodia. Cholesterol affects many properties of lipid bilayers, including viscosity, elasticity, permeability, and protein association. Perhaps the accessible cholesterol within the plasma membrane is less firmly attached to the cytoskeleton and is more prone to being “left behind” on vesicular particles as macrophages move across the substrate.

One limitation of our study is that all our studies dealt with cultured macrophages. Whether particles are released from macrophages *in vivo* is unknown, but we suspect that particle release will prove to be a feature of resident macrophages in mammalian tissues. Following the phagocytosis of senescent erythrocytes, splenic macrophages need to unload substantial amounts of cholesterol, and particle release could assist in that function. We further suspect that a failure to enrich particles in cholesterol in the setting of ABCA1 deficiency could help to explain the hallmark histopathology of Tangier disease (cholesterol-laden macrophages in the spleen and lymph nodes). Particle release from macrophages in atherosclerotic plaques could also be a mechanism for unloading cholesterol and promoting reverse cholesterol transport.

Whether the macrophage microparticles described by the laboratory of Phillips and coworkers (2) were similar to those in this study is unclear. The microparticles in the Phillips study

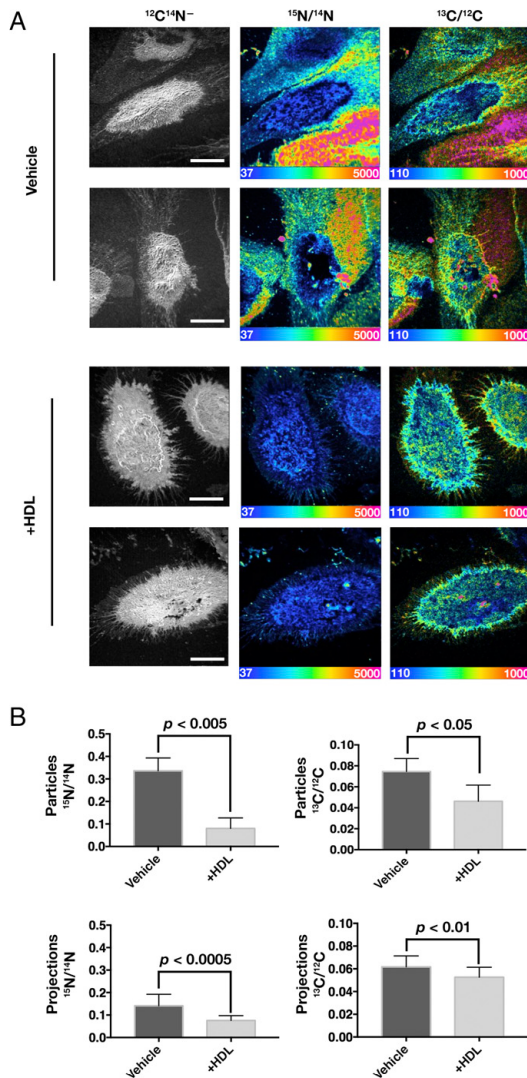


Fig. 9. HDL removes cholesterol from macrophage-derived particles. Macrophages were loaded with [^{13}C]cholesterol for 24 h before being lifted, replated, and incubated in the presence or absence of HDL for 24 h. After cells were incubated with [^{15}N]ALO-D4 for 2 h, nanoSIMS imaging was performed. (A) Cell morphology was visualized with $^{12}\text{C}/^{14}\text{N}$ images; the $^{15}\text{N}/^{14}\text{N}$ image reflects [^{15}N]ALO-D4 binding (accessible cholesterol); the $^{13}\text{C}/^{12}\text{C}$ ratio reflects total cholesterol. $^{15}\text{N}/^{14}\text{N}$ ratio and $^{13}\text{C}/^{12}\text{C}$ ratio scales are multiplied by 10,000. (Scale bars, 10 μm .) (B) Quantification of $^{15}\text{N}/^{14}\text{N}$ and $^{13}\text{C}/^{12}\text{C}$ ratios revealed reduced [^{13}C]cholesterol and [^{15}N]ALO-D4 binding in particles after incubation with HDL. Three or four $40 \times 40\text{-}\mu\text{m}$ images, each with one or two macrophages, were quantified. For particle quantification, a minimum of 50 particles per image were selected from the $^{12}\text{C}/^{14}\text{N}$ image (particles were visible after the contrast was adjusted), and the mean $^{15}\text{N}/^{14}\text{N}$ ratio for the particles was calculated. For the filopodial projections, the $^{15}\text{N}/^{14}\text{N}$ ratio of 15–30 projections per cell was calculated. Data are presented as mean \pm SD. Differences were assessed with a Student's *t* test with Welch's correction.

averaged 24 nm in diameter. By SEM, many of the vesicular particles that we observed were in a similar size range (30 ± 10 nm in cholesterol-loaded macrophages vs. 34 ± 17 nm in nonloaded macrophages; $n = 30$ particles for each). Kruth and coworkers (3–6, 9) have published a series of papers on the release of cholesterol microdomains from macrophages, but how they were released from cells was not defined. We believe it is likely that the cholesterol microdomains in the studies by Kruth and coworkers are the same as the particles that we document in the current studies, namely vesicular particles that are released from the plasma membrane of macrophage filopodia. The studies by Kruth relied largely on immunofluorescence microscopy with a cholesterol-specific antibody. In our studies, cholesterol enrichment of the macrophage particles was documented by nanoSIMS with [^{13}C]cholesterol and [^{15}N]ALO-D4. In the studies by Kruth and coworkers (4–6), microdomain production virtually disappeared in the absence of cholesterol loading. In our studies, we found particle release under a variety of cell-culture conditions, including in cells in the absence of cholesterol loading and cells incubated in 1% LPDS. However, the different cell-culture conditions (e.g., cholesterol loading, LXR/RXR agonists) in our studies clearly influenced the cholesterol content of the particles. We do not understand why particle release disappeared in the studies by Kruth and coworkers (4–6), but one possibility is that they used human monocyte-derived macrophages rather than mouse peritoneal macrophages.

The release of vesicular particles that we documented in macrophages is morphologically similar to the budding of HIV-1 virions from macrophages (18–21). HIV-1 virions are released by a budding process from cholesterol- and sphingolipid-rich regions of the plasma membrane (18). HIV-1 budding may be driven by the formation of a latticework of Gag proteins along budding sites. In the case of our studies, the identity of proteins important for particle release is unknown. Another process that closely resembles particle release from macrophages is the budding of vesicles from the canalicular membrane of hepatocytes (22, 23). Like macrophages, hepatocytes need to dispose of large amounts of cholesterol, and that involves releasing cholesterol-rich vesicular particles from the canalicular microvilli. Another physiological event resembling macrophage particle release is the release of vesicles from the tips of the microvilli of intestinal enterocytes (24, 25). In that case, the size of the vesicles released from the tips of microvilli was altered in mice lacking myosin 1a, implicating cytoplasmic motors in particle formation and/or release (25). Myosins are required for the formation of macrophage filopodia and their movement (26–29), but their relevance to particle release by macrophages is not yet known. However, we suspect that the application of motor-driven forces to the plasma membrane is important for the formation and release of particles.

Materials and Methods

Mouse Strains. Wild-type mice (C57BL/6) were purchased from the Jackson Laboratory. *Lxra/Lxrb* double-knockout mice were originally obtained from David Mangelsdorf (University of Texas Southwestern Medical Center, Dallas) and have been backcrossed to strain C57BL/6 for more than 10 generations (30).

Cell Lines. RAW 264.7 cell line murine macrophages (purchased from ATCC) and hamster CHO-K1 cells were grown in monolayer cultures at 37 $^{\circ}\text{C}$ with 8–9% CO_2 . RAW cells were maintained in macrophage medium (DMEM) (Thermo Fisher Scientific) containing 1 mM sodium pyruvate, 2 mM glutamine, and 10% (vol/vol) FBS (HyClone). CHO-K1 cells were maintained in Ham's F-12 Nutrient Mixture (Thermo Fisher Scientific) containing 10% (vol/vol) FBS (HyClone) and 2 mM glutamine.

Mouse Peritoneal Macrophages. Wild-type and *Lxra/Lxrb* double-knockout mice were injected i.p. with 1 mL of 3% (wt/vol) Difco Fluid Thioglycollate Medium (Becton, Dickinson and Co.). Three days later, peritoneal macro-

phages were harvested with 10 mL of cold Dulbecco's PBS without Ca^{2+} and Mg^{2+} . Cells were centrifuged at $400 \times g$ for 5 min at 4 °C, treated with 5 mL of red blood cell lysing buffer Hybri-Max (Sigma) for 5 min, and washed two times with cold PBS. Macrophages were plated on FBS-coated Petri dishes (8×10^6 cells per dish) and were cultured overnight in macrophage medium. Macrophages were then lifted by incubation in cold PBS without Ca^{2+} and Mg^{2+} containing 5% FBS and 5 mM EDTA for 45 min at 4 °C. For nanoSIMS and SEM, cells were replated on 0.5-cm² silicon wafers coated with 0.1 mg/mL poly-D-lysine hydrobromide (Sigma) in 24-well plates.

Preparation of [¹³C]cholesterol. [¹³C]cholesterol was produced as described (31) using a *Saccharomyces cerevisiae* strain (RH6829) engineered to produce cholesterol rather than ergosterol (32, 33). RH6829 yeast cells were grown in medium containing 0.7% yeast nitrogen base (US Biological), 0.5% yeast extract (BD), 1.5% glucose (>98% ¹³C; >99% glucose) (Martek Isotopes LLC), and 0.4 mg/L uracil and leucine. Precultures were diluted 1:2,000 in this medium and were grown for 3 d at 30 °C. The [¹³C]cholesterol was purified from harvested cells and analyzed by GC-MS and by NMR (32). The cholesterol contained 94% ¹³C, and the yield was ~10 mg/L of medium.

Cholesterol Loading of Macrophages. For some experiments, macrophages were loaded with 50 μg/mL of acetyl-LDL (Alfa Aesar) in macrophage medium containing 1% LPDS (15) instead of 10% FBS for 24 h at 37 °C. In other experiments, macrophages were loaded with [¹³C]cholesterol/MβCD (34). Briefly, [¹³C]cholesterol in 100% ethanol (7.5 mg/mL) was added in 50-μL aliquots to a stirring solution of 5% (wt/vol) methyl-β-cyclodextrin (Sigma) in double-distilled water (ddH₂O) in an 80 °C water bath to achieve an MβCD:cholesterol ratio of 10:1. The solution was lyophilized and then reconstituted in ddH₂O to a cholesterol concentration of 2.5 mM and an MβCD concentration of 25 mM. The [¹³C]cholesterol/MβCD solution was filtered through a 0.22-μm filter and stored at 4 °C. Macrophages were loaded with 20 μL of [¹³C]cholesterol/MβCD (final cholesterol concentration, 50 μM) in macrophage medium containing 0.1% LPDS, 50 μM mevastatin (Calbiochem), and 50 μM mevalonolactone (Sigma) for 24 h at 37 °C. RAW 267.4 cells were loaded with unlabeled cholesterol/MβCD complexes (Sigma).

Treatment of Macrophages with LXR/RXR Agonists, HDL, and MβCD. In some experiments, macrophages were treated with GW3965 (35), an LXR agonist, and LG268 (Ligand Pharmaceuticals), an RXR agonist. Cells were treated with 1 μM LXR ligand and 100 nM RXR ligand in DMSO or with DMSO alone in macrophage medium containing 1% LPDS for 12 h at 37 °C. In other experiments, cells were incubated with 200 μg/mL of human HDL (Alfa Aesar) in macrophage medium containing 1% LPDS for 24 h or were incubated with 10 mM MβCD in DMEM for 15 min at 37 °C.

Preparation of ¹⁵N-Labeled His-Tagged ALO-D4. A plasmid for ALO-D4 (ALO amino acids 404–512 with C472A and S404C substitutions) was obtained from Arum Radhakrishnan (University of Texas Southwestern Medical Center, Dallas), and ¹⁵N-labeled ALO-D4 was prepared (15, 36). Briefly, ALO-D4 was expressed in BL21(DE3) pLysS *Escherichia coli* (Invitrogen) and induced with 1 mM isopropyl β-D-1-thiogalactopyranoside (IPTG) in 1 L of minimal medium containing 20.2 mM ¹⁵NH₄Cl at 25 °C for 16 h. Cells were pelleted and lysed by sonication, and the lysate was centrifuged at 4 °C. The supernatant was mixed with 4 mL of HisPur Cobalt resin (50% bed volume; Thermo Fisher Scientific). The mixture was loaded into a column and allowed to flow through by gravity. The column was washed, and [¹⁵N]ALO-D4 was eluted with a buffer containing 300 mM imidazole. The eluates were pooled and concentrated to 1 mL with an Amicon 10-kDa cut off concentrator (Millipore). The purified [¹⁵N]ALO-D4 was stored at 4 °C.

Preparation of ¹³C-Labeled His-mCherry-Tagged Lysenin. To produce [¹³C]lysenin, *E. coli* BL21(DE3) (Invitrogen) was transformed with the plasmid encoding lysenin (15) and grown in 1 L of minimal medium containing 95.5 mM KH₂PO₄, 57.4 mM K₂HPO₄, 63.4 mM Na₂HPO₄, 13.8 mM K₂SO₄, 20.2 mM NH₄Cl, 5 MgCl₂, 0.2% (wt/vol) ¹³C₆ glucose (Cambridge Isotope Laboratories), and 100 μg/mL carbenicillin. The expression of lysenin was induced with 0.2% (wt/vol) arabinose at 25 °C for 16 h; [¹³C]lysenin was purified as described (15).

Binding of ALO-D4 and Lysenin to Cells. Primary macrophages were washed three times for 10 min in PBS/Ca/Mg containing 0.2% (wt/vol) BSA. Cells were then incubated with 20 μg/mL of [¹⁵N]ALO-D4 in PBS/Ca/Mg containing 0.2% (wt/vol) BSA for 2 h at 4 °C. RAW cells were incubated in macrophage medium containing 0.1% LPDS, unlabeled cholesterol/MβCD (final cholesterol concentration of 50 μM), 50 μM mevastatin (Calbiochem), and 50 μM

mevalonolactone (Sigma) for 2 h at 37 °C. Cells were lifted, washed, and replated onto fresh poly-D-lysine-coated silicon wafers for 20 h. Next, cells were incubated with 20 μg/mL of [¹³C]lysenin for 1 h and 20 μg/mL of [¹⁵N]ALO-D4 in PBS/Ca/Mg containing 0.2% (wt/vol) BSA for 2 h at 4 °C. Unbound [¹⁵N]ALO-D4 and [¹³C]lysenin were removed by washing with PBS/Ca/Mg containing 0.2% (wt/vol) BSA three times for 2 min each.

Preparing Samples for NanoSIMS and SEM. Cells were fixed with 4% paraformaldehyde (Electron Microscopy Sciences) and 2.5% glutaraldehyde (Electron Microscopy Sciences) in 0.1 M phosphate buffer (1.14 g NaH₂PO₄, 1.69 g Na₂HPO₄ in a 100-mL final volume of ddH₂O, pH 7.4) for 20 min at 4 °C followed by 1 h at room temperature. The samples were washed three times for 7 min each in 0.1 M phosphate buffer, postfixed with 1% osmium tetroxide (Electron Microscopy Sciences) in 0.1 M phosphate buffer for 45 min, and washed three times for 7 min each in ice-cold ddH₂O. For nanoSIMS, cells were air-dried. For SEM, cells were dehydrated with a graded series of ethanol concentrations (50, 70, 85, 95, and 100% ×3 for 7 min each) and then were critical-point dried with a Tousimis Autosamdri 810 critical point dryer (Tousimis). Samples were then coated with 2 nm of platinum (Pelco) with an ion-beam sputtering system (South Bay Technologies). Cells were imaged with a Zeiss Supra 40VP scanning electron microscope with a 3-KeV incident beam.

Preparing Samples for TEM. Primary macrophages were cholesterol-loaded and plated onto poly-D-lysine-coated Thermanox plastic coverslips (Thermo Scientific) in a 24-well plate. After 24 h, the cells were fixed with 2.5% glutaraldehyde in 0.1 M phosphate buffer for 2 h at 4 °C. The samples were then washed five times for 2 min each in 0.1 M phosphate buffer, postfixed with ice-cold 2% osmium tetroxide in 0.1 M phosphate buffer for 45 min, and washed five times for 2 min each in ice-cold ddH₂O. The cells were then incubated with 2% (vol/vol) aqueous uranyl acetate overnight at 4 °C, washed five times with ddH₂O, and dehydrated with a graded series of ethanol concentrations (30, 50, 70, 85, 95, and 100% ×3, 7 min each) before infiltration with increasing concentrations (33, 66, and 100%) of Epon (Ted Pella) (15). Next, the coverslips were embedded by inverting on a BEEM capsule (Ted Pella) filled with fresh resin and were polymerized for 48 h at 60 °C. The coverslips removed, and 65-nm-thick sections were cut *en face* with a Diatome diamond knife. Sections were placed on formvar-coated 100-mesh copper grids that had been glow-discharged. The sections on grids were stained with Reynold's lead citrate for 9 min. Next, samples were imaged at 200 kV with an FEI T12 iCorr microscope equipped with an Eagle 2K CCD camera or were imaged at 60 kV with a JEOL 100CX transmission electron microscope.

NanoSIMS Analyses. Platinum-coated (5-nm) cells were analyzed with a nanoSIMS 50L instrument (CAMECA) as described (15, 37) with some modifications. Briefly, samples were bombarded with a focused ¹³²Cs⁺ primary beam, and secondary ions (e.g., ¹²C⁻, ¹³C⁻, ¹⁶O⁻, ¹²C¹⁴N⁻, ¹²C¹⁵N⁻) and secondary electrons were collected. Before imaging, a high ¹³²Cs⁺ primary beam (1-nA beam current; primary aperture D1 = 1) was used to presputter an area of 50 × 50 μm for 25 s to remove the platinum coating and implant ¹³²Cs⁺. In the same region, low-magnification images (~40 × 40 μm) were obtained with an ~2.5-pA beam current (primary aperture D1 = 2), a dwell time of 2.5 ms per pixel, and scans of 512 × 512 pixels. High-magnification images (~10 × 10 μm) were obtained with an ~0.8-pA beam current (primary aperture D1 = 3), a dwell time of ~10 ms per pixel, and scans of 512 × 512 pixels.

To quantify ¹³C/¹²C and ¹⁵N/¹⁴N ratios in particles, we identified particles by SEM and/or ¹²C⁻, ¹²C¹⁴N⁻, ¹⁶O⁻, or secondary electron nanoSIMS images, and regions of interest in the middle of the particles were defined with the OpenMIMS plugin in ImageJ (NIH). The region in the middle of each particle was quantified rather than the whole particle because we wanted to avoid pixels overlapping the perimeter of the particle and/or the substrate immediately adjacent to the particle. For each image, 50–100 particles were selected. To quantify ¹³C/¹²C and ¹⁵N/¹⁴N ratios in macrophage filopodia, straight lines were drawn, pixel by pixel, in the middle of the filopodial projections, and line scan analyses were performed. The average ¹³C/¹²C and ¹⁵N/¹⁴N ratios of line scan analyses were calculated. For each cell, 15–30 projections were assessed. The mean ¹⁵N/¹⁴N and ¹³C/¹²C ratios of the regions of interest were measured and processed by Prism 7.0. Differences were assessed by a Student's *t* test with Welch's correction.

Gene-Expression Analyses. Peritoneal macrophages were isolated from wild-type and *Lxra/Lxrb* double-knockout mice as described earlier. Cells were plated in macrophage medium containing 10% FBS. On the next day, cells

were washed and were incubated in macrophage medium containing 1% LPDS and 50 $\mu\text{g}/\text{mL}$ acetyl-LDL for 24 h. Cells were treated with 1 mM LXR ligand (GW3965) and 100 nM RXR ligand (LG268) for 12 h, and then RNA and lipids were extracted. Total RNA was isolated with TRIzol reagent (Invitrogen) and reverse-transcribed with the iScript cDNA synthesis kit (Bio-Rad). cDNA was quantified by real-time PCR with SYBR Green Master Mix (Diagenode) on an ABI 7900 instrument. Gene-expression levels were determined with a standard curve. Each gene was normalized to the housekeeping gene *36B4* and analyzed in duplicate. Primers for real-time PCR were 5'-CGTTTCCGGGAGTGCTCA-3' (mABCA1 forward primer), 5'-GCTAGAGATGACAAGGAGGAT-3' (mABCA1 reverse primer), 5'-TCACCCAGTTCTGCATCTCT-3' (mABCG1 forward primer), and 5'-GCAGATGTGTCAGGACCGAGT-3' (mABCG1 reverse primer). In these experiments, cellular cholesterol was extracted with hexane/isopropanol (3:2). The organic phase was collected and dried under nitrogen and resuspended with Tag Replication Buffer (TRB) buffer [100 mM KH_2PO_4 , 100 mM K_2HPO_4 , 50 mM NaCl, 5 mM sodium chlorate, and 0.1% Triton X-100 (pH 7.4)]. Cholesterol was quantified with the Amplex Red Cholesterol kit (Thermo Fisher Scientific). The values were normalized to cellular protein content determined with a BCA protein assay kit (Thermo Fisher Scientific).

Study Approval. Mice were housed in an Association for Assessment and Accreditation of Laboratory Animal Care International-accredited vivarium at the University of California, Los Angeles (UCLA). All animal procedures were approved by the UCLA Chancellor's Animal Research Committee.

ACKNOWLEDGMENTS. We thank the nanoSIMS facilities at the California Institute of Technology and the University of Western Australia; Dr. Kevin Williams and Dylan Zhou for assistance in measuring [^{13}C]cholesterol by mass spectrometry; and Dr. Marianne Gulluffo at the UCLA Brain Research Institute for help in obtaining TEM images. This work was supported by Fondation Leducq Transatlantic Network Grant 12CVD04 (to S.G.Y.), NIH Grants P01 HL090553, R01 HL087228, R35 HL139725-01, and HL125335 (all to S.G.Y.), Ruth L. Kirschstein National Research Service Award F32 HL132471 (to C.H.), the Swiss National Science Foundation (H.R.), and the National Centre of Competence in Research in Chemical Biology (H.R.). H.J. is supported by Australian Research Council Discovery Early Career Researcher Award DE180100080 and a Healy Research Collaboration Award. Support was also received from the Australian Microscopy and Microanalysis Research Facility and the Science and Industry Endowment Fund for supporting the Ion Probe Facility at the Centre for Microscopy, Characterisation and Analysis at the University of Western Australia.

- Tall AR, Costet P, Wang N (2002) Regulation and mechanisms of macrophage cholesterol efflux. *J Clin Invest* 110:899–904.
- Duong PT, et al. (2006) Characterization of nascent HDL particles and microparticles formed by ABCA1-mediated efflux of cellular lipids to apoA-I. *J Lipid Res* 47:832–843.
- Jin X, et al. (2016) ABCA1 (ATP-binding cassette transporter A1) mediates ApoA-I (apolipoprotein A-I) and ApoA-I mimetic peptide mobilization of extracellular cholesterol microdomains deposited by macrophages. *Arterioscler Thromb Vasc Biol* 36: 2283–2291.
- Jin X, et al. (2015) ABCA1 contributes to macrophage deposition of extracellular cholesterol. *J Lipid Res* 56:1720–1726.
- Freeman SR, et al. (2014) ABCG1-mediated generation of extracellular cholesterol microdomains. *J Lipid Res* 55:115–127.
- Ong DS, et al. (2010) Extracellular cholesterol-rich microdomains generated by human macrophages and their potential function in reverse cholesterol transport. *J Lipid Res* 51:2303–2313.
- Hafiane A, Genest J (2017) ATP binding cassette A1 (ABCA1) mediates microparticle formation during high-density lipoprotein (HDL) biogenesis. *Atherosclerosis* 257: 90–99.
- Phillips MC (2014) Molecular mechanisms of cellular cholesterol efflux. *J Biol Chem* 289:24020–24029.
- Jin X, et al. (2018) Macrophages shed excess cholesterol in unique extracellular structures containing cholesterol microdomains. *Arterioscler Thromb Vasc Biol* 38: 1504–1518.
- Vedhachalam C, et al. (2007) Mechanism of ATP-binding cassette transporter A1-mediated cellular lipid efflux to apolipoprotein A-I and formation of high density lipoprotein particles. *J Biol Chem* 282:25123–25130.
- Friz JF, et al. (2013) Sphingolipid domains in the plasma membranes of fibroblasts are not enriched with cholesterol. *J Biol Chem* 288:16855–16861.
- Das A, Brown MS, Anderson DD, Goldstein JL, Radhakrishnan A (2014) Three pools of plasma membrane cholesterol and their relation to cholesterol homeostasis. *eLife* 3: 02882.
- Das A, Goldstein JL, Anderson DD, Brown MS, Radhakrishnan A (2013) Use of mutant 125I-perfringolysin O to probe transport and organization of cholesterol in membranes of animal cells. *Proc Natl Acad Sci USA* 110:10580–10585.
- Infante RE, Radhakrishnan A (2017) Continuous transport of a small fraction of plasma membrane cholesterol to endoplasmic reticulum regulates total cellular cholesterol. *eLife* 6:25466.
- He C, et al. (2017) High-resolution imaging and quantification of plasma membrane cholesterol by NanoSIMS. *Proc Natl Acad Sci USA* 114:2000–2005.
- Goldstein JL, Ho YK, Basu SK, Brown MS (1979) Binding site on macrophages that mediates uptake and degradation of acetylated low density lipoprotein, producing massive cholesterol deposition. *Proc Natl Acad Sci USA* 76:333–337.
- Moss FR, 3rd, Boxer SG (2016) Atomic recombination in dynamic secondary ion mass spectrometry probes distance in lipid assemblies: A nanometer chemical ruler. *J Am Chem Soc* 138:16737–16744.
- Nguyen DH, Hildreth JE (2000) Evidence for budding of human immunodeficiency virus type 1 selectively from glycolipid-enriched membrane lipid rafts. *J Virol* 74: 3264–3272.
- Sundquist WI, Krüsslich HG (2012) HIV-1 assembly, budding, and maturation. *Cold Spring Harb Perspect Med* 2:a006924.
- Abbas W, Herberich G (2014) Plasma membrane signaling in HIV-1 infection. *Biochim Biophys Acta* 1838:1132–1142.
- Ono A (2010) Relationships between plasma membrane microdomains and HIV-1 assembly. *Biol Cell* 102:335–350.
- Crawford AR, et al. (1997) Hepatic secretion of phospholipid vesicles in the mouse critically depends on mdr2 or MDR3 P-glycoprotein expression. Visualization by electron microscopy. *J Clin Invest* 100:2562–2567.
- Crawford JM, et al. (1995) Imaging biliary lipid secretion in the rat: Ultrastructural evidence for vesiculation of the hepatocyte canalicular membrane. *J Lipid Res* 36: 2147–2163.
- McConnell RE, et al. (2009) The enterocyte microvillus is a vesicle-generating organelle. *J Cell Biol* 185:1285–1298.
- Tyska MJ, et al. (2005) Myosin-1a is critical for normal brush border structure and composition. *Mol Biol Cell* 16:2443–2457.
- Stendahl OI, Hartwig JH, Brotschi EA, Stosel TP (1980) Distribution of actin-binding protein and myosin in macrophages during spreading and phagocytosis. *J Cell Biol* 84: 215–224.
- Wang FS, Wolenski JS, Cheney RE, Mooseker MS, Jay DG (1996) Function of myosin-V in filopodial extension of neuronal growth cones. *Science* 273:660–663.
- Tuxworth RJ, et al. (2001) A role for myosin VII in dynamic cell adhesion. *Curr Biol* 11: 318–329.
- Berg JS, Cheney RE (2002) Myosin-X is an unconventional myosin that undergoes intrafilopodial motility. *Nat Cell Biol* 4:246–250.
- Bensinger SJ, et al. (2008) LXR signalling couples sterol metabolism to proliferation in the acquired immune response. *Cell* 134:97–111.
- Alfonso-Garcia A, Pfisterer SG, Riezman H, Ikonen E, Potma EO (2016) D38-cholesterol as a Raman active probe for imaging intracellular cholesterol storage. *J Biomed Opt* 21:61003.
- Souza CM, et al. (2011) A stable yeast strain efficiently producing cholesterol instead of ergosterol is functional for tryptophan uptake, but not weak organic acid resistance. *Metab Eng* 13:555–569.
- Shivapurkar R, Souza CM, Jeannerat D, Riezman H (2011) An efficient method for the production of isotopically enriched cholesterol for NMR. *J Lipid Res* 52:1062–1065.
- Brown AJ, Sun L, Feramisco JD, Brown MS, Goldstein JL (2002) Cholesterol addition to ER membranes alters conformation of SCAP, the SREBP escort protein that regulates cholesterol metabolism. *Mol Cell* 10:237–245.
- Collins JL, et al. (2002) Identification of a nonsteroidal liver X receptor agonist through parallel array synthesis of tertiary amines. *J Med Chem* 45:1963–1966.
- Gay A, Rye D, Radhakrishnan A (2015) Switch-like responses of two cholesterol sensors do not require protein oligomerization in membranes. *Biophys J* 108:1459–1469.
- He C, Fong LG, Young SG, Jiang H (2017) NanoSIMS imaging: An approach for visualizing and quantifying lipids in cells and tissues. *J Invest Med* 65:669–672.

Chapter 6

Release of Cholesterol-Rich Particles from the Macrophage

Plasma Membrane

Release of cholesterol-rich particles from the plasma membrane of macrophages

Xuchen Hu¹, Thomas A. Weston¹, Cuiwen He¹, Rachel S. Jung¹, Patrick J. Heizer¹, Brian D. Young³, Yiping Tu¹, Howard Riezman⁴, Peter Tontonoz⁵, James A. Wohlschlegel³, Haibo Jiang^{1,6}, Loren G. Fong^{1,‡}, and Stephen G. Young^{1,2,‡}

Departments of ¹Medicine and ²Human Genetics, David Geffen School of Medicine, University of California, Los Angeles, CA 90095; ³Department of Biological Chemistry, University of California, Los Angeles, CA, 90095; ⁴Department of Biochemistry, National Centre of Competence in Research in Chemical Biology, University of Geneva, 1205 Geneva, Switzerland; ⁵Department of Pathology and Laboratory Medicine, University of California, Los Angeles, CA 90095; ⁶School of Molecular Sciences, University of Western Australia, 6009 Perth, WA, Australia

‡Address correspondence to Stephen G. Young or Loren G. Fong, University of California, Los Angeles, 4506 Gonda Bldg., 695 Charles E. Young Dr. South, Los Angeles, CA 90095. Tel: (310) 825-4422; Fax: (310) 206-0865; E-mail: lfong@mednet.ucla.edu, sgyoung@mednet.ucla.edu

Conflict of Interest: The authors have declared that no conflict of interest exists.

Abstract

Cultured mouse peritoneal macrophages release large numbers of cholesterol-rich particles onto the surrounding substrate. Scanning electron microscopy (SEM) revealed that 30–40-nm vesicular particles bud from the plasma membrane, but the mechanism underlying this process was not clear. One possibility was that particles are released by outward ballooning of lipid microdomains from the plasma membrane; another is that pieces of the plasma membrane are torn away and left behind during movement of macrophage filopodia and lamellipodia. In favor of the latter possibility, we found that particles are enriched in focal adhesion complex proteins. Also, we observed, by live-cell imaging and SEM, that particles are released during the projection and retraction of lamellipodia and filopodia and that particle release is abolished by inhibiting cell movement (either by depolymerizing actin with latrunculin A or inhibiting myosin II with blebbistatin). By confocal microscopy and NanoSIMS imaging, the particles released onto the substrate are enriched in “accessible cholesterol” (a mobile pool of cholesterol that can be detected with the modified cytolysin ALO-D4) and depleted in sphingolipid-sequestered cholesterol (detectable with the cytolysin OlyA). The release of free cholesterol-rich particles during macrophage movement could contribute to the extracellular accumulation of cholesterol in atherosclerotic plaques.

Keywords: accessible cholesterol, NanoSIMS, focal adhesions, cholesterol efflux

Introduction

A key function of macrophages is to engulf and digest cellular debris. The cholesterol in the debris can be esterified and stored in cytosolic lipid droplets (1), thereby avoiding toxicity from free cholesterol overload, but macrophages must ultimately dispose of the surplus cholesterol. This process is generally referred to as “cholesterol efflux” (2–5). One mechanism for cholesterol efflux involves moving plasma membrane phospholipids and free cholesterol to high density lipoprotein acceptors (HDL), a process that depends on ABC transporters (2–4, 6–8). A deficiency of ABCA1 impedes with cholesterol efflux by macrophages, resulting in “macrophage foam cells” containing numerous cholesterol ester–rich cytosolic droplets (9–12). Another potential mechanism for cholesterol efflux is the direct release of cholesterol–rich particles from the plasma membrane. Using a cholesterol-specific monoclonal antibody and immunocytochemical approaches, the laboratory of Howard Kruth showed that cultured human monocyte–derived macrophages release “cholesterol microdomains” onto the surrounding substrate (13–17). The release of these microdomains was impaired by reduced expression of ABC transporters (13, 14, 16, 17). Recently, He and coworkers demonstrated, by scanning electron microscopy (SEM), that large numbers of ~30-nm vesicular particles are released from the plasma membrane of the filopodia and lamellipodia of primary mouse macrophages and a mouse macrophage cell line (18). The particles were released directly from the plasma membrane onto the surrounding substrate in a process that morphologically resembles “plasma membrane budding.” The particles were enriched in “accessible cholesterol” (18), a mobile pool of plasma membrane cholesterol that can be detected by ALO-D4, a modified cholesterol-binding cytolysin (19). The accessible cholesterol content of the particles could be increased by loading macrophages with cholesterol or by treating the cells with a liver X receptor agonist (18). The cholesterol content of macrophages as well as the particles on the surrounding substrate could be depleted by an overnight incubation with HDL (18).

The electron microscopy studies by He and coworkers were instructive because they revealed, at high resolution, the deposition of plasma membrane–derived particles onto the substrate around

macrophages. However, the mechanism for particle release was unclear. One possibility was that particle budding is actively driven by the entry of cholesterol into a plasma membrane microdomain, causing outward ballooning of the microdomain and ultimately to the release of a lipid-rich particle. A second possibility posed by He and coworkers (18) was that the particles represent pieces of the plasma membrane that were tightly affixed to the underlying substrate and then were “torn away and left behind” during the movement of macrophage filopodia and lamellipodia. According to this scenario, the particles would presumably contain plasma membrane lipids as well as a variety of plasma membrane-associated proteins.

In the current study, we used live-cell microscopy and scanning electron microscopy to examine the mechanism for the release of particles from the macrophage plasma membrane. We also analyzed the protein content of particles. Finally, we used two different cholesterol-binding cytolysins (one specific for accessible cholesterol and the other for sphingomyelin-sequestered cholesterol), along with fluorescence microscopy and NanoSIMS imaging, to characterize the cholesterol pools in the plasma membrane-derived particles surrounding macrophages.

Results

Macrophages release plasma membrane–derived particles during movement of filopodia and lamellipodia

Mouse peritoneal macrophages, when plated in culture, release numerous vesicular particles onto the surrounding substrate (18). In the current studies, we again observed, by SEM, that particles are released from macrophage filopodia and lamellipodia by a process that morphologically resembles budding (Figure 1). Because the budding particles adhere to the underlying substrate, we imagined that the particles might simply be pieces of the plasma membrane that are torn away and left behind during movement of filopodia and lamellipodia. To explore this idea, we plated thioglycollate-elicited mouse peritoneal macrophages onto gridded glass bottom MatTek dishes and then recorded images of cells by live-cell light microscopy, allowing us to document the projection and retraction of filopodia/lamellipodia. The same cells were then imaged by SEM. By SEM, we observed lawns of 30–40-nm particles on the substrate surrounding macrophages, often located primarily on one pole of the cell. The lawns of particles were invariably located in regions where we had observed (by live cell imaging) the extension and retraction of filopodia/lamellipodia (Figure 2, Supplemental video file 1–2).

To investigate if the extension and retraction of filopodia/lamellipodia is essential for particle release, cell movement was blocked by treating macrophages with an actin depolymerizing agent (latrunculin A, 5 μ M) or a myosin II inhibitor (blebbistatin, 30 μ M). Live cell imaging showed that macrophages treated with either drug were unable to extend their filopodia (Supplement video file 3–8).

One group of macrophages was incubated with latrunculin A or blebbistatin in macrophage medium containing 10% FBS for 1 h in suspension (“pre-treatment”), then plated onto poly-D-lysine–coated silicon wafers and incubated with the drugs overnight (Figure 3). Both latrunculin A and blebbistatin abolished particle release (Figure 3). A second group was plated and allowed to adhere for 1 h before adding the drugs (“post-adherence”) (Figure 3). In the latrunculin A–treated

cells, we observed a “ring” of particles around the cell, left behind on the substrate as the membrane retracted (due to the actin depolymerization) (Figure 3A). Adding blebbistatin after the cells had adhered eliminated particle release (Figure 3B). Cells treated with vehicle alone (DMSO) released large numbers of particles onto substrate (Figure 3). As an additional control, macrophages that had been incubated with the drugs overnight were washed and then incubated for an additional 18 h in the absence of drugs. The morphology of those cells returned to normal and the release of particles resumed (Figure 3).

Macrophage particles contain plasma membrane proteins and are enriched in proteins related to focal adhesions

An earlier study revealed that the particles released by [¹³C]cholesterol-loaded macrophages contained [¹³C]cholesterol (18), consistent with high levels of cholesterol in plasma membrane lipids. However, given that the particles are derived from the plasma membrane, we suspected that they would also contain proteins. Two lines of experimentation lended support for this idea. First, we biotinylated the cell-surface proteins of macrophages in solution with sulfo-NHS-SS-biotin and then plated the macrophages onto coverslips for immunocytochemistry and SEM analyses. By super resolution STED microscopy, the lawn of particles outside of macrophages was readily bound with fluorescently labeled streptavidin, colocalizing with fluorescently labeled ALO-D4 (which binds to the accessible pool of cholesterol) (Figure 4). Also, by SEM, we observed binding of streptavidin-conjugated 40-nm gold nanoparticles to macrophage-derived particles outside of the cell (Figure 5). No gold particles were observed in macrophages that were not biotinylated (Figure 5). Second, by NanoSIMS, the lawn of particles outside of macrophages contained ³²S, which is found in all cellular proteins (Figure 6). In light of those observations, we prepared particles and plasma membrane preparations from biotinylated RAW 264.7 mouse macrophages (as described in the *Methods*) and then performed shotgun proteomics studies. By negative staining transmission electron microscopy (TEM), the sizes of particles in the particle preparations resembled those in the SEM images (Figure 7). Not surprisingly, TEMs of plasma membrane

preparations revealed aggregates of membranous material (Figure 7B). Shotgun proteomic studies on three independent particle preparations showed that they were enriched in proteins of focal adhesions and cytoskeletal components (Figure 8A–B). When we confined our analyses to the top 75th percentile of proteins by spectral count, we identified 653 proteins from the particle fraction and 715 proteins from the plasma membrane fraction, with 502 proteins present in both fractions (Figure 8C). When these proteins were annotated by Gene Ontology (GO) cellular components 2018, the particles were enriched in focal adhesion proteins (Figure 8A). The top 15 focal adhesion related proteins, as annotated by gene ontology, were abundant in both the particle fraction and the plasma membrane fraction (Figure 8D), but the majority were relatively more enriched in particles (Figure 8D).

Inhibition of focal adhesion disassembly increases macrophage particle release

Focal adhesions are macromolecular assemblies that link the actin cytoskeleton within cells to the extracellular substrate. Given the presence of focal adhesion proteins and cytoskeletal proteins in vesicular particles, we presume that these particles are released when focal adhesions complexes are torn away and left behind on the substrate during the movement of filopodia/lamellipodia. We further test this by treating peritoneal macrophages with two drugs that inhibited focal adhesion disassembly. Focal adhesion kinase (FAK) and clathrin have both been shown to be essential in disassembly of focal adhesions. Phosphorylation of Tyr397 of FAK is one of the first events that must occur in order to initiate the disassembly process, while clathrin-dependent endocytosis of integrin and focal adhesion proteins is a later step in the focal adhesion disassembly pathway. In macrophages treated with FAK inhibitor and clathrin inhibitor, we saw both an increased number of particles left behind outside of macrophages and an increased number of macrophages surrounded by lawns of particles compared to DMSO control (Supplemental Figure 1). Live cell microscopy showed that macrophages treated with these inhibitors retained their ability to move their filopodia and lamellipodia (Supplement video file 9–11). We also tested whether cholesterol content of macrophages has an effect on macrophage particle release. When we loaded the

macrophages with 50 $\mu\text{g}/\text{ml}$ of acLDL, we documented larger lawns of particles surrounding the macrophage compared to nonloaded macrophages (Supplemental Figure 2). This increase in particle number was associated with increased macrophage motion by live cell microscopy (Supplement video file 9, 12–13). When we treated acLDL loaded macrophages with FAK inhibitor, we observed an even larger increase in number of particles outside macrophages (Supplemental Figure 2).

Macrophage-derived particles are enriched in accessible cholesterol but not inaccessible cholesterol

To confirm that the particles left behind during macrophage filopodia and lamellipodia movement are the same lawn of particles enriched in ALO-D4, we performed correlative live cell, SEM, and NanoSIMS imaging. Indeed NanoSIMS imaging after [^{15}N]ALO-D4 binding revealed that these particles left behind during macrophage membrane movement were highly enriched in [^{15}N]ALO-D4 (Figure 9, Supplement video file 14–15). We next wondered if macrophage-derived particles were also enriched in other types of cholesterol. By taking advantage of another cytolysin (OlyA), which binds only to sphingomyelin-sequestered cholesterol, we performed super-resolution STED microscopy and correlative NanoSIMS imaging to determine if macrophage-derived particles were enriched in both accessible and sphingomyelin-sequestered cholesterol. STED imaging revealed that particles were highly enriched in accessible cholesterol (detected by fluorescently labeled ALO-D4) but not sphingomyelin-sequestered cholesterol (detected by fluorescently labeled OlyA) (Figure 10). STED microscopy using fluorescently labeled ALO-D4 and lysenin (which binds to sphingomyelin) showed a similar pattern of cholesterol distribution (Supplemental Figure 3). We found similar results with NanoSIMS imaging. [^{15}N]ALO-D4 bound preferentially to the lawn of particles outside of the cell while [^{13}C]OlyA bound strongly to areas at the edges of the macrophage plasma membrane (Figure 11, Supplemental Figure 4 and 7). Cells that were treated with FAK inhibitor did not alter this distribution of accessible and sphingomyelin-bound cholesterol (Supplemental Figure 5–7).

In a separate experiment, macrophages were treated with latrunculin A before performing STED microscopy. STED images revealed a similar binding of ALO-D4 and OlyA on the cell body in macrophages “pre-treated” with latrunculin A (Figure 12). There was no binding of ALO-D4 or OlyA to areas outside of the macrophage (Figure 12). In macrophages that were treated with latrunculin A “post-adherence”, we observed a “ring” of ALO-D4 signal outside of the macrophage, corresponding to the “ring” of particles observed previously by SEM. This “ring” was not detectable by OlyA (Figure 12).

Macrophages release cholesterol-rich particles on collagen

In most of our studies, macrophages were plated onto poly-D-lysine coated substrates. To determine if macrophages could release particles in a more physiologic condition, we plated macrophages onto glass coverslips that were coated with a polymerized collagen IV matrix. Immunogold SEM of biotinylated macrophages revealed that macrophages indeed released particles onto collagen fibers, detectable by gold-conjugated streptavidin (Figure 13A). We also observed by STED microscopy that macrophage plated onto fluorescently labeled collagen IV matrix released particles onto the collagen, detectable by both fluorescently labeled ALO-D4 and streptavidin (Figure 13B).

Discussion

In the current study, we sought to better understand the genesis of macrophage-derived particles. By using correlative live cell light microscopy, SEM, and NanoSIMS imaging, we identified that macrophages constantly project and retract their filopodia and lamellipodia, leaving behind accessible cholesterol-rich particles in the process. Using scanning electron microscopy, we documented that macrophages immobilized by treatment with an actin depolymerizing agent (latrunculin A) or myosin II (blebbistatin) released no particles onto the surrounding substrate. Lack of particle release during latrunculin A and blebbistatin treatments suggest that movement is required for particle release.

One crucial issue was whether these particles were simply “microdomains” of cholesterol left behind by the cell or whether they contain proteins and other lipids. STED microscopy and immunogold SEM studies on macrophages that had their surface membrane proteins biotinylated revealed that the particles released from these macrophages were detectable by streptavidin. Particles were also seen to have high amount of ^{32}S content. By isolating macrophage-derived particles and performing shotgun proteomics, we discovered that particles contained hundreds of proteins. Most of these proteins were also found in the plasma membrane preparation, consistent with our findings that particles are derived from the plasma membrane. There were also a few hundred proteins that were not present in the plasma membrane preparation. These proteins were generally categorized under granule or vesicle lumen, presumably proteins that came from the cytoplasm of the macrophage. Particles were highly enriched in proteins associated with focal adhesions and we hypothesized that particles form when areas of tight association between plasma membrane and substrate (focal adhesions) are left behind as the macrophage pulls away. Normally, most focal adhesions are recycled by an incompletely understood disassembly mechanism. Two of the proteins that are essential in the disassembly process are focal adhesion kinase (FAK) and clathrin. Drug inhibition of these proteins caused increase in particle release from macrophage, supporting the idea that particles are formed from tightly adherent membranes left behind.

Consistent with previous studies by He and coworkers (18), we showed that macrophage-derived particles were enriched in a pool of accessible cholesterol, detectable by ALO-D4. Radhakrishnan and coworkers recently demonstrated that the cytolysin, OlyA, binds to a pool of sphingomyelin-bound cholesterol on the plasma membrane (20). Our studies revealed that particles released by macrophages were not enriched in OlyA. In fact, OlyA bound preferentially to actin cytoskeleton rich areas at the edges of the plasma membrane. We do not completely understand why macrophage-derived particles are highly enriched in accessible cholesterol but not in sphingomyelin-sequestered cholesterol. Several studies have shown that actin filaments and other cytoskeletal proteins directly attach to lipids in the plasma membrane. Raghupathy *et al.* showed that actin filaments are able to immobilize phosphatidylserine on the inner leaflet of the plasma membrane, which in turn couples to long acyl chain fatty acids and GPI anchored proteins on the outer leaflet (21). A separate study by Garg *et al.* (22) demonstrated that physisorbed actin filaments are able to perturb lipid–lipid phase separation in lipid domains containing phosphatidylserine and cholesterol, but not in domains containing phosphatidylglycerol and cholesterol. They suggested a concept of competing interactions between actin and phosphatidylserine lipids and between phosphatidylserine lipids and cholesterol (22). We believe that as the macrophage retracts its membranes, the actin filaments pull on the phosphatidylserine on the inner leaflet, resulting in pulling of the sphingomyelin in the outer leaflet and any cholesterol that was bound to the sphingomyelin (*i.e.*, inaccessible cholesterol). Cholesterol that is not tightly bound (*i.e.*, accessible cholesterol) is left behind in particles on the substrate.

One limitation of our study is that all experiments were performed using cultured macrophages. Whether macrophages release particles *in vivo* is unknown. However, the fact that macrophages are able to leave cholesterol-rich particles on a polymerized type IV collagen matrix suggest that particle release may occur by resident macrophages in tissues. Macrophages normally migrate on basement membranes and epithelium surfaces of vessel wall as they scavenge for senescent erythrocytes or as they migrate along the arterial intima in an atherosclerotic plaque. The

release of particles from lipid-laden macrophages as they migrate could be a mechanism for unloading cholesterol for reverse cholesterol transport. In addition, if macrophages are able to directly transfer particles onto another cell during cell contact, this would drastically increase the ability of macrophages to offload excess cholesterol to another cell.

Methods

Mouse peritoneal macrophages

Wild-type C57BL/6 mice were injected intraperitoneally with 1 ml of 3% Difco Fluid Thioglycollate Medium (Becton, Dickinson and Co.). Three days later, macrophages were harvested by peritoneal lavage with 10 ml of cold Dulbecco's Phosphate Buffered Saline (PBS). Cells were centrifuged at $400 \times g$ for 5 min at 4°C, incubated with red blood cell lysing buffer (Sigma), and washed 2 times with cold PBS. Macrophages were plated onto FBS-coated Petri dishes (8×10^6 cell per dish) and incubated overnight in Dulbecco's Minimal Eagle Medium supplemented with 10% fetal bovine serum (FBS), 1% sodium pyruvate, and 1% glutamine. The next day, macrophages were lifted by incubating with PBS containing 5 mM EDTA for 30 min at 4°C. For fluorescence microscopy, cells were plated onto glass coverslips in 24-well plates (75,000 cells/well). For SEM and NanoSIMS, cells were plated onto 0.5-cm² silicon wafers in 24-well plates (75,000 cells/well). For correlative live cell, scanning electron microscopy, and NanoSIMS, cells were plated onto 35-mm glass-bottom gridded Petri dishes (50,000 cell/dish; MatTek). All substrates were sterilized and coated with 0.1 mg/ml of poly-D-lysine.

Correlative light microscopy, scanning electron microscopy, and NanoSIMS imaging

35-mm glass-bottom gridded Petri dishes (MatTek) were sputter coated with ~ 4 nm of iridium using an ion-beam sputtering system (South Bay Technologies). Dishes were then washed 3 times for 5 min with 100% ethanol, air dried, and then coated with 0.1 mg/ml poly-D-lysine for overnight at 4°C. The next day, the dish is rinsed three times with sterile water, dried, and peritoneal macrophages were plated at 50,000 cells per dish. Live cell movies were captured using a Zeiss LSM800 confocal microscope with a Plan Apochromat 20×/0.80 objective. The incubation chamber was maintained at 37°C and 5% CO₂ using TempModule S1 (Zeiss) and CO₂ Module S1 (Zeiss). Cells were located using the grids inscribed onto the dishes and images were captured at 5 min intervals for 24 h. After 24 h, cells were washed with PBS/Ca/Mg containing 0.2% BSA three times for 2 min, then incubated with [¹⁵N]ALO-D4 (20 ug/ml in PBS + 0.2% BSA) for 2 h

at 4°C. In some experiments, [¹³C]OlyA (20 µg/ml in PBS + 0.2% BSA) was included in addition to the [¹⁵N]ALO-D4. Next, cells were washed three times for 2 min with PBS + 0.2% BSA, then fixed with 3.7% paraformaldehyde (Electron Microscopy Sciences) and 2.5% glutaraldehyde (Electron Microscopy Sciences) in 0.1M sodium cacodylate (pH 7.4) for 1 h on ice. Cells were washed with 0.1M sodium cacodylate (pH 7.4) three times for 5 min, then fixed with 2% OsO₄ (Electron Microscopy Sciences) in 0.1M sodium cacodylate on ice for 1 h. Samples were rinsed three times for 5 min with distilled water, dehydrated with increasing amounts of ethanol (30, 50, 70, 85, 95, and 100%; 3 × 10 min), and air dried. The glass coverslip attached to the bottom side of the Petri dish was removed using a Coverglass Removal Fluid (MatTek). The detached coverglass was placed onto a pin stub using Pelco colloidal silver (Ted Pella, Inc.), then coated with ~5 nm of iridium. Samples were imaged using a Zeiss Supra 40VP scanning electron microscope with a 3-KeV incident beam, using the grids on the coverglass to image the exact cells found by live cell imaging. Next, the cells were analyzed with a NanoSIMS 50L instrument (CAMECA). Samples were scanned with a 16-KeV ¹³³Cs⁺ beam, and secondary electrons (SEs) and secondary ions (¹²C⁻, ¹³C⁻, ¹²C¹⁴N⁻, ¹²C¹⁵N⁻, ³²S) were collected. A 50 × 50-µm region of the section was pre-sputtered with a ~1.2-nA beam current (primary aperture D1=1) to reach a dose of ~1 × 10¹⁷ ions/cm² to remove the iridium coating and implant ¹³³Cs⁺ to ensure a steady state of secondary ion release. A ~25 × 25-µm region was imaged with an ~3-pA beam current (primary aperture D1=2) and a dwell time of ~1 ms/pixel per frame for multiple frames. 512 × 512-pixel images were obtained. Images were prepared using the OpenMIMS plugin in ImageJ. ¹⁵N/¹⁴N and ¹³C/¹²C ratios images were used to identify areas of enrichment of [¹⁵N]ALO-D4 and [¹³C]OlyA.

Macrophage particle isolation

RAW 264.7 macrophages were plated onto ten T175 cell culture flasks (Corning) overnight in DMEM media containing 1% lipoprotein deficient serum (Alfa Aesar), 1% glutamine, and 1% sodium pyruvate. The next day, cells were washed two times with ice-cold PBS, then incubated for 30 min at 4°C in PBS containing 10 mM EZ-link Sulfo-NHS-SS-biotin (ThermoFisher). The

biotinylation reaction was stopped using Quenching Buffer (ThermoFisher). Cells were then washed 3 times for 5 min with PBS, lifted by incubated in PBS containing 5mM EDTA, and centrifuged at $1000 \times g$ for 5 min. The supernatant was filtered through a $0.22 \mu\text{m}$ filter and then incubated with 1 mL of NeutrAvidin beads (ThermoFisher) for 1 h at 4°C . The pellet was sonicated at low power (1.5) on ice five cycles of 45 sec on and 30 sec off. The pellet was added to PBS containing 250 mM sucrose and centrifuged at $3000 \times g$ for 10 min at 4°C . The supernatant was then incubated with 1 mL of NeutrAvidin beads for 1 h at 4°C . The beads containing the particles and cell membrane were then packed into 2 mL columns and the sample was allowed to flow through. The columns were then washed 3 times (4 mL each) with PBS containing 0.2% Triton X-100. Particles and cell membrane were eluted with $500 \mu\text{L}$ of PBS containing 50 mM dithiothreitol (DTT).

Negative stain transmission electron microscopy

A freshly glow-discharged copper grid that has been coated with formvar and carbon (EMS) is held with tweezers. $5 \mu\text{L}$ of PBS containing 50 mM DTT is pipetted directly onto the grid and immediately blotted off using filter paper (Whatman #1). Next, $5 \mu\text{L}$ of the solution containing the particles, plasma membrane, or PBS only control was added and allowed to adsorb for 1 min before blotting off. Then, $5 \mu\text{L}$ of 2% uranyl acetate is pipetted onto the grid and blotted off followed by another $5 \mu\text{L}$ of 2% uranyl acetate which is allowed to incubate for 1 min before being blotted dry. Grids were imaged using an FEI Tecnai T12 set to 120kV accelerating voltage equipped with a Gatan $2k \times 2k$ CCD detector.

Drug treatment of macrophages

Thioglycollate elicited peritoneal macrophages were plated onto FBS coated Petri dishes in DMEM medium containing 10% FBS, 1% glutamine, and 1% sodium pyruvate for overnight at 37°C . The next day, macrophages were lifted by incubation with PBS containing 5mM EDTA. Macrophages were then incubated for 1 h in suspension in macrophage growth medium containing $5 \mu\text{M}$ latrunculin A (Sigma), $30 \mu\text{M}$ blebbistatin (Sigma), $2 \mu\text{M}$ focal adhesion kinase (FAK)

inhibitor (Calbiochem) or 20 μ M clathrin inhibitor (Abcam). All drugs are diluted in DMSO. After 1 h, macrophages and drug media were plated onto poly-D-lysine coated substrates (silicon wafers or glass bottom MatTek dish for SEM and NanoSIMS imaging; glass coverslips for confocal microscopy) and incubated for 24 h. In some experiments, macrophages were plated first onto the poly-D-lysine coated substrate and allowed to adhere for 1 h in macrophage media without drugs. Media were then removed and cells were re-incubated in medium containing drugs for 24 h.

Shotgun Proteomics

Protein samples were resuspended in 8M urea in 100 mM Tris pH 8.5 and reduced, alkylated and digested by the sequential addition of lys-C and trypsin proteases as previously described (23, 24). The digested peptide solution was fractionated using strong-cation exchange and reverse phase chromatography then eluted directly into an LTQ-Orbitrap mass spectrometer (ThermoFisher). MS/MS spectra were collected and subsequently analyzed using the ProLuCID and DTASelect algorithms (25, 26). Database searches were performed against a mouse database. Protein and peptide identifications were further filtered with a false positive rate of less than 5% as estimated by a decoy database strategy. Normalized spectral abundance factor (NSAF) values were calculated as described (27). Analysis of other potential background contaminants was performed using CRAPome (28). Gene-annotation enrichment analysis was performed using Enrichr (29, 30).

Immunogold SEM of macrophage particles

Peritoneal macrophages were grown on FBS coated Petri dishes overnight in DMEM containing 10% FBS, 1% glutamine, and 1% sodium pyruvate. The next day, cells were washed and lifted by incubating in PBS containing 50 μ M EDTA for 30 min at 4°C, then washed 3 times with PBS. Cells were then incubated in PBS containing 0.25 mg/ml of Sulfo-NHS-SS-Biotin (ThermoFisher) for 20 min at 4°C. One ml of biotin solution was used per 1×10^6 cells. Cells were pelleted at 300 \times g and washed 3 times with 10 ml of PBS before plating onto glass-bottom MatTek dishes. Cells were incubated for 24 h in macrophage growth media. Next day, cells were washed three times with PBS, then fixed with 4% PFA and 0.1% glutaraldehyde in PBS for 1 h at 4°C. Cells were

washed three times for 5 min with PBS, blocked with PBS containing 5% donkey serum, 5% BSA, and 0.1% cold water fish skin gelatin (Electron Microscopy Sciences) for 1 h at room temperature, and then incubated with 40-nm gold-conjugated streptavidin (Abcam) for 2 h at 4°C. Samples were then washed three times 5 min with blocking buffer and then fixed with 1% glutaraldehyde for 10 min on ice. Cells were washed five times for 2 min with PBS, then fixed with 2% osmium tetroxide for 45 min on ice. Cells were then washed three times 5 min with ice-cold water and then dehydrated using a graded concentration of ethanol. Secondary electron and backscatter electron images were taken with a Zeiss Supra 40VP scanning electron microscope with a 5-KeV incident beam with a backscatter detector.

Immunocytochemistry of macrophage particles

Peritoneal macrophages were plated onto glass coverslips coated with 0.1 mg/ml poly-D-lysine. Cells were incubated for 24 h in DMEM containing 10% FBS, 1% glutamine, and 1% sodium pyruvate. In some experiments, the 10% FBS was replaced with 1% LPDS (Alfa Aesar) and 50 µg/ml of acLDL (Alfa Aesar). The next day, cells were washed three times for 5 min with PBS containing Ca²⁺ and Mg²⁺ (PBS/Ca/Mg) and 0.2% bovine serum albumin (BSA), then incubated for 2 h at 4°C with an Alexa Fluor 488-conjugated ALO-D4 and an Atto 647N-conjugated OlyA (20 µg/ml each diluted in PBS/Ca/Mg + 0.2% BSA). In some experiments, cells were incubated with Alexa Fluor 488-conjugated ALO-D4 (20 µg/ml) and Atto 647N-conjugated streptavidin (Sigma; 1/100). In other experiments, cells were incubated with Alexa Fluor 488-conjugated ALO-D4 (20 µg/ml) and mCherry-conjugated lysenin (10 µg/ml). Next, cells were washed three times 2 min with PBS/Ca/Mg containing 0.2% BSA, fixed with 3% PFA, and mounted onto glass slides with Prolong Gold mounting media (ThermoFisher). Images were taken with a Leica TCS SP8 STED 3X confocal microscope using a 100×/1.4 objective. The white light laser and depletion lasers were aligned prior to imaging. Alexa Fluor 488 images were obtained using a 488-nm white light laser and a 592-nm depletion laser. Atto 647N images were obtained using a 647-nm white light laser and a 775-nm depletion laser. Sequential scans were taken at 2048 × 2048 pixels.

Plating macrophage on collagen

Collagen IV from human placenta was directly labeled with an Alexa Fluor 647 fluorophore (ThermoFisher). Alexa Fluor 647–conjugated collagen IV (1mg/ml) was added onto the glass bottom MatTek dishes on ice. Dishes were incubated overnight at 37°C and 5% CO₂ to induce polymerization. The next day, excess collagen was removed and dishes were rinsed three times with PBS before fixing the collagen with 0.1% glutaraldehyde in PBS. Dishes were washed ten times for 6 min with PBS. Macrophage were then plated onto collagen IV coated dishes (50,000 cell/dish) in macrophage growth medium containing 10% FBS for 24 h. The next day, cells were either incubated with gold-conjugated streptavidin for SEM or Alexa Fluor 568–conjugated streptavidin and Alexa Fluor 488–conjugated ALO-D4 for confocal microscopy (described above).

Statistics

Statistical analyses of data were performed with GraphPad Prism 7.0 software. All data are shown as the means ± standard deviations. Differences were assessed using a Student's *t*-test with Welch's correction.

Study approval

Animal housing and experimental protocols were approved by UCLA's Animal Research Committee. The animals were housed in an AAALAC (Association for Assessment and Accreditation of Laboratory Animal Care International)-approved facility and cared for according to guidelines established by UCLA's Animal Research Committee. The mice were fed a chow diet and housed in a barrier facility with a 12-h light-dark cycle.

Author contributions

XH performed experiments, analyzed the data, wrote the first draft of the manuscript, and edited the manuscript. TAW, CH, RSJ, BDY, PJH, YT, RE, and HJ performed experiments. JAW and HJ analyzed the data, edited the manuscript, and contributed to scientific discussions. HR and PT edited the manuscript and contributed to scientific discussions. SGY and LGF analyzed the data and wrote the manuscript.

Acknowledgments

This work was supported by grants from the NHLBI (HL090553, HL087228, HL125335), a Transatlantic Network Grant from the Leducq Foundation (12CVD04). Xuchen Hu was supported by a Ruth L. Kirschstein National Research Service Award (T32HL69766) and the UCLA Medical Scientist Training Program. Haibo Jiang was supported by an Australian Research Council Discovery Early Career Researcher Award and a Cancer Council Western Australia Early Career Investigator Grant.

References

1. Brown MS, Ho YK, & Goldstein JL (1980) The cholesteryl ester cycle in macrophage foam cells. Continual hydrolysis and re-esterification of cytoplasmic cholesteryl esters. *J. Biol. Chem.* 255:9344–9352.
2. Rosenson RS, *et al.* (2012) Cholesterol efflux and atheroprotection: advancing the concept of reverse cholesterol transport. *Circulation* 125(15):1905–1919.
3. Tall AR, Costet P, & Wang N (2002) Regulation and mechanisms of macrophage cholesterol efflux. *J Clin Invest* 110(7):899–904.
4. Rothblat GH & Phillips MC (2010) High-density lipoprotein heterogeneity and function in reverse cholesterol transport. *Curr Opin Lipidol* 21(3):229–238.
5. Adorni MP, *et al.* (2007) The roles of different pathways in the release of cholesterol from macrophages. *J Lipid Res* 48(11):2453–2462.
6. Yvan-Charvet L, Wang N, & Tall AR (2010) Role of HDL, ABCA1, and ABCG1 transporters in cholesterol efflux and immune responses. *Arterioscler Thromb Vasc Biol* 30(2):139–143.
7. Westerterp M, *et al.* (2014) ATP-binding cassette transporters, atherosclerosis, and inflammation. *Circ Res* 114(1):157–170.
8. Duong PT, *et al.* (2006) Characterization of nascent HDL particles and microparticles formed by ABCA1-mediated efflux of cellular lipids to apoA-I. *J Lipid Res* 47(4):832–843.
9. Brooks-Wilson A, *et al.* (1999) Mutations in *ABCI* in Tangier disease and familial high-density lipoprotein deficiency. *Nat Genet* 22:336–345.
10. Bodzioch M, *et al.* (1999) The gene encoding ATP-binding cassette transporter 1 is mutated in Tangier disease. *Nat Genet* 22:347–351.

11. Clee SM, *et al.* (2001) Common genetic variation in *ABCA1* is associated with altered lipoprotein levels and a modified risk for coronary artery disease. *Circulation* 103:1198–1205.
12. Rust S, *et al.* (1999) Tangier disease is caused by mutations in the gene encoding ATP-binding cassette transporter 1. *Nat. Genet.* 22:352–355.
13. Jin X, *et al.* (2016) ABCA1 (ATP-binding cassette transporter A1) mediates apoA-I (apolipoprotein A-I) and apoA-I mimetic peptide mobilization of extracellular cholesterol microdomains deposited by macrophages. *Arterioscler Thromb Vasc Biol* 36(12):2283–2291.
14. Freeman SR, *et al.* (2014) ABCG1-mediated generation of extracellular cholesterol microdomains. *J Lipid Res* 55(1):115–127.
15. Ong DS, *et al.* (2010) Extracellular cholesterol-rich microdomains generated by human macrophages and their potential function in reverse cholesterol transport. *J Lipid Res* 51(8):2303–2313.
16. Jin X, *et al.* (2015) ABCA1 contributes to macrophage deposition of extracellular cholesterol. *J Lipid Res* 56(9):1720–1726.
17. Jin X, *et al.* (2018) Macrophages shed excess cholesterol in unique extracellular structures containing cholesterol microdomains. *Arterioscler Thromb Vasc Biol* 38(7):1504–1518.
18. He C, *et al.* (2018) Macrophages release plasma membrane-derived particles rich in accessible cholesterol. *Proc Natl Acad Sci U S A* 115(36):E8499–E8508.
19. Gay A, Rye D, & Radhakrishnan A (2015) Switch-like responses of two cholesterol sensors do not require protein oligomerization in membranes. *Biophys J* 108(6):1459–1469.

20. Endapally S, *et al.* (2019) Molecular discrimination between two conformations of sphingomyelin in plasma membranes. *Cell* 176(5):1040–1053 e1017.
21. Raghupathy R, *et al.* (2015) Transbilayer lipid interactions mediate nanoclustering of lipid-anchored proteins. *Cell* 161(3):581–594.
22. Garg S, Tang JX, Ruhe J, & Naumann CA (2009) Actin-induced perturbation of PS lipid-cholesterol interaction: A possible mechanism of cytoskeleton-based regulation of membrane organization. *J Struct Biol* 168(1):11–20.
23. Kaiser P & Wohlschlegel J (2005) Identification of ubiquitination sites and determination of ubiquitin-chain architectures by mass spectrometry. *Methods Enzymol* 399:266–277.
24. Wohlschlegel JA (2009) Identification of SUMO-conjugated proteins and their SUMO attachment sites using proteomic mass spectrometry. *Methods Mol Biol* 497:33–49.
25. Xu T, *et al.* (2006) ProLuCID, a fast and sensitive tandem mass spectra-based protein identification program. *Mol Cell Proteom* 5(10):S174–S174.
26. Tabb DL, McDonald WH, & Yates JR, 3rd (2002) DTASelect and Contrast: tools for assembling and comparing protein identifications from shotgun proteomics. *J Proteome Res* 1(1):21–26.
27. Florens L, *et al.* (2006) Analyzing chromatin remodeling complexes using shotgun proteomics and normalized spectral abundance factors. *Methods* 40(4):303–311.
28. Mellacheruvu D, *et al.* (2013) The CRAPome: a contaminant repository for affinity purification-mass spectrometry data. *Nat Methods* 10(8):730–736.
29. Chen EY, *et al.* (2013) Enrichr: interactive and collaborative HTML5 gene list enrichment analysis tool. *Bmc Bioinformatics* 14.
30. Kuleshov MV, *et al.* (2016) Enrichr: a comprehensive gene set enrichment analysis web server 2016 update. *Nucleic Acids Research* 44(W1):W90–W97.

Figures and Figure Legends

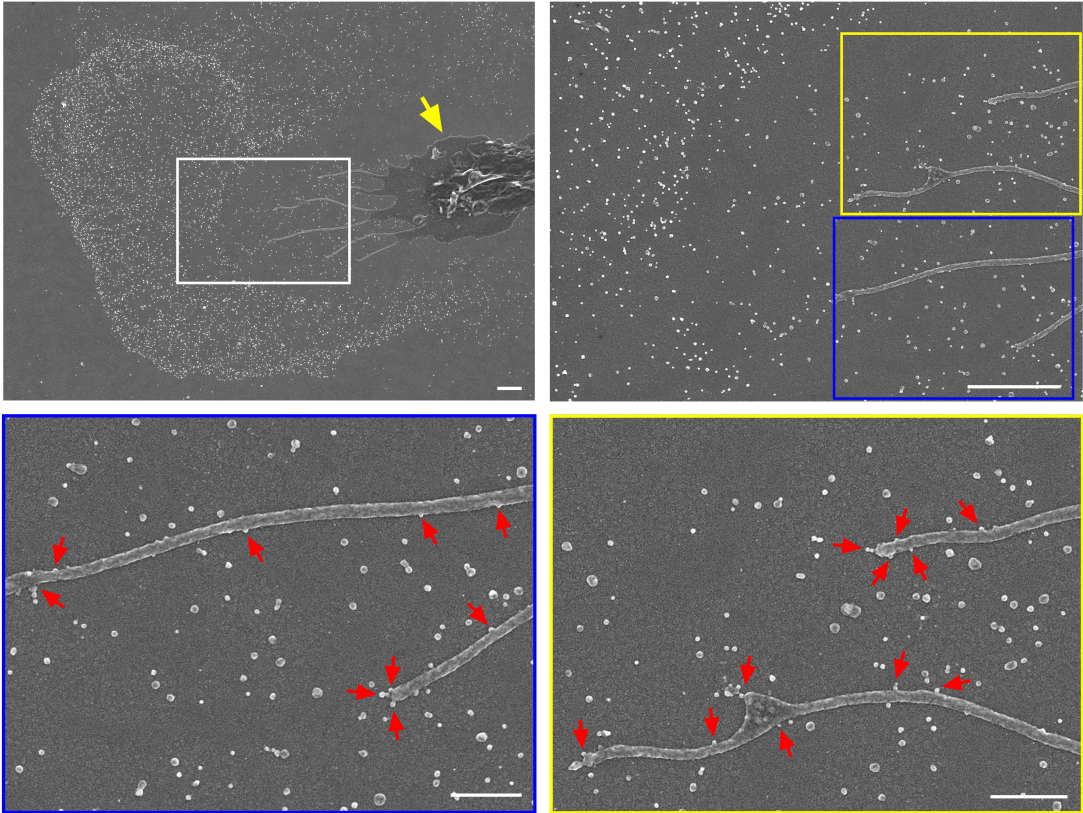


Figure 1: Macrophages release particles from the plasma membrane by a process that resembles budding. Upper left, scanning electron micrograph of a mouse peritoneal macrophage (yellow arrow), revealing a lawn of ~30-nm particles on the surrounding substrate. A higher magnification image of region in the white box is depicted in the image on the upper right. Higher magnification images of the regions in the *yellow* and *blue* boxes are shown below. Red arrows show the formation and release of particles from macrophage filopodia. Scale bar for the top two images, 2 μ m. Scale bar for the bottom two images, 500 nm.

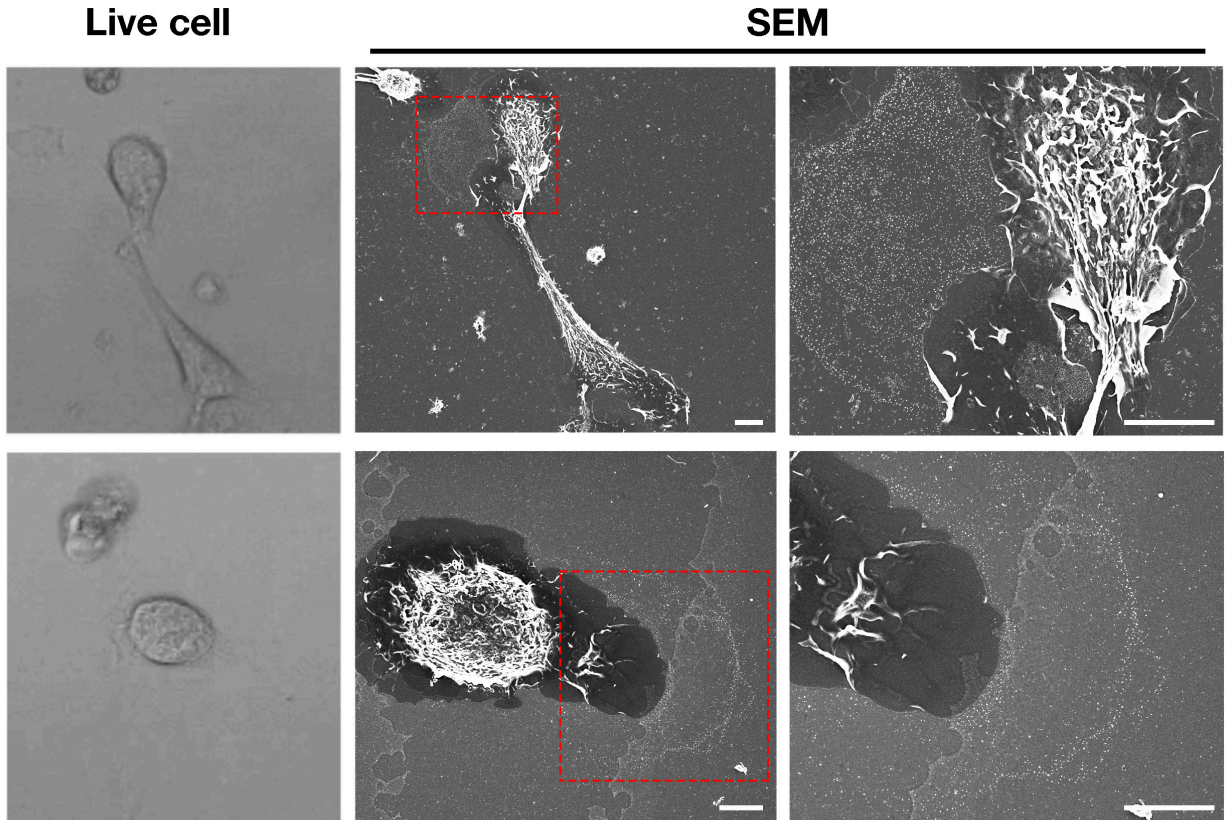


Figure 2: Macrophages release particles during movement (extension and retraction) of filopodia and lamellipodia. Correlative live-cell and scanning electron imaging show that movement of macrophage filopodia and lamellipodia is associated with the release of particles onto the substrate. Cells were plated onto poly-D-lysine-coated gridded glass-bottom Petri dishes, and movies were recorded for 24 h at 5-min intervals (Supplemental video files 1–2). White arrows in the movies point to the cell that was visualized by SEM, and the red arrow in the movies points to the region of the cell that was subsequently visualized by scanning electron microscopy (SEM). The “Live cell” image show the final frame of the movies. The imaging of cells by SEM made it possible to visualize particles that had been released onto the substrate. A higher magnification image of the region in the red box is shown on the right. Scale bar, 5 μm .

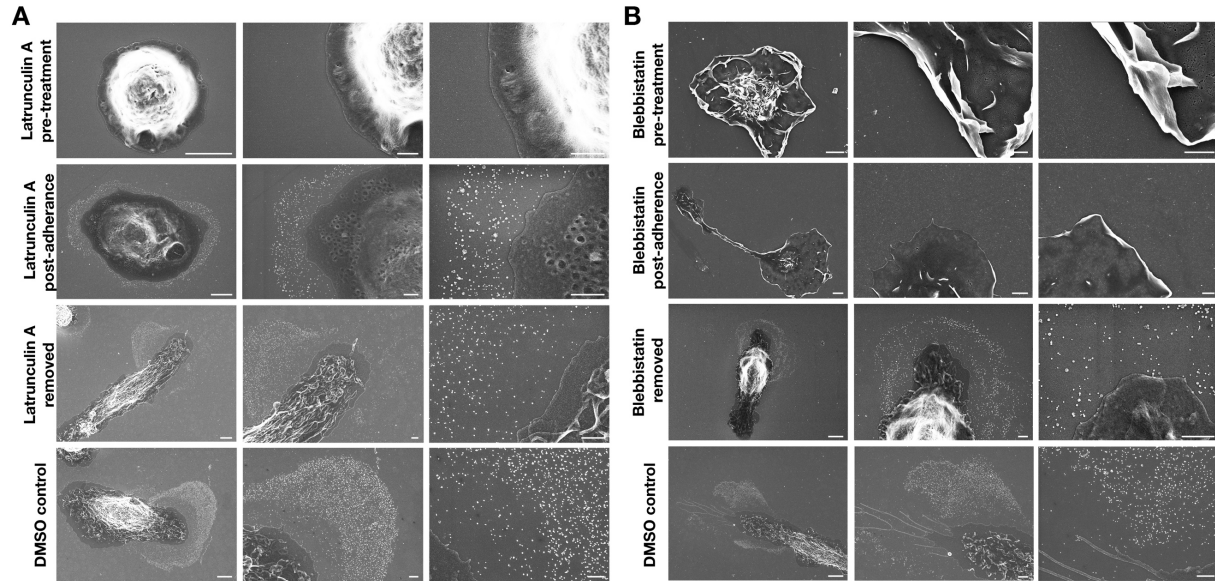


Figure 3. Inhibiting macrophage movement with latrunculin A or blebbistatin abolishes release of particles onto the surrounding substrate. Scanning electron micrographs of mouse peritoneal macrophages treated with latrunculin A (**A**) or blebbistatin (**B**), revealing an absence of particles on the surrounding substrate. Macrophages were treated with latrunculin A or blebbistatin overnight, with the treatments starting when the cells were in suspension 1 h prior to plating (pre-treatment) or starting 1 h after plating when the cells were adherent (post-adherence). Drugs were removed from some dishes on the following day, and cells were incubated for an additional 18 h in the absence of drugs. After removal of drugs, particles were deposited on the substrate. As a control, macrophages were treated with vehicle alone (DMSO control). Scale bars for images on the left in each panel are 4 μm . Scale bars for the images in the middle and right of each panel are 1 μm .

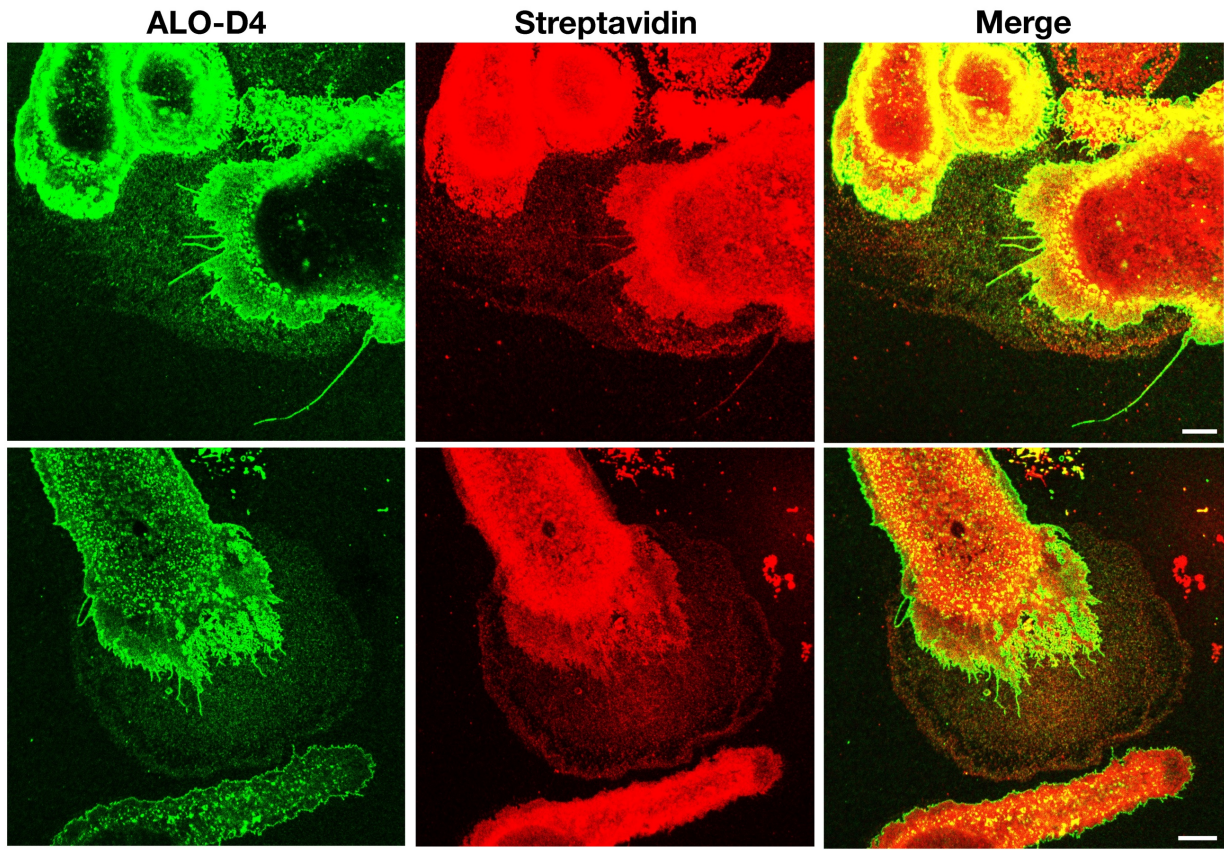


Figure 4. Particles released from macrophages are released from the plasma membrane and are enriched in accessible cholesterol. The plasma membrane proteins of mouse peritoneal macrophages were biotinylated with sulfo-NHS-SS-biotin. Next, the cells were plated onto glass coverslips and incubated overnight in macrophage growth medium containing 10% FBS. On the next day, the cells were incubated with Atto 647N–conjugated streptavidin (*red*) and Alexa Fluor 488–conjugated ALO-D4 (*green*). Cells were then fixed with 3% PFA and imaged with a super-resolution STED microscope. ALO-D4 and streptavidin bound to the cells as well as the lawn of vesicular particles on the substrate. Scale bar, 5 μm .

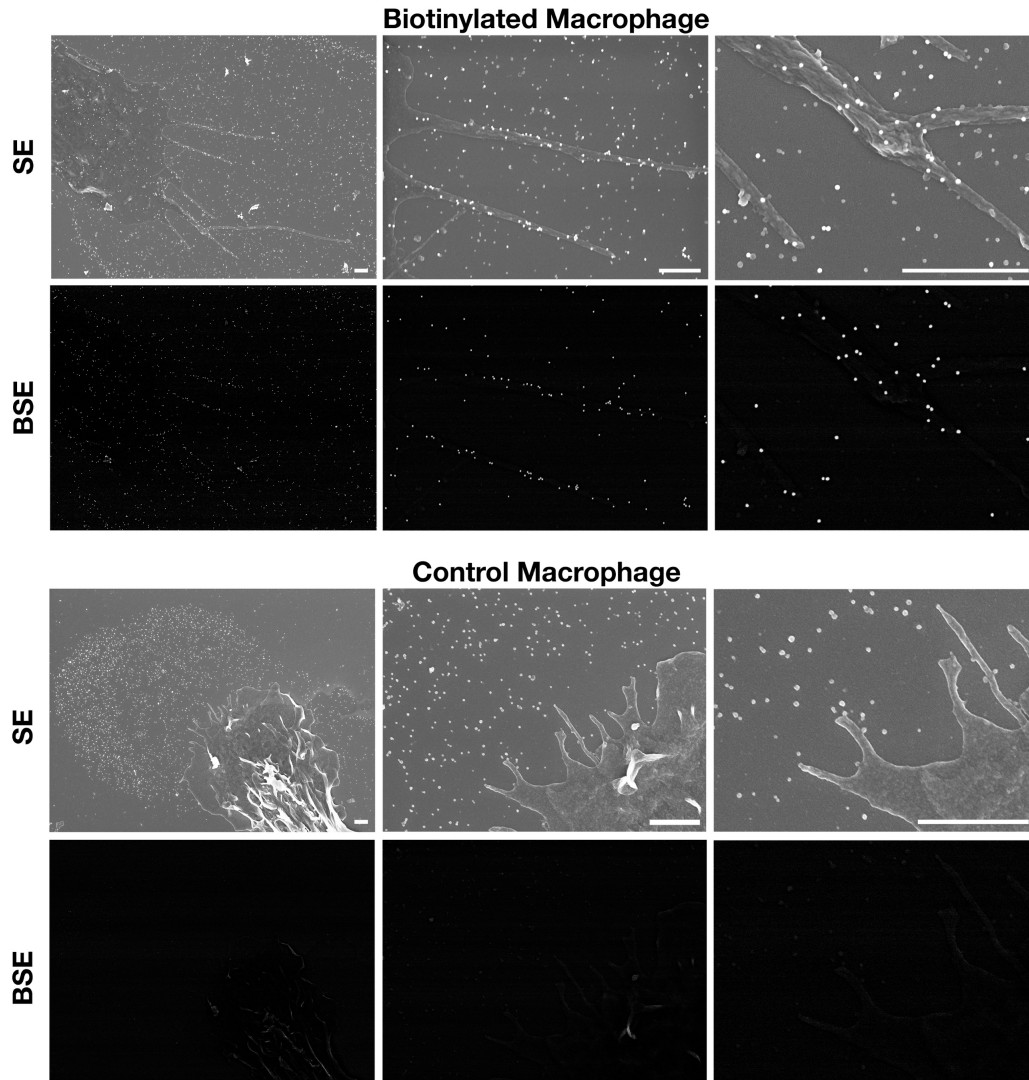


Figure 5. Visualization, by scanning EM, of particles released from the plasma membrane of macrophages. After biotinylating the plasma membrane of mouse peritoneal macrophages with sulfo-NHS-SS-biotin, cells were plated onto glass coverslips. On the following day, the cells were incubated with 40-nm gold-conjugated streptavidin. Cells were then fixed with 1% glutaraldehyde and processed for SEM. Secondary electron (SE) images revealed gold particles on the macrophage cell body, filopodia, and the plasma membrane-derived particles on the substrate. Backscatter secondary electron (BSE) images revealed colocalization of gold particles with the particles on substrate. As a control, we examined binding of the gold-conjugated streptavidin to macrophages that had not been biotinylated. Scale bar, 1 μm .

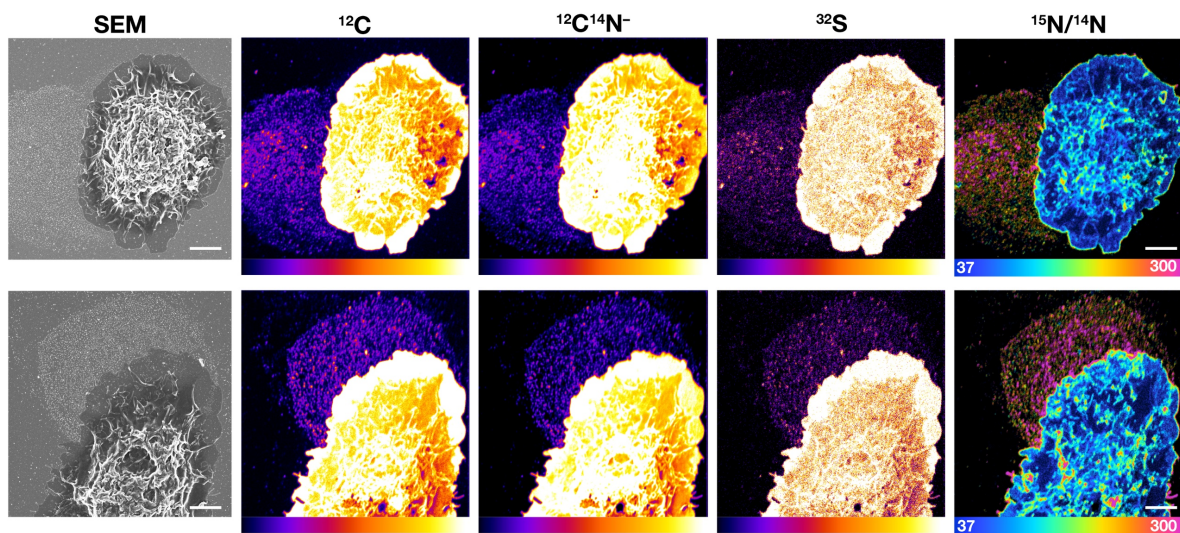


Figure 6. Correlative SEM and NanoSIMS imaging of macrophages and the plasma membrane-derived particles on the surrounding substrate. Mouse peritoneal macrophages were plated onto iridium and poly-D-lysine-coated gridded glass-bottom Petri dishes and incubated in medium containing 10% FBS for 24 h. Cells were then incubated with [^{15}N]ALO-D4 for 2 h. After recording SEM images, the same cells were imaged by NanoSIMS. Particles on the surrounding substrates were easily detectable with $^{12}\text{C}^-$, $^{12}\text{C}^{14}\text{N}^-$, and $^{32}\text{S}^-$ NanoSIMS images. Avid binding of [^{15}N]ALO-D4 to the lawn of particles was evident in a $^{15}\text{N}/^{14}\text{N}$ ratio image. Scale bar, 5 μm .

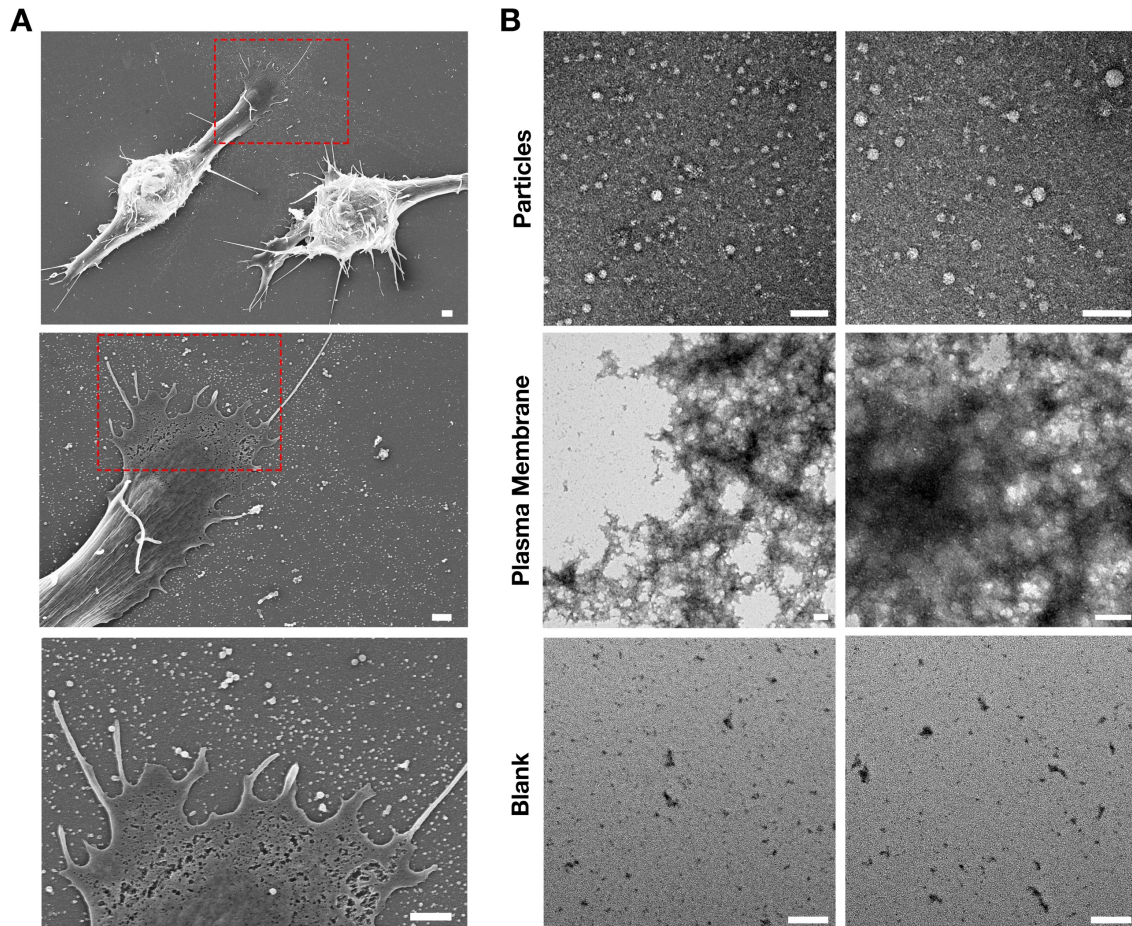


Figure 7. Isolation of particles released onto the substrate by RAW 264.7 macrophages. (A) RAW 264.7 macrophages were plated onto poly-D-lysine-coated silicon wafers. SEM images revealed large numbers of vesicular particles attached to the substrate surrounding macrophages. Higher magnification images of the boxed regions are shown below. Scale bar, 1 μm . (B) RAW macrophages were plated in tissue culture flasks, and both macrophages and macrophage-derived particles were biotinylated with sulfo-NHS-SS-biotin. The cells and the particles were released from the substrate with EDTA. The biotinylated particles along with the plasma membranes were separated by density gradient ultracentrifugation. Both the particle and plasma membrane fractions were captured on Neutravidin beads, washed, and then released from the beads with 50 mM DTT. Particle and plasma membrane fractions were placed on carbon/formar TEM grids, negatively stained with 2% uranyl acetate and visualized by transmission electron microscopy. Particles were 20–80 nm in diameter. Images of the plasma membrane fractions revealed aggregated membranous material. A blank grid, which was also subjected to negative staining, revealed an absence of particles or membranes. Scale bar, 100 nm.

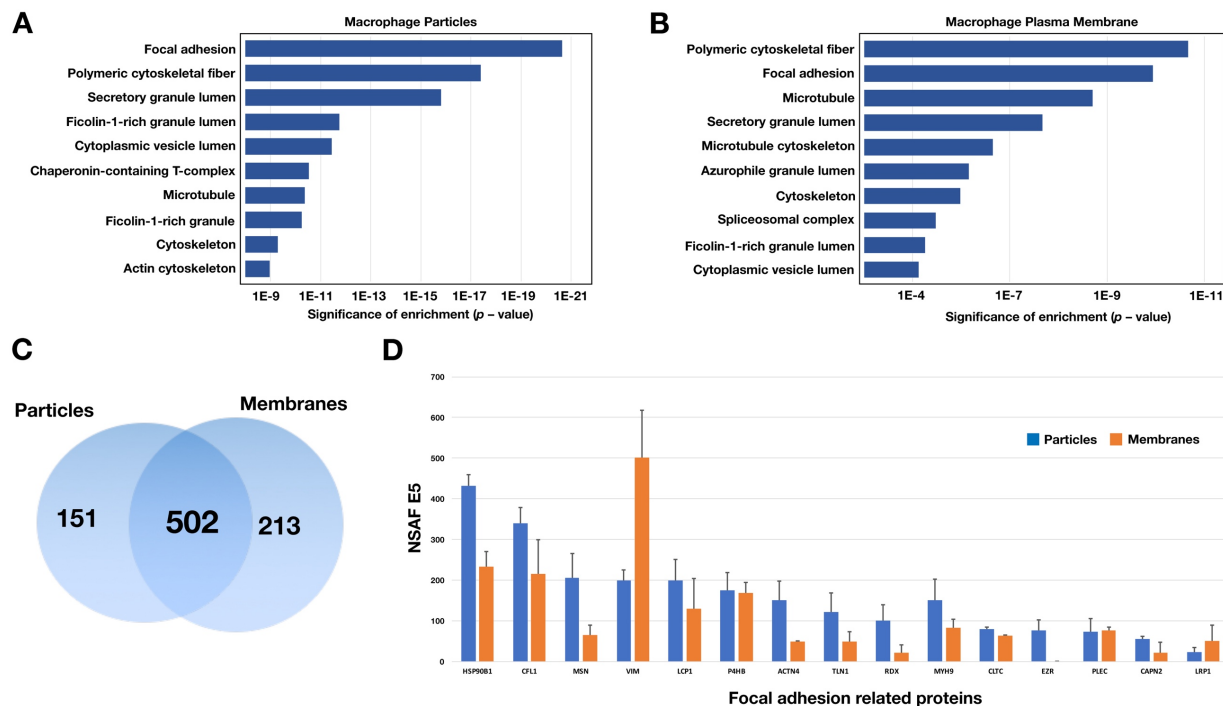


Figure 8. An enrichment in proteins of focal adhesion complexes in particles released by macrophages. The macrophage particles and plasma membrane fractions were analyzed by shotgun proteomics. The most abundant proteins (the top 75th percentile of proteins by spectral counts) were analyzed by Enrichr and categorized by GO Cellular Components 2018. **(A)** Analysis of proteins in macrophage particles ($n = 653$) by GO categories. **(B)** Analysis of proteins in macrophage plasma membranes ($n = 715$) by GO categories. The top 10 cellular components were ordered by level of statistical significance. **(C)** Venn diagram depicting the number of proteins in the particle fraction only, the plasma membrane fraction only, or both. **(D)** Bar graph showing the top 15 focal adhesion complex-related proteins by the normalized spectral abundance factor (NSAF) multiplied by 10,000. The particle fraction is shown in *blue*, and the plasma membrane fraction is shown in *orange*. The bar graph shows the mean \pm SD for three independent proteomic studies.

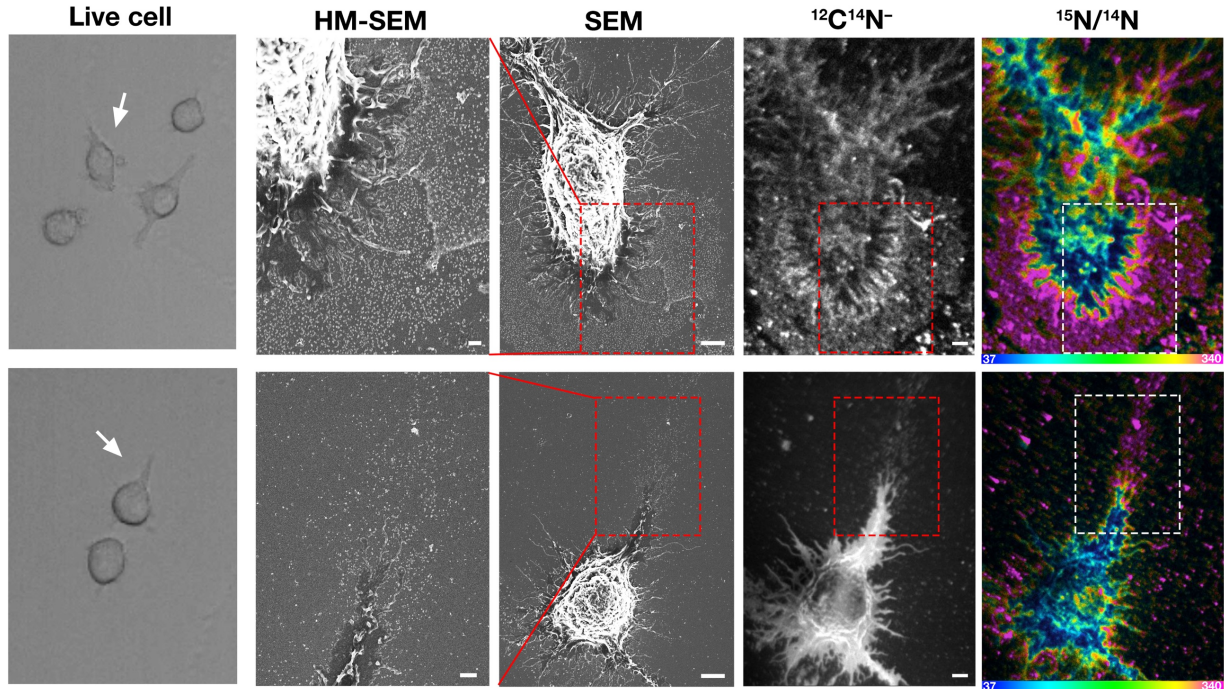


Figure 9. Correlative live-cell, scanning EM, and NanoSIMS imaging, revealing that the particles released onto the substrate during the movement of filopodia are enriched in accessible cholesterol. RAW 264.7 macrophages were plated onto iridium- and poly-D-lysine-coated gridded glass bottom Petri dishes. Movies were recorded for 24 h at 5-min intervals. “Live cell” images show the final frame of movies (Supplemental files 14–15); white arrows point the the cell that was subsequently visualized by SEM and NanoSIMS. After live-cell imaging, cells were incubated with [^{15}N]ALO-D4 (a modified cytolysin that binds to “accessible cholesterol”). The same cells that were imaged by video microscopy were imaged by SEM to visualize particles and subsequently by NanoSIMS to visualize [^{15}N]ALO-D4 binding. The particles left behind on the substrate during movement of lamellipodia and filopodia bound [^{15}N]ALO-D4 avidly and were therefore enriched in “accessible” cholesterol. $^{12}\text{C}^{14}\text{N}^-$ NanoSIMS images were used to visualize cell morphology; the $^{15}\text{N}/^{14}\text{N}$ images depict ^{15}N enrichment (*i.e.*, binding of [^{15}N]ALO-D4). The boxed region of the SEM and NanoSIMS images is shown at higher magnification in the HM-SEM image. Scale bar, 500 nm.

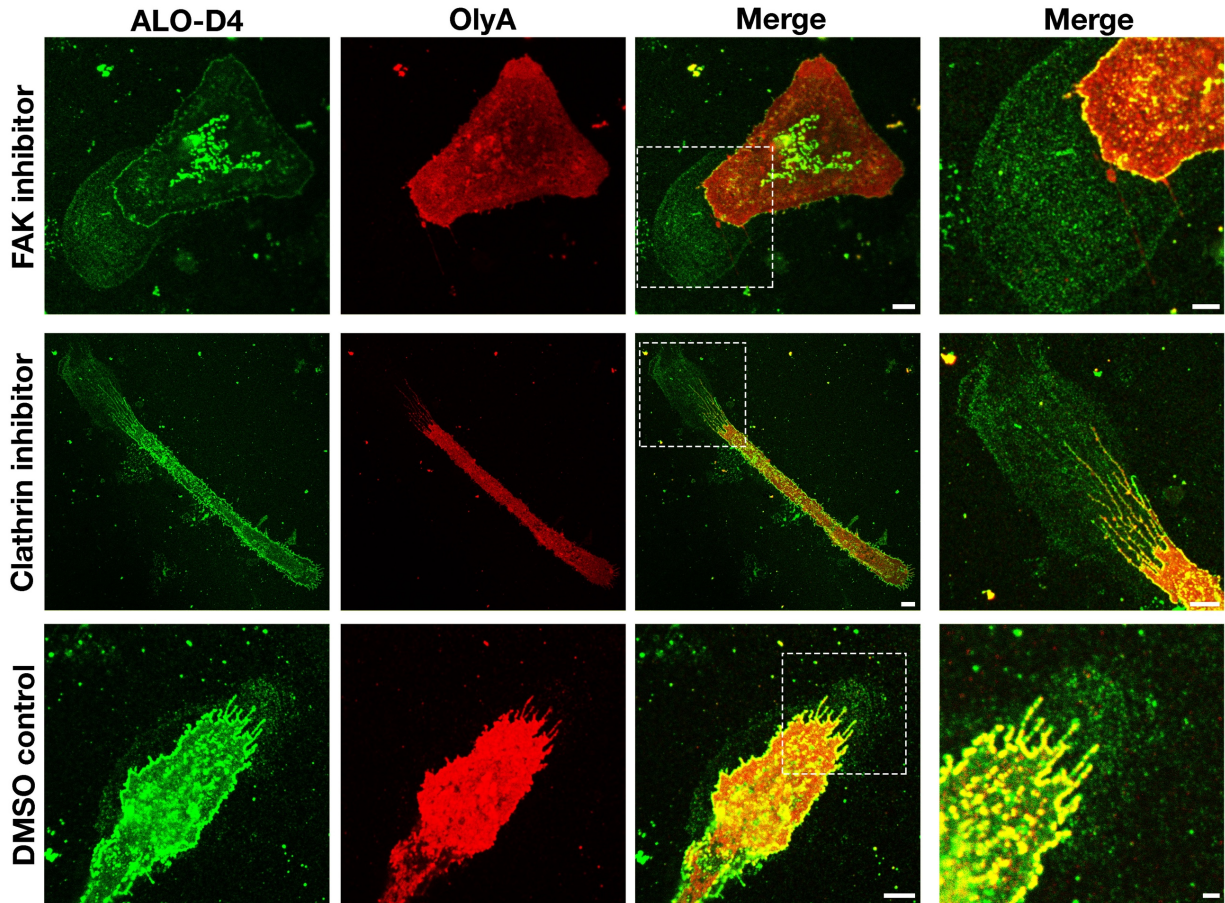


Figure 10. Particles released by macrophages onto the surrounding substrate are enriched in accessible cholesterol but not sphingomyelin-bound cholesterol. Peritoneal macrophages were plated onto poly-D-lysine-coated glass coverslips and incubated overnight in medium containing 10% FBS and either an FAK inhibitor, a clathrin inhibitor, or DMSO alone (DMSO control). On the next day, the cells were incubated with Alexa Fluor 488-conjugated ALO-D4, a marker of accessible cholesterol (*green*) and Atto 647N-conjugated OlyA, which binds to sphingomyelin-bound cholesterol (*red*) (both at 20 mg/ml). Cells were fixed with 3% PFA and imaged with a super-resolution STED microscope. The lawn of particles surrounding macrophages was easily detectable with ALO-D4 but not with OlyA. Scale bar, 5 μm . A higher magnification image of the boxed region is shown on the right. Scale bar, 2 μm .

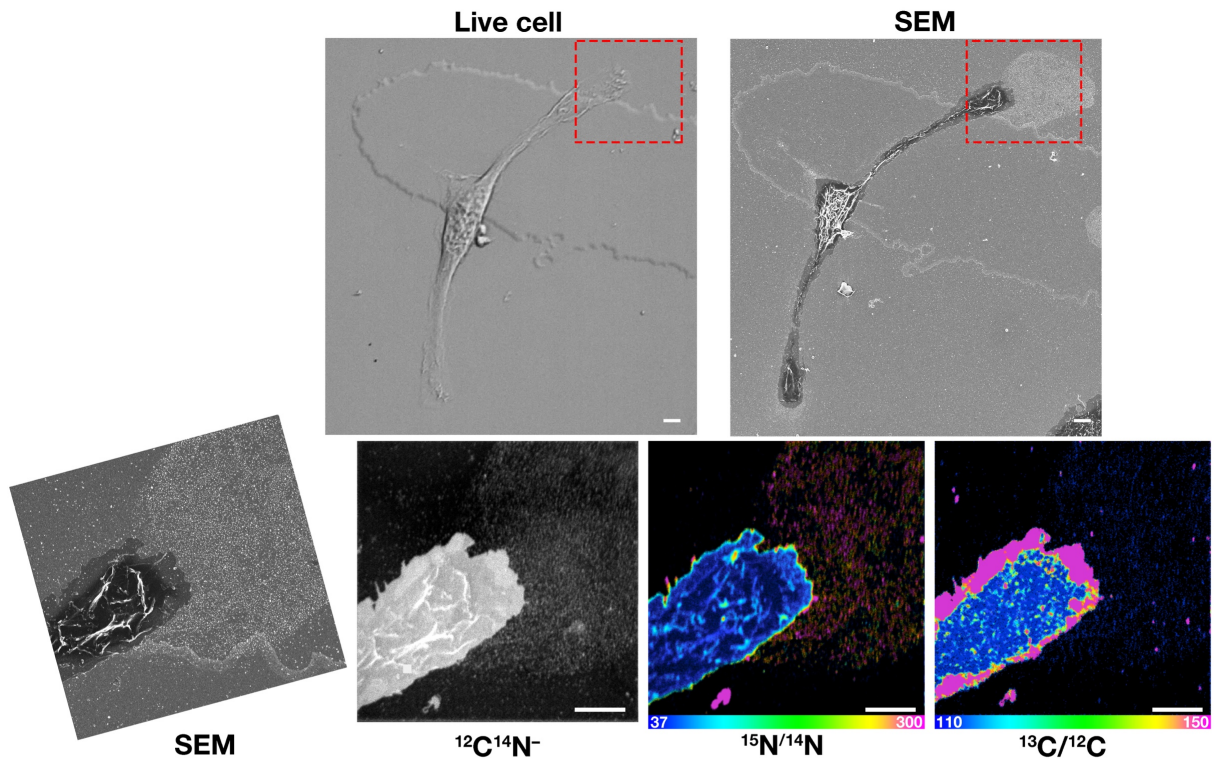


Figure 11. Correlative live-cell, SEM, and NanoSIMS imaging, demonstrating that particles left on the substrate during movement of filopodia and lamellipodia are enriched in accessible cholesterol but not sphingolipid-bound cholesterol. Mouse peritoneal macrophages were plated onto iridium and poly-D-lysine-coated gridded glass-bottom Petri dishes, and movies of cell movement were recorded for 24 h at 5-min intervals. The “Live cell” image shows the final frame of the movies (Supplemental File X). After the live-cell imaging, the cells were then incubated with [^{15}N]ALO-D4 (which binds to accessible cholesterol) and [^{13}C]OlyA (which binds to sphingomyelin-bound cholesterol). The cells were then imaged by SEM to visualize particles and subsequently by NanoSIMS to visualize [^{15}N]ALO-D4 and [^{13}C]OlyA binding. The particles left behind on the substrate were enriched in accessible cholesterol but not sphingomyelin-bound cholesterol. $^{12}\text{C}^{14}\text{N}^-$ images were useful for cell morphology. $^{15}\text{N}/^{14}\text{N}$ images show binding of [^{15}N]ALO-D4; $^{13}\text{C}/^{12}\text{C}$ images show binding of [^{13}C]OlyA. Scale bar, 5 μm .

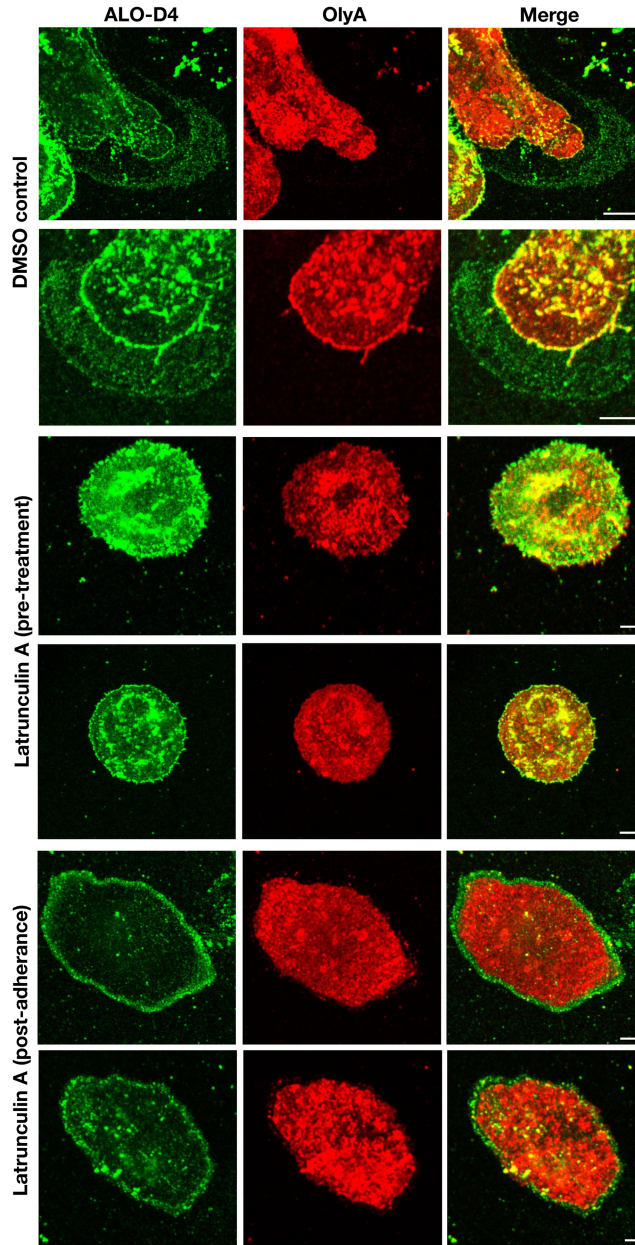


Figure 12. Incubating macrophages with latrunculin A alters the distribution of ALO-D4 on mouse peritoneal macrophages. Peritoneal macrophages were plated onto poly-D-lysine-coated glass coverslips and incubated with latrunculin A or vehicle alone (DMSO control). The incubation of latrunculin A was initiated either 1 h prior to plating the cells (pre-treatment) or was added to the cells 1 h after the cells had been plated and had adhered to the substrate (post-adherence). On the next day, cells were incubated with Alexa Fluor 488-conjugated ALO-D4 and Atto 647N-conjugated OlyA (20 mg/ml each). Cells were then fixed with 3% PFA and imaged with a STED microscope. The lawn of particles surrounding macrophages could be visualized with ALO-D4 but not OlyA. In the post-adherence cells, a circumferential ring of ALO-D4 binding was detected, reflecting ALO-D4 binding to particles released onto the substrate during retraction of the macrophage cell body. Scale bar, 5 μ m.

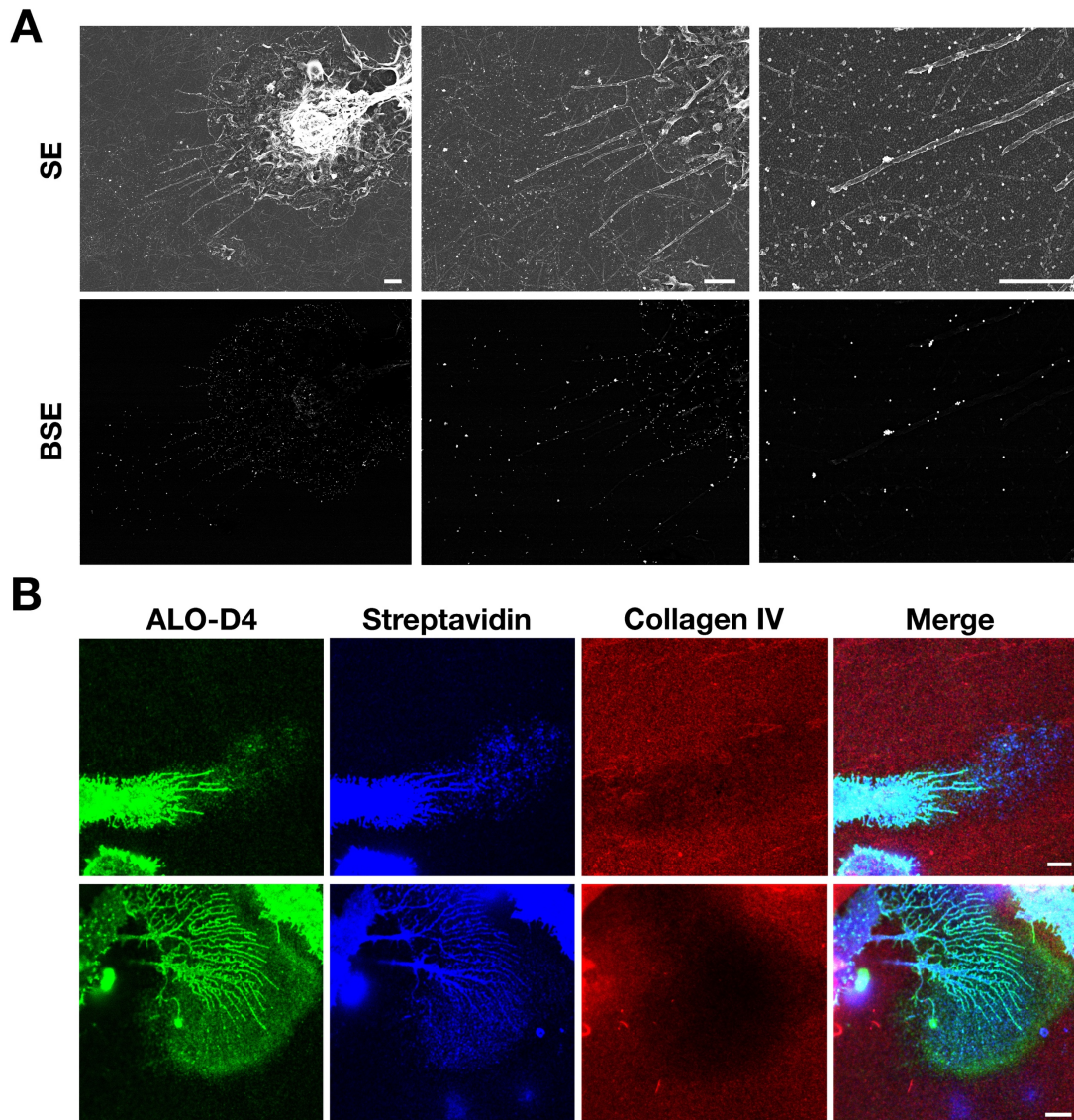


Figure 13. Macrophages release accessible cholesterol-rich particles onto a polymerized collagen IV matrix. The surface of peritoneal macrophages was biotinylated with sulfo-NHS-SS-biotin. The cells were then plated onto glass-bottom Petri dishes coated with polymerized Alexa Fluor 647-conjugated collagen IV. (A) SEM images showing binding of 40-nm gold-conjugated streptavidin to macrophages and macrophage-derived particles on the collagen substrate. Secondary electron (SE) images show plasma membrane-derived particles on the collagen fibers and the binding of gold particles to macrophage cell body, the filopodia, and plasma membrane-derived particles. Backscatter secondary electron (BSE) images were useful for defining the binding of gold nanoparticles. Scale bar, 2 μ m. (B) Cells were incubated with Alexa Fluor 488-conjugated ALO-D4 and Alexa Fluor 568-conjugated streptavidin and then fixed with 3% PFA. Images recorded with a STED microscope showed that particles detected with ALO-D4 (*green*) and streptavidin (*blue*) were located on the collagen IV matrix (*red*). Scale bar, 5 μ m.

Chapter 7

Conclusions and Future Directions

Conclusion—GPIHBP1 and Plasma Triglyceride Metabolism

Although LPL has been recognized for decades as critical for plasma triglyceride metabolism, the discovery of GPIHBP1 drastically changed our understanding of intravascular lipolysis. We understand now that GPIHBP1 captures LPL in the interstitial spaces and transports it to the capillary lumen (1–3). We now know that LPL is bound to GPIHBP1 in the capillary lumen, and that the GPIHBP1–LPL complex is required for lipoprotein margination and subsequent TRL processing (2, 4). A deficiency in GPIHBP1 causes LPL to be mislocalized to the interstitial spaces, resulting in severe hypertriglyceridemia (1, 2). These studies of GPIHBP1 performed in mice were crucial in our understanding of GPIHBP1’s role in intravascular lipolysis, but continued efforts to understand GPIHBP1’s function, regulation, and role in human disease are important. In the work described, we strived to understand GPIHBP1’s interaction with LPL in humans and the role GPIHBP1 plays in different diseases such as autoimmune disease and cancer.

In chapter 2, we created monoclonal antibodies against human GPIHBP1 to study the expression and function of GPIHBP1 in human tissues. We generated 5 high affinity mAbs against hGPIHBP1, four against the Ly6 domain and one against the acidic domain. These mAbs were useful for three lines of investigation. First, we found that two mAbs against the Ly6 domain (RG3 and RE3) blocked the binding of LPL to GPIHBP1, whereas a mAb against the acidic domain (RF4) did not. We also found that mAbs RG3 and RE3 bound with reduced affinity to GPIHBP1-W109S, an “Ly6 domain mutant” that lacks the capacity to bind LPL. These findings provided strong evidence that GPIHBP1’s Ly6 domain is responsible for the high-affinity interaction with LPL. Second, using these mAbs, we performed immunohistochemistry studies of human adipose tissue. We found that GPIHBP1 was expressed

only in capillary endothelial cells and not in larger blood vessels, recapitulating the same expression pattern observed previously in mice. This makes perfect sense from the standpoint of lipoprotein physiology. GPIHBP1 expressed in capillaries—the blood vessels that are immediately adjacent to adipocytes that secrete LPL—facilitates the capture of locally produced LPL and serves to focus lipolytic activity to nearby parenchymal cells. Third, using these mAbs in a sandwich ELISA, we found that GPIHBP1 can be detected in the plasma of normal subjects but not subjects with GPIHBP1 deficiency. Although more work will need to be done to determine why GPIHBP1 circulates in the plasma, the discovery that GPIHBP1 can be detected in the plasma is exciting. Clinical lipidologists would now be able to test the utility of plasma GPIHBP1 levels as a biomarker for metabolic and/or vascular disease. This was indeed the case as reported in chapter 3.

Using this GPIHBP1 monoclonal antibody–based immunoassay Beigneux and coworkers recently identified six patients with chylomicronemia caused by autoantibodies against GPIHBP1 (“GPIHBP1 autoantibody syndrome”) (5). They demonstrated that GPIHBP1 autoantibodies interfere with the ability of GPIHBP1 to bind LPL. However, the frequency of GPIHBP1 autoantibody syndrome had not been clearly defined. Beigneux and coworkers identified six cases of GPIHBP1 autoantibody syndrome from ~200 miscellaneous plasma samples (5). In chapter 3, we screened an additional 33 patients with previously unexplained hypertriglyceridemia for GPIHBP1 autoantibodies. We identified a single patient with GPIHBP1 autoantibody syndrome who was previously hospitalized for chylomicronemia and acute pancreatitis. We found that the patient’s autoantibodies interfered with GPIHBP1’s ability to bind LPL. Although further work in larger cohorts will be required to define the frequency of GPIHBP1 autoantibody syndrome, this study suggested that this disease is not rare and that all

clinical patients presenting with unexplained hypertriglyceridemia should be screen for GPIHBP1 autoantibodies.

In chapter 4, we further took advantage of our human and mouse monoclonal antibodies against GPIHBP1 to determine if GPIHBP1 is expressed in capillary endothelial cells of gliomas. GPIHBP1 is expressed in capillary endothelial cells of all peripheral tissues (1–3). In contrast, GPIHBP1 is absent from capillaries of the brain parenchyma (2, 6, 7), which depends on glucose for fuel (8). Despite the absence of GPIHBP1 expression in brain capillaries, we were curious about the possibility that GPIHBP1 would be expressed in capillaries of gliomas, a brain malignancy where capillaries are morphologically distinct from normal brain capillaries and the blood–brain barrier is often defective. By immunohistochemistry, we documented GPIHBP1 expression in capillary endothelial cells of human gliomas and in capillaries of CT-2A gliomas within the mouse cerebral cortex. In addition, immunohistochemistry studies also revealed that LPL is bound to GPIHBP1 in glioma capillaries, just as it is bound to GPIHBP1 in capillaries of heart and adipose tissue. This colocalization between GPIHBP1 and LPL implied that we might find evidence for TRL margination and processing in the tumors. Indeed, after an intravenous injection of [²H]TRLs, we observed, by NanoSIMS imaging, [²H]TRL margination along glioma capillaries and the entry of TRL nutrients into the surrounding glioma cells. These findings of fatty acid uptake were also observed after administering [¹³C]fatty acids by gastric gavage. Documenting GPIHBP1 and LPL in glioma capillaries, combined with the discovery that TRL-derived nutrients are taken up and utilized by glioma cells, opens an entirely new chapter in glioma metabolism research. However, more research will be needed to determine if GPIHBP1 and LPL in glioma capillaries could be medically important. For example, it is conceivable that fluorescently labeled GPIHBP1 antibodies could guide surgical resection of tumors or local

instillation of gold-conjugated GPIHBP1 monoclonal antibodies into tumors could help to improve targeting of chemotherapeutic agents.

The discovery of GPIHBP1 has furthered our understanding of mechanisms for intravascular lipolysis, but many questions still remain. The field needs to understand why GPIHBP1 is expressed in capillaries but not in larger blood vessels and what factors control GPIHBP1 expression. Are there paracrine factors secreted by parenchymal cells that turn on GPIHBP1 expression? We need to investigate why GPIHBP1 expression is absent in capillaries of the brain and how GPIHBP1 is turned on in gliomas. Does the brain parenchyma produce factors that inhibit GPIHBP1 expression in brain capillaries or does the presence of the blood–brain barrier prevent paracrine factors from activating GPIHBP1 expression? More research will be needed to determine GPIHBP1’s role in lipid metabolism of other tumors and whether targeting GPIHBP1 could lead to potential therapies. Finally, the field must investigate the cellular mechanisms by which the lipid products of GPIHBP1–LPL mediated TRL processing move across endothelial cells towards parenchymal cells.

Conclusion—Macrophage-derived Particles in Cholesterol Efflux

The role of macrophage in cholesterol efflux and reverse cholesterol transport has been studied for decades (9–11). Cholesterol efflux from macrophages is essential for maintaining cholesterol balance and for minimizing the inflammatory response caused by accumulation of cholesterol (12–14). Prevailing models typically show that macrophages unload excess cholesterol to HDL through direct interactions between HDL and ABC transporters on the plasma membrane of macrophages (9–11). The importance of plasma HDL cholesterol levels to the risk of coronary disease remains a matter of debate, but there is agreement that the ability of HDL to unload cholesterol from macrophages is important for preventing atherosclerotic disease (15–18). Indeed, several studies have suggested that an enhanced cholesterol efflux capacity is inversely correlated with coronary artery disease (15, 16). In the work described, we determined a potential new mode of cholesterol efflux from macrophages through the release of cholesterol-rich particles from the plasma membrane.

In chapter 5, we documented by scanning electron microscopy that macrophages release ~20 to 100-nm unilamellar particles from the plasma membrane. These particles are released from filopodia and lamellipodia of macrophages and attach to the substrate, forming a “lawn” of particles surrounding the cell. Using NanoSIMS imaging and [¹⁵N]ALO-D4 (a modified cholesterol-binding cytolysin), we showed that these particles are enriched in a mobile and metabolically active pool of “accessible cholesterol.” In addition, the accessible cholesterol content in the particles could be increased by loading the cells with acetyl-LDL or by treating the cells with an LXR/RXR agonists. Finally, incubating the cells with HDL reduced the cholesterol content in these particles. Although previous studies have reported that macrophages release of “microparticles” or “microdomains”, the mechanism for the biogenesis of these particles were

not elucidated. In our study, we showed that these particles appear to be released from the plasma membrane.

In chapter 6, we further characterized the macrophage-derived particles by SEM, NanoSIMS, and proteomic analysis. By using correlative light, scanning EM, and NanoSIMS imaging, we found that macrophages release cholesterol-rich particles during projection and retraction of their filopodia/lamellipodia. Inhibition of macrophage movement, by an actin depolymerizing agent or myosin II inhibitor, prevented particle formation. Through shotgun proteomics of isolated macrophage particles, we identified that these particles were enriched in proteins related to focal adhesion, suggesting that macrophages leave particles behind during the focal adhesion disassembly process. Indeed, inhibition of the focal adhesion disassembly process, through FAK and clathrin inhibitors, increased number of particles deposited on the substrate. Finally, using super-resolution confocal imaging and NanoSIMS imaging, we documented that these particles were enriched in accessible cholesterol (detected by ALO-D4), but not in sphingomyelin-bound cholesterol (detected by OlyA).

We propose that the release of macrophage-derived particles from the plasma membrane could assist in disposing of surplus cholesterol and increase the efficiency of efflux to HDL. However, one limitation of our studies is that all our studies dealt with cultured macrophages. Whether particles are released from macrophages *in vivo* is unknown. Further studies will need to be done in order to determine if macrophages release particles onto other cells in culture and if macrophage release cholesterol enriched particles *in vivo*. If so, particle release from macrophages in atherosclerotic plaques could also be a mechanism for unloading cholesterol and promoting reverse cholesterol transport. Finally, we need to better understand the mechanism of release of cholesterol-rich particles from macrophages, more specifically why particles are

enriched in accessible cholesterol and not sphingomyelin sequestered cholesterol and how particle release is regulated.

Reference

1. Beigneux, A. P., B. Davies, P. Gin, M. M. Weinstein, E. Farber, X. Qiao, P. Peale, S. Bunting, R. L. Walzem, J. S. Wong, W. S. Blaner, Z. M. Ding, K. Melford, N. Wongsiriroj, X. Shu, F. de Sauvage, R. O. Ryan, L. G. Fong, A. Bensadoun, and S. G. Young. 2007. Glycosylphosphatidylinositol-anchored high density lipoprotein-binding protein 1 plays a critical role in the lipolytic processing of chylomicrons. *Cell Metab* **5**: 279–291.
2. Davies, B. S., A. P. Beigneux, R. H. Barnes, 2nd, Y. Tu, P. Gin, M. M. Weinstein, C. Nobumori, R. Nyren, I. Goldberg, G. Olivecrona, A. Bensadoun, S. G. Young, and L. G. Fong. 2010. GPIHBP1 is responsible for the entry of lipoprotein lipase into capillaries. *Cell Metab* **12**: 42–52.
3. Fong, L. G., S. G. Young, A. P. Beigneux, A. Bensadoun, M. Oberer, H. Jiang, and M. Ploug. 2016. GPIHBP1 and plasma triglyceride metabolism. *Trends Endocrinol Metab* **27**: 455–469.
4. Goulbourne, C., P. Gin, A. Tatar, C. Nobumori, A. Hoenger, H. Jiang, C. Grovenor, O. Adeyo, J. Esko, I. Goldberg, K. Reue, P. Tontonoz, A. Bensadoun, A. Beigneux, S. Young, and L. Fong. 2014. The GPIHBP1–LPL complex is responsible for the margination of triglyceride-rich lipoproteins in capillaries. *Cell Metab* **19**: 849–860.
5. Beigneux, A. P., K. Miyashita, M. Ploug, D. J. Blom, M. Ai, M. F. Linton, W. Khovidhunkit, R. Dufour, A. Garg, M. A. McMahon, C. R. Pullinger, N. P. Sandoval, X. Hu, C. M. Allan, M. Larsson, T. Machida, M. Murakami, K. Reue, P. Tontonoz, I. J. Goldberg, P. Moulin, S. Charrière, L. G. Fong, K. Nakajima, and S. G. Young. 2017. Autoantibodies against GPIHBP1 as a cause of hypertriglyceridemia. *N Engl J Med* **376**: 1647–1658.
6. Olafsen, T., S. G. Young, B. S. J. Davies, A. P. Beigneux, V. E. Kenanova, C. Voss, G. Young, K.-P. Wong, R. H. Barnes, Y. Tu, M. M. Weinstein, C. Nobumori, S.-C. Huang, I. J.

- Goldberg, A. Bensadoun, A. M. Wu, and L. G. Fong. 2010. Unexpected expression pattern for glycosylphosphatidylinositol-anchored HDL-binding protein 1 (GPIHBP1) in mouse tissues revealed by positron emission tomography scanning. *J Biol Chem* **285**: 39239–39248.
7. Young, S. G., B. S. J. Davies, C. V. Voss, P. Gin, M. M. Weinstein, P. Tontonoz, K. Reue, A. Bensadoun, L. G. Fong, and A. P. Beigneux. 2011. GPIHBP1, an endothelial cell transporter for lipoprotein lipase. *J Lipid Res* **52**: 1869–1884.
 8. Mergenthaler, P., U. Lindauer, G. A. Dienel, and A. Meisel. 2013. Sugar for the brain: the role of glucose in physiological and pathological brain function. *Trends Neurosci* **36**: 587–597.
 9. Rosenson, R. S., H. B. Brewer, Jr., W. S. Davidson, Z. A. Fayad, V. Fuster, J. Goldstein, M. Hellerstein, X. C. Jiang, M. C. Phillips, D. J. Rader, A. T. Remaley, G. H. Rothblat, A. R. Tall, and L. Yvan-Charvet. 2012. Cholesterol efflux and atheroprotection: advancing the concept of reverse cholesterol transport. *Circulation* **125**: 1905–1919.
 10. Fisher, E. A., J. E. Feig, B. Hewing, S. L. Hazen, and J. D. Smith. 2012. High-density lipoprotein function, dysfunction, and reverse cholesterol transport. *Arterioscler Thromb Vasc Biol* **32**: 2813–2820.
 11. Tall, A. R., P. Costet, and N. Wang. 2002. Regulation and mechanisms of macrophage cholesterol efflux. *J Clin Invest* **110**: 899–904.
 12. Lusis, A. J. 2000. Atherosclerosis. *Nature* **407**: 233–241.
 13. Moore, K. J., F. J. Sheedy, and E. A. Fisher. 2013. Macrophages in atherosclerosis: a dynamic balance. *Nat Rev Immunol* **13**: 709–721.
 14. Linton, M. R. F., P. G. Yancey, S. S. Davies, W. G. Jerome, E. F. Linton, W. L. Song, A. C. Doran, and K. C. Vickers. 2000. The role of lipids and lipoproteins in atherosclerosis. *In*

- Endotext. K. R. Feingold, B. Anawalt, A. Boyce, G. Chrousos, K. Dungan, A. Grossman, J. M. Hershman, G. Kaltsas, C. Koch, P. Kopp, M. Korbonits, R. McLachlan, J. E. Morley, M. New, L. Perreault, J. Purnell, R. Rebar, F. Singer, D. L. Trencle, A. Vinik, and D. P. Wilson, editors, South Dartmouth (MA).
15. Khera, A. V., M. Cuchel, M. de la Llera-Moya, A. Rodrigues, M. F. Burke, K. Jafri, B. C. French, J. A. Phillips, M. L. Mucksavage, R. L. Wilensky, E. R. Mohler, G. H. Rothblat, and D. J. Rader. 2011. Cholesterol efflux capacity, high-density lipoprotein function, and atherosclerosis. *N Engl J Med* **364**: 127–135.
 16. Rohatgi, A., A. Khera, J. D. Berry, E. G. Givens, C. R. Ayers, K. E. Wedin, I. J. Neeland, I. S. Yuhanna, D. R. Rader, J. A. de Lemos, and P. W. Shaul. 2014. HDL cholesterol efflux capacity and incident cardiovascular events. *N Engl J Med* **371**: 2383–2393.
 17. Li, X. M., W. H. Tang, M. K. Mosior, Y. Huang, Y. Wu, W. Matter, V. Gao, D. Schmitt, J. A. Didonato, E. A. Fisher, J. D. Smith, and S. L. Hazen. 2013. Paradoxical association of enhanced cholesterol efflux with increased incident cardiovascular risks. *Arterioscler Thromb Vasc Biol* **33**: 1696–1705.
 18. Investigators, A.-H., W. E. Boden, J. L. Probstfield, T. Anderson, B. R. Chaitman, P. Desvignes-Nickens, K. Koprowicz, R. McBride, K. Teo, and W. Weintraub. 2011. Niacin in patients with low HDL cholesterol levels receiving intensive statin therapy. *N Engl J Med* **365**: 2255–2267.

Appendix I

An LPL-specific Monoclonal Antibody, 88B8, that Abolishes the Binding of LPL to GPIHBP1



Supplemental Material can be found at:
<http://www.jlr.org/content/suppl/2016/08/05/jlr.M070813.DC1.html>

An LPL-specific monoclonal antibody, 88B8, that abolishes the binding of LPL to GPIHBP1[®]

Christopher M. Allan,^{1,*} Mikael Larsson,^{1,*} Xuchen Hu,^{*} Cuiwen He,^{*} Rachel S. Jung,^{*} Alaleh Mapar,^{*} Constance Voss,^{*} Kazuya Miyashita,[†] Tetsuo Machida,[†] Masami Murakami,[†] Katsuyuki Nakajima,[†] André Bensadoun,[§] Michael Ploug,^{**††} Loren G. Fong,^{2,*} Stephen G. Young,^{2,*§§} and Anne P. Beigneux^{2,*}

Departments of Medicine* and Human Genetics,^{§§} David Geffen School of Medicine, University of California Los Angeles, Los Angeles, CA; Gunma University,[†] Graduate School of Medicine, Maebashi, Japan; Division of Nutritional Science,[§] Cornell University, Ithaca, NY; Finsen Laboratory,^{**} Rigshospitalet, Copenhagen N, Denmark; and Biotech Research and Innovation Centre (BRIC),^{††} University of Copenhagen, Copenhagen N, Denmark

Abstract LPL contains two principal domains: an amino-terminal catalytic domain (residues 1–297) and a carboxyl-terminal domain (residues 298–448) that is important for binding lipids and binding glycosylphosphatidylinositol-anchored high density lipoprotein binding protein 1 (GPIHBP1) (an endothelial cell protein that shuttles LPL to the capillary lumen). The LPL sequences required for GPIHBP1 binding have not been examined in detail, but one study suggested that sequences near LPL's carboxyl terminus (residues ~403–438) were crucial. Here, we tested the ability of LPL-specific monoclonal antibodies (mAbs) to block the binding of LPL to GPIHBP1. One antibody, 88B8, abolished LPL binding to GPIHBP1. Consistent with those results, antibody 88B8 could not bind to GPIHBP1-bound LPL on cultured cells. Antibody 88B8 bound poorly to LPL proteins with amino acid substitutions that interfered with GPIHBP1 binding (e.g., C418Y, E421K). However, the sequences near LPL's carboxyl terminus (residues ~403–438) were not sufficient for 88B8 binding; upstream sequences (residues 298–400) were also required. Additional studies showed that these same sequences are required for LPL binding to GPIHBP1. **In conclusion, we identified an LPL mAb that binds to LPL's GPIHBP1-binding domain. The binding of both antibody 88B8 and GPIHBP1 to LPL depends on large segments of LPL's carboxyl-terminal domain.**—Allan, C. M., M. Larsson, X. Hu, C. He, R. S. Jung, A. Mapar, C. Voss, K. Miyashita, T. Machida, M. Murakami, K. Nakajima, A. Bensadoun, M. Ploug, L. G. Fong, S. G. Young, and A. P. Beigneux. An LPL-specific monoclonal antibody, 88B8, that abolishes the binding of LPL to GPIHBP1. *J. Lipid Res.* 2016. 57: 1889–1898.

Supplementary key words chylomicrons • endothelial cells • lipids/chemistry • lipolysis and fatty acid metabolism • triglycerides • lipoprotein lipase • glycosylphosphatidylinositol-anchored high density lipoprotein binding protein 1

For more than 50 years, it has been known that LPL, a triglyceride hydrolase secreted by myocytes and adipocytes, is crucial for the intravascular processing of triglyceride-rich lipoproteins (TRLs) (1–3). For most of that time, it was assumed that LPL was attached to the heparan-sulfate proteoglycans along the lumen of blood vessels (4), but how LPL reached the lumen of blood vessels was a stubborn mystery. Within the past few years, that mystery has been solved (5, 6). Glycosylphosphatidylinositol-anchored high density lipoprotein binding protein 1 (GPIHBP1), a GPI-anchored protein of capillary endothelial cells, picks up freshly secreted LPL within the interstitial spaces and shuttles it across endothelial cells to the capillary lumen (7, 8). In the absence of GPIHBP1, LPL remains in the interstitial spaces and never reaches the capillary lumen, resulting in an accumulation of plasma TRLs and extremely high plasma triglyceride levels (“chylomicronemia”) (8). Recent studies showed that GPIHBP1 (and GPIHBP1-bound LPL) are also crucial for the margination of TRLs along the capillary lumen, allowing triglyceride hydrolysis to proceed (9).

GPIHBP1 has two main structural features—an amino-terminal acidic domain and a cysteine-rich three-fingered “LU domain” (7, 10). Recent studies have shown that the

This work was supported by grants from the National Heart, Lung, and Blood Institute (HL090553, HL087228, and HL125335) and a Transatlantic Network Grant from the Fondation Leducq (12CVD04). C.M.A. was supported by a Ruth L. Kirschstein National Research Service Award (T32HL69766). The content is solely the responsibility of the authors and does not necessarily represent the official views of the National Institutes of Health. The authors have no financial interests to declare.

Manuscript received 8 July 2016 and in revised form 2 August 2016.

*Published, JLR Papers in Press, August 5, 2016
 DOI 10.1194/jlr.M070813*

Copyright © 2016 by the American Society for Biochemistry and Molecular Biology, Inc.
 This article is available online at <http://www.jlr.org>

Abbreviations: DAPI, 4',6-diamidino-2-phenylindole; GPIHBP1, glycosylphosphatidylinositol-anchored high density lipoprotein binding protein 1; hLPL, human LPL; mAb, monoclonal antibody; mLPL, mouse LPL; TRL, triglyceride-rich lipoprotein.

¹M. Larsson and C. M. Allan wish to be considered co-first authors.

²To whom correspondence should be addressed.

e-mail: abeigneux@mednet.ucla.edu (A.P.B.); lfong@mednet.ucla.edu (L.G.F.); sgyoung@mednet.ucla.edu (S.G.Y.)

[®] The online version of this article (available at <http://www.jlr.org>) contains a supplement.

Supplemental Material can be found at:
<http://www.jlr.org/content/suppl/2016/08/05/jlr.M070813.DC1.html>

LU domain is primarily responsible for high-affinity binding of LPL, while the acidic domain augments the interaction and promotes an initial interaction complex between LPL and GPIHBP1 (6, 11). A variety of missense mutations in GPIHBP1's LU domain have been identified in patients with chylomicronemia (12–22), and all of those abolish the ability of GPIHBP1 to bind LPL (6). Most of these mutations interfere with the formation of disulfide bonds in the LU domain, leading to disulfide-linked dimers and multimers (23). Alanine-scanning mutagenesis studies showed that the highly conserved second finger of the three-fingered LU domain is particularly important for binding LPL (24). Mutagenizing W109 in finger 2 abolishes LPL binding without promoting the formation of GPIHBP1 dimers/multimers, suggesting that W109 participates directly in binding LPL (23).

In contrast to the situation with GPIHBP1, our understanding of the LPL sequences required for binding to GPIHBP1 is meager, but the relevant sequences appear to be located in LPL's carboxyl-terminal "lipid-binding" domain (residues 298–448) rather than in LPL's catalytic domain (residues 1–297). A pair of LPL mutations (C418Y, E421K), first identified in patients with hypertriglyceridemia (25, 26), interfere with the binding of LPL to GPIHBP1. Mutation of nearby LPL sequences (residues 403–438) also

impaired LPL binding to GPIHBP1 (27). Those studies were interpreted as showing that sequences near the carboxyl terminus of LPL are singularly important for mediating LPL binding to GPIHBP1.

Here, we sought to better define LPL sequences that are important for GPIHBP1 binding. As part of these efforts, we tested the capacity of three LPL-specific monoclonal antibodies (mAbs) (5D2, 88B8, 57A5) (28–30) to block the binding of LPL to GPIHBP1. We reasoned that if we were to identify a "blocking antibody," then efforts to define the epitope would lead to new insights into LPL sequences that are important for LPL binding to GPIHBP1.

MATERIALS AND METHODS

Monoclonal antibodies

We examined three LPL-specific mouse mAbs (5D2, 57A5, 88B8) (28–30). The epitope for 5D2 has been studied in detail and is located between residues 380 and 410 in LPL's carboxyl-terminal domain (29, 30). mAbs 57A5 and 88B8 were generated against human LPL (hLPL) and have been used previously in LPL immunoassays (28), but data on the epitopes for these antibodies have never been reported. Fab' fragments were prepared with immobilized papain and Fc fragments removed with Protein

Human LPL/ mouse LPL chimeras	
Name	Description
hLPL	hLPL[1–448]
mLPL	mLPL[1–447]
298–448	mLPL[1–297] hLPL[298–448]
330–448	mLPL[1–329] hLPL[330–448]
370–448	mLPL[1–369] hLPL[370–448]
400–448	mLPL[1–399] hLPL[400–448]
420–448	mLPL[1–419] hLPL[420–448]
m(327–331)	hLPL[1–326] mLPL[327–331] hLPL[332–448]
h(327–331)	mLPL[1–326] hLPL[327–331] mLPL[332–447]
h(327–403)	mLPL[1–326] hLPL[327–403] mLPL[404–447]
Human LPL/ human HL chimeras	
Name	Description
hLPL	hLPL[1–448]
hHL	hHL[1–477]
313–448	hHL[1–328] hLPL[313–448]
330–448	hHL[1–344] hLPL[330–448]
335–448	hHL[1–349] hLPL[335–448]
340–448	hHL[1–354] hLPL[340–448]
345–448	hHL[1–359] hLPL[345–448]

Fig. 1. List of the mLPL-hLPL chimeras, and of the human HL-hLPL chimeras generated for the studies. Numbers in brackets correspond to amino acid residues.

Supplemental Material can be found at:
<http://www.jlr.org/content/suppl/2016/08/05/jlr.M070813.DC1.html>

A-Sepharose. mAb 5D2 was a gift from Dr. John Brunzell, and mAbs 57A5 and 88B8 were acquired from Immuno-Biological Laboratories (Gunma, Japan).

LPL–GPIHBP1 binding assays

Cell-free assay. Secreted versions of wild-type human GPIHBP1 and GPIHBP1-W109S were stably expressed in *Drosophila* S2 cells. Both GPIHBP1 proteins contain a uPAR epitope tag (23) as well as the epitope for mAb 11A12 (31). For the assay, the conditioned medium from *Drosophila* S2 cells expressing soluble human GPIHBP1 was incubated for 1 h at 4°C with V5-tagged hLPL (32), with or without mAbs (20 µg/ml final), and agarose beads coated with mAb 11A12 (33). After washing the beads, GPIHBP1 and any GPIHBP1-bound LPL were eluted from the antibody-coated beads by heating the beads in SDS sample buffer for 5 min at 90°C. The amounts of GPIHBP1 and LPL in the starting material, unbound fractions, wash fractions, and elution fractions were assessed by Western blotting. Proteins were separated on a 12% NuPAGE SDS-PAGE gel with MES buffer, followed by transfer to a sheet of nitrocellulose membrane. The membrane was then incubated with IRdye680-conjugated antibody 11A12 and an IRdye800-conjugated V5-antibody.

Cell-based assay. CHO pgsA-745 cells (2×10^6) were electroporated with 2 µg plasmids encoding either an S-protein-tagged wild-type human GPIHBP1 or an S-protein-tagged mutant human GPIHBP1 (W109S) and then plated on coverslips in 24-well plates. After 24 h, the cells were incubated with either V5-tagged hLPL alone, or V5-tagged hLPL with one of the three mAbs (5D2, 57A5, 88B8) (20 µg/ml) for 1 h at 4°C. The cells were then washed and processed for Western blots or immunofluorescence microscopy. For the Western blots, cell lysates were collected by incubating cells with M-PER mammalian protein extraction reagent (ThermoFisher Scientific) with EDTA-free complete protease inhibitor cocktail (Roche) for 5 min at 4°C, followed by centrifugation at 14,000 g for 10 min to remove insoluble material. The nitrocellulose membrane was then blocked for 1 h at room temperature with Odyssey blocking buffer (Li-Cor), and then incubated with an IRdye800-conjugated mouse mAb against the V5 tag (ThermoFisher Scientific; 2.32 µg/ml) and a goat polyclonal antibody against the S-protein tag (Abcam; 1:1,000) followed by an IRdye680-conjugated donkey anti-goat IgG (Li-Cor). Signals were visualized and quantified with a Li-Cor Odyssey scanner. For the immunofluorescence microscopy assay, cells were fixed in 3% paraformaldehyde for 15 min and blocked with 10% donkey serum in PBS/Mg/Ca. Cells were then incubated overnight at 4°C with an Alexa 647-conjugated mouse mAb against the V5 tag (ThermoFisher Scientific; 11.6 µg/ml) and a goat polyclonal antibody against the S-protein tag (Abcam; 1:800), followed by a 30-min incubation with an Alexa 568-conjugated donkey anti-goat IgG (ThermoFisher Scientific; 1:800). After washing, the cells were fixed with 3% paraformaldehyde for 15 min and stained with 4',6-diamidino-2-phenylindole (DAPI) to visualize DNA. Images were recorded with an Axiovert 200M microscope and processed with Zen 2010 software (all from Zeiss). Within each experiment, the exposure conditions for each construct were identical.

Testing the binding of hepatic lipase–LPL chimeras to GPIHBP1 on the surface of cultured cells

Earlier studies by Wong et al. (34) showed that it was possible to express catalytically active, dimeric HL–LPL chimeras by exchanging sequences in HL with the corresponding sequences in LPL. Here, we used that approach to create HL–LPL chimeras containing hLPL residues 313–448, 330–448, 335–448, 340–448, or 345–448 (Fig. 1). To test the ability of HL, LPL, and the HL–LPL chimeras to bind to GPIHBP1, we used a “co-plating assay”

described previously by Beigneux et al. (24). CHO-K1 cells (1×10^6) were electroporated with 1.0 mg of either an S-protein-tagged human GPIHBP1 construct or an expression vector for one of the V5-tagged lipases. The independently transfected cells were then mixed together and plated on coverslips in 24-well plates. Twenty-four hours later, the cells were fixed in 3% paraformaldehyde. When indicated, the cells were permeabilized with 0.2% Triton X-100. Cells were blocked with 10% donkey serum in PBS/Mg/Ca and then incubated for 1 h in the blocking buffer containing a goat antibody against the S-protein tag (Abcam; 1:500) and a mouse mAb against the V5 tag (Invitrogen; 1:100),

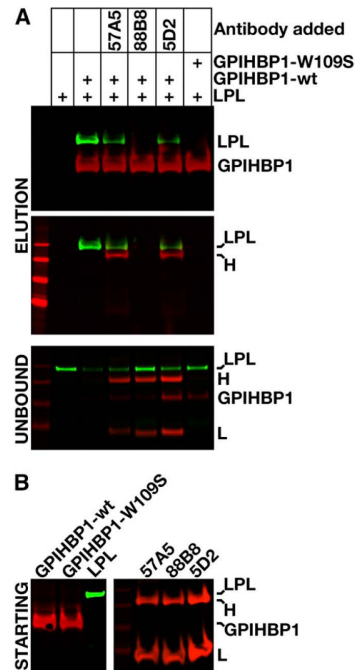


Fig. 2. A cell-free LPL–GPIHBP1 binding assay to test the ability of LPL-specific mAbs 5D2, 57A5, and 88B8 to block the binding of V5-tagged hLPL to GPIHBP1. Secreted versions of wild-type (wt) GPIHBP1 and GPIHBP1-W109S were expressed in *Drosophila* S2 cells. Both GPIHBP1 proteins contain a uPAR epitope tag (23) as well as the epitope for mAb 11A12. The GPIHBP1 proteins (7.25 µg) were incubated with agarose beads coated with mAb 11A12, V5-tagged hLPL (825 ng), and either no antibody or mAbs 57A5, 88B8, or 5D2 (20 µg/ml final). We used a high molar concentration of mAbs so as to minimize the impact of differences in the affinity of the three different mAbs. After a 1-h incubation at 4°C, the beads were washed. GPIHBP1 and GPIHBP1-bound LPL were then released from the agarose beads by heating the beads in SDS-sample buffer. A: Western blots on the “unbound” fraction (proteins that did not bind to the agarose beads) and “elution” fractions with an IRdye800-V5 antibody (green), an IRdye680-antibody 11A12 (red), and an IRdye680-donkey anti-mouse IgG (red). LPL binding to GPIHBP1 was inhibited 53.8% with 57A5, 94.9% with 88B8, and 63.5% with 5D2, as judged by quantification with a Li-Cor scanner. H, heavy chain; L, light chain. B: Western blots performed on the “starting material” proteins that were added to the assay (mAbs, GPIHBP1, LPL).

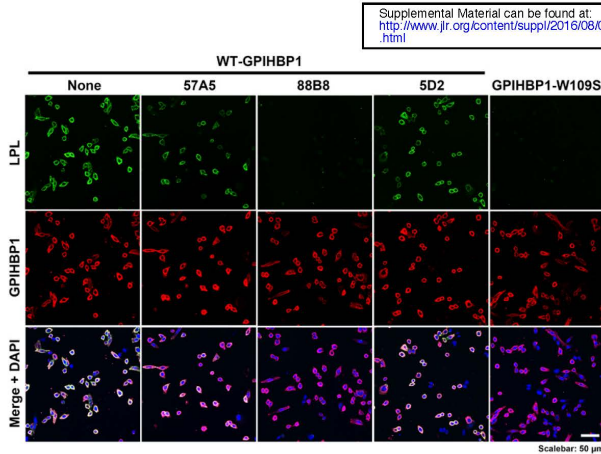


Fig. 3. Immunofluorescence microscopy assay to evaluate the ability of mAbs 57A5, 88B8, and 5D2 to block the binding of LPL to GPIHBP1. CHO pgsA-745 cells were transiently transfected with S-protein-tagged wild-type human GPIHBP1 (or GPIHBP1-W109S, which lacks the ability to bind LPL). The cells were then incubated with V5-tagged hLPL and either no antibody or mAbs 57A5, 88B8, or 5D2 (20 mg/ml). After a 1-h incubation at 4°C, nonpermeabilized cells were stained for GPIHBP1 with an antibody against the S-protein tag (red) and LPL with a V5 antibody (green). Cell nuclei were stained with DAPI (blue).

followed by a 30-min incubation with an Alexa 568-conjugated donkey anti-goat IgG (Invitrogen; 1:800) and an Alexa 488-conjugated donkey anti-mouse IgG (Invitrogen; 1:800). After washing, the cells were stained with DAPI to visualize DNA. Images were recorded with the Axiovert 200M microscope. The exposure conditions for each construct were identical. In this system, cells that expressed wild-type GPIHBP1 captured LPL that was secreted by the LPL-transfected cells, thus, GPIHBP1 and LPL signals colocalized on the merged image (24). HL does not bind to GPIHBP1 (31); consequently, there was no colocalization of HL and GPIHBP1 signals.

Lipase expression vectors

hLPL-mouse LPL (mLPL) chimeras, and HL-LPL chimeras (Fig. 1) were created with a PCR-based method (In-Fusion HD cloning kit, Clontech). Point mutations were introduced with the QuikChange Lightning kit (Agilent Technologies).

Testing the ability of the mAbs to bind to GPIHBP1-bound LPL

CHO pgsA-745 cells (2×10^6) were electroporated with 2 μ g of a plasmid encoding an S-protein-tagged wild-type human GPIHBP1 and plated on coverslips in 24-well plates. Twenty-four

hours later, cells were incubated with a V5-tagged hLPL or buffer for 1 h at 4°C. Cells were then washed and incubated with either buffer or Alexa 568-conjugated mAbs (5D2, 57A5, or 88B8) (20 μ g/ml) for 1 h at 4°C. The cells were then washed and processed for immunocytochemistry. Cells on coverslips were fixed in 3% paraformaldehyde for 15 min, blocked with 10% donkey serum in PBS/Mg/Ca, and then incubated overnight at 4°C with an Alexa 647-conjugated mouse mAb against the V5 tag (ThermoFisher Scientific; 11.6 μ g/ml) and a goat polyclonal antibody against the S-protein tag (Abcam; 1:800), followed by a 30-min incubation with an Alexa 488-conjugated donkey anti-goat IgG (ThermoFisher Scientific; 1:800). After washing, the cells were fixed with 3% paraformaldehyde for 15 min and stained with DAPI to visualize DNA. Microscopy was performed as described earlier.

Testing the ability of the mAbs to bind to LPL in capillaries of tissue sections

Wild-type and *Lpl*^{-/-} MCK-hLPL mice (35) were perfused with PBS followed by 3% paraformaldehyde; quadriceps muscle was harvested and embedded in OCT on dry ice. Tissue sections (7 μ m) were fixed in methanol at -20°C for 10 min, permeabilized with 0.2% Triton X-100 for 5 min, and blocked with 5% donkey serum, 10% FBS, and 0.2% BSA in PBS/Mg/Ca. Tissues were incubated

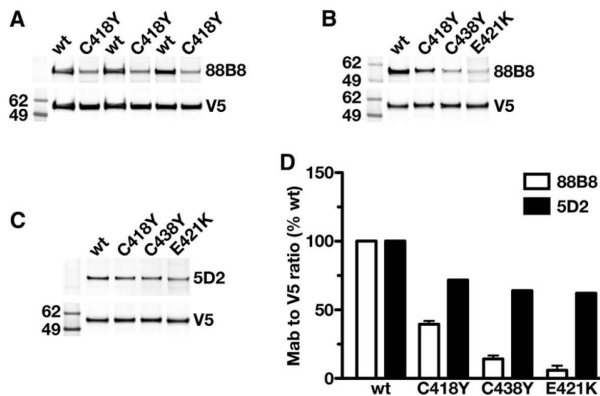


Fig. 4. Testing the ability of mAbs 88B8 and 5D2 to bind to mutant forms of LPL with impaired ability to bind to GPIHBP1. CHO pgsA-745 cells were transfected with V5-tagged wild-type (wt) hLPL or mutant forms of hLPL (LPL-C418Y, LPL-C421K, LPL-C438Y) with either no ability (LPL-C418Y, LPL-C421K) or reduced ability (LPL-C438Y) to bind to GPIHBP1 (27). On the next day, the cells were washed, and cell lysates were prepared for Western blotting. Western blots were performed under nonreducing conditions. A: Western blot with IRdye800-labeled mAb 88B8 and an IRdye680-labeled V5 antibody. B: Western blot with mAb 88B8 (10 mg/ml) followed by an IRdye-800 donkey anti-mouse IgG, along with an IRdye680-V5 antibody. C: Western blot with IRdye800-labeled mAb 5D2 and an IRdye680-labeled V5 antibody. D: Quantification of mAbs 88B8 and 5D2 binding to LPL-C418Y, LPL-C438Y, and LPL-C421K (as determined by a Li-Cor scanner). Compared with wild-type LPL, the binding of the antibodies to LPL-C418Y was reduced by 70% for 88B8, 37% for 57A5, and 26% for 5D2.

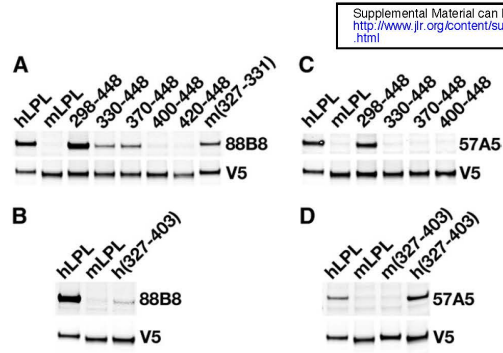


Fig. 5. Western blot studies to assess epitopes for mAbs 88B8 and 57A5. CHO pgsA-745 cells were transfected with V5-tagged versions of mLPL, hLPL, or mLPL-hLPL chimeras (mLPL containing hLPL sequences 298–448, 330–448, 370–448, 400–448, 420–448, or 327–403; or hLPL containing mLPL sequences 327–331 or 327–403) (see Fig. 1 for description of the chimeras). After 24 h, the cells were washed and cell lysates were prepared for SDS-PAGE (non-reducing conditions) and Western blot studies. A, B: Binding of mAb 88B8 to different V5-tagged lipases. Blots were incubated with mAb 88B8 and an IRdye800-labeled donkey anti-mouse IgG, followed by an IRdye680-labeled V5 antibody. C, D: Binding of mAb 57A5 to different V5-tagged lipases. Blots were incubated with mAb 57A5 followed by an IRdye800-labeled donkey anti-mouse IgG and an IRdye680-V5 antibody.

overnight at 4°C with Alexa 568-conjugated mouse mAbs (5D2, 57A5, or 88B8) (8 µg/ml) and a rabbit polyclonal antibody against mouse CD31 (Abcam; 1:50), followed by a 45-min incubation with Alexa 647-conjugated 11A12 antibody (3 µg/ml) and Alexa 488-conjugated donkey anti-rabbit IgG (ThermoFisher Scientific; 1:200). After washing, the cells were fixed with 3% paraformaldehyde for 5 min and stained with DAPI to visualize DNA. Microscopy was performed as described earlier. Mice were fed a chow diet and housed in a barrier facility with a 12 h light-dark cycle. All studies were approved by UCLA's Animal Research Committee.

Measurements of LPL activity

hLPL was prepared from a CHO cell line expressing V5-tagged hLPL (from Dr. Mark Doolittle, University of California, Los

Angeles). LPL was purified by heparin-Sepharose chromatography on an ÄKTA pure HPLC (GE Healthcare) and eluted with a 0.1–2 M NaCl gradient in 20 mM NaPO₄, pH 7.4. Taurodeoxycholate (final concentration, 5 mM) was added to the LPL (i.e., fractions eluting at ≥1 M NaCl) before storing at –80°C. The activity of purified hLPL was compared with that of a known quantity of bovine LPL. Lipase activity was measured with [³H]triolein that had been incorporated into Intralipid (0.5 µCi [³H]triolein/mg triglyceride). hLPL (6 µl, corresponding to the enzymatic activity of 5 ng of bovine LPL) was added to 200-µl incubation mixtures containing 5 mg of triglyceride/ml in 0.15 M Tris (pH 8.5) containing 0.1 M NaCl, 6% BSA (w/v), 16.7 units of heparin/ml, and 5% (v/v) heat-inactivated rat serum (as a source of apo-CII). mAbs (20 µg/ml, final concentration) were added to incubation mixtures 5 min before adding the LPL. Esterase activities were analyzed by adding 30 µl of the hLPL to 100-µl incubation mixtures of 50 mM Tris, 50 µM 1,2-di-O-lauryl-rac-glycero-3-glutaric acid 6'-methylresorufin ester (DGGR), 120 mM NaCl, 10 mg/ml BSA, and 0.5% Triton X-100 (pH 7.4). mAbs (200 µg/ml final concentration) were added to incubations 5 min before adding the LPL. Ester hydrolysis was determined by measuring the increase of resorufin fluorescence at λ_{ex} 530 nm and λ_{em} 590 nm during the first 15 min of the incubation.

RESULTS

Testing the ability of LPL-specific mAbs to block the binding of LPL to GPIIIBP1

We used cell-free and cell-based LPL-GPIIIBP1 binding assays (18, 23, 31, 33) to test the ability of three LPL-specific mAbs (5D2, 88B8, 57A5) (29, 30) to block the binding of hLPL to GPIIIBP1. In the cell-free assay, we incubated GPIIIBP1, LPL, and an LPL-specific mAb with agarose beads that had been coated with a GPIIIBP1-specific mAb (11A12). After a 1-h incubation, the beads were washed, and the amounts of GPIIIBP1 and GPIIIBP1-bound LPL bound to the beads were assessed by Western blotting. mAb 88B8 abolished LPL binding to GPIIIBP1; thus, no LPL could be eluted from the beads (Fig. 2). The ability of 88B8 (and 88B8 Fab' fragments) to block the

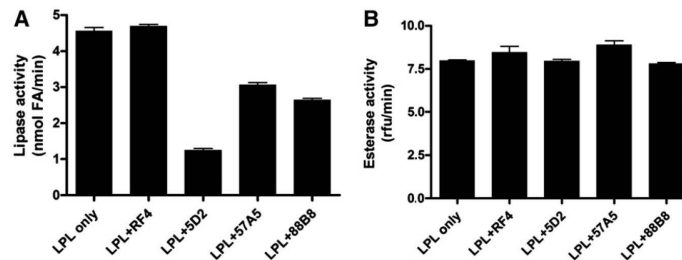


Fig. 6. Testing the ability of mAbs 5D2, 57A5, and 88B8 to inhibit the catalytic activity of purified hLPL. A: LPL was added to incubation mixtures of lipid emulsion particles containing [³H]triolein in the presence of an irrelevant mAb (RF4) or each of the three LPL-specific mAbs (20 µg/ml). The activity of the hLPL in each assay corresponded to activity observed with 0.45 nM bovine LPL. B: hLPL, in an amount corresponding to the activity of 4.5 nM bovine LPL, was added to incubation mixtures containing the ester substrate DGGR in the presence of the mAbs (200 µg/ml). We deliberately used a high molar concentration of mAbs so as to minimize the impact of differences in the affinity of the three different mAbs. Data represent mean values of triplicate measurements ± SD.

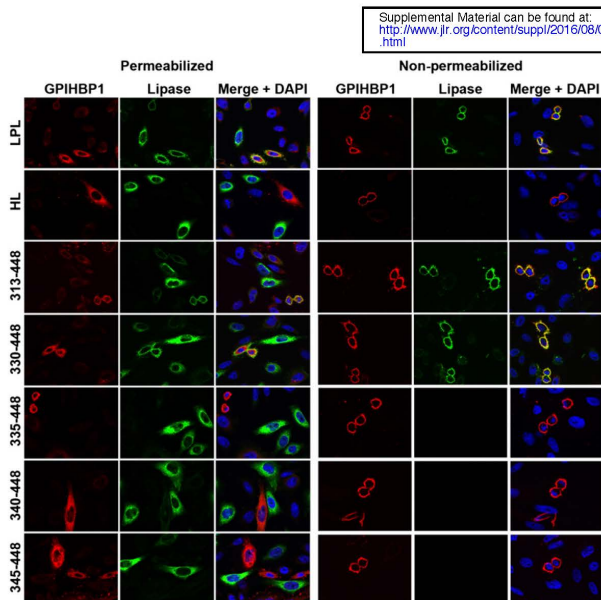


Fig. 7. Immunofluorescence microscopy studies to assess the ability of LPL, HL, and LPL–HL chimeras to bind to GPIHBP1. CHO-K1 cells were electroporated with an S-protein–tagged human GPIHBP1 construct or a V5-tagged lipase expression vector (either LPL, HL, or HL–LPL chimeras containing LPL residues 313–448, 330–448, 335–448, 340–448, and 345–448) (see Fig. 1 for description of the constructs). The separately transfected cells were then mixed and plated on coverslips in 24-well plates. Twenty-four hours later, the cells were fixed in 3% paraformaldehyde, and blocked with 10% donkey serum in PBS/Mg/Ca. Some cells were permeabilized with 0.2% Triton X-100. Cells were then incubated for 1 h in blocking buffer with a goat polyclonal antibody against the S-protein tag (red) and a mouse mAb against the V5 tag (green), followed by a 30-min incubation with an Alexa 568–conjugated donkey anti-goat IgG (Invitrogen; 1:800) and an Alexa 488–conjugated donkey anti-mouse IgG (Invitrogen; 1:800). Cell nuclei were visualized with DAPI (blue). Cells expressing wild-type GPIHBP1 captured LPL secreted by neighboring LPL-expressing cells; hence, the GPIHBP1 and LPL signals colocalized on the merged image. HL–LPL (313–448) and HL–LPL (330–448) bound to GPIHBP1. HL and the remaining HL–LPL chimeras did not bind to GPIHBP1 (no colocalization of GPIHBP1 and the lipase on the merged image). HL–LPL chimeras containing LPL residues 370–448, 380–448, and 389–448 also failed to bind to GPIHBP1.

binding of LPL to GPIHBP1 was confirmed in additional independent experiments (supplemental Figs. S1, S2). mAbs 5D2 and 57A5 did not abolish the binding of LPL to GPIHBP1, but they did reduce LPL binding (Fig. 2).

mAb 88B8 completely blocked binding of LPL to GPIHBP1 on the surface of GPIHBP1-transfected cells, as judged by immunofluorescence microscopy and Western blots of cell extracts (Fig. 3, supplemental Fig. S3). mAbs 57A5 and 5D2 caused partial inhibition of LPL binding to GPIHBP1 (Fig. 3, supplemental Fig. S3).

Defining the epitopes for LPL-specific mAbs

The 5D2 epitope is located within LPL residues 380–410 (29, 30), but data on the epitopes for mAbs 57A5 and 88B8 have not been reported. Preliminary Western blot studies indicated that both mAbs 57A5 and 88B8 bind to the carboxyl-terminal region of LPL (residues 298–448) (supplemental Fig. S4). Identical conclusions were reached by performing ELISAs on the medium of cells that had been transfected with Flag-tagged constructs encoding LPL's amino- and carboxyl-terminal domains (K. Miyashita, unpublished observations). Because 88B8 and 88B8 Fab' fragments block LPL binding to GPIHBP1 and also bound to LPL's carboxyl-terminal domain, we suspected that the binding sites for mAb 88B8 and GPIHBP1 on LPL were similar and that LPL mutations known to interfere with GPIHBP1 binding (e.g., C418Y, E421K, C438Y) (27) would also interfere with 88B8 binding. Indeed, 88B8 bound more avidly to wild-type LPL than to mutant LPLs harboring C418Y, E421K, or C438Y mutations (Fig. 4A, B). The effect of those mutations on 5D2 binding was minimal (Fig. 4C, D). As expected, 88B8 bound avidly to hLPL but not

mLPL; it bound avidly to a mLPL–hLPL chimera containing the entire carboxyl-terminal domain of hLPL (residues 298–448).

Earlier studies implied LPL's GPIHBP1-binding domain involved amino acids 403–438 (27), and the reduced binding of 88B8 to the LPL mutants suggested that the 88B8 epitope might be located in the same stretch of amino acids. To our surprise, the binding of 88B8 to LPL depended on upstream sequences within the primary sequence. mAb 88B8 bound weakly to mLPL–hLPL chimeras containing hLPL residues 330–448 or 370–448, and it failed to bind to chimeras containing hLPL residues 400–448 or 420–448 (Fig. 5A). The same pattern was observed for 88B8 Fab' fragments (supplemental Fig. S5). These results suggested that LPL residues 298–330 are quite relevant to 88B8 binding. Within that region, the only amino acids that differ between the hLPL and mLPL sequences are residues 327–331. Those residues were important for the 88B8 epitope; when residues 327–331 in hLPL were replaced with the mLPL sequences, the binding of 88B8 was significantly reduced (Fig. 5A).

The finding that 88B8 bound (albeit weakly) to mLPL–hLPL chimeras containing hLPL residues 330–448 and 370–448 but failed to bind to a chimera with human residues 400–448 indicates that hLPL residues 330–400 are important for 88B8 binding. However, these results do not mean that residues 400–448 have no role in 88B8 binding, but rather that residues 400–448 are insufficient. First, the C418Y, E421K, and C438Y mutations clearly interfere with 88B8 binding (Fig. 4). Second, introducing human residues 327–403 into the mLPL expression vector resulted in only minimal restoration of 88B8 binding (Fig. 5B),

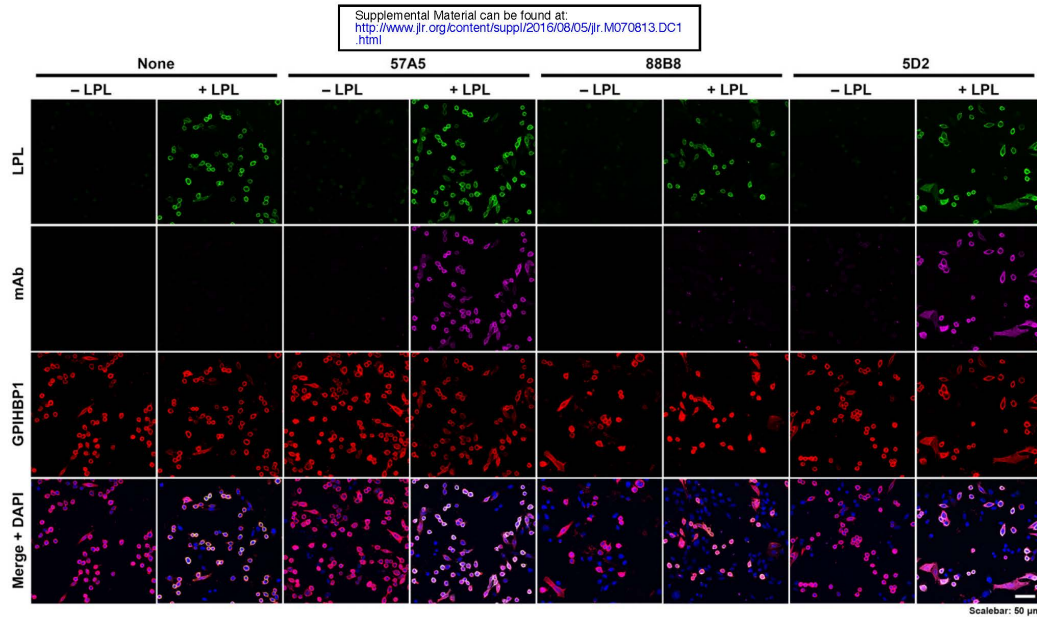


Fig. 8. Assessing the ability of mAbs 57A5, 88B8, and 5D2 bind to GPIHBP1-bound LPL. CHO pgsA-745 cells were transiently transfected with S-protein–tagged human GPIHBP1. After 24 h, the cells were incubated with V5-tagged LPL for 1 h. The LPL was then removed and the cells were washed. mAbs 57A5, 88B8, and 5D2 (20 μ g/ml) were then added to the cells and incubated for 1 h at 4°C. The cells were washed, fixed with paraformaldehyde, and then stained for GPIHBP1 with an antibody against the S-protein tag (red), and for LPL with a V5 antibody (green). mAbs 57A5, 88B8, and 5D2 were directly labeled (magenta).

implying that additional sequences at the carboxyl terminus of LPL (i.e., residues 403–448) were important for the 88B8 epitope.

mAb 57A5 bound avidly to hLPL and to a mLPL–hLPL chimera containing human residues 298–448 but not to chimeras containing human residues 330–448, 370–448, or 400–448 (Fig. 5C). In contrast to 88B8, 57A5 bound avidly to a mLPL–hLPL chimera containing human residues 327–403 (Fig. 5D).

Testing the impact of the LPL-specific mAbs on LPL activity

The tryptophan-rich motif within the 5D2 epitope (residues 380–410) is important for the ability of LPL to hydrolyze long-chain triacylglycerols but not short-chain water-soluble triacylglycerols (36). Thus, in our studies, antibody 5D2, which binds to the tryptophan-rich motif, inhibited LPL activity against triolein but not a soluble substrate (Fig. 6). mAbs 88B8 and 57A5 also reduced LPL activity against triolein but to a lesser degree (Fig. 6). None of the antibodies inhibited LPL catalytic activity with a water-soluble substrate (Fig. 6).

Assessing LPL sequences relevant to binding GPIHBP1

Earlier studies suggested that the binding of LPL to GPIHBP1 depended on LPL residues 403–438 (27). However, given that sequences throughout LPL's carboxyl-terminal domain (residues 298–448) were important for 88B8 binding, we suspected that the same sequences might also play

a role in GPIHBP1 binding. To explore this idea, we tested the ability of HL–LPL chimeras to bind to GPIHBP1 on the surface of CHO cells. Wong et al. (34) showed that it was possible to produce HL–LPL chimeras that are secreted and are catalytically active. We created HL–LPL chimeras containing hLPL residues 313–448, 330–448, 335–448, 340–448, and 345–448 (Fig. 1, supplemental Fig. S6). We then tested the ability of LPL, HL, and the HL–LPL chimeras to bind to GPIHBP1. We mixed CHO cells that had been transfected with a lipase construct with CHO cells that had been transfected with GPIHBP1. We then used immunofluorescence microscopy to assess the binding of the freshly secreted lipases to GPIHBP1 on GPIHBP1-transfected cells. As expected, full-length LPL bound avidly to GPIHBP1, but HL did not. HL–LPL chimeras containing LPL residues 313–448 and 330–448 bound to GPIHBP1, but chimeras containing LPL residues 335–448, 340–448, and 345–448 did not (Fig. 7). A Western blot experiment showed that cells expressing GPIHBP1 were capable of binding LPL as well as chimeras containing LPL residues 313–448 and 330–448, but not HL or a chimera containing LPL residues 335–448 (supplemental Fig. S7). Thus, a large segment of LPL's carboxyl-terminal domain is required for GPIHBP1 binding—as was the case for 88B8 binding.

mAb 88B8 cannot bind to GPIHBP1-bound LPL but is still useful for immunohistochemistry studies

Because 88B8 and GPIHBP1 bind to similar sequences, we suspected that 88B8 would not bind to GPIHBP1-bound

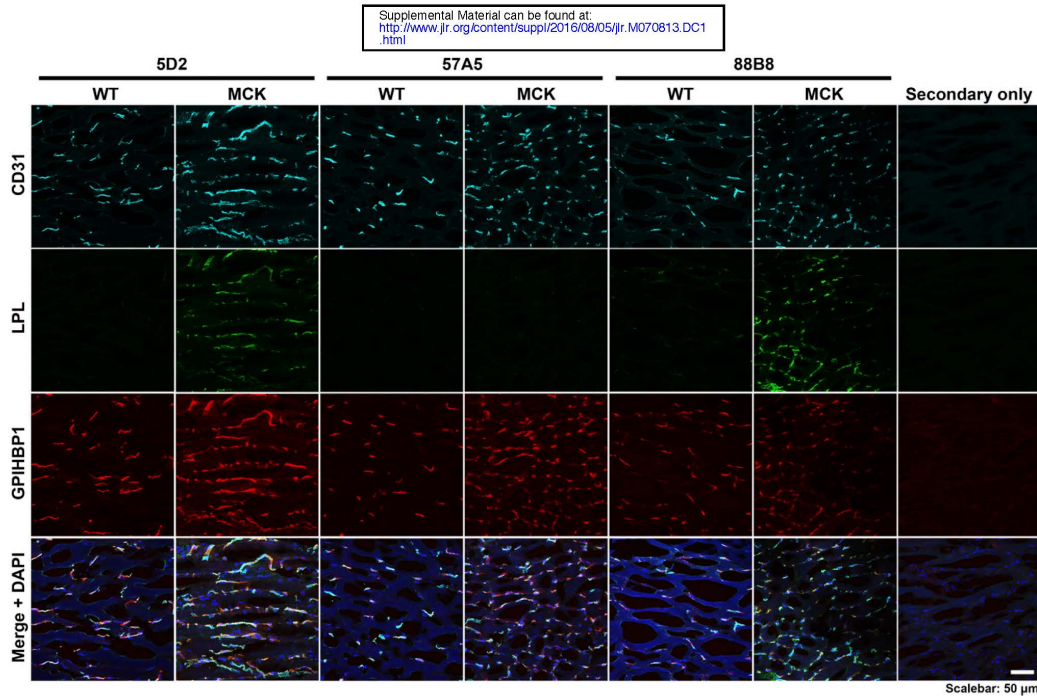


Fig. 9. Testing the capacity of mAbs 57A5, 88B8, and 5D2 to bind to hLPL in capillaries of the skeletal muscle of *Lpl*^{-/-} mice carrying a hLPL transgene driven by the muscle creatine kinase promoter (*Lpl*^{-/-}MCK-hLPL). For these studies, skeletal muscle from wild-type mice and *Lpl*^{-/-}MCK-hLPL mice was harvested and embedded in OCT, and 7-mm-thick sections were cut, placed on slides, and fixed in methanol. Tissue sections were stained with a rabbit antibody against mouse CD31 (cyan), Alexa Fluor 568-labeled mAb (57A5, 88B8, or 5D2; green), and an Alexa Fluor 647-labeled antibody against GPIHBP1 (11A12, red).

LPL on the surface of CHO cells. Indeed, this was the case (Fig. 8). In contrast, 5D2 and 57A5 did bind to GPIHBP1-bound LPL. Interestingly, the inability of 88B8 to bind to GPIHBP1-bound LPL did not interfere with its utility for immunohistochemistry studies. mAb 88B8 readily detected hLPL on capillaries after the LPL–GPIHBP1 complex was disrupted by methanol fixation (Fig. 9). mAb 5D2 also was useful for immunohistochemistry, but 57A5 was not (Fig. 9).

DISCUSSION

In the current studies, we identified a hLPL-specific mAb, 88B8, that abolishes the binding of hLPL to GPIHBP1 in both cell-free and cell-based LPL–GPIHBP1 binding assays. mAb 88B8 binding to LPL was impaired by the very same LPL missense mutations (C418Y, E421K, C438Y) that are known to interfere with the binding of LPL to GPIHBP1 (27), suggesting that 88B8 and GPIHBP1 binding sites are very similar. We suspected initially that the LPL sequences required for 88B8 binding would be confined to residues ~403–438, but this was not the case. Additional upstream sequences (residues 298–400) proved to be important for 88B8 binding. mAb 88B8 bound avidly to a mLPL–hLPL chimera containing hLPL residues 298–448 and weakly to chimeras containing residues 330–448 and

370–448. mAb 88B8 did not bind to a chimera containing hLPL residues 400–448. The fact that extensive sequences within LPL's carboxyl-terminal domain are required for 88B8 binding led us to suspect that the same sequences would be required for GPIHBP1 binding. Indeed, studies with HL–LPL chimeras showed that a large portion of LPL's carboxyl-terminal domain was required for GPIHBP1 binding. HL–LPL chimeras containing hLPL residues 313–448 and 330–448 bound to GPIHBP1, but chimeras containing LPL residues 335–448 or 340–448 did not. Thus, the ability of GPIHBP1 to bind to LPL depends on residues 330–448 and not simply residues 403–438 (as we had originally suspected). These results add considerably to our understanding of LPL sequences required for LPL–GPIHBP1 interactions.

To fully understand 88B8–LPL interactions or LPL–GPIHBP1 interactions, cocrystal structures are required. However, with the mutagenesis-based binding data that are in hand, we believe that the simplest interpretation is that both 88B8 and GPIHBP1 interact with a complex epitope that depends on the proper folding of a large portion of LPL's carboxyl-terminal domain (residues 298–448). It is equally possible that LPL residues 298–400 are simply required for the proper conformation of a more compact binding site (residues ~400–448). We do not believe that the absence of GPIHBP1 binding to the HL–LPL chimera

Supplemental Material can be found at:
<http://www.jlr.org/content/suppl/2016/08/05/jlr.M070813.DC1.html>

containing residues 389–448 means that residues 389–448 are unimportant for GPIHBP1 binding. First, the C418Y and E421K mutations abolished GPIHBP1 binding and do so without affecting LPL catalytic activity—implying that those mutations did not cause global changes in LPL structure. Second, and perhaps more importantly, Mysling et al. (11) recently reported, using hydrogen–deuterium exchange/mass spectrometry studies, that the amide hydrogens in LPL residues 419–425 were protected from deuterium exchange by GPIHBP1 binding (i.e., that the binding of GPIHBP1 to those LPL sequences limited their accessibility to solvent). In a similar fashion, we believe that residues 400–448 are relevant to 88B8 binding, despite the fact that 88B8 did not bind to the mLPL–hLPL chimera containing hLPL residues 400–448. First, 88B8 binding was disrupted by C418Y, E421K, and C438Y mutations. Second, 88B8 could not bind to the mLPL–hLPL chimera containing hLPL residues 298–403.

The epitope for 57A5 was simpler: it bound to hLPL residues 298–448 but not to residues 330–448, implying that residues 298 to 330 were crucial for the epitope. Unlike 88B8, 57A5 and 5D2 did not abolish LPL binding to GPIHBP1, but partial inhibition was clearly evident. We suspect that the binding of 5D2 and 57A5 locks LPL into a conformation with reduced affinity for GPIHBP1—or alternatively that these antibodies create a steric hindrance to GPIHBP1 binding. In earlier studies, 5D2 inhibited LPL activity against triolein but not a soluble short-chain triacylglycerol (37). We confirmed those findings and found that the same property applies, at least to some degree, to 88B8 and 57A5. We suspect that the binding of all three antibodies creates a steric hindrance or locks the carboxyl-terminal domain into a suboptimal conformation for triolein hydrolysis.

mAbs 5D2 and 57A5 had no difficulty binding to GPIHBP1-bound LPL on the surface of cultured cells, whereas 88B8 was unable to bind, reflecting the fact that GPIHBP1 and 88B8 have overlapping binding sites. Remarkably, 88B8 was still useful for immunohistochemistry. Once the LPL–GPIHBP1 complex had been disrupted by methanol fixation, mAb 88B8 readily bound to the LPL on capillaries, colocalizing with GPIHBP1 and the endothelial cell marker CD31. mAb 5D2, but not 57A5, also detected LPL in capillaries. ■

REFERENCES

- Korn, E. D. 1955. Clearing factor, a heparin-activated lipoprotein lipase. II. Substrate specificity and activation of coconut oil. *J. Biol. Chem.* **215**: 15–26.
- Korn, E. D. 1955. Clearing factor, a heparin-activated lipoprotein lipase. I. Isolation and characterization of the enzyme from normal rat heart. *J. Biol. Chem.* **215**: 1–14.
- Havel, R. J., and R. S. Gordon, Jr. 1960. Idiopathic hyperlipemia: metabolic studies in an affected family. *J. Clin. Invest.* **39**: 1777–1790.
- Merkel, M., R. H. Eckel, and I. J. Goldberg. 2002. Lipoprotein lipase: genetics, lipid uptake, and regulation. *J. Lipid Res.* **43**: 1997–2006.
- Young, S. G., and R. Zechner. 2013. Biochemistry and pathophysiology of intravascular and intracellular lipolysis. *Genes Dev.* **27**: 459–484.
- Fong, L. G., S. G. Young, A. P. Beigneux, A. Bensadoun, M. Oberer, H. Jiang, and M. Ploug. 2016. GPIHBP1 and plasma triglyceride metabolism. *Trends Endocrinol. Metab.* **27**: 455–469.
- Beigneux, A. P., B. Davies, P. Gin, M. M. Weinstein, E. Farber, X. Qiao, P. Peale, S. Bunting, R. L. Walzem, J. S. Wong, et al. 2007. Glycosylphosphatidylinositol-anchored high density lipoprotein-binding protein 1 plays a critical role in the lipolytic processing of chylomicrons. *Cell Metab.* **5**: 279–291.
- Davies, B. S. J., A. P. Beigneux, R. H. Barnes II, Y. Tu, P. Gin, M. M. Weinstein, C. Nobumori, R. Nyrén, I. J. Goldberg, G. Olivecrona, et al. 2010. GPIHBP1 is responsible for the entry of lipoprotein lipase into capillaries. *Cell Metab.* **12**: 42–52.
- Goulbourne, C. N., P. Gin, A. Tatar, C. Nobumori, A. Hoenger, H. Jiang, C. R. Grovenor, O. Adeyo, J. D. Esko, I. J. Goldberg, et al. 2014. The GPIHBP1-LPL complex is responsible for the margination of triglyceride-rich lipoproteins in capillaries. *Cell Metab.* **19**: 849–860.
- Ioka, R. X., M.-J. Kang, S. Kamiyama, D.-H. Kim, K. Magoori, A. Kamataki, Y. Ito, Y. A. Takei, M. Sasaki, T. Suzuki, et al. 2003. Expression cloning and characterization of a novel glycosylphosphatidylinositol-anchored high density lipoprotein-binding protein, GPI-HBP1. *J. Biol. Chem.* **278**: 7344–7349.
- Mysling, S., K. K. Kristensen, M. Larsson, A. P. Beigneux, H. Gardsvoll, L. G. Fong, A. Bensadoun, T. J. Jorgensen, S. G. Young, and M. Ploug. 2016. The acidic domain of the endothelial membrane protein GPIHBP1 stabilizes lipoprotein lipase activity by preventing unfolding of its catalytic domain. *eLife*. **5**: e12095.
- Franssen, R., S. G. Young, F. Peelman, J. Hertecant, J. A. Sierts, A. W. M. Schimmel, A. Bensadoun, J. J. P. Kastelein, L. G. Fong, G. M. Dallinga-Thie, et al. 2010. Chylomicronemia with low post-heparin lipoprotein lipase levels in the setting of GPIHBP1 defects. *Circ Cardiovasc Genet.* **3**: 169–178.
- Olivecrona, G., E. Ehrenborg, H. Semb, E. Makoveichuk, A. Lindberg, M. R. Hayden, P. Gin, B. S. Davies, M. M. Weinstein, L. G. Fong, et al. 2010. Mutation of conserved cysteines in the Ly6 domain of GPIHBP1 in familial chylomicronemia. *J. Lipid Res.* **51**: 1535–1545.
- Charrière, S., N. Peretti, S. Bernard, M. Di Filippo, A. Sassolas, M. Merlin, M. Delay, C. Debar, E. Lefai, A. Lachaux, et al. 2011. GPIHBP1 C89F neomutation and hydrophobic C-terminal domain G175R mutation in two pedigrees with severe hyperchylomicronemia. *J. Clin. Endocrinol. Metab.* **96**: E1675–E1679.
- Yamamoto, H., M. Onishi, N. Miyamoto, R. Oki, H. Ueda, M. Ishigami, H. Hiraoka, Y. Matsuzawa, and S. Kihara. 2013. Novel combined GPIHBP1 mutations in a patient with hypertriglyceridemia associated with CAD. *J. Atheroscler. Thromb.* **20**: 777–784.
- Rios, J. J., S. Shastry, J. Jasso, N. Hauser, A. Garg, A. Bensadoun, J. C. Cohen, and H. H. Hobbs. 2012. Deletion of GPIHBP1 causing severe chylomicronemia. *J. Inher. Metab. Dis.* **35**: 531–540.
- Coca-Prieto, I., O. Kroupa, P. Gonzalez-Santos, J. Magne, G. Olivecrona, E. Ehrenborg, and P. Valdivielso. 2011. Childhood-onset chylomicronaemia with reduced plasma lipoprotein lipase activity and mass: identification of a novel GPIHBP1 mutation. *J. Intern. Med.* **270**: 224–228.
- Plengpanich, W., S. G. Young, W. Khovidhunkit, A. Bensadoun, H. Karman, M. Ploug, H. Gardsvoll, C. S. Leung, O. Adeyo, M. Larsson, et al. 2014. Multimerization of glycosylphosphatidylinositol-anchored high density lipoprotein-binding protein 1 (GPIHBP1) and familial chylomicronemia from a serine-to-cysteine substitution in GPIHBP1's Ly6 domain. *J. Biol. Chem.* **289**: 19491–19499.
- Beigneux, A. P., R. Franssen, A. Bensadoun, P. Gin, K. Melford, J. Peter, R. L. Walzem, M. M. Weinstein, B. S. Davies, J. A. Kuivenhoven, et al. 2009. Chylomicronemia with a mutant GPIHBP1 (Q115P) that cannot bind lipoprotein lipase. *Arterioscler. Thromb. Vasc. Biol.* **29**: 956–962.
- Gonzaga-Jauregui, C., S. Mir, S. Penney, S. Jhangiani, C. Midgen, M. Finegold, D. M. Muzny, M. Wang, C. A. Bacino, R. A. Gibbs, et al. 2014. Whole-exome sequencing reveals GPIHBP1 mutations in infantile colitis with severe hypertriglyceridemia. *J. Pediatr. Gastroenterol. Nutr.* **59**: 17–21.
- Rabacchi, C., S. D'Addato, S. Palmisano, T. Lucchi, S. Bertolini, S. Calandra, and P. Tarugi. 2016. Clinical and genetic features of three patients with familial chylomicronemia due to mutations in GPIHBP1 gene. *J. Clin. Lipidol.* In press.
- Ariza, M. J., P. L. Martínez-Hernández, D. Ibarretxe, C. Rabacchi, J. Rioja, C. Grande-Aragon, N. Plana, P. Tarugi, G. Olivecrona, S. Calandra, and P. Valdivielso. 2016. Novel mutations in the GPIHBP1 gene identified in 2 patients with recurrent acute pancreatitis. *J. Clin. Lipidol.* **10**: 92–100.e1.
- Beigneux, A. P., L. G. Fong, A. Bensadoun, B. S. Davies, M. Oberer, H. Gardsvoll, M. Ploug, and S. G. Young. 2015. GPIHBP1 missense

Supplemental Material can be found at:
<http://www.jlr.org/content/suppl/2016/08/05/jlr.M070813.DC1.html>

- mutations often cause multimerization of GPIHBP1 and thereby prevent lipoprotein lipase binding. *Circ. Res.* **116**: 624–632.
24. Beigneux, A. P., B. S. Davies, S. Tat, J. Chen, P. Gin, C. V. Voss, M. M. Weinstein, A. Bensadoun, C. R. Pullinger, L. G. Fong, et al. 2011. Assessing the role of the glycosylphosphatidylinositol-anchored high density lipoprotein-binding protein 1 (GPIHBP1) three-finger domain in binding lipoprotein lipase. *J. Biol. Chem.* **286**: 19735–19743.
 25. Henderson, H. E., F. Hassan, D. Marais, and M. R. Hayden. 1996. A new mutation destroying disulphide bridging in the C-terminal domain of lipoprotein lipase. *Biochem. Biophys. Res. Commun.* **227**: 189–194.
 26. Henderson, H., F. Leisegang, F. Hassan, M. Hayden, and D. Marais. 1998. A novel Glu421Lys substitution in the lipoprotein lipase gene in pregnancy-induced hypertriglyceridemic pancreatitis. *Clin. Chim. Acta.* **269**: 1–12.
 27. Voss, C. V., B. S. Davies, S. Tat, P. Gin, L. G. Fong, C. Pelletier, C. D. Mottler, A. Bensadoun, A. P. Beigneux, and S. G. Young. 2011. Mutations in lipoprotein lipase that block binding to the endothelial cell transporter GPIHBP1. *Proc. Natl. Acad. Sci. USA.* **108**: 7980–7984.
 28. Machida, T., K. Miyashita, T. Sone, S. Tanaka, K. Nakajima, M. Saito, K. Stanhope, P. Havel, H. Sumino, and M. Murakami. 2015. Determination of serum lipoprotein lipase using a latex particle-enhanced turbidimetric immunoassay with an automated analyzer. *Clin. Chim. Acta.* **442**: 130–135.
 29. Chang, S-F., B. Reich, J. D. Brunzell, and H. Will. 1998. Detailed characterization of the binding site of the lipoprotein lipase-specific monoclonal antibody 5D2. *J. Lipid Res.* **39**: 2350–2359.
 30. Liu, M. S., Y. Ma, M. R. Hayden, and J. D. Brunzell. 1992. Mapping of the epitope on lipoprotein lipase recognized by a monoclonal antibody (5D2) which inhibits lipase activity. *Biochim. Biophys. Acta.* **1128**: 113–115.
 31. Gin, P., A. P. Beigneux, C. Voss, B. S. Davies, J. A. Beckstead, R. O. Ryan, A. Bensadoun, L. G. Fong, and S. G. Young. 2011. Binding preferences for GPIHBP1, a glycosylphosphatidylinositol-anchored protein of capillary endothelial cells. *Arterioscler. Thromb. Vasc. Biol.* **31**: 176–182.
 32. Ben-Zeev, O., H. Z. Mao, and M. H. Doolittle. 2002. Maturation of lipoprotein lipase in the endoplasmic reticulum. Concurrent formation of functional dimers and inactive aggregates. *J. Biol. Chem.* **277**: 10727–10738.
 33. Beigneux, A. P., P. Gin, B. S. J. Davies, M. M. Weinstein, A. Bensadoun, L. G. Fong, and S. G. Young. 2009. Highly conserved cysteines within the Ly6 domain of GPIHBP1 are crucial for the binding of lipoprotein lipase. *J. Biol. Chem.* **284**: 30240–30247.
 34. Wong, H., R. C. Davis, J. Nikazy, K. E. Seebart, and M. C. Schotz. 1991. Domain exchange: characterization of a chimeric lipase of hepatic lipase and lipoprotein lipase. *Proc. Natl. Acad. Sci. USA.* **88**: 11290–11294.
 35. Sattler, W., S. Levak-Frank, H. Radner, G. M. Kostner, and R. Zechner. 1996. Muscle-specific overexpression of lipoprotein lipase in transgenic mice results in increased alpha-tocopherol levels in skeletal muscle. *Biochem. J.* **318**: 15–19.
 36. Lookene, A., N. B. Groot, J. J. Kastelein, G. Olivecrona, and T. Bruin. 1997. Mutation of tryptophan residues in lipoprotein lipase. Effects on stability, immunoreactivity, and catalytic properties. *J. Biol. Chem.* **272**: 766–772.
 37. Wong, H., R. C. Davis, T. Thuren, J. W. Goers, J. Nikazy, M. Waite, and M. C. Schotz. 1994. Lipoprotein lipase domain function. *J. Biol. Chem.* **269**: 10319–10323.

Appendix II

**Lipoprotein lipase reaches the capillary lumen in chickens
despite an apparent absence of GPIHBP1**

Lipoprotein lipase reaches the capillary lumen in chickens despite an apparent absence of GPIHBP1

Cuiwen He,¹ Xuchen Hu,¹ Rachel S. Jung,¹ Mikael Larsson,¹ Yiping Tu,¹ Sandra Duarte-Vogel,¹ Paul Kim,¹ Norma P. Sandoval,¹ Tara R. Price,³ Christopher M. Allan,¹ Brian Raney,⁴ Haibo Jiang,^{1,5} André Bensadoun,⁶ Rosemary L. Walzem,³ Richard I. Kuo,⁷ Anne P. Beigneux,¹ Loren G. Fong,¹ and Stephen C. Young^{1,2}

¹Department of Medicine and ²Department of Human Genetics, David Geffen School of Medicine, University of California Los Angeles, Los Angeles, California, USA. ³Department of Poultry Science and Faculty of Nutrition, Texas A&M University, College Station, Texas, USA. ⁴University of California, Santa Cruz Genomics Institute and ⁵Centre for Microscopy, Characterisation, and Analysis, The University of Western Australia, Western Australia, Perth, Australia. ⁶Division of Nutritional Science, Cornell University, Ithaca, New York, USA. ⁷The Roslin Institute and Royal (Dick) School of Veterinary Studies, University of Edinburgh, Edinburgh, United Kingdom.

In mammals, GPIHBP1 is absolutely essential for transporting lipoprotein lipase (LPL) to the lumen of capillaries, where it hydrolyzes the triglycerides in triglyceride-rich lipoproteins. In all lower vertebrate species (e.g., birds, amphibians, reptiles, fish), a gene for LPL can be found easily, but a gene for GPIHBP1 has never been found. The obvious question is whether the LPL in lower vertebrates is able to reach the capillary lumen. Using purified antibodies against chicken LPL, we showed that LPL is present on capillary endothelial cells of chicken heart and adipose tissue, colocalizing with von Willebrand factor. When the antibodies against chicken LPL were injected intravenously into chickens, they bound to LPL on the luminal surface of capillaries in heart and adipose tissue. LPL was released rapidly from chicken hearts with an infusion of heparin, consistent with LPL being located inside blood vessels. Remarkably, chicken LPL bound in a specific fashion to mammalian GPIHBP1. However, we could not identify a gene for GPIHBP1 in the chicken genome, nor could we identify a transcript for GPIHBP1 in a large chicken RNA-seq data set. We conclude that LPL reaches the capillary lumen in chickens – as it does in mammals – despite an apparent absence of GPIHBP1.

Introduction

GPIHBP1, a glycoprotein expressed by capillary endothelial cells, is crucial for lipoprotein lipase-mediated (LPL-mediated) processing of triglyceride-rich lipoproteins (TRLs) (1–3). In mammals, GPIHBP1 can be considered as a partner protein for LPL. First, GPIHBP1 is responsible for binding LPL in the interstitial spaces and shuttling it across endothelial cells to the capillary lumen (2). In the absence of GPIHBP1, LPL is stranded within the interstitial spaces where it is useless for processing TRLs in the bloodstream (2). Second, the GPIHBP1–LPL complex on capillary endothelial cells is essential for TRL margination along capillaries (3). In the absence of GPIHBP1-bound LPL, TRLs do not stop along capillaries and simply flow on by in the bloodstream. Third, GPIHBP1 preserves the structural integrity and catalytic activity of LPL (4). In the absence of GPIHBP1, LPL's triglyceride hydrolase domain unfolds, resulting in a rapid decline in catalytic activity (4). GPIHBP1 and LPL are equally important for intravascular lipolysis; a deficiency of either protein markedly impairs intravascular triglyceride hydrolysis and leads to severe hypertriglyceridemia (chylomicronemia) (5–19). The importance of GPIHBP1 and LPL for plasma triglyceride metabolism in mammals has been underscored by human genetics; specific missense mutations in either protein can abolish LPL–GPIHBP1 interactions, resulting in reduced delivery of LPL to the capillary lumen, impaired TRL processing, and severe hypertriglyceridemia (6, 7, 9–14).

GPIHBP1 is a GPI-anchored protein of the Ly6 superfamily (35 Ly6 family members in human; 61 in mouse) (20). All Ly6 proteins have at least one approximately 80-amino acid Ly6 domain with 8 or 10

Conflict of interest: The authors have declared that no conflict of interest exists.

Submitted: August 9, 2017

Accepted: September 11, 2017

Published: October 19, 2017

Reference information:

JCI Insight. 2017;2(20):e96783.

<https://doi.org/10.1172/jci.insight.96783>.

insight.96783.

cysteines, all arranged in a characteristic spacing pattern and all disulfide bonded, creating a 3-fingered structural domain (21). GPIHBP1 is unique among Ly6 proteins in having a disordered acidic domain at its amino terminus, with 21 of 26 consecutive residues in the human protein being aspartate or glutamate (22). Recent work by Mysling et al. (4) showed that GPIHBP1, and more specifically GPIHBP1's acidic domain, prevents the spontaneous unfolding of LPL's hydrolase domain (4). GPIHBP1's Ly6 domain is responsible for high-affinity LPL binding, with the acidic domain playing only an accessory role (4). The second finger of GPIHBP1's Ly6 domain is particularly important for LPL binding (4, 23). A variety of amino acid substitutions within the second finger abolish GPIHBP1's capacity to bind LPL, in some cases by interfering with the proper formation of disulfide bonds (11, 23, 24). Mutations in W109 in human GPIHBP1 abolish the capacity of GPIHBP1 to bind LPL and do so without disrupting disulfide bond formation, suggesting that W109 is directly involved in LPL–GPIHBP1 interactions (24). W109 is perfectly conserved in the GPIHBP1 of all mammalian species (Supplemental Table 1).

Genes for GPIHBP1 and LPL are easily detectable in the genomes of all mammals, including marsupials and the egg-laying platypus (20, 25–27). Human and mouse LPL are 92% identical at the amino acid level; the Ly6 domains of human and mouse GPIHBP1 are 59% identical. Because LPL and GPIHBP1 are partners in plasma triglyceride metabolism, the conservation of both proteins during mammalian evolution is not surprising. However, when one examines the genomes of lower vertebrates (e.g., fish, birds, reptiles), there is a striking discrepancy between GPIHBP1 and LPL. LPL is highly conserved in every lower vertebrate species (e.g., the amino acid sequences of human and chicken LPL [cLPL] are 72% identical), but no one has yet identified a GPIHBP1 ortholog in the chicken or any other lower vertebrate species (25, 26). The function of LPL in plasma triglyceride metabolism is conserved in lower vertebrates. When goat polyclonal antibodies against cLPL were injected intravenously into chickens, they inactivated LPL, blocking TRL processing and resulting in hypertriglyceridemia (28).

Given that the structure of LPL as well as its function in TRL processing are conserved in lower vertebrates, the absence of LPL's partner protein (i.e., GPIHBP1) is surprising. Since GPIHBP1 is essential for shuttling LPL into capillaries in mammals, the obvious question is whether the LPL in lower vertebrates is able to reach the capillary lumen. It is conceivable that TRL processing in lower vertebrates might be fundamentally different, with TRLs being transported across capillaries and undergoing processing by the LPL within the interstitial spaces. This possibility may not be farfetched, given that TRLs produced by the chicken intestine are said to move into capillaries by vesicular transport (29). Another possibility is that the LPL in lower vertebrates reaches the capillary lumen, but by a mechanism independent of GPIHBP1.

To gain further insights into TRL processing in lower vertebrate species, we used cLPL-specific antibodies to define the localization of LPL in chicken tissues. We also tested whether cLPL has the capacity to bind to human and mouse GPIHBP1.

Results

We took advantage of goat antibodies against cLPL (30, 31) to examine the localization of LPL in chicken tissues. The first step was to assess the specificity of the antibodies, which had been purified on a cLPL immunoaffinity column (generated with LPL purified from chicken adipose tissue). We examined, by Western blotting, the ability of the immunopurified antibodies to bind to LPL in crude homogenates of chicken tissues. The immunopurified IgGs against cLPL bound to a single protein of the expected size (~52 kDa), except in the heart where the IgGs also bound to a 38-kDa protein (Figure 1A). We were confident that the 38-kDa band in the heart extracts was a cLPL breakdown fragment, but to be certain about that conclusion we repeated the Western blot studies with IgGs that had been further purified on a second cLPL immunoaffinity column (generated with a cLPL polypeptide produced in *E. coli*). Again, the antibodies bound exclusively to LPL (along with the 38-kDa LPL breakdown fragment in the heart) (Figure 1B). To determine if the purified IgG fraction would be useful for immunohistochemistry studies, we first tested their ability to bind to CHO cells that had been transfected with an expression vector for V5-tagged cLPL. Regardless of whether the cells were fixed with methanol or paraformaldehyde, the purified IgGs against cLPL bound avidly and specifically to transfected cells, colocalizing with an antibody against the V5 tag (Figure 2).

Most of the LPL in mouse tissues is bound to GPIHBP1 on capillary endothelial cells (2). In the absence of GPIHBP1, LPL remains within the interstitial spaces and never reaches the capillary lumen (2). In immunohistochemistry studies, we found that much of the LPL in the chicken heart is associated with capillary endothelial cells, colocalizing with an endothelial cell marker (von Willebrand factor; vWF)

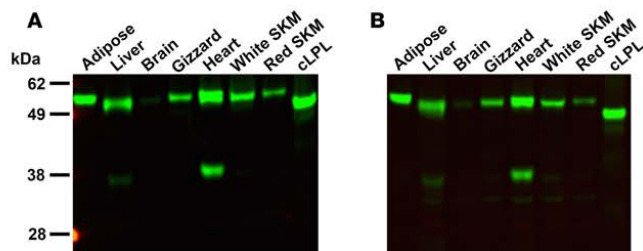


Figure 1. Testing the specificity of an immunopurified goat IgG against chicken lipoprotein lipase (cLPL) with Western blots. Proteins from chicken tissue extracts (30 μ g/lane) were size-fractionated by SDS-PAGE and then examined by Western blotting. (A) Western blot with an immunopurified goat IgG against cLPL. The antibodies bound specifically to cLPL from *E. coli* and recognized a band of similar size in chicken tissues. In heart, the anti-cLPL antibodies also bound to a smaller fragment of approximately 38 kDa. (B) Western blot with the same antibodies after they had been repurified on a second cLPL immunoaffinity column generated with cLPL from *E. coli*. SKM: skeletal muscle.

(Figure 3A). There was no binding of nonimmune goat IgGs or the secondary antibody alone to capillaries in chicken tissues (Figure 3A). The presence of cLPL on capillaries of heart and adipose tissue was confirmed in a second experiment (Figure 3B). In a third experiment, we also observed colocalization of vWF and LPL (Supplemental Figure 1; supplemental material available online with this article; <https://doi.org/10.1172/jci.insight.96783DS1>). There was occasional LPL staining that did not coincide with vWF staining, more so than in comparable experiments in mouse tissues, raising the possibility that a fraction of the cLPL in tissues remained within the interstitial spaces (Figure 3 and Supplemental Figure 1).

To determine if cLPL is located along the luminal surface of capillaries, 9-day-old chickens were injected intravenously with an Alexa Fluor 555-labeled goat IgG against cLPL, a fluorescein-labeled *Lens culinaris* agglutinin (a lectin), and an Alexa Fluor 647-labeled nonimmune goat IgG. After perfusion-fixation, white adipose tissue (WAT), heart, liver, and cerebellum were harvested for immunohistochemistry. The goat IgGs against cLPL bound to capillaries in heart and WAT, colocalizing with the lectin (Figure 4). The lectin also bound to the luminal surface of large blood vessels, whereas IgGs against cLPL did not. Also, there was no binding of cLPL antibodies to capillaries of the cerebellum (Figure 4). Only trace amounts of the nonimmune goat IgG were detectable in capillaries of chicken heart, WAT, or cerebellum, demonstrating that the perfusion of tissues was adequate (Figure 4). As expected, the nonimmune goat IgGs were bound by immunoglobulin receptors in the liver (Figure 4). Additional images showing the binding of the cLPL-specific IgGs to capillaries of chicken tissues are shown in Supplemental Figure 2. The binding of cLPL-specific IgGs to the luminal surface of heart and WAT capillaries was confirmed with further experiments in which chickens were injected with the Alexa Fluor 555-labeled goat IgG against cLPL and a fluorescein-labeled *Lens culinaris* agglutinin (Supplemental Figure 3).

LPL was released rapidly from isolated chicken hearts by perfusing the hearts with heparin (Figure 5A). The cLPL released by heparin was catalytically active (Figure 5B), and the enzymatic activity could be abolished with the goat antiserum against cLPL (Figure 5C). The rapid release of LPL from isolated chicken hearts during the heparin perfusion was consistent with results with isolated mouse hearts. LPL was released rapidly from hearts of wild-type mice with heparin, but LPL release from hearts of *Gpihbp1*-deficient mice (where the LPL is mislocalized to the interstitial spaces) was reduced in amount and substantially delayed (Figure 5D). We also examined the release of LPL into the plasma compartment after giving chickens an intravenous injection of heparin. Again, the release of LPL into the plasma was rapid (Figure 5, E and F), consistent with the LPL being located inside blood vessels (2). LPL protein and LPL activity could also be released from isolated chicken hearts with a perfusion of phosphatidylinositol-specific phospholipase C (PIPLC) (Figure 6).

The location of cLPL within tissues (i.e., bound to capillaries but not large blood vessels of the heart; absent in brain capillaries) resembles the localization of GPIHBP1 and LPL in mouse tissues (1, 2). In mice, the presence of LPL in capillaries depends on GPIHBP1 (1, 2). To explore the possibility that the distribution of LPL in chickens might be governed by GPIHBP1, we first used a cell-based binding assay to test whether cLPL (produced in CHO cells) is capable of binding to human or mouse

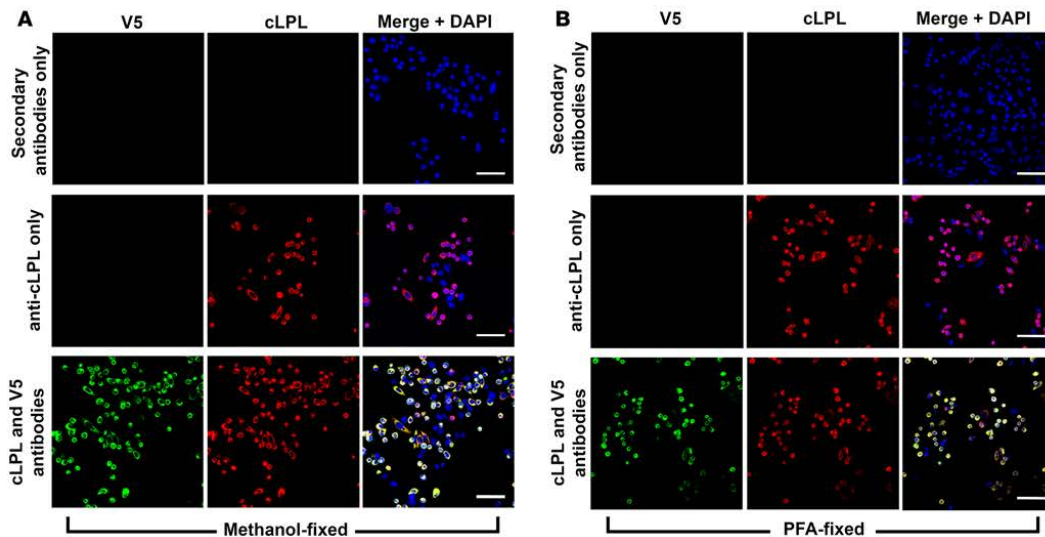


Figure 2. Testing the ability of an immunopurified goat IgG against chicken lipoprotein lipase (cLPL) to bind to cLPL in cultured cells. CHO pgsA-745 cells were transiently transfected with V5-tagged cLPL. Immunocytochemistry studies were performed on fixed and permeabilized cells with a goat antibody against cLPL and a mouse monoclonal antibody against the V5 tag. Binding of the primary antibodies was detected with an Alexa Fluor 555-conjugated donkey anti-goat IgG (red) and an Alexa Fluor 488-conjugated donkey anti-mouse IgG (green). As experimental controls, we included transfected cells that had been incubated with secondary antibodies alone and cells that had been incubated with the anti-cLPL antibody alone. DNA was stained with DAPI (blue). (A) Immunocytochemistry studies on cells that had been fixed with methanol. (B) Studies of cells fixed with paraformaldehyde (PFA). Scale bars: 50 μm .

GPIHBP1. We also examined the ability of mouse, human, and cLPL to bind to mutant GPIHBP1 proteins that lack the ability to bind LPL (human GPIHBP1-W109S, mouse GPIHBP1-W108S) (23). As expected, human and mouse LPL bound to wild-type versions of mouse and human GPIHBP1, but not to human GPIHBP1-W109S or mouse GPIHBP1-W108S (Figure 7). Remarkably, cLPL also bound to wild-type human or mouse GPIHBP1 but not to the mutant GPIHBP1 proteins (Figure 7). We observed small amounts of cLPL binding to a few of the nontransfected cells (Figure 7B), but most of the binding of cLPL was to cells that had been transfected with GPIHBP1.

A p.C418Y substitution in human LPL abolishes LPL's ability to bind to human or mouse GPIHBP1 (14). Introducing the corresponding mutation into cLPL (p.C420Y) abolished the ability of cLPL to bind to human or mouse GPIHBP1 (Figure 8).

A segment of human chromosome 8 containing *GPIHBP1* is syntenic to a segment of chicken chromosome 2 (Table 1). In both species, the upstream portion of the syntenic region encodes genes for several Ly6 proteins (PSCA, SLURP1, LYPD2). The Ly6 domains of chicken and human PSCA, SLURP1, and LYPD2 are 47%–65% identical. The downstream portion of the syntenic region contains genes for *TOP1MT*, *MAFA*, and *ZC3H3*. Fifteen genes on human chromosome 8, including *GPIHBP1*, are located between *LYPD2* and *TOP1MT*, whereas only 4 genes have been identified between *LYPD2* and *TOP1MT* on chicken chromosome 2 (Table 1); those genes encode Ly6E-like proteins (ENSGALG00000039585, ENSGALG00000041621, ENSGALG00000043582, ENSGALG00000045170). None of the 4 Ly6E-like proteins resembles human or platypus GPIHBP1, none contains an amino-terminal acidic domain, and the level of amino acid sequence identity with human or platypus GPIHBP1 is similar to the level of sequence identity to SLURP1 (a protein involved in keratinocyte differentiation) (32) (Supplemental Table 1, A and B). None of the 4 chicken Ly6E-like proteins displayed significant sequence homology to the most conserved region of mammalian GPIHBP1 (residues 106–115 in human GPIHBP1) (Supplemental Table 1C). Aside from the 4 Ly6E-like genes within the syntenic region of chicken chromosome 2, 10 other Ly6 genes exist in the chicken databases; none of those proteins resembles GPIHBP1 (Supplemental Table 2).

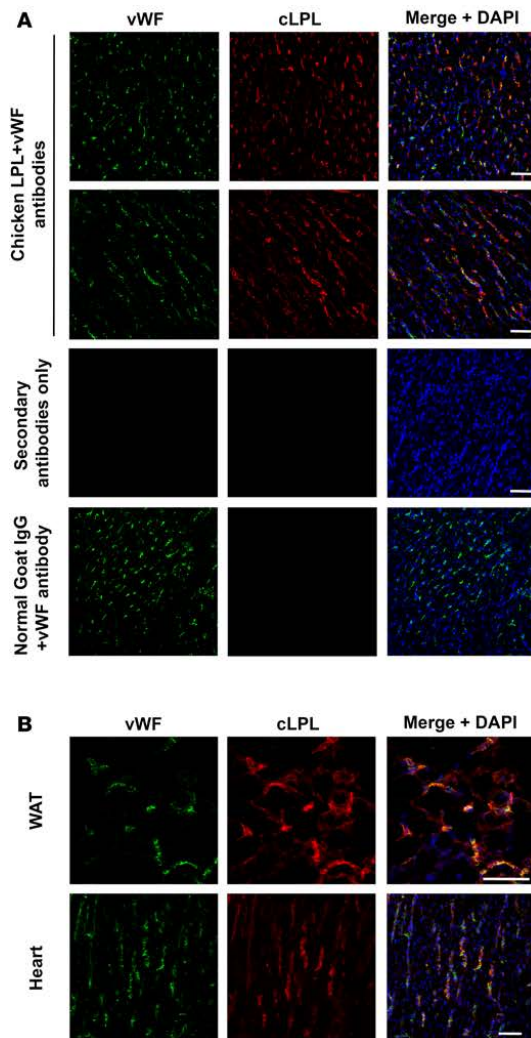


Figure 3. LPL in chicken tissues is associated with capillaries. Frozen sections from chicken white adipose tissue (WAT) and heart were stained with a rabbit antibody against von Willebrand factor (vWF), followed by an Alexa Fluor 488-conjugated donkey anti-rabbit IgG (green) and an Alexa Fluor 555-conjugated goat anti-chicken lipoprotein lipase (anti-cLPL) IgG (red). DNA was stained with DAPI (blue). **(A)** Sections of heart stained with both cLPL and vWF antibodies, revealing colocalization of cLPL and vWF in capillaries. As controls, we examined a section incubated with secondary antibodies alone and a section stained with the vWF antibody and nonimmune goat IgG. **(B)** An independent chicken immunohistochemistry study in which sections of WAT and heart were stained with cLPL and vWF antibodies. Scale bars: 50 μ m.

The expression patterns of the 4 chicken Ly6E-like proteins did not closely resemble the pattern of GPIHBP1 in mammals (high in heart, adipose tissue, lung; medium levels in skeletal muscle; low levels in liver; absent from the brain). As judged by RNA sequencing (RNA-seq), ENSGALG00000041621 was expressed at high levels in lung and gizzard; medium levels in the optic lobe, thyroid, Harderian gland, and liver; and low levels in trachea, cerebellum, and heart. ENSGALG00000039585 was expressed at high levels in the skin, medium to low levels in the Harderian gland, and very low levels in the heart. ENSGALG00000045170 was expressed at high levels in skin, Harderian gland, and thymus; medium levels in thyroid and gizzard; and low levels in the heart. ENSGALG00000043582 was expressed at high levels in the trachea and medium to low levels in heart, Harderian gland, lung, and skin.

Even though the homology between GPIHBP1 and the 4 chicken Ly6E-like proteins and the pattern of expression did not seem consistent with a role in plasma triglyceride metabolism, we expressed S-protein-tagged versions of the 4 Ly6E-like proteins in CHO cells and tested their ability to bind cLPL. All of the Ly6E-like proteins could be released from the surface of cells with PIPLC (data not shown), but none bound cLPL (Figure 9). We again observed binding of cLPL to human GPIHBP1 (Figure 9).

It is possible that the failure to identify a chicken GPIHBP1 gene was due to gaps in the chicken genomic DNA sequences or incomplete annotation. With the assistance from the UC Santa Cruz Genomics Institute, we examined *GPIHBP1* sequences from 46 mammals and examined genomes of 26 lower vertebrates for sequences similar to the sequences of the human and platypus

GPIHBP1 genes, but no matches were found. To address the possibility that the chicken GPIHBP1 gene is located in an unassembled region of the genome or that the annotation was incomplete, we examined short-read RNA-seq and long-read isoform sequencing (Iso-Seq) chicken data sets for transcripts similar to mammalian GPIHBP1. The short-read RNA-seq data set was generated from 20 chicken tissues, including heart and adipose tissue (>3 billion paired-end reads). The Iso-Seq data were generated from adult chicken brain, Hamburger-Hamilton (HH) stage 26 whole embryos, and pooled embryonic heart samples (HH stages 18–20, 25, and 32).

Transcriptome annotations were generated from both the RNA-seq and Iso-Seq data, and the resulting transcript models were mapped to human, mouse, platypus, and sheep GPIHBP1 sequences and to other chicken Ly6 proteins with Blastx. All hits were manually examined for GPIHBP1 sequence motifs. We defined the GPIHBP1 sequence motifs by several conserved features in mammalian GPIHBP1, as outlined in the Methods. No chicken transcript contained these GPIHBP1 hallmarks. The short-read RNA-seq data set represented a high-depth search of the mapped exome. Thus, the failure to find candidate sequences for

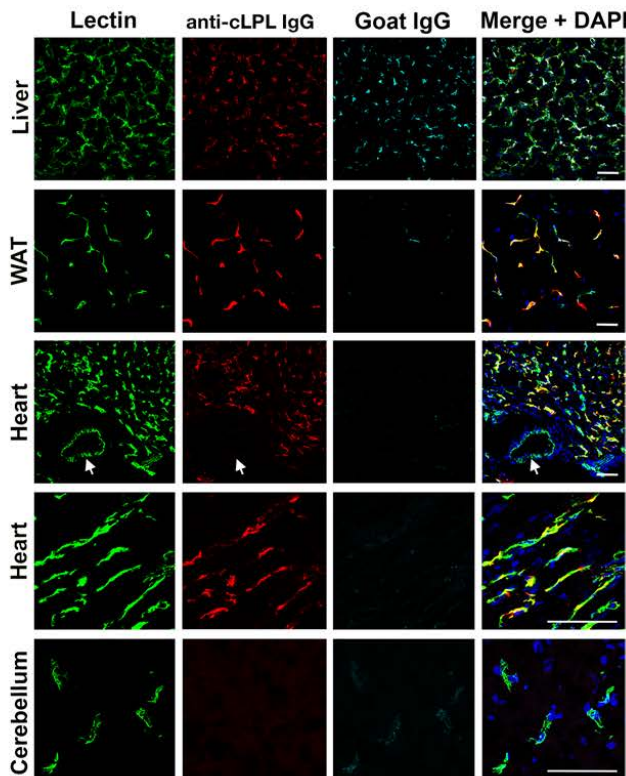


Figure 4. Chicken lipoprotein lipase (cLPL) is located along the luminal surface of capillaries. A 9-day-old chicken was given an intravenous injection of 0.7 mg of an Alexa Fluor 555-labeled goat IgG against cLPL (red), 0.5 mg of fluorescein-labeled *Lens culinaris* agglutinin (Lectin, green), and 0.7 mg of Alexa Fluor 647-labeled nonimmune goat IgG (cyan). After 4 minutes, the chicken was perfused with 50 ml of PBS followed by 30 ml of 3% paraformaldehyde (PFA) in PBS. Liver, white adipose tissue (WAT), heart, and cerebellum were harvested, fixed in 3% PFA, and 50- μ m sections of WAT and 10- μ m sections of heart, liver, and cerebellum were prepared. The lectin bound to endothelial cells of capillaries and larger blood vessels; the goat IgG against cLPL bound to capillaries but not larger blood vessels (arrows). The nonimmune goat IgG did not bind to blood vessels of the heart, WAT, or cerebellum (indicating an effective perfusion) but as expected did bind to macrophages in the liver. DNA was stained with DAPI (blue). Scale bars: 50 μ m.

a chicken GPIHBP1 strongly suggests that a gene for GPIHBP1 is not present in the *Gallus gallus* genome assembly 4.0. The Iso-Seq data set allowed us to identify unmapped chicken transcripts (i.e., transcripts not present in the *Gallus gallus* genome assembly 4.0). Again, no transcripts encoding a chicken GPIHBP1 were identified (i.e., no transcripts encoding a Ly6 protein with an acidic domain; no transcripts resembling human or platypus GPIHBP1; no Ly6 proteins with homology to the most conserved region of GPIHBP1).

Discussion

In mammals, GPIHBP1 plays 3 crucial roles in intravascular triglyceride metabolism — shuttling LPL to its site of action in the capillary lumen, facilitating the margination of lipoproteins along capillaries, and stabilizing the structure and activity of LPL (2–4). However, GPIHBP1 — the protein that is so essential for intravascular lipolysis in mammals — has never been identified in the chicken or any other lower vertebrate species. In the current study, our goal was to determine if LPL in chickens, despite an apparent absence of GPIHBP1, could reach the capillary lumen. The results were clear: LPL in chickens does reach the capillary lumen. First, by immunohistochemistry, LPL is present on capillaries of chicken heart and adipose tissue, colocalizing with vWF (an endothelial cell marker). Second, a goat IgG against cLPL, when injected intravenously into chickens, binds to LPL on the luminal surface of capillary endothelial cells, whereas a nonimmune chicken IgG does not. Third, LPL protein and catalytic activity are released rapidly from isolated chicken hearts after an infusion of heparin, mirroring results obtained with isolated hearts of wild-type mice (where the LPL is unequivocally intravascular). When we performed studies on isolated hearts of *Gpihbp1*-deficient mice (where the LPL is extravascular), the release of LPL by heparin was substantially delayed. Finally, we found that cLPL enters the bloodstream rapidly after an intravenous injection of heparin, consistent with LPL being located within capillaries. In earlier studies of wild-type mice (2), we found that LPL enters the plasma rapidly after an intravenous injection of heparin, whereas the entry of LPL into plasma was substantially delayed in *Gpihbp1*-deficient mice (33).

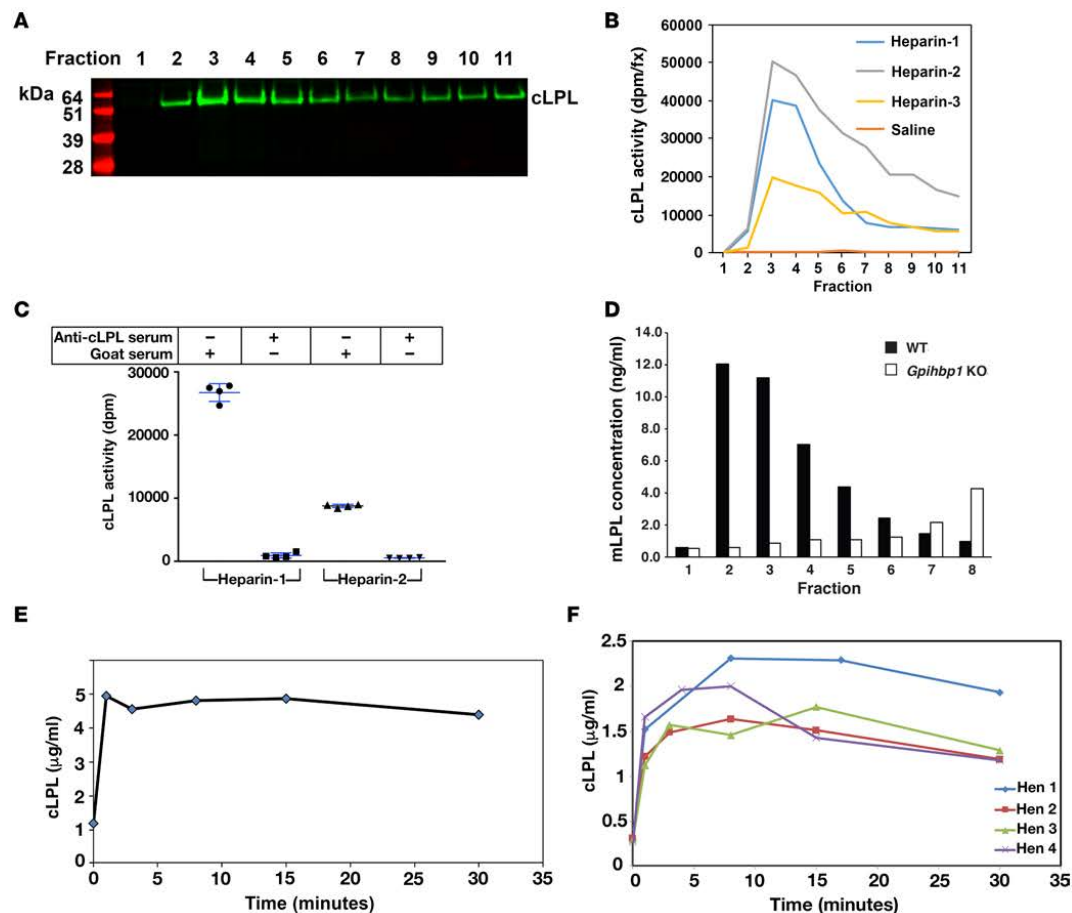


Figure 5. Chicken lipoprotein lipase (cLPL) can be released from tissues with heparin. (A) Isolated chicken hearts were perfused with 20 U/ml heparin, and cLPL protein was detected in individual fractions (0.2 ml/fraction) by Western blotting with a goat antibody against cLPL. (B) cLPL activity in the fractions from 3 different chickens (Heparin-1, Heparin-2, Heparin-3) was measured with a [3 H]triolein substrate. As a control, a chicken heart was perfused with saline only (Saline). (C) Inhibition of the LPL activity with a goat antiserum against cLPL. For these studies, we pooled fractions 3–5 from 2 of the chickens (Heparin-1 and Heparin-2). We aliquoted 25 μ l of the pooled fractions and then added either 50 μ l of the goat antiserum against cLPL or normal goat serum. We then performed LPL activity assays. The 4 data points represent duplicate lipase assays on the fractions from 2 chickens. (D) Bar graph showing rapid heparin-mediated release of mouse LPL (mLPL) from an isolated heart of a wild-type mouse (black bars). Heparin-mediated release of mLPL from the heart of a *Gpihbp1*-deficient mouse was delayed (white bars). Similar results were observed in 2 other pairs of wild-type and *Gpihbp1*-deficient mice. (E) Rapid release of cLPL (as measured by ELISA) into the plasma of a cockerel after an intravenous injection of heparin (2 U/g body weight). (F) Rapid release of cLPL into the plasma of 4 hens after an intravenous injection of heparin (2 U/g body weight).

Finding LPL within chicken capillaries implies that plasma triglyceride metabolism is similar in mammals and birds, with LPL working inside capillaries to carry out the lipolytic processing of TRLs. While we are confident that LPL is primarily intravascular in the chicken (and presumably other avian species), we would caution against extrapolating the findings in chickens to other lower vertebrates (e.g., reptiles, amphibians, and fish). In those species, the processing of TRLs may be significantly different. Of note, the plasma triglyceride levels in Burmese pythons increase 50- to 150-fold after a meal and remain elevated for several days (34), implying that TRL processing by LPL, if it occurs intravascularly in that species, may be rather inefficient.

What explains intravascular LPL in chickens? One possibility is that chickens actually have a bona fide GPIHBP1, but this gene has not yet been uncovered, either because of gaps in genomic DNA sequences or

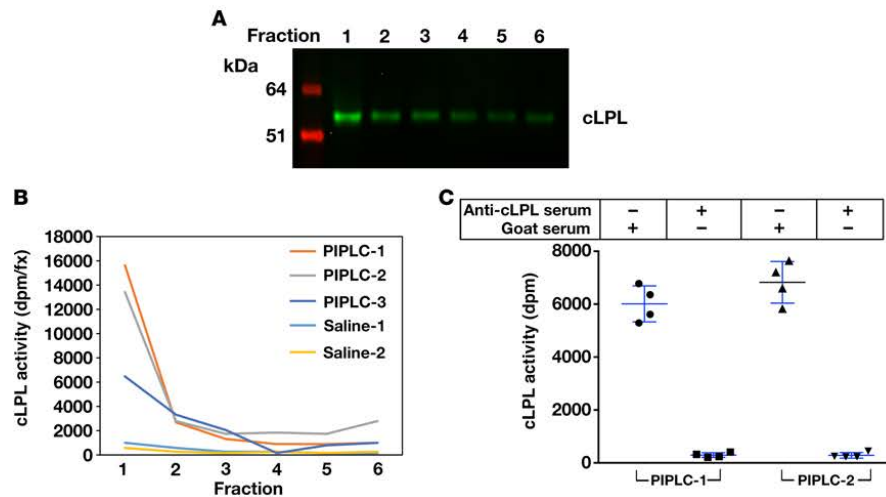


Figure 6. Chicken lipoprotein lipase (cLPL) is released from chicken hearts by phosphatidylinositol-specific phospholipase C (PIPLC). Isolated chicken hearts were perfused with 6 U/ml PIPLC or normal saline alone and incubated in a water bath for 10 minutes at 37°C. The hearts were then perfused with Tyrode's buffer. Six fractions were collected, and cLPL mass and activity were measured. **(A)** Western blots demonstrating that PIPLC releases cLPL into the perfusate. **(B)** Activity assays with a [3 H]triolein substrate, revealing that PIPLC releases catalytically active cLPL into the perfusate. Three independent experiments with PIPLC were performed (PIPLC-1, PIPLC-2, PIPLC-3), and 2 studies were performed with normal saline alone (Saline-1, Saline-2). **(C)** Inhibition of PIPLC-released cLPL activity with a goat antibody against cLPL. We pooled the fractions from the PIPLC-1 and PIPLC-2 experiments, and cLPL activity was measured in the presence of either the goat antiserum against cLPL or normal goat serum. The 4 data points represent lipase assays, performed in duplicate, on the fractions from 2 chickens.

incomplete annotation. Interestingly, the chicken gene for APOC2, an LPL cofactor, has never appeared in the genomic DNA databases, despite the fact that chicken APOC2 was identified and characterized more than 20 years ago (35). Notwithstanding the APOC2 example, we are skeptical that the apparent absence of GPIHBP1 in the chicken genomic DNA databases is due to incomplete sequences or annotation, simply because GPIHBP1 has not been identified in any lower vertebrate. Also, after examining the sequences for more than 3 billion RNA sequence tags, no transcripts for GPIHBP1 were found (i.e., no Ly6 proteins with an acidic domain; no Ly6 proteins with strong similarity to mammalian GPIHBP1). Given that GPIHBP1 should be expressed at a relatively high level in at least one of the tissue types sequenced, it seems unlikely that a GPIHBP1 transcript would evade the depth of the RNA-seq efforts. However, the results from the short-read RNA-seq data set include only genes present in the *Gallus gallus* genome assembly 4.0, and it is possible that the GPIHBP1 locus is simply missing from that assembly. The absence of GPIHBP1 motifs in the long-read Iso-Seq data (where unmapped transcripts were assessed) provides strong support for the notion that GPIHBP1 is absent in the chicken, particularly since these data included transcripts from embryonic chicken heart at several different HH stages. While it is still conceivable that a chicken GPIHBP1 might evade these sequence-based searches, we believe that it is rather unlikely and that our results favor the view that chickens do not have GPIHBP1 and instead express a distinct protein for transporting LPL into capillaries.

The stretch of chicken chromosome 2 syntenic to the *GPIHBP1* locus on human chromosome 8 encodes 4 Ly6E-like proteins of unknown function. None of those proteins bound cLPL. The absence of LPL binding was not particularly surprising because the sequences of the 4 Ly6E-like proteins did not resemble the sequences for human or platypus GPIHBP1 (including the most highly conserved segment of GPIHBP1). Indeed, the sequences for the 4 Ly6E-like proteins were no more similar to GPIHBP1 than to SLURP1, a protein involved in keratinocyte differentiation (32). Also, the expression patterns of the 4 Ly6E-like proteins, as judged by RNA-seq, appear to be inconsistent with a role for those proteins in triglyceride metabolism. For example, none were expressed at high levels in the heart; ENSGALG00000041621 was expressed in the central nervous system; ENSGALG00000039585 and ENSGALG00000045170 were expressed at high levels in the skin; and ENSGALG00000043582 was expressed at high levels in the trachea.

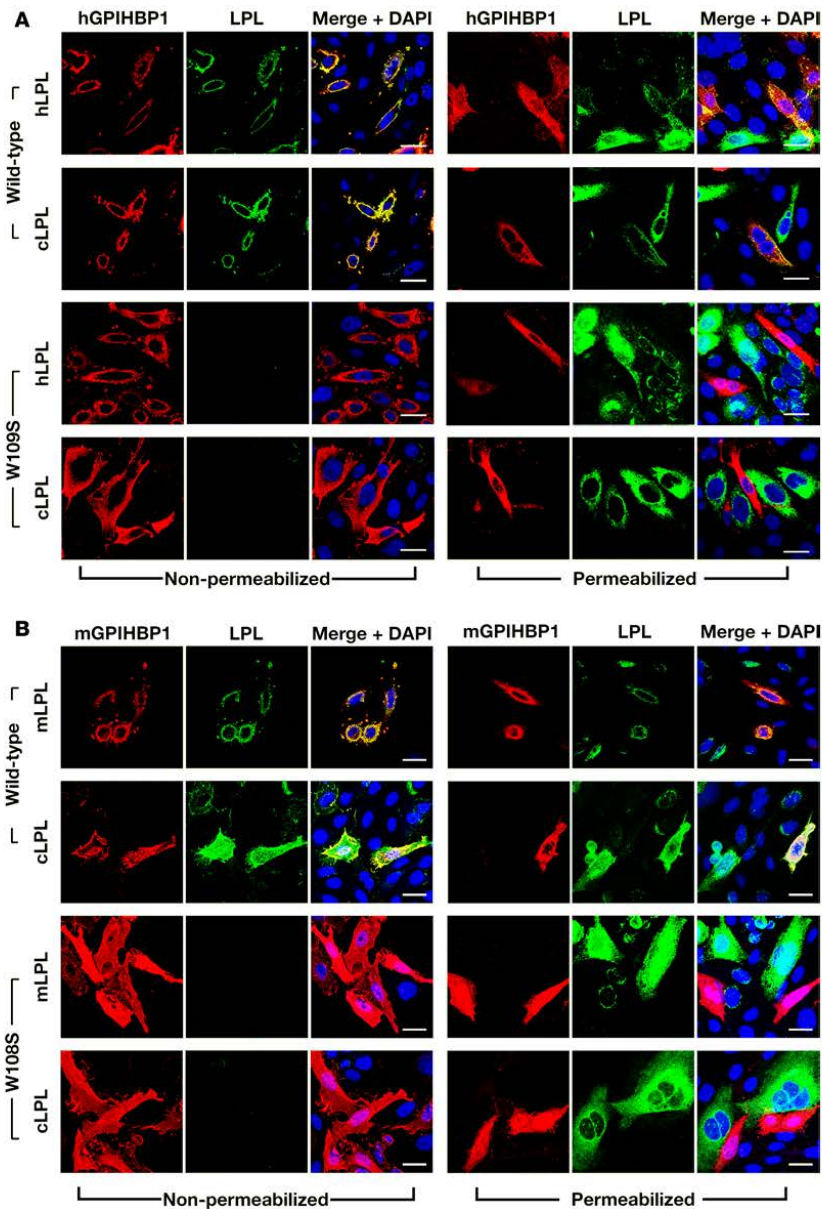


Figure 7. Chicken lipoprotein lipase (cLPL) binds to wild-type mouse GPIHBP1 (mGPIHBP1) or human GPIHBP1 (hGPIHBP1) but not to mutant GPIHBP1 proteins (mGPIHBP1-W108S, hGPIHBP1-W109S) that lack the ability to bind cLPL. CHO pgsA-745 cells were transiently transfected with S-protein-tagged versions of wild-type or mutant GPIHBP1 and coplated with cells that had been transfected with V5-tagged versions of cLPL. Immunocytochemistry studies were performed on permeabilized and nonpermeabilized cells with a goat antibody against the S-protein tag (red) and a mouse antibody against the V5 tag (green). DNA was stained with DAPI (blue). **(A)** Immunocytochemistry studies showing that the secreted human (hLPL) or cLPL bound avidly to neighboring CHO cells expressing wild-type hGPIHBP1 (hence, hLPL and cLPL colocalized with hGPIHBP1) but not to CHO cells expressing hGPIHBP1-W109S (no colocalization). **(B)** Immunocytochemistry studies showing that the secreted mouse LPL (mLPL) or cLPL bound avidly to neighboring CHO cells expressing wild-type mGPIHBP1 (colocalization) but not to CHO cells expressing mGPIHBP1-W108S (no colocalization). Scale bars: 20 μ m.

It is possible that another protein, completely unrelated to GPIHBP1, transports LPL to the capillary lumen in chickens, perhaps by interacting with sequences not present in mammalian LPL proteins. cLPL contains a 15-residue carboxyl-terminal extension enriched in positively charged residues (Supplemental Table 3). That extension is highly conserved among other avian species (Supplemental Table 3). Perhaps another transporter binds those sequences and mediates the transport of LPL across capillaries. Another possibility is that the positively charged extension augments binding to endothelial cell heparan sulfate proteoglycans (HSPGs), perhaps including GPI-anchored glypicans. The possible involvement of HSPGs

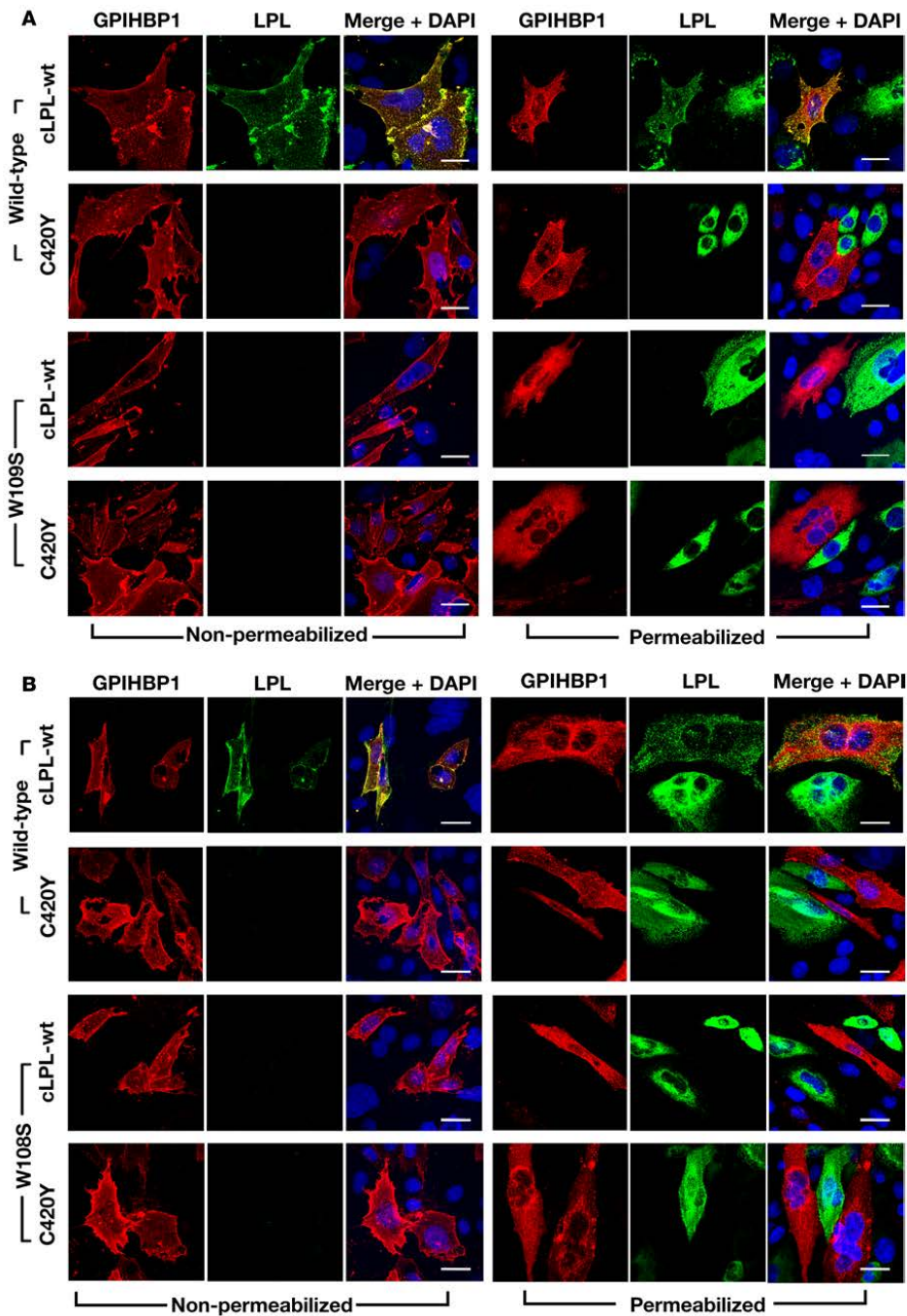


Figure 8. Wild-type chicken lipoprotein lipase (cLPL-wt), but not a mutant cLPL with a p.C420Y mutation, binds to GPIHBP1. CHO pgsA-745 cells were transiently transfected with S-protein-tagged wild-type human (h) or mouse (m) GPIHBP1 (or hGPIHBP1-W109S or mGPIHBP1-W108S) and coplated with cells that had been transfected with V5-tagged versions of cLPL (wt or C420Y). Immunocytochemistry studies were performed on permeabilized and nonpermeabilized cells with a goat antibody against the S-protein tag (red) and a mouse monoclonal antibody against the V5 tag (green). DNA was

stained with DAPI (blue). (A) Immunocytochemistry studies showing that cLPL-wt bound avidly to neighboring CHO cells expressing wild-type hGPIHBP1 (hence cLPL-wt colocalized with hGPIHBP1), whereas cLPL-C420Y had no capacity to bind to cells expressing wild-type hGPIHBP1 (no colocalization). Cells expressing hGPIHBP1-W109S did not bind cLPL-wt. (B) Immunocytochemistry studies showing that cLPL-wt bound avidly to CHO cells expressing wild-type mGPIHBP1 (colocalization), while LPL-C420Y had no capacity to bind to cells expressing wild-type mGPIHBP1 (no colocalization). Cells expressing mGPIHBP1-W108S did not bind cLPL-wt. Scale bars: 20 μm .

in LPL transport has been proposed previously (36). In our studies, perfusing chicken hearts with PIPLC released cLPL protein and activity. That observation implies that some or all of the LPL on chicken capillaries could be bound to a GPI-anchored protein, but caution is warranted. We know that perfusing isolated mouse hearts with large amounts of PIPLC can result in lysis of endothelial cells and adjacent cardiomyocytes. In our chicken experiments, we used low amounts of PIPLC and observed no visual evidence of myocardial damage, but we cannot exclude the possibility that some or all of the LPL released by PIPLC originated from parenchymal cells.

cLPL binds avidly to mouse and human GPIHBP1 but not to mutant versions of human or mouse GPIHBP1 lacking the capacity to bind LPL (e.g., human GPIHBP1-W109S, mouse GPIHBP1-W108S) (23, 24). Also, cLPL-C420Y could not bind to human or mouse GPIHBP1. These findings suggest that the interaction between cLPL and GPIHBP1 is rather specific. One might be tempted to infer from these observations that GPIHBP1 must be present in chickens, but we doubt that any such inference is justified. We suspect that the structure of LPL was conserved during vertebrate evolution based on the protein's ability to hydrolyze triglycerides. We further suspect that GPIHBP1 evolved to fit this highly conserved structure. According to this viewpoint, it would not be particularly surprising that cLPL would retain some ability to bind to GPIHBP1, nor would it be surprising that amino acid substitutions that disrupt the binding of human LPL to GPIHBP1 would also disrupt the binding of cLPL to GPIHBP1. The notion that GPIHBP1 in mammals evolved to fit an ancient and highly conserved enzyme is not farfetched. The estrogen receptor appeared early in animal evolution as a protein that activates gene transcription in response to a specific sterol (estrogen). During vertebrate evolution, additional sterol receptors evolved to fit the structures of sterols that had always been present as intermediates in the synthesis of estrogen (37). Also, it is noteworthy that mammalian apo-E binds avidly to a member of the LDL receptor family in chickens (the oocyte receptor for very low density lipoproteins) (38), despite the fact that chickens do not produce apo-E.

Given that LPL is capable of reaching the capillary lumen in chickens, what prompted the appearance of GPIHBP1 in mammals? We do not have a clear answer, but we speculate that intravascular lipolysis in mammals needed to be particularly efficient because mammals — unlike avian species — nurse their young. In mammals, intravascular TRL processing by LPL is crucial for the production of milk fat by the mammary gland (39, 40). We suspect that GPIHBP1 appeared in mammals to enhance the activity and stability of intravascular LPL and to increase the capacity of vital tissues to extract lipid nutrients from the plasma lipoproteins. Recent biochemical studies have proven that GPIHBP1, and in particular the acidic domain of GPIHBP1, stabilizes LPL's hydrolase domain, limiting inactivation of the enzyme (4). Also, LPL binding to GPIHBP1 protects LPL from inactivation by ANGPTL4 (41). GPIHBP1's ability to stabilize LPL likely increased the capacity of many tissues, including the mammary gland, to extract lipid nutrients from the plasma compartment.

Methods

Goat antibodies against cLPL. cLPL purified from chicken adipose tissue was used to immunize a goat (30). Goat immunoglobulins against cLPL were first purified from the goat antiserum on a Sepharose-cLPL immunoaffinity column (31). The immunopurified goat IgG was further purified on a second immunoaffinity column generated with a His-tagged cLPL polypeptide from *E. coli*. To produce His-tagged cLPL in *E. coli*, the coding sequences of mature cLPL were amplified from a chicken cDNA clone with PrimeStar GXL polymerase (Clontech) and subcloned into the pMAPLe3 expression vector (42, 43). The plasmid was transformed into *E. coli* BL21 (DE3) and Rosetta (DE3). Once the culture reached an OD₆₀₀ of approximately 1.0, the expression of cLPL was induced with 1 mM IPTG. After 4 hours, cells were harvested by centrifugation, and the cell pellets were resuspended in lysis buffer (50 mM Tris pH 8.0, 300 mM NaCl, 20 mM imidazole, 8 M urea). The cells were lysed using an Emulsiflex C-3 (Avestin), and the lysate was clarified by centrifugation. The supernatant fluid was loaded onto a Ni-NTA column; the column was washed with lysis buffer, and the bound protein eluted with lysis buffer containing 300 mM imidazole. The eluted proteins were

Table 1. The *GPIHBP1* locus on human chromosome 8 and the syntenic region on chicken chromosome 2

Human genes	Location	Chicken genes	Location
PSCA (ENSG00000167653)	8:142670308–142682724	PSCA (ENSGALG00000045875)	2:148396683–148400734
Ly6K (ENSG00000160886)	8:142700111–142705127	no homolog	
THEM6 (ENSG00000130193)	8:142727203–142736927	no homolog	
SLURP1 (ENSG00000126233)	8:142740944–142742411	SLURP1 (ENSGALG00000046632)	2:148421473–148427755
LYPD2 (ENSG00000197353)	8:142750150–142752534	LYPD2 (ENSGALG00000035166)	2:148445058–148447137
LYNX1 (ENSG00000284505)	8:142764334–142778224	no homolog	
LYNX1 (ENSG00000283992)	8:142764338–142769844	no homolog	
LYNX1 (ENSG00000180155)	8:142771197–142777810	no homolog	
Ly6D (ENSG00000167656)	8:142784880–142786592	no homolog	
GML (ENSG00000104499)	8:142834247–142916506	no homolog	
CYP11B1 (ENSG00000160882)	8:142872356–142879846	no homolog	
CYP11B2 (ENSG00000179142)	8:142910559–142917843	no homolog	
Ly6E (ENSG00000160932)	8:143017982–143023832	ENSGALG00000041621	2:148464758–148470888
		ENSGALG00000043582	2:148492682–148497873
		ENSGALG00000039585	2:148501300–148505443
		ENSGALG00000045170	2:148482043–148486885
Ly6L (ENSG00000261667)	8:143080457–143083001	no homolog	
Ly6H (ENSG00000176956)	8:143157914–143160711	no homolog	
GPIHBP1 (ENSG00000277494)	8:143213193–143217170	no homolog	
ZFP41 (ENSG00000181638)	8:143246821–143262705	no homolog	
AC138696.1 (ENSG00000264668)	8:143247110–143276403	no homolog	
GLI4 (ENSG00000250571)	8:143267433–143276931	no homolog	
ZNF696 (ENSG00000185730)	8:143289676–143298061	no homolog	
TOP1MT (ENSG00000184428)	8:143304384–143359979	TOP1MT (ENSGALG00000029572)	2:148535366–148546919
RHPN1 (ENSG00000158106)	8:143368887–143384220	no homolog	
MAFA (ENSG00000182759)	8:143419182–143430406	MAFA (ENSGALG00000026264)	2:148778575–148780708
ZC3H3 (ENSG0000014164)	8:143437655–143541453	ZC3H3 (ENSGALG00000043265)	2:148783909–148939588

Data are from the Ensembl database. In this region, many human genes, including *GPIHBP1*, do not appear to have chicken orthologs.

ENSGALG00000041621 is 46.03% identical to human Ly6E; ENSGALG00000043582, ENSGALG00000039585, and ENSGALG00000045170 are 40.48%, 34.48%, and 33.07% identical, respectively, to human Ly6E.

concentrated and further purified by size-exclusion chromatography on a Superdex 200 column (GE Healthcare) equilibrated with 50 mM Tris (pH 8.0), 300 mM NaCl, and 8 M urea. The fractions containing cLPL were pooled, dialyzed against 50 mM Tris (pH 8.0) containing 8 M urea, loaded onto a Q-Sepharose column equilibrated with dialysis buffer, and then eluted with a 0–1 M NaCl gradient. cLPL eluted at approximately 300 mM NaCl. Fractions containing cLPL were pooled and concentrated to approximately 5 mg/ml. cLPL was then dialyzed against PBS with 4 M urea and coupled to AminoLink Coupling Resin (ThermoFisher Scientific). The cLPL–resin was used as a second immunopurification step to purify goat anti-cLPL antibodies. Briefly, the goat anti-chicken antibodies from the Sepharose–cLPL immunoaffinity column were added to the cLPL–resin affinity column. After washing with PBS, goat IgGs were eluted with 0.2 M glycine-HCl (pH 2.7). The resulting IgG fraction against cLPL was then neutralized with 1 M phosphate (pH 9).

Detecting cLPL in extracts of chicken tissues by Western blotting. Adipose tissue, liver, brain, gizzard, heart, white skeletal muscle, and red skeletal muscle were harvested from 9-day-old chickens (approved by UCLA's Animal Research Committee). Tissue samples (~2 mm³) were placed in 1.0 ml of ice-cold RIPA buffer (50 mM Tris [pH 7.4], 150 mM NaCl, 1 mM EDTA, 1% NP40 [vol/vol], 0.25% sodium deoxycholate, 1 mM PMSF, and 1 mM NaF) containing a protease inhibitor cocktail (cOmplete ULTRA EDTA-free, Roche) and homogenized with a motorized homogenizer on ice. The lysate was centrifuged at 18,000 g in a microcentrifuge at 4°C, and the supernatant was collected for analysis. Tissue extracts (30 µg protein) and recombinant cLPL from *E. coli* were electrophoresed in 12% Bis-Tris SDS-PAGE gels in MES buffer (ThermoFisher Scientific). Size-fractionated proteins were transferred to a nitrocellulose membrane, and Western blots were performed with anti-chicken goat antibodies purified over a Sepharose–cLPL immunoaffinity column (1.75 µg/ml) or the same immunopurified antibodies that had been purified again with the immunoaffinity column

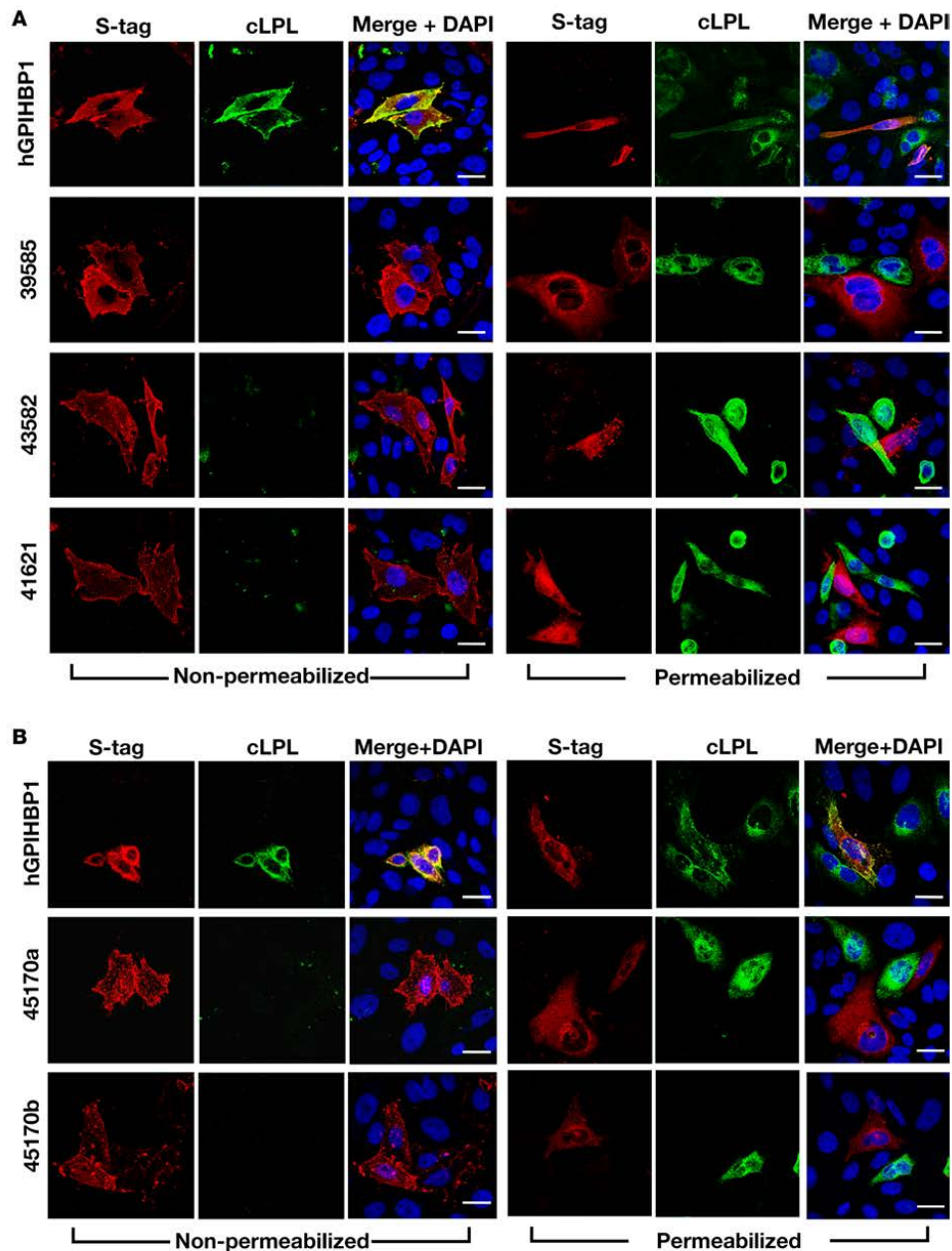


Figure 9. Testing the ability of chicken lipoprotein lipase (cLPL) to bind to chicken Ly6E-like proteins on the surface of transfected cells. CHO pgsA-745 cells were transfected with an expression vector for S-protein-tagged human GPIHBP1 (hGPIHBP1) or for S-protein-tagged versions of the chicken Ly6E-like proteins. Immunocytochemistry studies were performed on permeabilized and non-permeabilized cells with a goat antibody against the S-protein tag (red) and a mouse antibody against the V5 tag (green). DNA was stained with DAPI (blue). **(A)** Immunocytochemistry studies performed with expression vectors for ENSGALG00000039585, ENSGALG00000043582, and ENSGALG00000041621 showing that none of these chicken Ly6E-like proteins bound cLPL (no colocalization). **(B)** Immunocytochemistry studies performed with 2 different expression vectors for ENSGALG00000045170 (45170a and 45170b). Vector 45170a contained the Ly6 domain of ENSGALG00000045170 and also included the acidic domain of hGPIHBP1; vector 45170b contained the Ly6 domain of ENSGALG00000045170. Neither vector conferred upon CHO cells the ability to bind cLPL. Scale bars: 20 μ m.

generated with *E. coli*-expressed cLPL (1.75 µg/ml). Binding of goat IgGs was detected with an IRDye800-conjugated donkey anti-goat IgG (LI-COR; 1:2,000). Antibody binding was detected with an Odyssey infrared scanner (LI-COR).

Detecting cLPL in CHO cells that had been transfected with V5-tagged cLPL. A modified version of CHO pgsA-745 cells (in which the small amounts of hamster LPL expression were eliminated by CRISPR/Cas9 genome editing) were electroporated with a plasmid encoding V5-tagged cLPL (2 µg DNA for 2×10^6 cells). After 24 hours, the cells were washed with PBS/Ca/Mg, fixed in methanol at -20°C for 10 minutes or with 3% paraformaldehyde (PFA) at room temperature for 15 minutes, permeabilized with 0.2% Triton X-100, and blocked with 10% donkey serum. Cells were then incubated for 1 hour at room temperature with the immunopurified goat anti-cLPL antibody (5 µg/ml) and a mouse anti-V5 tag antibody (ThermoFisher Scientific; 11.6 µg/ml), followed by a 30-minute incubation at room temperature with an Alexa Fluor 555-conjugated donkey anti-goat IgG (ThermoFisher Scientific; 1:800) and an Alexa Fluor 488-conjugated donkey anti-mouse IgG (ThermoFisher Scientific; 1:800). All antibodies were diluted in 3% donkey serum in PBS. After the staining of cells, they were fixed with 3% PFA at room temperature for 15 minutes. DNA was stained with 4',6-diamidino-2-phenylindole (DAPI). Images were recorded with an LSM700 confocal fluorescence microscope (Zeiss) and processed with Zen 2010 software (Zeiss). Microscope exposure conditions were identical within each experiment.

Detecting cLPL in tissues by immunohistochemistry. A 9-day-old chicken was anesthetized and perfused through the heart with 50 ml of PBS. WAT and heart were collected, rinsed in PBS, embedded in OCT compound (Tissue Tek), and frozen sections prepared (50-µm sections for WAT; 10-µm sections for heart). Sections were fixed in methanol at -20°C for 10 minutes, permeabilized with 0.2% Triton X-100 for 5 minutes, and incubated with a blocking buffer containing 10% FBS (HyClone) and 0.2% BSA in PBS/Ca/Mg. Tissues were incubated overnight at 4°C with a rabbit polyclonal antibody against human vWF (Dako; 1:200), followed by a 1-hour incubation with Alexa Fluor 555-labeled goat anti-cLPL IgG (5 µg/ml) and an Alexa Fluor 488-labeled donkey anti-rabbit IgG (ThermoFisher Scientific; 1:1,000). After washing with PBS, tissues were fixed with 3% PFA in PBS for 5 minutes at room temperature. DNA was stained with DAPI. Immunofluorescence microscopy was performed as described above. Microscope exposure conditions were identical for each tissue.

Detecting LPL in capillaries of chicken tissues. A 9-day-old chicken was anesthetized and injected intravenously through the brachial vein with a solution containing 73 µl of Alexa Fluor 555-labeled goat anti-cLPL IgG (9.5 mg/ml), 50 µl of fluorescein-labeled *Lens culinaris* agglutinin (lectin, 10 mg/ml; Vector Laboratories), and 70 µl of Alexa Fluor 647-labeled nonimmune goat IgG (10 mg/ml). After 4 minutes, the chicken was perfused through the heart with 50 ml of PBS, followed by 30 ml of PBS containing 3% PFA. WAT, heart, liver, and cerebellum were harvested and fixed in 3% PFA at 4°C for 2 hours. Tissues were embedded in OCT compound, and 10-µm sections prepared. Immunofluorescence microscopy was performed as described above. Microscope exposures were identical within each experiment.

Release of cLPL from isolated chicken hearts with heparin or PIPLC. Chickens between 9 and 21 days of age were anesthetized and perfused with 20 ml of Tyrode's buffer (136 mM NaCl, 5.4 mM KCl, 0.33 mM NaH_2PO_4 , 1 mM MgCl_2 , 10 mM Hepes, pH 7.4, and 10 mM glucose) containing 1 mM CaCl_2 . The hearts were removed, cannulated through the aorta, and perfused with 3 ml of Tyrode's buffer. To release LPL from blood vessels, the hearts were perfused with 20 U/ml of heparin in 4 ml of Tyrode's buffer (or buffer alone). The LPL in the perfusate (0.2 ml/fraction) was stabilized by diluting in DOC buffer (0.1 M Tris, pH 8.5, 0.1 mM SDS, and 5 mM deoxycholate) and stored at -80°C until analysis. LPL in the perfusate was documented by Western blotting or by measuring triglyceride hydrolase activity (44). For the activity measurements, 25 µl of the sample was added to 175 µl of substrate solution composed of Intralipid containing [^3H]triolein and heat-inactivated rat serum (as a source of APOC2). In some studies, LPL activity was inhibited with 50 µl of the goat antiserum against cLPL. Released fatty acids were extracted and counted in a scintillation counter (45). In other studies, isolated mouse hearts were perfused with PIPLC (6 U/ml) (1) in 1 ml Tyrode's buffer (or with buffer alone). Hearts were incubated at 37°C for 10 minutes and then perfused with 2 ml of Tyrode's buffer. Fractions (0.3 ml) were collected, and LPL mass and activity were measured (1).

Releasing LPL from chickens with an intravenous injection of heparin. Young male (0.5–1.0 kg) or female chickens (0.7–0.9 kg) were anesthetized, and the brachial vein was cannulated with a 20-gauge catheter. Chickens were injected intravenously with heparin (2 U/g body weight). Blood samples (1 ml) were drawn from the contralateral brachial vein at baseline and 1, 3, 8, 15, and 30 minutes after the injection of heparin. LPL activity and mass measurements were assessed as described (46, 47).

Assessing binding of cLPL to GPIHBP1. CHO pgsA-745 cells (2×10^6) were electroporated with 2 μ g of expression vector encoding S-protein-tagged versions of mouse or human GPIHBP1 or with V5-tagged versions of human, mouse, or cLPL. The GPIHBP1-transfected cells were then coplated with the LPL-transfected cells on coverslips in 24-well plates at a ratio of 1:2 (a total of 1×10^6 cells/well). After 48 hours, cells were washed with PBS/Ca/Mg, fixed with 3% PFA, and blocked with 10% donkey serum (vol/vol). In some studies, the cells were permeabilized with 0.2% Triton X-100 (vol/vol) after PFA fixation. Cells were then incubated overnight at 4°C with a goat polyclonal antibody against the S-protein tag (Abcam; 1:800) followed by an Alexa Fluor 568-conjugated donkey anti-goat IgG (ThermoFisher Scientific; 1:800) and a mouse monoclonal antibody against the V5 tag (ThermoFisher Scientific; 11.6 μ g/ml) followed by an Alexa Fluor 488-conjugated donkey anti-mouse IgG (ThermoFisher Scientific; 1:800). All antibodies were diluted in 3% donkey serum in PBS. Cells were washed 3 times with 3% donkey serum in PBS and 2 times with PBS before being fixed with 3% PFA. DNA was stained with DAPI. Images were recorded and processed as described above; microscope exposures were identical within each experiment.

Expression vectors for chicken Ly6E-like proteins. The open reading frames for ENSGALG00000039585, ENSGALG00000041621, ENSGALG00000043582, and ENSGALG00000045170 were prepared by RT-PCR from a chicken adipose tissue cDNA library with oligo(dT), random primers, and SuperScript III (ThermoFisher Scientific). PCR fragments were initially introduced into the pGEM-T Easy Vector (Promega). The sequences for the mature proteins were amplified and subcloned into the pTriEx-4 mammalian expression vector (Novagen) as described for expression vectors for human GPIHBP1 or human CD59 (48). In addition, we also introduced the sequences for the Ly6 domain of ENSGALG00000045170 in frame with the acidic domain of human GPIHBP1 in the pTriEx-4 vector. All vectors contained an amino-terminal S-protein tag. The integrity of the expression vectors was verified by DNA sequencing.

Chicken transcriptome sequencing search. Data were acquired from 2 chicken transcriptome sequencing projects (49, 50). The data comprise Pacific Biosciences Iso-Seq sequencing of chicken brain (PRJEB13246), whole embryo (HH stage 26, PRJEB13248), and embryonic heart (pooled HH stages 18–20, 25, and 32; SRR1177086) samples along with Illumina short-read RNA-seq for 20 tissues of adult female J-line chickens (PRJEB12891). For the Iso-Seq data, mapped and unmapped transcript models were examined with Blastx for potential GPIHBP1 transcripts, known Ly6 protein transcripts, and LPL transcripts. For the GPIHBP1 Blastx runs, we compared human, mouse, platypus, and sheep GPIHBP1 amino acid sequences to chicken transcripts. For the Ly6 protein runs, we examined chicken transcripts for the Ly6 proteins present in the Uniprot database. For the LPL runs, we used the annotated cLPL amino acid sequence. For the short-read RNA-seq data, transcript models were assembled with Cufflinks as described in the chicken transcriptome sequencing project (49) and examined with identical Blastx protocols. Mapped and unmapped chicken transcript models with hits from the GPIHBP1 and Ly6 Blastx runs were analyzed for 3 conserved features of mammalian GPIHBP1. The first is a characteristic pattern of cysteines in all mammalian GPIHBP1 proteins (CXXXXXXXXXXXXCXXXXC). We allowed a range of 7 to 19 amino acids between the first and second cysteines, and a range of 3 to 5 amino acids between the third and fourth cysteines. The second is a region with more than 15 acidic residues (D or E) within a 26-amino acid window at the amino terminus of the protein. The third feature was a WCXXXC motif (allowing a range of 3 to 5 residues between the 2 cysteines).

Study approval. All the animals used in this study were housed in a facility accredited by Association for Assessment and Accreditation of Laboratory Animal Care (AAALAC International). All animal protocols are approved by the Chancellor's Animal Research Committee (ARC). The ARC-approved protocols covering the work in our laboratory include 2015-097-11, 2004-127-12B, and 2015-097-03.

Author contributions

CH, LGE, and SGY designed the research. CH, LGE, XH, RSJ, ML, YT, SDV, PK, TRP, CMA, BR, NPS, A. Bensadoun, RLW, RIK, and A.P. Beigneux performed the research. CH, LGE, RSJ, ML, HJ, and SGY analyzed the data. SGY and CH wrote the manuscript.

Acknowledgments

This work was supported by grants from the NIH National Heart, Lung and Blood Institute (HL090553, HL087228, HL125335), the National Human Genome Research Institute (4U41HG002371), and a Transatlantic Network Grant from the Leducq Foundation (12CVD04). Cuiwen He was supported by

a Ruth L. Kirschstein National Research Service Award (F32HL132471). Christopher M. Allan was supported by a Ruth L. Kirschstein National Research Service Award (T32HL69766). The recombinant cLPL described in this publication was prepared by the UCLA-DOE Institute Protein Expression Technology Center, which is supported by the U.S. Department of Energy, Office of Biological and Environmental Research (BER) program under Award Number DE-FC02-02ER63421. This work was also supported in part by Texas AgriLife Research project number 8738. We thank Mark Arbing for expressing cLPL in *E. coli*. We thank the UCLA Brain Research Institute and Marianne Cilluffo for help in preparing chicken tissue sections.

Address correspondence to: Loren G. Fong, Stephen G. Young, or Anne P. Beigneux, University of California, Los Angeles, 4506 Gonda Building, 695 Charles E. Young Drive South, Los Angeles, California 90095, USA. Phone: 310.825.4422; Email: lfong@mednet.ucla.edu (L.G.Fong); sgyoung@mednet.ucla.edu (S.G. Young); abeigneux@mednet.ucla.edu (A.P. Beigneux).

1. Beigneux AP, et al. Glycosylphosphatidylinositol-anchored high-density lipoprotein-binding protein I plays a critical role in the lipolytic processing of chylomicrons. *Cell Metab.* 2007;5(4):279–291.
2. Davies BS, et al. GPIHBP1 is responsible for the entry of lipoprotein lipase into capillaries. *Cell Metab.* 2010;12(1):42–52.
3. Goulbourne CN, et al. The GPIHBP1-LPL complex is responsible for the margination of triglyceride-rich lipoproteins in capillaries. *Cell Metab.* 2014;19(5):849–860.
4. Mysling S, et al. The acidic domain of the endothelial membrane protein GPIHBP1 stabilizes lipoprotein lipase activity by preventing unfolding of its catalytic domain. *Elife.* 2016;5:e12095.
5. Ameis D, et al. Familial chylomicronemia (type I hyperlipoproteinemia) due to a single missense mutation in the lipoprotein lipase gene. *J Clin Invest.* 1991;87(4):1165–1170.
6. Beigneux AP, et al. Chylomicronemia with a mutant GPIHBP1 (Q115P) that cannot bind lipoprotein lipase. *Arterioscler Thromb Vasc Biol.* 2009;29(6):956–962.
7. Charrière S, et al. GPIHBP1 C89F neomutation and hydrophobic C-terminal domain G175R mutation in two pedigrees with severe hyperchylomicronemia. *J Clin Endocrinol Metab.* 2011;96(10):E1675–E1679.
8. Coca-Prieto I, et al. Childhood-onset chylomicronaemia with reduced plasma lipoprotein lipase activity and mass: identification of a novel GPIHBP1 mutation. *J Intern Med.* 2011;270(3):224–228.
9. Franssen R, et al. Chylomicronemia with low postheparin lipoprotein lipase levels in the setting of GPIHBP1 defects. *Circ Cardiovasc Genet.* 2010;3(2):169–178.
10. Olivecrona G, et al. Mutation of conserved cysteines in the Ly6 domain of GPIHBP1 in familial chylomicronemia. *J Lipid Res.* 2010;51(6):1535–1545.
11. Plengpanich W, et al. Multimerization of glycosylphosphatidylinositol-anchored high density lipoprotein-binding protein I (GPIHBP1) and familial chylomicronemia from a serine-to-cysteine substitution in GPIHBP1 Ly6 domain. *J Biol Chem.* 2014;289(28):19491–19499.
12. Rios JJ, et al. Deletion of GPIHBP1 causing severe chylomicronemia. *J Inher Metab Dis.* 2012;35(3):531–540.
13. Surendran RP, et al. Mutations in LPL, APOC2, APOA5, GPIHBP1 and LMF1 in patients with severe hypertriglyceridaemia. *J Intern Med.* 2012;272(2):185–196.
14. Voss CV, et al. Mutations in lipoprotein lipase that block binding to the endothelial cell transporter GPIHBP1. *Proc Natl Acad Sci USA.* 2011;108(19):7980–7984.
15. Brunzell JD, Deeb SS. Familial lipoprotein lipase deficiency, apo C-II deficiency, and hepatic lipase deficiency. In: Scriver CR, Beaudet AL, et al., eds. *The Metabolic and Molecular Bases of Inherited Disease*. New York, USA:McGraw-Hill; 2001:2789–2816.
16. Havel RJ, Gordon RS. Idiopathic hyperlipemia: metabolic studies in an affected family. *J Clin Invest.* 1960;39:1777–1790.
17. Hayden MR, Ma Y, Brunzell J, Henderson HE. Genetic variants affecting human lipoprotein and hepatic lipases. *Curr Opin Lipidol.* 1991;2(2):104–109.
18. Fojo SS, Brewer HB. Hypertriglyceridaemia due to genetic defects in lipoprotein lipase and apolipoprotein C-II. *J Intern Med.* 1992;231(6):669–677.
19. Henderson HE, Hassan F, Marais D, Hayden MR. A new mutation destroying disulphide bridging in the C-terminal domain of lipoprotein lipase. *Biochem Biophys Res Commun.* 1996;227(1):189–194.
20. Loughner CL, Bruford EA, McAndrews MS, Delp EE, Swamynathan S, Swamynathan SK. Organization, evolution and functions of the human and mouse Ly6/uPAR family genes. *Hum Genomics.* 2016;10:10.
21. Fry BG, et al. Molecular evolution and phylogeny of elapid snake venom three-finger toxins. *J Mol Evol.* 2003;57(1):110–129.
22. Ioka RX, et al. Expression cloning and characterization of a novel glycosylphosphatidylinositol-anchored high density lipoprotein-binding protein, GPIHBP1. *J Biol Chem.* 2003;278(9):7344–7349.
23. Beigneux AP, et al. Assessing the role of the glycosylphosphatidylinositol-anchored high density lipoprotein-binding protein I (GPIHBP1) three-finger domain in binding lipoprotein lipase. *J Biol Chem.* 2011;286(22):19735–19743.
24. Beigneux AP, et al. GPIHBP1 missense mutations often cause multimerization of GPIHBP1 and thereby prevent lipoprotein lipase binding. *Circ Res.* 2015;116(4):624–632.
25. Holmes RS, Cox LA. Comparative studies of glycosylphosphatidylinositol-anchored high-density lipoprotein-binding protein I: evidence for a eutherian mammalian origin for the GPIHBP1 gene from an LY6-like gene. *3 Biotech.* 2012;2(1):37–52.
26. Young SG, et al. GPIHBP1: an endothelial cell molecule important for the lipolytic processing of chylomicrons. *Curr Opin Lipidol.* 2007;18(4):389–396.

27. Holmes RS, Vandeberg JL, Cox LA. Comparative studies of vertebrate lipoprotein lipase: a key enzyme of very low density lipoprotein metabolism. *Comp Biochem Physiol Part D Genomics Proteomics*. 2011;6(2):224–234.
28. Kompang IP, Bensadoun A, Yang MW. Effect of an anti-lipoprotein lipase serum on plasma triglyceride removal. *J Lipid Res*. 1976;17(5):498–505.
29. Fraser R, Heslop VR, Murray FE, Day WA. Ultrastructural studies of the portal transport of fat in chickens. *Br J Exp Pathol*. 1986;67(6):783–791.
30. Bensadoun A, Hsu J, Hughes B. Large-scale lipoprotein lipase purification from adipose tissue. *Methods Mol Biol*. 1999;109:145–150.
31. Bensadoun A, Kompang IP. Role of lipoprotein lipase in plasma triglyceride removal. *Fed Proc*. 1979;38(12):2622–2626.
32. Favre B, et al. SLURP1 is a late marker of epidermal differentiation and is absent in Mal de Meleda. *J Invest Dermatol*. 2007;127(2):301–308.
33. Weinstein MM, et al. Abnormal patterns of lipoprotein lipase release into the plasma in GPIHBP1-deficient mice. *J Biol Chem*. 2008;283(50):34511–34518.
34. Riquelme CA, et al. Fatty acids identified in the Burmese python promote beneficial cardiac growth. *Science*. 2011;334(6055):528–531.
35. Andersson Y, Nilsson S, Lindberg A, Thelander L, Olivecrona G. Apolipoprotein CII from chicken (*Gallus domesticus*). The amino-terminal domain is different from corresponding domains in mammals. *J Biol Chem*. 1996;271(51):33060–33066.
36. Saxena U, Klein MG, Goldberg IJ. Transport of lipoprotein lipase across endothelial cells. *Proc Natl Acad Sci USA*. 1991;88(6):2254–2258.
37. Eick GN, Thornton JW. Evolution of steroid receptors from an estrogen-sensitive ancestral receptor. *Mol Cell Endocrinol*. 2011;334(1-2):31–38.
38. Steyrer E, Barber DL, Schneider WJ. Evolution of lipoprotein receptors. The chicken oocyte receptor for very low density lipoprotein and vitellogenin binds the mammalian ligand apolipoprotein E. *J Biol Chem*. 1990;265(32):19575–19581.
39. Camps L, Reina M, Llobera M, Vilaró S, Olivecrona T. Lipoprotein lipase: cellular origin and functional distribution. *Am J Physiol*. 1990;258(4 Pt 1):C673–C681.
40. Goldberg IJ, Soprano DR, Wyatt ML, Vanni TM, Kirchgessner TG, Schotz MC. Localization of lipoprotein lipase mRNA in selected rat tissues. *J Lipid Res*. 1989;30(10):1569–1577.
41. Mysling S, et al. The angiotensin-like protein ANGPTL4 catalyzes unfolding of the hydrolase domain in lipoprotein lipase and the endothelial membrane protein GPIHBP1 counteracts this unfolding. *Elife*. 2016;5.
42. Arbing MA, et al. Heterologous expression of mycobacterial Exx complexes in *Escherichia coli* for structural studies is facilitated by the use of maltose binding protein fusions. *PLoS ONE*. 2013;8(11):e81753.
43. Gibson DG. Enzymatic assembly of overlapping DNA fragments. *Meth Enzymol*. 2011;498:349–361.
44. Larsson M, Vorrjög E, Talmud P, Lookene A, Olivecrona G. Apolipoproteins C-I and C-III inhibit lipoprotein lipase activity by displacement of the enzyme from lipid droplets. *J Biol Chem*. 2013;288(47):33997–34008.
45. Bengtsson-Olivecrona G, Olivecrona T. Assay of lipoprotein lipase and hepatic lipase. In: Converse C, Skinner ER, eds. *Lipoprotein Analysis. A Practical Approach*. Oxford, UK:IRL; 1992:169–185.
46. Hocquette JF, Graulet B, Olivecrona T. Lipoprotein lipase activity and mRNA levels in bovine tissues. *Comp Biochem Physiol B, Biochem Mol Biol*. 1998;121(2):201–212.
47. Cisar LA, Hoogewerf AJ, Cupp M, Rapport CA, Bensadoun A. Secretion and degradation of lipoprotein lipase in cultured adipocytes. Binding of lipoprotein lipase to membrane heparan sulfate proteoglycans is necessary for degradation. *J Biol Chem*. 1989;264(3):1767–1774.
48. Gin P, et al. The acidic domain of GPIHBP1 is important for the binding of lipoprotein lipase and chylomicrons. *J Biol Chem*. 2008;283(43):29554–29562.
49. Kuo RI, Tseng E, Eory L, Paton IR, Archibald AL, Burt DW. Normalized long read RNA sequencing in chicken reveals transcriptome complexity similar to human. *BMC Genomics*. 2017;18(1):323.
50. Thomas S, Underwood JG, Tseng E, Holloway AK, Bench To Basinet CvDC Informatics Subcommittee. Long-read sequencing of chicken transcripts and identification of new transcript isoforms. *PLoS ONE*. 2014;9(4):e94650.

Appendix III

High-resolution Imaging and Quantification of Plasma

Membrane Cholesterol by NanoSIMS

High-resolution imaging and quantification of plasma membrane cholesterol by NanoSIMS

Cuiwen He^a, Xuchen Hu^a, Rachel S. Jung^a, Thomas A. Weston^a, Norma P. Sandoval^a, Peter Tontonoz^{b,c}, Matthew R. Kilburn^d, Loren G. Fong^a, Stephen G. Young^{a,e,1,2}, and Haibo Jiang^{d,1,2}

^aDepartment of Medicine, University of California, Los Angeles, CA 90095; ^bDepartment of Pathology and Laboratory Medicine, University of California, Los Angeles, CA 90095; ^cHoward Hughes Medical Institute, University of California, Los Angeles, CA 90095; ^dCentre for Microscopy, Characterisation and Analysis, University of Western Australia, Perth 6009, Australia; and ^eDepartment of Human Genetics, University of California, Los Angeles, CA 90095

Contributed by Stephen G. Young, January 3, 2017 (sent for review December 21, 2016; reviewed by Yunbin Guan, Fredric B. Kraemer, Sampath Parthasarathy, and Joseph L. Witztum)

Cholesterol is a crucial lipid within the plasma membrane of mammalian cells. Recent biochemical studies showed that one pool of cholesterol in the plasma membrane is “accessible” to binding by a modified version of the cytolysin perfringolysin O (PFO*), whereas another pool is sequestered by sphingomyelin and cannot be bound by PFO* unless the sphingomyelin is destroyed with sphingomyelinase (SMase). Thus far, it has been unclear whether PFO* and related cholesterol-binding proteins bind uniformly to the plasma membrane or bind preferentially to specific domains or morphologic features on the plasma membrane. Here, we used nanoscale secondary ion mass spectrometry (NanoSIMS) imaging, in combination with ¹⁵N-labeled cholesterol-binding proteins (PFO* and ALO-D4, a modified anthrolysin O), to generate high-resolution images of cholesterol distribution in the plasma membrane of Chinese hamster ovary (CHO) cells. The NanoSIMS images revealed preferential binding of PFO* and ALO-D4 to microvilli on the plasma membrane; lower amounts of binding were detectable in regions of the plasma membrane lacking microvilli. The binding of ALO-D4 to the plasma membrane was virtually eliminated when cholesterol stores were depleted with methyl- β -cyclodextrin. When cells were treated with SMase, the binding of ALO-D4 to cells increased, largely due to increased binding to microvilli. Remarkably, lysenin (a sphingomyelin-binding protein) also bound preferentially to microvilli. Thus, high-resolution images of lipid-binding proteins on CHO cells can be acquired with NanoSIMS imaging. These images demonstrate that accessible cholesterol, as judged by PFO* or ALO-D4 binding, is not evenly distributed over the entire plasma membrane but instead is highly enriched on microvilli.

NanoSIMS | cholesterol | microvilli | anthrolysin O | perfringolysin O

In recent biochemical studies, Das et al. analyzed the binding of PFO*, a mutant version of the cytolysin perfringolysin O, to cholesterol in the plasma membrane of several mammalian cells, including human fibroblasts and Chinese hamster ovary (CHO) cells (1, 2). They found that plasma membrane cholesterol is “accessible” to ¹²⁵I-PFO* binding when cholesterol levels are high (exceeding 35 mol% of all membrane lipids). When cholesterol stores were depleted with 2-hydroxypropyl- β -cyclodextrin, the binding of ¹²⁵I-PFO* to cells was virtually abolished. Interventions that increased plasma membrane cholesterol levels resulted in more ¹²⁵I-PFO* binding (1). They went on to show that much of the cholesterol in the plasma membrane is sequestered by sphingomyelin and cannot bind ¹²⁵I-PFO* unless the sphingomyelin is destroyed with sphingomyelinase (SMase) (2). The studies by Das et al. were very important because they characterized distinct pools of cholesterol in the plasma membrane (an accessible pool and a sphingomyelin-sequestered pool); however, the distribution of PFO* binding sites on the plasma membrane was not addressed.

The plasma membrane of mammalian cells is often assumed to contain microdomains (called “lipid rafts”) enriched in sphingomyelin and cholesterol. These microdomains can be purified

from the plasma membrane by taking advantage of their resistance to detergent extraction at low temperatures (3). Cholesterol- and sphingolipid-rich microdomains are transient and small (<200 nm), making them very difficult to visualize by confocal microscopy (4). To better define the distributions of cholesterol and sphingolipids in the plasma membrane, Frisz et al. (5) used nanoscale secondary ion mass spectrometry (NanoSIMS) imaging to visualize ¹⁸O-labeled cholesterol and ¹⁵N-labeled sphingolipids in the plasma membrane of 3T3 fibroblasts. They reported that the cholesterol in the plasma membrane was evenly distributed, whereas sphingolipids were found in large (~2–3 μ m) and unevenly distributed patches (5). The distinct distributions of cholesterol and sphingolipids in the plasma membrane were somewhat surprising, given that these lipids are thought to interact within the plasma membrane. Of course, the conclusions regarding the plasma membrane distributions of cholesterol and sphingolipids in this NanoSIMS study relied on the assumption that the ¹⁸O and ¹⁵N ions originated exclusively from the plasma membrane (rather than being derived in part from internal membrane compartments).

In our current study, we used NanoSIMS imaging along with ¹⁵N-labeled cholesterol- and sphingomyelin-binding proteins (cytolysins) to visualize distributions of cholesterol and sphingomyelin in the plasma membrane. We reasoned that NanoSIMS imaging with lipid-binding proteins would hold several advantages.

Significance

Biochemical studies have demonstrated that one pool of cholesterol in the plasma membrane is accessible to binding by bacterial cholesterol-binding proteins, whereas another pool is “sequestered” and inaccessible to binding by those proteins. Here, we used nanoscale secondary ion mass spectrometry (NanoSIMS) imaging, along with cholesterol-binding proteins that had been labeled with a stable isotope, to visualize and quantify the distribution of “accessible cholesterol” on the plasma membrane of mammalian cells. Our studies revealed that accessible cholesterol, as judged by cholesterol-binding proteins, is not evenly distributed on the plasma membrane but instead is enriched on the surface of microvilli. The accessible cholesterol on microvilli could be relevant to the movement of cholesterol away from the plasma membrane.

Author contributions: C.H., L.G.F., S.G.Y., and H.J. designed research; C.H., X.H., R.S.J., T.A.W., N.P.S., M.R.K., and H.J. performed research; C.H., P.T., S.G.Y., and H.J. analyzed data; and S.G.Y. and H.J. wrote the paper.

Reviewers: Y.G., California Institute of Technology; F.B.K., VA Palo Alto Health Care System and Stanford University; S.P., University of Central Florida; and J.L.W., University of California, San Diego.

The authors declare no conflict of interest.

¹S.G.Y. and H.J. contributed equally to this work.

²To whom correspondence may be addressed. Email: sgyoung@mednet.ucla.edu or haibo.jiang@uwa.edu.au.

This article contains supporting information online at www.pnas.org/lookup/suppl/doi:10.1073/pnas.1621432114/-DCSupplemental.

First, we suspected that the ^{15}N signal would be robust. The cholesterol- and sphingomyelin-binding proteins were uniformly labeled with ^{15}N and therefore contained >100 ^{15}N atoms. In contrast, there is only a single ^{18}O atom in [^{18}O]cholesterol. Second, when lipid-binding cytolysins such as PFO* are incubated with cells, one can be confident that they bind to the plasma membrane and not to internal membrane compartments. Third, NanoSIMS instruments can collect ion images with spatial resolutions that are higher than typically obtained with confocal microscopy (6). Fourth, the NanoSIMS instrument collects millions of ions, making it possible to quantify binding of ^{15}N -labeled proteins to morphologically distinct regions within the plasma membrane. Finally, one can judge the validity of NanoSIMS imaging studies according to the lessons from earlier biochemical studies (e.g., the fact that PFO* binding is reduced by cholesterol depletion and increased by treating cells with SMase).

Materials and Methods

CHO-K1 Cells. Stock cultures of hamster CHO-K1 cells were grown in monolayer cultures at 37°C with 8–9% (vol/vol) CO_2 and maintained in medium A [Ham's F-12 Nutrient Mixture (Thermo Fisher Scientific) containing 10% (vol/vol) FBS (HyClone), 2 mM glutamine, and antibiotic-antimycotic from Gibco containing 100 units/mL of penicillin, 100 $\mu\text{g}/\text{mL}$ of streptomycin, and 0.25 $\mu\text{g}/\text{mL}$ of amphotericin B]. Medium B is identical to medium A except that it contains 10% (vol/vol) lipoprotein-deficient serum (LPDS) rather than FBS. Medium C is medium B containing 50 μM mevastatin (Calbiochem) and 50 μM mevalonolactone (Sigma). To produce LPDS, FBS was adjusted to a density of 1.21 g/mL with NaBr and centrifuged in a SW41 rotor at 38,000 rpm for 48 h. The top layer (lipoproteins) was discarded, and the bottom fraction (LPDS) was dialyzed against PBS and sterilized with a 0.22- μm filter. For NanoSIMS analysis, cells were grown on 0.5-cm 2 silicon wafers coated with poly-L-lysine or were plated on Thermanox plastic coverslips (Thermo Fisher Scientific). For immunofluorescence microscopy, CHO-K1 cells were plated on glass coverslips in 24-well plates.

To load CHO-K1 cells with cholesterol, cholesterol was dissolved in ethanol and then added to medium C [final cholesterol concentration, 300 μM ; final ethanol concentration, 1.17% (vol/vol)]. The cells were then grown in cholesterol-supplemented medium C for 2 d. After three 10-min washes with Dulbecco's PBS containing Mg^{2+} and Ca^{2+} (DPBS+ Mg^{2+} + Ca^{2+}), cells were incubated in medium B without cholesterol for 44 h. Finally, the cells were washed three times for 10 min in DPBS+ Mg^{2+} + Ca^{2+} containing 0.2% (wt/vol) BSA. To deplete cholesterol, cells were incubated with 10 mM methyl- β -cyclodextrin (M β CD, Sigma) in Ham's F-12 Nutrient Mixture at 37°C for 15 min. To release the sphingomyelin-sequestered pool of cholesterol on the plasma membrane, cells were incubated at 37°C for 30 min in medium A containing 100 milliu/ml of sphingomyelinase from *Staphylococcus aureus* (Sigma). For a "no treatment" control, cells were simply incubated in medium A at 37°C for 30 min.

Preparation of ^{15}N -labeled His-Tagged PFO*. PFO* is a 500-amino acid nontoxic cysteine-less version of perfringolysin O (PFO) carrying a Y181A substitution (1). A plasmid for His-tagged PFO* (1) (from Arun Radhakrishnan, University of Texas Southwestern, Dallas, TX) was expressed in BL21(DE3) pLysS *Escherichia coli* (Invitrogen), and the cells were induced with 0.5 mM IPTG in minimal medium containing 95.5 mM KH_2PO_4 , 57.4 mM K_2HPO_4 , 63.4 mM Na_2HPO_4 , 13.8 mM K_2SO_4 , 20.2 mM $^{15}\text{NH}_4\text{Cl}$ (Cambridge Isotope Laboratories), 5 mM MgCl_2 , 0.2% (wt/vol) glucose, and 100 $\mu\text{g}/\text{mL}$ carbenicillin at 37°C for 16 h. Cells were pelleted at $8,000 \times g$ for 20 min at 4°C and resuspended in 20 mL of buffer containing 50 mM NaH_2PO_4 (pH 7.0), 300 mM NaCl, 2 mM PMSF, and a protease inhibitor mixture tablet (Roche Complete, Mini, EDTA-free; 1 tablet/10 mL). Cells were disrupted by sonication, pulse 1.5 min on and 30 s off (four times). The lysate was centrifuged at $18,000 \times g$ for 40 min at 4°C , and the supernatant was mixed with 4 mL of HisPur Cobalt resin [50% (vol/vol) slurry, Thermo Fisher Scientific] equilibrated in an equilibration buffer [50 mM NaH_2PO_4 (pH 7.0) and 300 mM NaCl] with 10 mM imidazole for 45 min at 4°C . The mixture was then loaded into a column and the flow through was allowed to drain by gravity from the resin. The column was washed with four column volumes (CVs) of the equilibration buffer plus 10 mM imidazole and 4 CVs of equilibration buffer containing 50 mM imidazole. [^{15}N]PFO* was eluted with 12 CVs of the equilibration buffer containing 300 mM imidazole. Eluates were pooled and concentrated to 2 mL with an Amicon 10-kDa MWCO concentrator (Millipore). Purified protein was stored in 50% (vol/vol) antibody stabilizer PBS (CANDOR Bioscience) at 4°C .

Preparation of ^{15}N -Labeled His-Tagged Domain 4 of Anthrolysin O. A plasmid for domain 4 of anthrolysin O (ALO-D4, ALO amino acids 404–512 with C472A and S404C substitutions) was obtained from Arun Radhakrishnan. ALO-D4 was expressed and purified in BL21(DE3) pLysS *E. coli* (7). ^{15}N -labeled ALO-D4 was purified as described for ^{15}N -labeled PFO*.

Preparation of ^{15}N -Labeled His-mCherry-Tagged Lysenin. To express a nontoxic version of lysenin, the sequences for lysenin amino acids 161–297 were cloned into the vector pBADmCherry (Addgene). The cDNA for lysenin was synthesized by Integrated DNA Technologies. The vector pBADmCherry was linearized by PCR with primers 5'-TAAGAATTCGAAGCTGGTG-3' and 5'-CTTGACAGCTGCTCCATGC-3', and the lysenin cDNA was inserted with the In-Fusion HD Cloning kit (Clontech). Lysenin was expressed in BL21(DE3) *E. coli* (Invitrogen). To produce [^{15}N]lysenin, *E. coli* were grown in 1 L $^{15}\text{NH}_4\text{Cl}$ minimum media and induced with 0.2% (wt/vol) arabinose at 20°C for 16 h. Cells were pelleted at $8,000 \times g$ for 20 min at 4°C and resuspended in 20 mL of lysis buffer containing 20 mM NaH_2PO_4 (pH 8.0), 150 mM NaCl, 1 mg/mL lysozyme, 0.4 mg/mL PMSF, and a protease inhibitor mixture tablet (1 tablet/20 mL, Roche, Complete, Mini, EDTA-free). Cells were disrupted with 15 strokes in a Dounce homogenizer, incubated at 4°C for 3 h and again subjected to Dounce homogenization and sonication. The lysate was centrifuged at $25,000 \times g$ for 1 h at 4°C . The supernatant was loaded onto a 1-mL nickel-nitrilotriacetic acid (Ni-NTA) column (GE Healthcare) equilibrated in equilibration buffer (20 mM NaH_2PO_4 , pH 8.0, 150 mM NaCl). The column was washed with 50 column volumes of equilibration buffer containing 30 mM imidazole; the [^{15}N]lysenin was eluted with equilibration buffer containing a linear gradient of imidazole (30–300 mM). Fractions containing lysenin were pooled and concentrated to 1 mL with an Amicon 10-kDa MWCO concentrator (Millipore). The 1-mL eluate was further purified by gel filtration on a Superdex 200 10/300 column (GE Healthcare). Purified protein was stored in 50% (vol/vol) antibody stabilizer PBS (CANDOR Bioscience) at 4°C .

[^{15}N]PFO* and [^{15}N]ALO-D4 Binding to Cells. CHO-K1 cells were washed three times (10 min each) with DPBS+ Mg^{2+} + Ca^{2+} plus 0.2% BSA to remove M β CD or SMase. Each coverslip or silicon wafer containing CHO-K1 cells was incubated in 24-well plates for 2 h at 4°C with 0.4 mL of binding buffer (25 mM Hepes-KOH, pH 7.4, 150 mM NaCl, 0.2% BSA) containing 20 $\mu\text{g}/\text{mL}$ of [^{15}N]ALO-D4 or 20 $\mu\text{g}/\text{mL}$ of [^{15}N]PFO*. The cells were washed three times (3 min each) with ice-cold DPBS+ Mg^{2+} + Ca^{2+} to remove unbound [^{15}N]ALO-D4 or [^{15}N]PFO*.

[^{15}N]Lysenin Binding to Cells. Cells grown on silicon wafers were washed three times for 10 min with DPBS+ Mg^{2+} + Ca^{2+} plus 0.2% BSA to remove M β CD or SMase. Each wafer was incubated in a 24-well plate for 1 h at 4°C with 0.4 mL of DPBS+ Mg^{2+} + Ca^{2+} containing 0.2% BSA and 20 $\mu\text{g}/\text{mL}$ of [^{15}N]lysenin. To remove unbound protein, cells were washed three times for 3 min with ice-cold DPBS+ Mg^{2+} + Ca^{2+} .

Preparing Cells on Silicon Wafers for NanoSIMS Imaging and Scanning Electron Microscopy. CHO cells were fixed with 4% (vol/vol) paraformaldehyde (PFA) and 1% glutaraldehyde for 20 min at 4°C , followed by 2.5% (vol/vol) glutaraldehyde in 0.1 M phosphate buffer for 1 h at room temperature. Cells were then washed three times for 10 min with 0.1 M phosphate buffer followed by two 5-min washes with ddH $_2$ O. The cells were then air dried and used for NanoSIMS imaging. For scanning electron microscopy, cells were coated with 5-nm platinum and transferred to a FEI Verios SEM. Images were taken with a 2-keV incident beam of 50-pA current at a 2.5-mm working distance. In a separate fixation method, cells were fixed in a solution containing 2.5% (vol/vol) glutaraldehyde in 0.1 M sodium cacodylate for 1 h. The samples were rinsed three times with 0.1 M sodium cacodylate before being postfixed in a solution of 1% osmium tetroxide in 0.1 M sodium cacodylate for 40 min followed by three rinses with H $_2$ O. Next, the cells were dehydrated with a graded series of ethanol concentrations and then by critical point drying (Tousimis Autosam-dri 810). The samples on stubs were then coated with gold palladium (Pelco SC-70) and imaged with a Zeiss Supra 40VP scanning electron microscope with a 7-keV incident beam.

Preparation of Epoxy-Embedded Cells for NanoSIMS Imaging. CHO-K1 cells were plated on Thermanox plastic coverslips in a 24-well plate. Cells were loaded with cholesterol, treated with M β CD or SMase, and incubated with [^{15}N]ALO-D4 as described. Next, the cells were fixed with ice-cold 4% (vol/vol) PFA and 1% glutaraldehyde for 20 min at 4°C , followed by 2.5% (vol/vol) glutaraldehyde in 0.1 M phosphate buffer for 1 h at room temperature. The cells were washed, then incubated in 1% osmium tetroxide in 0.1 M phosphate buffer for 1 h, and washed again with ddH $_2$ O. The cells were then incubated with 2% (vol/vol) aqueous uranyl acetate overnight

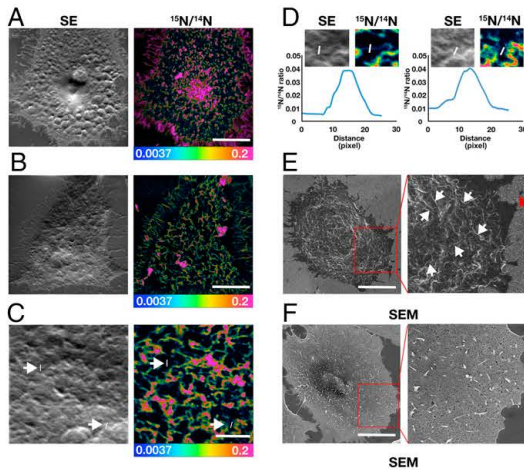


Fig. 1. NanoSIMS imaging of cholesterol-binding proteins on the plasma membrane of CHO-K1 cells. CHO-K1 cells were plated on silicon wafers and grown in Ham's F-12 medium containing 10% lipoprotein-deficient serum (*Materials and Methods*) for 5 d. The cells were then loaded with cholesterol as described in *Materials and Methods*. The cells were subsequently grown in medium lacking supplemental cholesterol for 44 h. Next, the cells were incubated with 20 $\mu\text{g}/\text{mL}$ [^{15}N]PFO* (A) or [^{15}N]ALO-D4 (B) for 2 h at 4 $^{\circ}\text{C}$. NanoSIMS images were generated based on secondary electrons (SEs); other images were created based on the $^{15}\text{N}/^{14}\text{N}$ ratio. (Scale bar, 10 μm .) The color scale shows the range of $^{15}\text{N}/^{14}\text{N}$ ratios. (C) High-magnification image of the cell shown in B. (Scale bar, 3 μm .) (D) Line scan demonstrating the $^{15}\text{N}/^{14}\text{N}$ isotope ratio across microvilli on the surface of the plasma membrane (white lines in C and D). Pixel, ~ 19.5 nm. (E) SEM image of a CHO-K1 cell grown on a silicon wafer and fixed with 4% (vol/vol) PFA plus 1% glutaraldehyde followed by 2.5% (vol/vol) glutaraldehyde. A higher-magnification image of the boxed area on the *Left* is shown in the image on the *Right*. Red arrow shows a microvillus at the perimeter of the cell; white arrows show microvilli on the surface of the cell. (F) SEM image of CHO-K1 cells grown on a silicon wafer and fixed with 2.5% (vol/vol) glutaraldehyde in 0.1 M sodium cacodylate followed by 1% osmium tetroxide in 0.1 M sodium cacodylate. (Scale bar, 10 μm .)

at 4 $^{\circ}\text{C}$, washed, dehydrated with a graded series of ethanol, transferred to propylene oxide, and infiltrated with a 1:1 mix of propylene oxide:eponate 12 resin (Ted Pella) for 1 h and a 1:2 mix of propylene oxide:resin overnight. The cells were then transferred to fresh resin and embedded by inverting the coverslip onto a Beem capsule filled with fresh resin and polymerized for 24 h at 60 $^{\circ}\text{C}$. The coverslips were removed and 500-nm thick sections were cut en face with a Diatome diamond knife. The sections were placed on a silicon wafer for NanoSIMS imaging.

Imaging of ALO-D4 and Lysoenin Binding with NanoSIMS and Confocal Microscopy. Samples of cells on silicon wafers were coated with 5-nm platinum and transferred to a NanoSIMS 50L instrument (CAMECA) for analysis. An 8-KeV $^{133}\text{Cs}^+$ beam was used as the primary ion beam to bombard the sample; secondary ions of -8 KeV ($^{12}\text{C}^-$, $^{16}\text{O}^-$, $^{12}\text{C}^{14}\text{N}^-$, $^{12}\text{C}^{15}\text{N}^-$) and secondary electrons (SEs) were collected. An area of 30×30 μm was imaged with a ~ 1.5 -pA beam current (primary aperture D1 = 2) and a dwell time of 10,000 $\mu\text{s}/\text{pixel}$. Scans of 256×256 or 512×512 pixels were obtained. To obtain high-resolution images, a smaller primary aperture (D1 = 3, ~ 0.8 pA) was used to image a region of 10×10 μm . For embedded sections on silicon wafers, a high primary beam current of ~ 3.5 nA was used to presputter a 40×40 μm region for 2 min to remove the platinum coating and implant $^{133}\text{Cs}^+$ for a steady state of secondary ions. In the same region, an area of 30×30 μm was then imaged with a ~ 1.5 pA beam current and a dwell time of 30,000 $\mu\text{s}/\text{pixel}$. Scans of 256×256 pixels were obtained. To quantify the $^{15}\text{N}/^{14}\text{N}$ ratio, regions of interest were defined and $^{15}\text{N}/^{14}\text{N}$ ratios were measured with the OpenMIMS plugin and then processed by Prism 7.0. Regions of interest (including line scans) on images were drawn pixel by pixel for

microvilli and nonmicrovilli regions. The mass ratio of $^{15}\text{N}/^{14}\text{N}$ was measured with a median filter of 1-pixel radius. The mean and SDs of the $^{15}\text{N}/^{14}\text{N}$ ratio data points were then calculated and processed by Prism 7.0. Confocal fluorescence microscopy images were obtained with standard experimental approaches (*SI Materials and Methods*) and recorded with an Axiovert 200 M microscope.

Results

In our first experiments, we used NanoSIMS imaging of [^{15}N]PFO* to visualize the accessible pool of cholesterol on the plasma membrane of CHO-K1 cells. Cells were grown on silicon wafers (1) in cholesterol-rich medium and then incubated with [^{15}N]PFO*. After washing the cells and fixing them with paraformaldehyde, NanoSIMS imaging was performed (Fig. 1A). The binding of [^{15}N]PFO* to cells was visualized with images generated from the ratio of $^{12}\text{C}^{15}\text{N}$ and $^{12}\text{C}^{14}\text{N}$ secondary ions (i.e., $^{15}\text{N}/^{14}\text{N}$ images). The $^{15}\text{N}/^{14}\text{N}$ ratio was high in microvilli extending from the edge of cells and in microvilli fixed to the top surface of cells (Fig. 1A). SE images were useful for cell morphology (Fig. 1A).

PFO* forms large oligomers when it binds to membranes containing cholesterol (8), and we were concerned that PFO* oligomerization might influence the distribution of [^{15}N]PFO* binding. For that reason, we performed NanoSIMS imaging with another cholesterol-binding protein, ALO-D4, which binds cholesterol in a manner similar to PFO* but does not form large oligomers (7). NanoSIMS images of [^{15}N]ALO-D4 binding to CHO cells were similar to those obtained with [^{15}N]PFO* (Fig. 1B); both bound preferentially to microvilli. Preferential binding of [^{15}N]ALO-D4 to microvilli was also evident in high-resolution

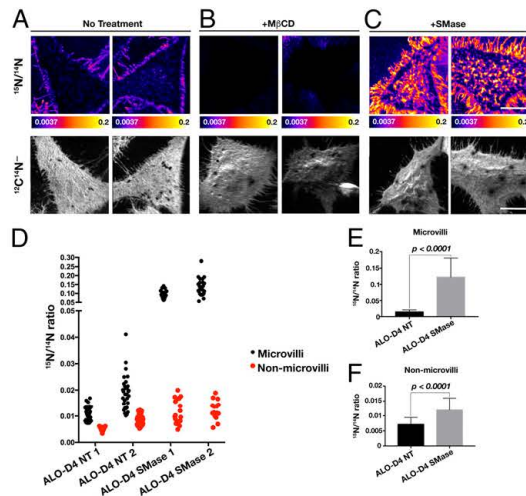


Fig. 2. NanoSIMS analysis of [^{15}N]ALO-D4 binding to the plasma membrane of CHO-K1 cells grown under standard conditions. CHO-K1 cells (imaged in A–C) were plated on silicon wafers and grown overnight and given either no treatment (A), treated with 10 mM methyl- β -cyclodextrin (+MBCD) for 15 min at 37 $^{\circ}\text{C}$ (B), or treated with 100 milliunits/mL of sphingomyelinase for 30 min at 37 $^{\circ}\text{C}$ (+SMase) (C). The cells were then washed and incubated with 20 $\mu\text{g}/\text{mL}$ [^{15}N]ALO-D4 for 2 h at 4 $^{\circ}\text{C}$. NanoSIMS images were generated based on $^{12}\text{C}^{15}\text{N}^-$ ions (to visualize cell morphology) and on the $^{15}\text{N}/^{14}\text{N}$ ratio. (Scale bar, 10 μm .) The color scale shows the range of $^{15}\text{N}/^{14}\text{N}$ ratios. (D) $^{15}\text{N}/^{14}\text{N}$ ratios in microvilli (black solid circles) and nonmicrovilli regions (red solid circles) ($n = 30$) of the plasma membrane of two nontreated (NT) and SMase-treated (SMase) CHO-K1 cells. (E and F) Bar graphs depicting $^{15}\text{N}/^{14}\text{N}$ ratios in microvilli and nonmicrovilli regions of the plasma membrane in NT and SMase-treated cells. Data were analyzed with an unpaired Student's t test with Welch's correction.

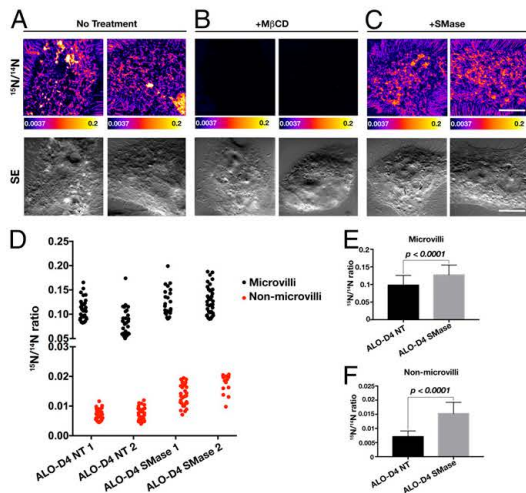


Fig. 3. NanoSIMS imaging of [^{15}N]ALO-D4 binding to the plasma membrane of CHO-K1 cells that had been loaded with cholesterol. CHO-K1 cells were plated on silicon wafers and grown for 5 d. The cells were then loaded with cholesterol by incubating the cells for 2 d in medium containing 300 μM cholesterol (*Materials and Methods*). The cells were then washed and grown without supplemental cholesterol for 44 h. Next, the cells were plated on silicon wafers, grown overnight, and then given no treatment (A); treated with 10 mM methyl- β -cyclodextrin for 15 min at 37 $^{\circ}\text{C}$ (+M β CD) (B); or treated with 100 milliunits/mL of sphingomyelinase for 30 min at 37 $^{\circ}\text{C}$ (+SMase) (C). The cells were then washed and incubated with 20 $\mu\text{g}/\text{mL}$ [^{15}N]ALO-D4 for 2 h at 4 $^{\circ}\text{C}$. NanoSIMS images were generated based on secondary electrons (SEs) and on the ratio of $^{12}\text{C}^{15}\text{N}^{-}$ to $^{12}\text{C}^{14}\text{N}^{-}$ secondary ions ($^{15}\text{N}/^{14}\text{N}$). (Scale bar, 10 μm .) The color scale shows the range of $^{15}\text{N}/^{14}\text{N}$ ratios. (D) $^{15}\text{N}/^{14}\text{N}$ ratios in microvilli (black solid circles) and nonmicrovilli regions (red solid circles) ($n = 30$) of two nontreated (NT) and SMase-treated (SMase) cells. (E and F) Bar graphs of $^{15}\text{N}/^{14}\text{N}$ ratios in microvilli and nonmicrovilli regions on the plasma membrane of NT and SMase-treated cells. Data were analyzed with an unpaired Student's t test with Welch's correction.

NanoSIMS images (Fig. 1C). Using those images, we analyzed the $^{15}\text{N}/^{14}\text{N}$ ratio along straight lines that traversed microvilli; these line scans revealed that $^{15}\text{N}/^{14}\text{N}$ ratios were about fivefold higher in microvilli than in surrounding regions free of microvilli ("meadows") (Fig. 1D). The high-resolution NanoSIMS images had a lateral resolution of 70 nm (Fig. 1F) by the 16–84% definition (9). Microvilli on CHO-K1 cells on silicon wafers were also documented by scanning electron microscopy (Fig. 1E and F).

To gauge the specificity of [^{15}N]ALO-D4 binding to cholesterol, we performed NanoSIMS imaging of cells in which cholesterol stores had been depleted with M β CD and cells in which the sphingomyelin-sequestered cholesterol pool had been released with SMase. In our first such experiments, we used CHO cells that had been cultured under standard conditions (i.e., no supplemental cholesterol) (Fig. 2). In the absence of M β CD or SMase, the $^{15}\text{N}/^{14}\text{N}$ images revealed preferential binding of [^{15}N]ALO-D4 to microvilli on the plasma membrane (Fig. 2A). Treatment of cells with M β CD virtually eliminated [^{15}N]ALO-D4 binding to cells (Fig. 2B). After SMase treatment of cells, the binding of [^{15}N]ALO-D4 increased (Fig. 2C). Further analyses revealed that SMase treatment resulted in an average sixfold increase in the $^{15}\text{N}/^{14}\text{N}$ ratio on microvilli but only an approximately twofold increase in adjacent meadows (Fig. 2D–F). When $^{15}\text{N}/^{14}\text{N}$ ratios from entire cells were considered, they were 0.014 ± 0.003 in nontreated cells, 0.0037 ± 0.0002 in M β CD-treated cells

(identical to the natural abundance of ^{15}N), and 0.057 ± 0.0096 in SMase-treated cells.

NanoSIMS imaging of [^{15}N]ALO-D4 binding was also performed on CHO-K1 cells that had been loaded with cholesterol (Fig. 3). As expected, the amount of [^{15}N]ALO-D4 binding to cells was higher in cholesterol-loaded cells ($^{15}\text{N}/^{14}\text{N}$ ratio of 0.033 ± 0.0025 vs. 0.014 ± 0.003 in cells grown without supplemental cholesterol). Again, [^{15}N]ALO-D4 bound preferentially to microvilli (Fig. 3A), and the binding of [^{15}N]ALO-D4 to cells was virtually eliminated by M β CD (Fig. 3B). Treatment of cholesterol-loaded cells with SMase resulted in increased [^{15}N]ALO-D4 binding ($^{15}\text{N}/^{14}\text{N}$ ratio of 0.042 ± 0.0018 vs. 0.033 ± 0.0025 in nontreated cells) (Fig. 3C). In the cholesterol-loaded cells, SMase treatment increased the $^{15}\text{N}/^{14}\text{N}$ ratio in microvilli but only by $\sim 30\%$ (Fig. 3D–F), whereas the $^{15}\text{N}/^{14}\text{N}$ ratio in meadows nearly doubled.

NanoSIMS imaging was sufficiently sensitive to visualize nonspecific binding of [^{15}N]ALO-D4 to the polysiloxane-coated silicon wafer substrate (Fig. S1). When we quantified ^{15}N enrichment in cell-free regions of the silicon wafer substrate (between microvilli at the edges of cells), we found a $^{15}\text{N}/^{14}\text{N}$ ratio of ~ 0.006 (greater than ^{15}N 's natural abundance), implying that there was nonspecific binding of [^{15}N]ALO-D4 to the polylysine-coated silicon wafer substrate. The $^{15}\text{N}/^{14}\text{N}$ ratio in the plasma membrane of cells on the

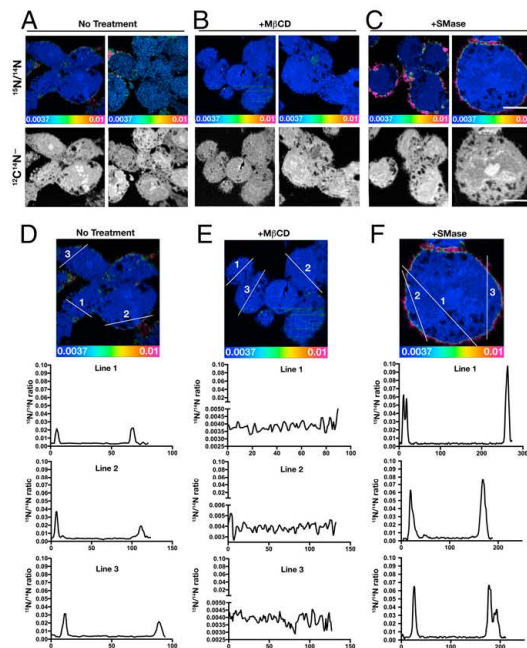


Fig. 4. NanoSIMS analysis of [^{15}N]ALO-D4 binding to CHO-K1 cells. CHO-K1 cells were plated on Thermanox plastic coverslips and grown for 5 d. The cells were then loaded with cholesterol as described in *Materials and Methods*. Coverslips received no treatment (A); treatment with 10 mM methyl- β -cyclodextrin for 15 min at 37 $^{\circ}\text{C}$ (+M β CD) (B); or treatment with 100 milliunits/mL of sphingomyelinase for 30 min at 37 $^{\circ}\text{C}$ (+SMase) (C). The cells were then washed and incubated with 20 $\mu\text{g}/\text{mL}$ [^{15}N]ALO-D4 at 4 $^{\circ}\text{C}$ for 2 h. Next, the cells were fixed, dehydrated, resin embedded, and sectioned. NanoSIMS images were generated based on $^{12}\text{C}^{14}\text{N}^{-}$ secondary ions (to define cell morphology) and $^{15}\text{N}/^{14}\text{N}$ ratios (to visualize binding of [^{15}N]ALO-D4). Peaks in $^{15}\text{N}/^{14}\text{N}$ ratios on the line graphs are centered above the plasma membrane. (Scale bar, 10 μm .) (D–F) Line graphs showing $^{15}\text{N}/^{14}\text{N}$ ratios across cells.

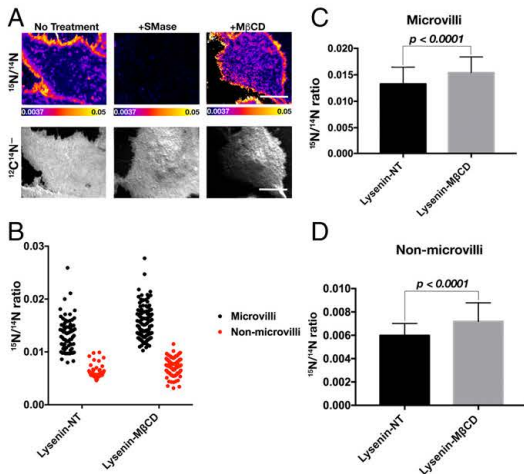


Fig. 5. NanoSIMS imaging of [¹⁵N]lysine binding to CHO-K1 cells. CHO-K1 cells were plated on silicon wafers. (A) The cells received either no treatment (NT); treatment with 100 milliunits/mL of sphingomyelinase for 30 min at 37 °C (+SMase); or treatment with 10 mM MβCD for 15 min (+MβCD) at 37 °C. The cells were then washed and incubated with 20 μg/mL [¹⁵N]lysine for 1 h at 4 °C. NanoSIMS images were generated based on ¹²C/¹³C secondary ions (to define cell morphology) and on the ¹⁵N/¹⁴N ratio (to visualize [¹⁵N]lysine binding). (Scale bar, 10 μm.) (B) ¹⁵N/¹⁴N ratios in microvilli (black solid circles) and nonmicrovilli regions (red solid circles) (*n* = 60) of nontreated and MβCD-treated cells. (C and D) Bar graphs depicting ¹⁵N/¹⁴N ratios in microvilli and in nonmicrovilli regions of NT cells and MβCD-treated cells. Data were analyzed with a Student's *t* test with Welch's correction and with a Mann-Whitney test. Both tests yielded the same level of statistical significance.

same silicon wafer was 0.033 ± 0.0025 . In cells that had been treated with MβCD, the ¹⁵N/¹⁴N ratio in the plasma membrane fell to 0.0038 ± 0.0001 (very close to the natural abundance of ¹⁵N), demonstrating that MβCD was effective in eliminating specific binding of [¹⁵N]ALO-D4 to plasma membrane cholesterol. In contrast, the ¹⁵N/¹⁴N ratio of the cell-free substrate was 0.006 (Fig. S1). Thus, the low levels of nonspecific [¹⁵N]ALO-D4 binding to the polylysine-coated silicon wafer substrate were not altered by MβCD.

In the NanoSIMS images shown in Figs. 1–3, which were acquired with cells plated on silicon wafers, our assumption was that [¹⁵N]ALO-D4 binding was confined to the plasma membrane. To assess the validity of this assumption, we performed NanoSIMS analysis on sections of cells. The NanoSIMS images of sectioned cells (Fig. 4) revealed that the ¹⁵N-enrichment was confined to the plasma membrane (Fig. 4 A–C). Again, [¹⁵N]ALO-D4 binding to the plasma membrane was virtually eliminated by MβCD, whereas [¹⁵N]ALO-D4 binding increased after SMase treatment (Fig. 4 A–C). Line diagrams revealed a high ¹⁵N/¹⁴N ratio over the plasma membrane, whereas the ¹⁵N/¹⁴N ratio inside the cells was identical to the natural value (0.0037) (Fig. 4 D–F).

An earlier NanoSIMS study found large patches of sphingolipids on the plasma membrane of 3T3 fibroblasts, whereas cholesterol was distributed evenly (5). However, because cholesterol and sphingomyelin are thought to interact loosely and transiently in the plasma membrane, we wanted to examine sphingomyelin distribution on the plasma membrane with lysenin (a sphingomyelin-binding protein). We prepared a ¹⁵N-labeled lysenin, incubated it with CHO-K1 cells, and then used NanoSIMS imaging to assess the distribution of lysenin binding (Fig. 5). As judged by ¹⁵N/¹⁴N images, [¹⁵N]lysine appeared to bind preferentially to microvilli (Fig. 5A). Treatment of cells with SMase markedly reduced [¹⁵N]lysine

binding (Fig. 5B). The ¹⁵N/¹⁴N ratio in the entire plasma membrane of SMase-treated cells was 0.0043 ± 0.0003 vs. 0.012 ± 0.0001 in nontreated cells. In MβCD-treated cells, the ¹⁵N/¹⁴N ratio was slightly higher (0.016 ± 0.0063) (Fig. 5C). Further analyses showed a higher ¹⁵N/¹⁴N ratio in microvilli of MβCD-treated cells (Fig. 5 D–F). The finding of increased lysenin binding to MβCD-treated cells contrasts with findings of an earlier study (10) and raises the possibility that depletion of plasma membrane cholesterol might increase accessibility of plasma membrane sphingomyelin to lysenin.

Confocal microscopy confirmed that ALO-D4 and lysenin bind preferentially to microvilli at the edges of cells (Fig. 6) but the colocalization of ALO-D4 and lysenin was not perfect (e.g., there were patches of lysenin binding that did not coincide with ALO-D4 binding). Confocal microscopy allowed us to detect large differences in ALO-D4 and lysenin binding (e.g., reduced ALO-D4 binding to MβCD-treated cells or reduced lysenin binding to SMase-treated cells) (Fig. 6). However, confocal imaging did not allow us to be confident about smaller changes, for example increased binding of ALO-D4 to SMase-treated cells (Fig. 6).

Discussion

We used NanoSIMS imaging to visualize and quantify the binding of ¹⁵N-labeled cholesterol- and sphingomyelin-binding proteins to the plasma membrane of CHO cells. Earlier biochemical studies (2) thoroughly characterized ¹²⁵I-PFO* to fibroblasts and CHO cells but did not address whether the amount of PFO* binding is influenced by morphologic or topographic features of the plasma membrane. In this study, we chose to investigate the binding of PFO* and ALO-D4 to CHO cells because ultrastructural studies had shown that the surface of CHO cells is not flat and featureless but instead complex—with numerous microvilli projecting from the surface of the cells (11). One of our goals was to define (and quantify) the relationship between cell morphology and PFO* and ALO-D4 binding. NanoSIMS is ideal for this purpose because it provides high-resolution images—higher than those obtained by

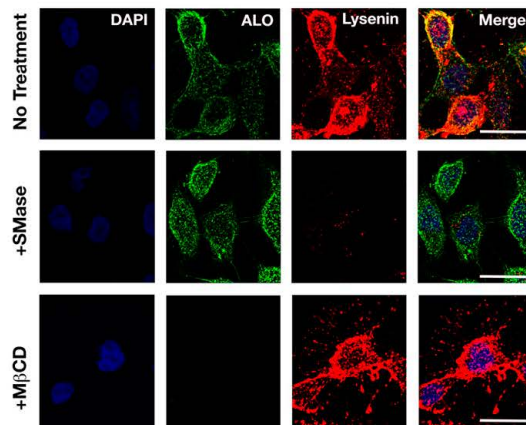


Fig. 6. Immunofluorescence microscopy to assess the binding of ALO-D4 and mCherry-lysenin to CHO-K1 cells. CHO-K1 cells were plated on glass coverslips and grown overnight before receiving one of three treatments: incubating cells in medium alone at 37 °C for 30 min (i.e., no treatment); incubating cells with medium containing 100 milliunits/mL of SMase at 37 °C for 30 min (+SMase); or incubating cells with medium containing 10 mM MβCD at 37 °C for 15 min (+MβCD). Binding of ALO-D4 and lysenin to the surface of cells was assessed by confocal microscopy as described in *SI Materials and Methods*. Cell nuclei were visualized with DAPI (blue). (Scale bar, 20 μm.)

confocal microscopy (12). Also, NanoSIMS offers the unique capability to correlate chemical information (e.g., specific secondary ions) to high-resolution morphology. In our study, we assessed binding of the lipid-binding proteins to cells by calculating the ratio of $^{12}\text{C}^{15}\text{N}$ ions (from ^{15}N -labeled proteins) to $^{12}\text{C}^{14}\text{N}$ ions (from lipids and proteins of the plasma membrane). Images of secondary electrons or $^{12}\text{C}^{14}\text{N}$ ions were used to define cell morphology. We found that the binding of PFO* and ALO-D4 to the plasma membrane was not uniform; instead, these proteins bind preferentially to microvilli. Lysenin, a sphingomyelin-binding protein, also bound preferentially to microvilli on cells.

Our NanoSIMS images showed markedly reduced [^{15}N]ALO-D4 binding to M β CD-treated cells and significantly increased [^{15}N]ALO-D4 binding to SMase-treated cells. These findings are entirely consistent with the biochemical findings by Das et al. (2). However, NanoSIMS analysis provided a more nuanced understanding of ALO-D4 binding to cells, showing that [^{15}N]ALO-D4 binds in a preferential fashion to microvilli. In addition, when CHO-K1 cells grown under standard conditions were treated with SMase, NanoSIMS analysis revealed an ~10-fold increase in [^{15}N]ALO-D4 binding to microvilli. When the cells were loaded with cholesterol and subsequently treated with SMase, [^{15}N]ALO-D4 binding to microvilli increased by only about 30%. These results suggest that numbers of ALO-D4 binding sites on microvilli of cholesterol-loaded cells were close to maximal, such that release of "sphingomyelin-sequestered cholesterol" had a limited capacity to increase ALO-D4 binding.

The finding that accessible cholesterol is enriched in microvilli is potentially relevant to cholesterol transport. Microvilli vastly increase the surface area of the plasma membrane without necessitating a large increase in cell volume. In intestinal enterocytes, microvilli are essential for absorption of nutrients. However, microvilli exist in many other cell types and are likely relevant to nutrient transfer as well. For example, microvilli on parenchymal cells of the adrenal gland have been proposed to play a role in cholesterol transport (13). Along these lines, we suspect that the high levels of accessible cholesterol on microvilli of CHO cells (as judged by high levels of ALO-D4 binding), could facilitate transfer of cholesterol away from the plasma membrane.

Studies of model membranes have suggested that cholesterol can affect membrane curvature and in some cases may promote positive membrane curvature (14, 15). Thus, one possibility is that a large amount of cholesterol in plasma membrane microvilli is relevant to both membrane curvature and increased ALO-D4 binding. A second possibility (perhaps more likely and not mutually exclusive) is that the curvature of the plasma membrane (dictated by the actin cytoskeleton) causes cholesterol to be more exposed, thereby facilitating ALO-D4 binding. In highly curved membranes, such as those covering microvilli, it is possible that the polar regions of lipids at the surface of the exofacial leaflet are less densely packed than the acyl chains of plasma

membrane phospholipids. Such a scenario might facilitate ALO-D4 binding. The NanoSIMS images in the current studies cannot distinguish between the two possibilities, but it is conceivable that future NanoSIMS experiments could be useful. In principle, it might be possible to load cultured cells with [^{18}O]cholesterol (5) and then use NanoSIMS imaging to quantify [^{15}N]ALO-D4 binding, relative to [^{18}O]cholesterol, in both microvilli and regions of the plasma membrane lacking microvilli. In preliminary studies, we attempted to visualize [^{18}O]cholesterol in the plasma membrane of [^{18}O]cholesterol-loaded cells, but we were not successful. We found abundant [^{18}O]cholesterol in cytosolic lipid droplets, but the amounts of [^{18}O]cholesterol in the plasma membrane were not sufficient to visualize microvilli at the edges of cells.

Our NanoSIMS images suggested that the distributions of ALO-D4 and lysenin binding sites on the plasma membrane were similar (but not identical) to preferential binding to microvilli. Earlier NanoSIMS images of 3T3 fibroblasts revealed distinct distributions for [^{18}O]cholesterol and [^{15}N]sphingolipids on the plasma membrane (5). One obvious explanation for the different results is that the two studies used different cell lines. Another is that the numbers of ^{18}O secondary ions in the 3T3 fibroblast studies may not have been sufficient to discern non-homogeneities in cholesterol distribution. Also, the ^{18}O secondary ions in the 3T3 cell studies would likely reflect all cholesterol molecules in the plasma membrane, whereas the ^{15}N ions in our studies would reflect only the accessible cholesterol pool. Again, it is conceivable that one could resolve the distribution of accessible cholesterol from the total cholesterol pool by examining [^{15}N]ALO-D4 binding to cells that had been loaded with ^{13}C - or ^{18}O -labeled cholesterol, but those sorts of studies could prove to be challenging. Aside from needing to enrich cells with sufficient amounts of labeled cholesterol for imaging, one would need to be confident that the secondary ions released from cells actually originate from labeled cholesterol on the plasma membrane. Recent time-of-flight secondary ion mass spectrometry (TOF-SIMS) studies of cholesterol in fixed mouse brain sections suggested that cholesterol can migrate from deeper portions of the section to the surface of the section, and that this apparent migration occurs under experimental conditions similar to those used in NanoSIMS imaging (16).

ACKNOWLEDGMENTS. We thank Dr. Arun Radhakrishnan for PFO* and ALO-D4 vectors and for scientific discussions, Frederick Maxfield for helpful discussions, and the NanoSIMS facilities at Caltech and the University of Western Australia for technical guidance. We acknowledge support from Leducq Foundation Transatlantic Network Grant 12CVD04 (to S.G.Y.); National Institutes of Health Grants P01 HL090553 (to S.G.Y.), R01 HL087228 (to S.G.Y.), and HL125335 (to S.G.Y.); the Ruth L. Kirschstein National Research Service Award F32 HL132471 (to C.H.); the Australian Microscopy and Microanalysis Research Facility; the Science and Industry Endowment Fund; and the State Government of Western Australia.

- Das A, Goldstein JL, Anderson DD, Brown MS, Radhakrishnan A (2013) Use of mutant 125I-perfringolysin O to probe transport and organization of cholesterol in membranes of animal cells. *Proc Natl Acad Sci USA* 110(26):10580–10585.
- Das A, Brown MS, Anderson DD, Goldstein JL, Radhakrishnan A (2014) Three pools of plasma membrane cholesterol and their relation to cholesterol homeostasis. *eLife* 3:02882.
- Brown DA, Rose JK (1992) Sorting of GPI-anchored proteins to glycolipid-enriched membrane subdomains during transport to the apical cell surface. *Cell* 68(3):533–544.
- Owen DM, Magenau A, Williamson D, Gaus K (2012) The lipid raft hypothesis revisited: New insights on raft composition and function from super-resolution fluorescence microscopy. *BioEssays* 34(9):739–747.
- Frizz Jr, et al. (2013) Sphingolipid domains in the plasma membranes of fibroblasts are not enriched with cholesterol. *J Biol Chem* 288(23):16855–16861.
- Jiang H, et al. (2014) High-resolution imaging of dietary lipids in cells and tissues by NanoSIMS analysis. *J Lipid Res* 55(10):2156–2166.
- Gay A, Rye D, Radhakrishnan A (2015) Switch-like responses of two cholesterol sensors do not require protein oligomerization in membranes. *Biophys J* 108(6):1459–1469.
- Hotze EM, et al. (2002) Monomer-monomer interactions drive the prepore to pore conversion of a beta-barrel-forming cholesterol-dependent cytotoxin. *J Biol Chem* 277(13):11597–11605.
- Lechene C, et al. (2006) High-resolution quantitative imaging of mammalian and bacterial cells using stable isotope mass spectrometry. *J Biol* 5(6):20.
- Mizuno H, et al. (2011) Fluorescent probes for superresolution imaging of lipid domains on the plasma membrane. *Chem Sci* 2:1548–1553.
- Carpentier JL, Paccaud JP, Gorden P, Rutter WJ, Orci L (1992) Insulin-induced surface redistribution regulates internalization of the insulin receptor and requires its autophosphorylation. *Proc Natl Acad Sci USA* 89(1):162–166.
- Saka SK, et al. (2014) Correlated optical and isotopic nanoscopy. *Nat Commun* 5:3664.
- Reaven E, Spicher M, Azhar S (1989) Microvillar channels: A unique plasma membrane compartment for concentrating lipoproteins on the surface of rat adrenal cortical cells. *J Lipid Res* 30(10):1551–1560.
- Chen Z, Rand RP (1997) The influence of cholesterol on phospholipid membrane curvature and bending elasticity. *Biophys J* 73(1):267–276.
- Sodt AJ, Venable RM, Lyman E, Pastor RW (2016) Nonadditive compositional curvature energetics of lipid bilayers. *Phys Rev Lett* 117(13):138104.
- Sjovall P, Johansson B, Lausmaa J (2006) Localization of lipids in freeze-dried mouse brain sections by imaging TOF-SIMS. *Appl Surf Sci* 252:6966–6974.